Novel TiO2-based composite co-catalysts for solar driven water purification

dela Rosa, Francis Monserrata

University of Zagreb

FACULTY OF CHEMICAL ENGINEERING AND TECHNOLOGY

Universitat de Girona

FACULTY OF SCIENCES

Francis Monserrata dela Rosa

NOVEL TiO_2 – BASED COMPOSITE CO-CATALYSTS FOR SOLAR DRIVEN WATER PURIFICATION

INTERNATIONAL DUAL DOCTORATE

Zagreb, 2023.

SVEUČILIŠTE U ZAGREBU
FAKULTET KEMIJSKOG INŽENJERSTVA I TEHNOLOGIJE

Kandidat **Francis Monserrata dela Rosa**

predao je dana: 26. siječnja 2023. doktorski rad izrađen pod mentorstvom prof. dr. sc. Hrvoja Kušića, Sveučilište u Zagrebu Fakultet kemijskog inženjerstva i tehnologije i prof. dr. sc. Mire Petrović, Catalan Institute for Water Research (ICRA), Girona, Španjolska.

Povjerenstvo za ocjenu doktorskog rada u sastavu:

1. prof. dr. sc. Sandra Babić, Sveučilište u Zagrebu Fakultet kemijskog inženjerstva i tehnologije – predsjednik Povjerenstva
2. izv. prof. dr. sc. Dajana Kučić Grgić, Sveučilište u Zagrebu Fakultet kemijskog inženjerstva i tehnologije
3. prof. dr. sc. Lidija Ćurković Sveučilište u Zagrebu Fakultet strojarstva i brodogradnje
4. dr. sc. Gianluigi Buttiglieri, Catalan Institute for Water Research (ICRA), Girona, Španjolska
5. dr. sc. Meritxell Gross, Catalan Institute for Water Research (ICRA), Španjolska

pozitivno je ocijenilo doktorski rad doktoranda Vedrana Đurine, a Fakultetsko vijeće Sveučilišta u Zagrebu Fakulteta kemijskog inženjerstva i tehnologije na sjednici održanoj dana 20. ožujka 2023. prihvatilo je ocjenu i odobrilo obranu doktorskog rada pred povjerenstvom u istom sastavu.

Obrana doktorskog rada održana je dana 17. travnja 2023.

D e k a n

prof. dr. sc. Ante Jukić

University of Zagreb

FACULTY OF CHEMICAL ENGINEERING AND TECHNOLOGY

Universitat de Girona

FACULTY OF SCIENCES

Francis Monserrata dela Rosa

NOVEL TiO_2 – BASED COMPOSITE CO-CATALYSTS FOR SOLAR DRIVEN WATER PURIFICATION

INTERNATIONAL DUAL DOCTORATE

Supervisors:

Prof. Hrvoje Kušić, PhD

Prof. Mira Petrović, PhD

Zagreb, 2023.

University of Zagreb

Universitat de Girona

FAKULTET KEMIJSKOG INŽENJERSTVA I TEHNOLOGIJE

FACULTY OF SCIENCES

Francis Monserrata dela Rosa

NOVI KOMPOZITNI KOKATALIZATORI TEMELJENI NA TiO_2 ZA PROČIŠĆAVANJE VODE POD DJELOVANJEM SUNČEVA ZRAČENJA

MEĐUNARODNI DVOJNI DOKTORAT

Mentori:

Prof. dr. sc. Hrvoje Kušić

Prof. dr. sc. Mira Petrović

Zagreb, 2023.

University of Zagreb

FACULTY OF CHEMICAL ENGINEERING AND TECHNOLOGY

Universitat de Girona

FACULTAD DE CIENCIAS

Francis Monserrata dela Rosa

NUEVOS COCATALIZADORES COMPUESTOS A BASE DE TiO_2 PARA LA PURIFICACIÓN DE AGUA IMPULSADA POR SOLAR

DOCTORADO DUAL INTERNACIONAL

Supervisores:

Prof. Dr. Hrvoje Kušić

Prof.ª Dr.ª Mira Petrović

Zagreb, 2023.

- Bibliographic page
- UDK: 628.3:544.526.5:549.514.6(043.3)=111
- Scientific area: Technical Sciences
- Scientific field: Chemical Engineering
- Scientific branch: Environmental Protection in Chemical Engineering
- Institutions:

  University of Zagreb, Faculty of Chemical Engineering and Technology

  University of Girona, Girona, Spain

  Catalan Institute for Water Research, Girona, Spain
- Supervisors: Prof. Hrvoje Kušić, PhD and Prof. Mira Petrović, PhD
- Number of pages: 151 (with Appendix)
- Number of figures: 57
- Number of tables: 19
- Number of appendices: 26
- Number of references: 250
- Date of defense: 17 April 2023
- Defense Committee:
  Prof. Sandra Babić, PhD, University of Zagreb, Faculty of Chemical Engineering and Technology

  Assoc. Prof.Dajana Kučić Grgić, PhD, University of Zagreb, Faculty of Chemical Engineering and Technology

  Prof. Lidija Ćurković, PhD, University of Zagreb, Faculty of Mechanical Engineering and Naval Architecture

  Dr. Gianluigi Buttiglieri, PhD Catalan Institute for Water Research (ICRA), Spain

  Dr. Meritxell Gros, PhD, Catalan Institute for Water Research (ICRA), Spain
- The thesis is stored at:

  National and University Library in Zagreb, Hrvatske bratske zajednice bb; Library of Faculty

  of Chemical Engineering and Technology, University of Zagreb, Marulićev trg 20.

The topic of this thesis

NOVEL TiO_2 – BASED COMPOSITE CO-CATALYSTS FOR SOLAR DRIVEN WATER PURIFICATION

was accepted at the 249th session of the Faculty of Chemical Engineering and Technology, University of Zagreb Faculty Council, held on November 22, 2021, and approved at the 6th session of the University of Zagreb Senate held on February 15, 2022.

ACKNOWLEDGEMENTS

First of all, I would like to thank and acknowledge European Union (EU) for creating Marie Sklodowska-Curie Actions (MSCA). MSCA brings equality regardless of race, gender and societal status, and I feel really blessed to be part of it. Also, I thank Nowelties project and everyone involved in its creation and development. Special thanks to our overall coordinator and my co-supervisor, Prof. Mira Petrović, for organizing this wonderful consortium.

To my host mentor, Prof. Hrvoje Kušić, we made it. Thank you for guiding me through this rocky-road three years consisting of COVID-19 and earthquakes. Also, I would like to thank you both including Prof. Mira Petrović, for choosing me as the Early Stage Researcher (ESR 10). Words are not enough to express my gratitude to both of you.

To my 13 colleagues in Nowelties, we have come a long way. I hope that our paths will cross again someday. I wish you all the best.

To colleagues who helped me through this journey, my warmest thanks to all of you. Special mention to Prof. Maria Jose Farre (from ICRA) for helping me conduct LC-Orbitrap analysis. It was an amazing opportunity to work with you. To Prof. Marijana Kraljić-Roković (from FKIT), I would like to thank you a lot for opening the doors of Electrochemistry Department to me. I learn a lot from you and I hope that I can still work with you in the future. Also, I would like to thank you as well for inviting me in picnic in your backyard and swimming together with your family. You made me feel that Croatia is my real home.

To my FKIT family, first I would like to thank Assist. Prof. Marin Kovačić for helping me in LC-MS/MS, HPLC, equipments/software and all other inquiries needed for my Thesis. Without you, this work is not possible. I also would like to thank Prof. Ana Lončarić Božić for the support and help through out these years. Special thanks to Assist. Prof. Zvonimir Katančić for letting me use your laboratory and other equipments. It is really a great help for me. To Prof. Zlata for the chit-chat and also to Neda. I would like also to thank my fellow PhD colleagues, Marin B, Ana Maria and Lucija for time to time chit-chat and sometimes drinks in Krivi put. Also, I would like to thank Andrej Vidak for touring me in restaurants and exploring Croatian cuisine. Also, i would like to thank Marjan for teaching and inviting me for swimming in Krk.

Special mention to my beautiful former and current colleagues, first i would like to thank my undergraduate classmate Rob for sharing your erasmus and PhD experience here in EU, without you i will not know about euraxess and marie curie fellowships. Thank you for being a real friend to me. Next, here in FKIT, I would like to thank Stefani for being a nice and calm friend to me. I wish you the best for your new upcoming baby. To Antonija, it has been 3 rocky-road years for our PhDs. Congratulations to you, and I also thank you a lot for helping us in the Police during our first time in Croatia. I wish you all the best. To Marin Popović, first, I would like to thank you for all the support regarding instrumentations in Karlovac. I will miss our train and bus trip going there. Also, I would like to thank you for being a good friend of mine, for sharing stories in Anime and other comic and comedic things in life. I found a brother in you. I wish you all the best. To Josipa, first, I would like to thank you for sharing me different food that you had specially on my first months in Croatia. Thank you for teaching me healthy stuffs. In addition, I would like to thank you for all the help inside (for helping me run toxicity studies) and outside of laboratory. You are one of the people who made my stay in Croatia so memorable and fruitful. Like what I have said earlier above, words are not enough to thank you. I found a sister in you. I wish you all the best. Lastly, to Klara, first, I would like to thank you for being my review-paper buddy, this means a lot to me. We work very well together. Second, I would like to thank you for opening the doors of your home in Zadar, together with Dino and Marijana. My stay in Croatia will not be the same without you. When I think about Croatia, the first thing that will come to my mind is you. Thank you for all the happy and crazy memories here. This PhD is not possible without your care and positive aura that I absorb.

To my parents, Rizalito and Josephine whom consistently support me all the time. Thank you very much for everything. Your words of encouragement brings light to me. This journey is not possible without the two of you.

Last but not the least, To my Savior, Jesus Christ. All of these knowledge are from you. To GOD be the glory!

Taos pusong pasasalamat!

Francis M. dela Rosa
Franjo

Nowelties

European Joint Doctorate

This work is supported by the European Union's Horizon 2020 research and innovation program under Marie Sklodowska-Curie grant agreement № 812880 – Nowelties ITN-EJD project.

EXTENDED ABSTRACT

Accessible clean water is among the highest priorities for sustainable economic growth and societal wellbeing. Water supports life and is a crucial resource for humanity; it is also at the core of natural ecosystems and climate regulation. Water stress is primarily a water quantity issue, but it also occurs as a consequence of a deterioration of water quality and a lack of appropriate water management. Environmental problems that are associated with water pollution have been a persistently important issue over recent decades, correlated negatively with the health and ecosystem. The occurrence of trace amounts of antibiotics in various bodies of water was directly linked to the development of antibiotic resistant pathogens. Over the last two decades, penicillins have been widely prescribed and used across Europe. Recently, Amoxicillin (AMX) was added to the second and third EU "watch list" based on the Decision 2018/840/EU and 2020/1161/EU, respectively. Its presence in wastewater effluents is related to limited removal by common municipal wastewater treatment plants (WWTP's) based on primary (physical) and secondary (biological) treatment. Therefore, the new remediation techniques must be implemented within the water treatment train to remove such recalcitrant substances.

Advanced oxidation processes (AOPs) have gained much research attention due to their innate ability to provide effective oxidation of a wide variety of organic pollutants persistent to conventional wastewater treatment methods. AOPs effectiveness rely on highly reactive and non-selective species, primarily hydroxyl radicals (HO•). Among various AOPs, semiconductor photocatalysis greatly attracts attention due to stability of the semiconductor material and potential to use abundant solar energy to degrade organic pollutants.

The most widely investigated and employed photocatalyst in water purification is TiO_2. However, TiO_2 suffers from the fast recombination of photogenerated charges (i.e., electron/hole pairs; e^-/h^+) and is only active under UV light due its wide band gap (3.0-3.2 eV), thus hindering its potential for solar-driven applications. These deficiencies can be improved by the following strategies: doping with metals and/or non-metals, dye sensitization, incorporation with carbon nanotubes, reduced graphene oxide and coupling with other semiconductors with narrow band gaps. Coupling of TiO_2 with narrow band gap semiconductors with visible light response may promote synergistic effects between two semiconducting materials leading to more efficient charge separation and high photocatalytic activity under visible light irradiation.

Iron oxide (α-Fe_2O_3, also known as hematite) is a promising candidate for coupling with TiO_2, due to its abundance, low cost, stability and visible light activity due to its narrow band gap (2.0–2.2 eV). Most importantly, suitable band-edge positions of hematite promote photogenerated charge separation in TiO_2 via heterojunction transfer. Despite several photocatalytic applications of Fe_2O_3/TiO_2 composites for the removal of contaminants of emerging concern (CECs), all studies investigated their applications in the suspension system (i.e., employing a powdered form of photocatalyst), while the application of immobilized Fe_2O_3/TiO_2 composites are scarcely reported. Moreover, treatment of AMX under solar/visible light using Fe_2O_3/TiO_2, as well as the ecotoxicity of AMX degradation/transformation by-products is rarely explored.

In this dissertation, removal of AMX in pure water was investigated using sandwich-type Fe_2O_3/TiO_2 layered films made of commercially available nanomaterials (Part 1) and using synthesized Fe_2O_3/TiO_2 made of pure chemical precursors (Part 2).

In part 1, sandwich-type composites made of commercial TiO_2-P25 and α-Fe_2O_3 are obtained in a form of thin films by spin coating, possessing different layer configurations, namely: (i) TiO_2 layer over α-Fe_2O_3 (TiO_2@α-Fe_2O_3), (ii) α-Fe_2O_3 layer over TiO_2 (α-Fe_2O_3@TiO_2), and (iii) physically mixed 50% (*w/w*) of TiO_2/Fe_2O_3. Photocatalytic activity under simulated solar irradiation of the aforementioned composites and their pure components is investigated for the degradation of AMX in the presence and absence of persulfate (PS). In both cases, TiO_2@α-Fe_2O_3 sandwich-type achieved the highest degradation rates of AMX and a marked effect of PS addition on the AMX degradation rate is noted. The influence of pH and PS concentration on AMX degradation rate is established by means of experimental design and response surface modeling which revealed optimum conditions at [$S_2O_8^{2-}$] = 0.334 mM and pH = 4.0. The AMX degradation mechanisms and pathways are studied by means of reactive oxygen species scavenging and identification of intermediates by liquid chromatography with tandem mass spectrometry (LC-MS/MS), respectively. Evolution of formed intermediates is directly correlated with an increased toxicity assessed by *Daphnia magna* and *Vibrio fischeri* assays. Furthermore, biodegradability changes are correlated with the mineralization profile of AMX solution. The influence of water matrix constituents (Cl^-, CO_3^{2-}, NO_3^-, PO_4^{3-} and Suwannee river natural organic matter) on AMX degradation is established as well.

In part 2, Fe_2O_3/TiO_2 nanocomposites were fabricated via a facile impregnation/calcination technique employing different amounts of iron (III) nitrate onto commercial TiO_2 (P25 Aeroxide). The as-prepared Fe_2O_3/TiO_2 nanocomposites were characterized by X-ray diffraction (XRD), Raman spectroscopy (RS), scanning electron microscopy/energy-dispersive spectroscopy (SEM/EDXS), X-ray photoelectron spectroscopy (XPS), Brunauer–Emmett–Teller analysis (BET), electron impedance spectroscopy (EIS), photoluminescence spectroscopy (PL), and diffuse reflectance spectroscopy (DRS). The Fe_2O_3/TiO_2 composite possessing 5% (*w/w*) of Fe_2O_3 showed the highest photocatalytic activity in the slurry system and was thereafter successfully immobilized on glass support. Photocatalytic activity under visible-light irradiation was assessed by treating AMX in the presence and absence of additional oxidants: hydrogen peroxide (H_2O_2) and PS. The influence of pH and PS concentration on AMX conversion rate was established by means of statistical planning and response surface modeling. Results revealed optimum conditions of $[S_2O_8^{2-}]$ = 1.873 mM and pH = 4.808; these were also utilized in presence of H_2O_2 instead of PS in long-term tests. The fastest AMX conversion possessing a zero-order rate constant of 1.51×10^{-7} $M \cdot min^{-1}$ was achieved with the photocatalysis + PS system. The AMX conversion pathway was established, and the evolution/conversion of formed intermediates was correlated with the changes in toxicity toward *Vibrio fischeri*. Reactive oxygen species (ROS) scavenging was also utilized to investigate the AMX conversion mechanism, revealing the major contribution of photogenerated h^+ in all processes.

Key words: Semiconductor solar photocatalysis; Fe_2O_3/TiO_2 composite; amoxicillin; persulfate; transformation products; toxicity

PROŠIRENI SAŽETAK NA HRVATSKOM

Dostupna čista voda jedan je od najvećih prioriteta za održivi gospodarski rast i društvenu dobrobit. Voda podržava život i ključni je resurs za čovječanstvo; također je u srži prirodnih ekosustava i regulacije klime. Vodeni stres prvenstveno je uzrokovan problemom količine vode, ali se javlja i kao posljedica pogoršanja kvalitete vode i nedostatka odgovarajućeg gospodarenja vodom. Problemi okoliša povezani s onečišćenjem vode važno su pitanje tijekom posljednjih desetljeća, te su u negativnoj korelaciji sa zdravljem i ekosustavom. Pojava tragova antibiotika u raznim vodama u okolišu izravno je povezana s razvojem patogena otpornih na antibiotike. Tijekom posljednja dva desetljeća penicilini su naširoko propisivani i korišteni diljem Europe. Nedavno je amoksicilin (AMX) dodan na drugi EU „popis za praćenje" na temelju Odluke Komisije (EU) 2018/840/EU. Njegova prisutnost u otpadnim vodama povezana je s ograničenim uklanjanjem na komunalnim uređajima za pročišćavanje otpadnih voda (UPOV) koji se temelje na primarnom (fizičkom) i sekundarnom (biološkom) pročišćavanju. Stoga se moraju primijeniti nove tehnike remedijacije za uklanjanje takvih tvari.

Nedavno su napredni oksidacijski procesi (AOP) privukli veliku pažnju istraživanča jer osiguravaju učinkovitu oksidaciju širokog spektra organskih onečišćivala koja su otporna na konvencionalne metode obrade vode. Učinkovitost AOP-a oslanja se na visoko reaktivne i neselektivne vrste, prvenstveno hidroksilne radikale (HO•). Među raznim AOP-ima, fotokataliza uz korištenje poluvodičkih materijala uvelike privlači pozornost zbog stabilnosti primjenjenih fotokatalizatora i potencijala korištenja sunčeve energije za razgradnju organskih onečišćivala.

Najviše istraživan i korišten fotokatalizator u pročišćavanju vode je TiO_2. Međutim, nedostatak TiO_2 je brza rekombinacija fotogeneriranih naboja (tj. parova elektron/šupljina; e^-/h^+) te je aktivan samo pod UV svjetlom zbog široke zabranjene zone (3,0-3,2 eV), čime se smanjuje njegov potencijal u primjeni uz sunčevo zračenje. Ovi nedostaci mogu se poboljšati sljedećim strategijama: dopiranjem metalima i/ili nemetalima, senzibilizacijom boje, ugradnjom ugljičnih nanocijevi, reduciranim grafen oksidom i spajanjem s drugim poluvodičima s uskim propusnim pojasima. Spajanje TiO_2 s poluvodičima s uskim razmakom i odzivom na vidljivo svjetlo može pospješiti sinergističke učinke između dva poluvodička materijala što dovodi do učinkovitijeg odvajanja naboja i visoke fotokatalitičke aktivnosti pod zračenjem vidljivim svjetlom.

Željezni oksid (α-Fe_2O_3, također poznat kao hematit) obećavajući je kandidat za spajanje s TiO_2, zbog svoje zastupljenosti, niske cijene, stabilnosti i aktivnosti pod vidljivom svjetlosti zbog uske zabranjene zone (2,0–2,2 eV). Ono što je najvažnije, prikladni rubni položaji hematita promiču fotogenerirano odvajanje naboja u TiO_2 putem prijenosa heterospojnice. Unatoč nekoliko fotokatalitičkih primjena kompozita Fe_2O_3/TiO_2 za uklanjanje postojanih onečišćivala (engl, contaminants of emerging concern, CECs), sve te studije istraživale su njihovu primjenu u suspenziji (tj. upotrebom praškastog oblika fotokatalizatora), dok je primjena imobiliziranih kompozita Fe_2O_3/TiO_2 vrlo rijetka. Štoviše, tretman AMX-a pod sunčevim/vidljivim svjetlom pomoću Fe_2O_3/TiO_2, kao i ekotoksičnost nusproizvoda razgradnje/transformacije AMX-a rijetko se istražuje.

U ovoj disertaciji, uklanjanje AMX-a istraženo je korištenjem slojevitih filmova Fe_2O_3/TiO_2 sendvič tipa izrađenih od komercijalno dostupnih nanomaterijala (1. dio) i korištenjem sintetiziranog Fe_2O_3/TiO_2 napravljenog od čistih kemijskih prekursora (2. dio).

U dijelu 1, kompoziti sendvič tipa izrađeni od komercijalnog TiO_2-P25 i α-Fe_2O_3 dobiveni su centrifugiranjem tankih filmova s različitim konfiguracijama slojeva: i) sloj TiO_2 preko α-Fe_2O_3 (TiO_2@Fe_2O_3), ii) α-Fe_2O_3 sloj preko TiO_2 (α-Fe_2O_3@TiO_2), i iii) fizički pomiješano 50% (*w/w*) TiO_2/ Fe_2O_3. Fotokatalitička aktivnost pod simuliranim sunčevim zračenjem gore spomenutih kompozita i njihovih čistih komponenti istražena je kroz praćenje razgradnje amoksicilina (AMX) u prisutnosti i odsutnosti persulfata (PS). U oba slučaja, TiO_2@α-Fe_2O_3 sendvič tip postigao je najviše stope razgradnje AMX-a i primjećuje se značajan učinak dodatka PS na stopu razgradnje AMX-a. Utjecaj pH i koncentracije PS na brzinu razgradnje AMX-a utvrđen je primjenom eksperimentalnog dizajna i modeliranja površine odziva kojima su određeni optimalni ujveti [$S_2O_8^{2-}$] = 0,334 mM i pH = 4,0. Put razgradnje AMX proučavao je pomoću uklanjanja reaktivnih kisikovih vrsta i identifikacije međuprodukata tekućinskom kromatografijom s tandemskom spektrometrijom mase (LC-MS/MS). Njihovo nastajanje je u izravnoj korelaciji s povećanom toksičnošću procijenjenom testovima *Daphnia magna* i *Vibrio fischeri*. Nadalje, promjene biorazgradljivosti povezane su s profilom mineralizacije AMX otopine. Utvrđen je i utjecaj sastojaka vodene matrice (Cl^-, CO_3^{2-}, NO_3^-, PO_4^{3-} i prirodne organske tvari rijeke Suwannee) na razgradnju AMX-a.

U 2. dijelu, nanokompoziti Fe_2O_3/TiO_2 proizvedeni su jednostavnom tehnikom impregnacije/kalcinacije korištenjem različitih količina željezovog (III) nitrata na komercijalnom TiO_2 (P25 aeroksid). Pripremljeni nanokompoziti Fe_2O_3/TiO_2 karakterizirani su difrakcijom X-zraka (XRD), Ramanovom spektroskopijom (RS), skenirajućom

elektronskom mikroskopijom/energetsko-disperzijom spektroskopije (SEM/EDXS), fotoelektronskom spektroskopijom X-zraka (XPS), Brunauer– Emmett-Tellerova analiza (BET), spektroskopija elektronske impedancije (EIS), fotoluminiscencijska spektroskopija (PL) i spektroskopija difuzne refleksije (DRS). Kao rezultat toga, 5% (*w/w*) Fe_2O_3/ TiO_2 postigao je najveću fotokatalitičku aktivnost u suspenzijskom sustavu i uspješno je imobilizirano na staklenoj podlozi. Fotokatalitička aktivnost pod zračenjem vidljivim svjetlom procijenjena je tretiranjem farmaceutskog amoksicilina (AMX) u prisutnosti i odsutnosti dodatnih oksidansa: vodikovog peroksida (H_2O_2) i persulfatnih soli (PS). Utjecaj pH i koncentracije PS na stopu konverzije AMX utvrđen je pomoću statističkog planiranja i modeliranja površine odziva. Određeni su optimalni uvjeti [$S_2O_8^{2-}$] = 1,873 mM i pH = 4,808; oni su također korišteni u prisutnosti H_2O_2 umjesto PS u dugoročnim testovima. Najbrža AMX pretvorba s konstantom brzine nultog reda od $1{,}51 \times 10^{-7}$ $M \cdot min^{-1}$ postignuta je sustavom fotokataliza + PS. Utvrđen je put pretvorbe AMX, a evolucija/pretvorba nastalih međuprodukata povezana je s promjenama toksičnosti prema *Vibrio fischeri*. Uklanjanje reaktivnih kisikovih vrsta (ROS) također je korišteno za istraživanje mehanizma pretvorbe AMX, otkrivajući glavni doprinos fotogeneriranog h^+ u svim procesima.

Ključne riječi: fotokataliza uz Sunčevo zračenje; Fe_2O_3/TiO_2 kompozit; amoksicilin; persulfat; nusprodukti transformacije; toksičnost

RESUMEN EXTENDIDO EN CASTELLANO

El agua limpia accesible es una de las principales prioridades para el crecimiento económico sostenible y el bienestar social. El agua sustenta la vida y es un recurso crucial para la humanidad; también está en el centro de los ecosistemas naturales y la regulación del clima. El estrés hídrico es principalmente un problema de cantidad de agua, pero también ocurre como consecuencia del deterioro de la calidad del agua y la falta de una gestión adecuada del agua. Los problemas ambientales asociados con la contaminación del agua han sido un problema persistentemente importante en las últimas décadas, correlacionados negativamente con la salud y el ecosistema. La aparición de cantidades mínimas de antibióticos en varios cuerpos de agua estuvo directamente relacionada con el desarrollo de patógenos resistentes a los antibióticos. Durante las últimas dos décadas, las penicilinas se han recetado y utilizado ampliamente en toda Europa. Recientemente, la amoxicilina (AMX) se agregó a la segunda "lista de vigilancia" de la UE con base en la Decisión Europea propuesta 2018/840/EU. Su presencia en los efluentes de aguas residuales está relacionada con la eliminación limitada por parte de las plantas de tratamiento de aguas residuales (PTAR) comunes municipales basadas en el tratamiento primario (físico) y secundario (biológico). Por lo tanto, las nuevas técnicas de remediación deben aplicarse para eliminar dichas sustancias recalcitrantes.

Recientemente, los procesos de oxidación avanzada (POA) han ganado mucha atención en la investigación debido a su capacidad innata para proporcionar una oxidación eficaz de una amplia variedad de contaminantes orgánicos persistentes en los métodos de tratamiento de aguas residuales convencionales. La eficacia de los AOP se basa en especies altamente reactivas y no selectivas, principalmente basadas en radicales hidroxilo (HO•). Entre varios AOP, la fotocatálisis de semiconductores atrae mucho la atención debido a la estabilidad del material semiconductor y el potencial para usar abundante energía solar para degradar contaminantes orgánicos.

El fotocatalizador más ampliamente investigado y empleado en la purificación del agua es el TiO_2. Sin embargo, el TiO_2 sufre la rápida recombinación de las cargas fotogeneradas (es decir, pares de electrones/huecos; e^-/h^+) y solo es activo bajo la luz ultravioleta debido a su ancho de banda prohibida (3,0-3,2 eV), lo que dificulta su potencial para aplicaciones impulsadas por energía solar. Estas deficiencias se pueden mejorar mediante las siguientes estrategias: dopaje con metales y/o no metales, sensibilización de

colorantes, incorporación con nanotubos de carbono, óxido de grafeno reducido y acoplamiento con otros semiconductores con bandas prohibidas estrechas. El acoplamiento de TiO_2 con semiconductores de banda estrecha con respuesta de luz visible puede promover efectos sinérgicos entre dos materiales semiconductores que conducen a una separación de carga más eficiente y una alta actividad fotocatalítica bajo la irradiación de luz visible.

El óxido de hierro (α-Fe_2O_3, también conocido como hematita) es un candidato prometedor para el acoplamiento con TiO_2, debido a su abundancia, bajo costo, estabilidad y actividad de luz visible debido a su estrecha banda prohibida (2.0–2.2 eV). Lo que es más importante, las posiciones adecuadas del borde de la banda de hematita promueven la separación de carga fotogenerada en TiO_2 a través de la transferencia de heterounión. A pesar de varias aplicaciones fotocatalíticas de los compuestos de Fe_2O_3/TiO_2 para la eliminación de contaminantes emergentes (CEC), todos los estudios investigaron sus aplicaciones en la suspensión (es decir, empleando una forma de fotocatalizador en polvo), mientras que la aplicación de compuestos de Fe_2O_3/TiO_2 inmovilizados es escasamente conocida. Informado. Además, rara vez se explora el tratamiento de AMX bajo luz solar/visible usando Fe_2O_3/TiO_2, así como la ecotoxicidad de los subproductos de degradación/transformación de AMX.

En esta disertación, se investigó la eliminación de AMX usando películas en capas tipo sándwich de Fe_2O_3/TiO_2 hechas de nanomateriales disponibles comercialmente (Parte 1) y usando Fe_2O_3/TiO_2 sintetizado hecho de precursores químicos puros (Parte 2).

En la parte 1, se obtienen compuestos tipo sándwich hechos de TiO_2-P25 y α- Fe_2O_3 comerciales mediante recubrimiento por rotación de películas delgadas con diferentes configuraciones de capa, a saber: i) capa de TiO_2 sobre α- Fe_2O_3 (TiO_2@α-Fe_2O_3), ii) capa de α-Fe_2O_3 sobre TiO_2 (α-Fe_2O_3@TiO_2), y iii) mezclado físicamente al 50 % (*p/p*) de TiO_2/ Fe_2O_3. Se investiga la actividad fotocatalítica bajo irradiación solar simulada de los compuestos antes mencionados y sus componentes puros para la degradación de amoxicilina (AMX) en presencia y ausencia de persulfato (PS). En ambos casos, el tipo sándwich de TiO_2@α-Fe_2O_3 logró las tasas de degradación más altas de AMX y se observa un marcado efecto de la adición de PS en la tasa de degradación de AMX. La influencia del pH y la concentración de PS en la tasa de degradación de AMX se establece mediante un diseño experimental y un modelo de superficie de respuesta que reveló condiciones óptimas de $[S_2O_8^{2-}]$ = 0,334 mM y pH = 4,0. La ruta de degradación de AMX se estudia mediante la eliminación de especies reactivas de oxígeno y la identificación de intermediarios mediante

cromatografía líquida con espectrometría de masas en tándem (LC-MS/MS). Su evolución está directamente relacionada con una mayor toxicidad evaluada por los ensayos de *Daphnia magna* y *Vibrio fischeri*. Además, los cambios de biodegradabilidad están correlacionados con el perfil de mineralización de la solución AMX. También se establece la influencia de los componentes de la matriz del agua (Cl^-, CO_3^{2-}, NO_3^-, PO_4^{3-} y la materia orgánica natural del río Suwannee) en la degradación de AMX.

En la parte 2, se fabricaron nanocompuestos de Fe_2O_3/TiO_2 mediante una sencilla técnica de impregnación/calcinación empleando diferentes cantidades de nitrato de hierro (III) sobre TiO_2 comercial (aeróxido P25). Los nanocompuestos de Fe_2O_3/TiO_2 preparados se caracterizaron mediante difracción de rayos X (XRD), espectroscopia Raman (RS), microscopia electrónica de barrido/espectroscopia de dispersión de energía (SEM/EDXS), espectroscopia de fotoelectrones de rayos X (XPS), Brunauer– Análisis de Emmett-Teller (BET), espectroscopia de impedancia de electrones (EIS), espectroscopia de fotoluminiscencia (PL) y espectroscopia de reflectancia difusa (DRS). Como resultado, el 5 % (*p/p*) de Fe_2O_3/ TiO_2 logró la actividad fotocatalítica más alta en el sistema de suspensión y se inmovilizó con éxito en un soporte de vidrio. La actividad fotocatalítica bajo irradiación de luz visible se evaluó mediante el tratamiento de amoxicilina farmacéutica (AMX) en presencia y ausencia de oxidantes adicionales: peróxido de hidrógeno (H_2O_2) y sales de persulfato (PS). La influencia de la concentración de pH y PS en la tasa de conversión de AMX se estableció mediante planificación estadística y modelado de superficie de respuesta. Los resultados revelaron condiciones óptimas de [$S_2O_8^{2-}$] = 1,873 mM y pH = 4,808; estos también se utilizaron en presencia de H_2O_2 en lugar de PS en pruebas a largo plazo. La conversión AMX más rápida que poseía una constante de velocidad de orden cero de 1,51 × 10^{-7} M·min^{-1} se logró con el sistema de fotocatálisis + PS. Se estableció la ruta de conversión de AMX y se correlacionó la evolución/conversión de los intermedios formados con los cambios en la toxicidad hacia *Vibrio fischeri*. También se utilizó la eliminación de especies reactivas de oxígeno (ROS) para investigar el mecanismo de conversión de AMX, lo que reveló la principal contribución del h^+ fotogenerado en todos los procesos.

Palabras clave: Solar fotocatálisis de semiconductores; Fe_2O_3/TiO_2 compuesto; amoxicilina; persulfato; subproductos de transformación; toxicidad

RESUM AMPLIAT EN CATALÀ

L'aigua neta accessible és una de les màximes prioritats per al creixement econòmic sostenible i el benestar social. L'aigua dóna suport a la vida i és un recurs crucial per a la humanitat; també és el nucli dels ecosistemes naturals i la regulació del clima. L'estrès hídric és principalment un problema de quantitat d'aigua, però també es produeix com a conseqüència d'un deteriorament de la qualitat de l'aigua i la manca d'una gestió adequada de l'aigua. Els problemes ambientals associats a la contaminació de l'aigua han estat un tema persistentment important durant les últimes dècades, correlacionats negativament amb la salut i l'ecosistema. L'aparició de traces d'antibiòtics en diverses masses d'aigua estava directament relacionada amb el desenvolupament de patògens resistents als antibiòtics. Durant les dues últimes dècades, les penicil·lines s'han prescrit i utilitzat àmpliament a tot Europa. Recentment, l'amoxicil·lina (AMX) es va afegir a la segona "llista de seguiment" de la UE basada en la proposta de Decisió europea 2018/840/UE. La seva presència en els efluents d'aigües residuals està relacionada amb l'eliminació limitada de les depuradores municipals comunes (EDAR) basades en el tractament primari (físic) i secundari (biològic). Per tant, cal aplicar les noves tècniques de remediació per eliminar aquestes substàncies recalcitrants.

Recentment, els processos d'oxidació avançats (AOP) han guanyat molta atenció en la investigació a causa de la seva capacitat innata de proporcionar una oxidació eficaç d'una àmplia varietat de contaminants orgànics persistents als mètodes convencionals de tractament de WW. L'eficàcia dels AOP es basa en espècies altament reactives i no selectives, basades principalment en radicals hidroxil (HO•). Entre els diversos AOP, la fotocatàlisi de semiconductors crida molt l'atenció a causa de l'estabilitat del material semiconductor i el potencial d'utilitzar energia solar abundant per degradar els contaminants orgànics.

El fotocatalitzador més investigat i emprat en la purificació d'aigua és el TiO_2, no obstant això, el TiO_2 pateix la recombinació ràpida de càrregues fotogenerades (és a dir, parells d'electrons/forats; e^-/h^+) i només està actiu sota llum UV a causa de la seva gran bretxa de banda (3,0).-3,2 eV), dificultant així el seu potencial per a aplicacions impulsades per l'energia solar. Aquestes deficiències es poden millorar amb les següents estratègies: dopatge amb metalls i/o no metalls, sensibilització de colorants, incorporació amb nanotubs de carboni, òxid de grafè reduït i acoblament amb altres semiconductors amb bandes buides estretes. L'acoblament de TiO_2 amb semiconductors de banda estreta amb resposta a la llum visible pot promoure efectes sinèrgics entre dos materials semiconductors que condueixen a

una separació de càrrega més eficient i una alta activitat fotocatalítica sota irradiació de llum visible.

L'òxid de ferro (α-Fe_2O_3, també conegut com a hematita) és un candidat prometedor per acoblar-se amb TiO_2, a causa de la seva abundància, baix cost, estabilitat i activitat de la llum visible a causa de la seva banda estreta (2,0–2,2 eV). El més important és que les posicions de banda adequades de l'hematita promouen la separació de càrrega fotogenerada en TiO_2 mitjançant transferència d'heterounió. Malgrat diverses aplicacions fotocatalítiques de compostos de Fe_2O_3/TiO_2 per a l'eliminació de contaminants de preocupació emergent (CEC), tots els estudis van investigar les seves aplicacions a la suspensió (és a dir, emprant una forma de fotocatalitzador en pols), mentre que l'aplicació de compostos de Fe_2O_3/TiO_2 immobilitzats amb prou feines són reportat. A més, rarament s'explora el tractament d'AMX sota llum solar / visible mitjançant Fe_2O_3/TiO_2, així com l'ecotoxicitat dels subproductes de degradació / transformació d'AMX.

En aquesta tesi, es va investigar l'eliminació d'AMX mitjançant pel·lícules en capes de Fe_2O_3/TiO_2 tipus sandvitx fetes de nanomaterials disponibles comercialment (part 1) i utilitzant Fe_2O_3/TiO_2 sintetitzat fet de precursors químics purs (part 2).

A la part 1, els compostos de tipus sandvitx fets de TiO_2-P25 i α-Fe_2O_3 comercials s'obtenen mitjançant pel·lícules primes de recobriment per gir amb diferents configuracions de capes, a saber: i) Capa de TiO_2 sobre α-Fe_2O_3 (TiO_2@α-Fe_2O_3), ii) La capa d'α-Fe_2O_3 sobre TiO_2 (α-Fe_2O_3@TiO_2) i iii) es va barrejar físicament el 50% (*p/p*) de TiO_2/Fe_2O_3. S'investiga l'activitat fotocatalítica sota irradiació solar simulada dels compostos esmentats i dels seus components purs per a la degradació de l'amoxicil·lina (AMX) en presència i absència de persulfat (PS). En ambdós casos, el tipus sandvitx TiO_2@α-Fe_2O_3 va aconseguir les taxes de degradació més altes d'AMX i es nota un efecte marcat de l'addició de PS sobre la taxa de degradació d'AMX. La influència de la concentració de pH i PS sobre la taxa de degradació d'AMX s'estableix mitjançant un disseny experimental i un modelatge de superfícies de resposta que va revelar condicions òptimes de [$S_2O_8^{2-}$] = 0,334 mM i pH = 4,0. La via de degradació de l'AMX s'estudia mitjançant l'eliminació d'espècies reactives d'oxigen i la identificació d'intermedis mitjançant cromatografia líquida amb espectrometria de masses en tàndem (LC-MS/MS). La seva evolució està directament correlacionada amb una toxicitat augmentada avaluada pels assaigs de *Daphnia magna* i *Vibrio fischeri*. A més, els canvis de biodegradabilitat estan correlacionats amb el perfil de mineralització de la solució AMX. També s'estableix la influència dels components de la matriu de l'aigua (Cl^-, CO_3^{2-}, NO_3^-,

PO_4^{3-} i matèria orgànica natural del riu Suwannee) en la degradació de l'AMX.

A la part 2, es van fabricar nanocomposites Fe_2O_3/TiO_2 mitjançant una tècnica d'impregnació / calcinació fàcil que utilitzava diferents quantitats de nitrat de ferro (III) en TiO_2 comercial (aeròxid P25). Els nanocomposites Fe_2O_3/TiO_2 preparats es van caracteritzar per difracció de raigs X (XRD), espectroscòpia Raman (RS), microscòpia electrònica d'escaneig/espectroscòpia dispersiva d'energia (SEM/EDXS), espectroscòpia fotoelectrònica de raigs X (XPS), Brunauer– Anàlisi Emmett-Teller (BET), espectroscòpia d'impedància electrònica (EIS), espectroscòpia de fotoluminescència (PL) i espectroscòpia de reflectància difusa (DRS). Com a resultat, el 5% (*p/p*) de Fe_2O_3/TiO_2 va aconseguir l'activitat fotocatalítica més alta en el sistema de purins i es va immobilitzar amb èxit sobre suport de vidre. L'activitat fotocatalítica sota irradiació de llum visible es va avaluar tractant amoxicil·lina farmacèutica (AMX) en presència i absència d'oxidants addicionals: peròxid d'hidrogen (H_2O_2) i sals de persulfat (PS). La influència del pH i la concentració de PS en la taxa de conversió d'AMX es va establir mitjançant la planificació estadística i el modelatge de superfícies de resposta. Els resultats van revelar condicions òptimes de $[S_2O_8^{2-}]$ = 1,873 mM i pH = 4,808; aquests també es van utilitzar en presència d' H_2O_2 en lloc de PS en proves a llarg termini. La conversió AMX més ràpida amb una constant de velocitat d'ordre zero d'$1{,}51 \times 10^{-7}$ $M \cdot min^{-1}$ es va aconseguir amb el sistema fotocatàlisi + PS. Es va establir la via de conversió AMX i l'evolució/conversió dels intermedis formats es va correlacionar amb els canvis de toxicitat cap a *Vibrio fischeri*. També es va utilitzar l'eliminació d'espècies reactives d'oxigen (ROS) per investigar el mecanisme de conversió d'AMX, revelant la principal contribució de l' h^+ fotogenerat en tots els processos.

Paraules clau: Solar fotocatàlisi de semiconductors; Fe_2O_3/TiO_2 compuesto; amoxicillina; persulfat; subproductes de transformació; toxicitat

LIST OF ACRONYMS

AMX	Amoxicillin	**ANOVA**	Analysis of variance
AOP	Advanced oxidation process	**BG**	Band gap
BQ	Benzoquinone	**CB**	Conduction Band
CECs	Contaminants of emerging concern	**DM**	*Daphnia magna*
DoE	Design of experiments	**DRS**	Diffuse Reflectance Spectroscopy
EIS	Electron Impedance Spectroscopy	**EU**	European Union
FA	Formic Acid	**HA**	Humic acid
HOMO	Highest Occupied Molecular Orbital	**HPLC**	High performance liquid chromatography
LC	Liquid chromatography	**LC-MS**	Liquid chromatography-mass spectrometry
LUMO	Lowest Occupied Molecular Orbital	**MQ**	MilliQ
MS	Mass spectrometry	**NOM**	Natural organic matter
PC	Photocatalysis	**PL**	Photoluminescence
PS	Persulfate	**ROS**	Radical oxygen species
RS	Raman Spectroscopy	**RSM**	Response Surface Methodology
SEM	Scanning Electron Microscopy	**TB**	*tert*-Butanol
TOC	Total organic carbon	**TU**	Toxicity Units
TPs	Transformation products	**UV**	Ultraviolet
VB	Valence band	**VF**	*Vibrio fischeri*
VIS	Visible light	**WWTP**	Wastewater treatment plant
XPS	X-ray photoelectron spectroscopy	**XRD**	X-ray Diffraction

TABLE OF CONTENTS

1. INTRODUCTION

Semiconductor-based photocatalysis has emerged as a promising technology for water purification, particularly as a tertiary treatment. Among photocatalysts studied, Titanium (IV) dioxide (TiO_2) has been regarded as the "benchmark photocatalyst" due to its chemical and thermal stability, biological inertness, suitable mechanical properties, low cost, and nontoxicity [1–3]. However, TiO_2 suffers from the fast recombination of photogenerated charges (i.e., electron/hole pairs; e^-/h^+) and is active only under UV light due to its wide bandgap (3.0–3.2 eV), thus hindering its potential for visible-light-driven applications [1,4]. Consequently, these deficiencies can be improved by coupling TiO_2 with a narrow-bandgap semiconductor with a visible-light response. As such, the formation of heterojunction between the two semiconductors promotes synergistic effects, leading to more efficient charge separation and improved photocatalytic activity under visible-light irradiation [2,4,5]. Hematite (α-Fe_2O_3) is a well-suited candidate for coupling with TiO_2 due to its visible-light activity (bandgap energy (E_g) = 2.0–2.2 eV) [6], natural abundance, low cost, and stability in a wide range of pH in aqueous solutions [7]. In recent years, the application of Fe_2O_3/TiO_2-based composite photocatalysts has gained attention due to their efficiency for the removal of contaminants of emerging concern (CECs) from water [8]. Further photocatalytic activity enhancement can be accomplished using electron acceptors such as persulfate ($S_2O_8^{2-}$, PS) and hydrogen peroxide (H_2O_2), which promote suppression of e^-/h^+ recombination in Fe_2O_3/TiO_2 photocatalysts, thus leading to the increased availability of photogenerated h^+ for the generation of additional reactive oxygen species (ROS) and for subsequent oxidation reactions [9,10].

However, several knowledge gaps need to be addressed regarding Fe_2O_3/TiO_2 application in real environmental conditions, including the following:

(i) *Unequal distribution of solar energy around Earth's surface.* Most applications of Fe_2O_3/TiO_2 for CEC removal are reported under solar irradiation [8]. In fact, solar light is composed of 3% UV light, 44% visible light, and 53% infrared light [11,12]. The UV light portion within solar irradiation plays an important role for the activation of the overall photocatalytic composite (i.e., Fe_2O_3/TiO_2), and its absence may result in different mechanisms [13]. It must also be noted that UV distribution at the Earth's surface is unequal and influenced by several factors [14]. As such, focusing on the utilization of visible light is favorable for such environmental applications.

(ii) *Toxicity assessment*. Transformation and/or degradation byproducts of CECs after Fe_2O_3/TiO_2 photocatalytic processes are scarcely reported. Clearly, the formation of more toxic byproducts has already been reported using different TiO_2/semiconductor-based composites [15]. Accordingly, such potential treatment drawbacks must receive well-deserved attention since they can impose additional risk to the environment.

(iii) *Photocatalyst recovery*. Fe_2O_3/TiO_2 immobilization in various supports is scarcely reported and is usually applied in powder form, thus requiring secondary treatment to remove fine nano-sized composite particles. Immobilization of photocatalysts provides a potential decrease in operating costs for the water treatment process by avoiding in-treatment agglomeration and post-treatment separation issues [1,3,9,16,17].

Herein, the aim of the study was to provide an insight on removal of amoxicillin (AMX), a pharmaceutical that is included in the second and third EU "watch list" based on the Decision 2018/840/EU and 2020/1161/EU, respectively [18,19]. AMX removal were explored by solar or visible-light photocatalytic activation of PS using Fe_2O_3/TiO_2 layered films made of commercially available nanomaterials (*part 1*) and synthesized Fe_2O_3/TiO_2 (*part 2*) composite made from pure chemical precursors.

The specific goals for *part 1* were to: (i) study the effect of photocatalyst layer configuration along with the influence of initial pH and PS concentration, on AMX degradation kinetics; (ii) study the mechanism of AMX degradation using common scavenging agents for formed ROS; (iii) study the influence of water matrix constituents on AMX degradation; (iv) and correlate environmental aspects of the treatment process such as mineralization, biodegradability, and toxicity profiles with identified AMX degradation by-products.

The specific goals of *part 2* were to: (i) prepare Fe_2O_3/TiO_2 via an impregnation/calcination; (ii) characterize the as-prepared photocatalyst with superior catalytic activity using instrumental techniques specific for the inspection of structural and elemental composition, as well as morphological, textural, optical, and electrochemical properties; (iii) determine Fe_2O_3 content for optimal photocatalytic activity; (iv) optimize the combined effect of pH and PS concentration for the removal of AMX using the immobilized Fe_2O_3/TiO_2, and (v) correlate AMX transformation byproducts under different photocatalytic processes (i.e., photocatalysis alone, photocatalysis + H_2O_2, and photocatalysis + PS) with each toxicity profile.

2. BACKGROUND

2.1. Wastewater quality

The need for water is expected to increase by 55% by 2050, and the demand for water used in manufacturing will rise by 400%. Ensuring access to clean water is one of the major challenges facing the world in this century [20]. The Intergovernmental Panel on Climate Change (IPCC) predicts that the number of people in Europe facing water scarcity will increase from 28 million to 44 million by the 2070s [21]. Using treated wastewater is an underutilized option and its reuse is considered crucial for communities facing water shortages. Despite the advancements in technology, traditional methods of treating wastewater are still a major obstacle to using it as a source of potable water and for other forms of reuse. In fact, wastewater treatment plants (WWTPs) have been found to be the main sources of CECs in the aquatic environment due to their limited effectiveness in removing CECs [22,23]. WWTPs final effluent is often discharged into surface waters, but the remaining sludge may be disposed of in landfills or it can be used as fertilizer in agricultural fields, which can lead to the contamination of surface and groundwater posing a risk of run-off into different water bodies [24,25]. WWTPs effluents have a significant impact on the presence of CECs in water systems, particularly in recipients with low water flow or recipients that receive wastewater from multiple or large WWTPs [26]. Nevertheless, such inefficiencies of WWTPs to remove CECs are one of the main barriers for obtaining a sustainable water quality that may be reused directly or indirectly for potable purposes.

2.1.1. Contaminants of emerging concern (CECs)

Contaminants of emerging concern (CECs) refer to a wide range of chemical and biological substances that are not currently regulated but have the potential to impact human health and the environment [27]. These include pharmaceuticals, personal care products, endocrine-disrupting compounds, flame retardants, pesticides, and artificial sweeteners, etc. Besides, their metabolites are also an issue of major concern. **Table 1** summarizes various classes of the abovementioned CECs [27]. CECs can enter the environment through various pathways, such as sewage discharge, agricultural runoff, and atmospheric deposition. The effects of CECs on human health and the environment are still not well understood, and research is ongoing to better understand their potential impacts.

Pharmaceuticals, including antibiotics, have revolutionized healthcare and have been essential in treating and preventing a wide range of diseases and infections. Antibiotics are a type of pharmaceutical that specifically target bacterial infections, and they have been responsible for saving countless lives and preventing the spread of infectious diseases. However, the widespread use of antiobiotics has also led to the emergence of antibiotic-resistant strains of bacteria, which poses a significant threat to public health.

Table 1. Classification of CECs (Adapted from [27])

Classes	Use/Function	Examples
Pharmaceuticals and Personal Care Products (PPCPs)		
Psychiatric drugs	Antidepressant	Fluoxetine, Sertraline, and Citalopram
Analgesics	Pain reliever	Acetaminophen and acetylsalicylic acid
Anti-epileptic drugs	Anticonvulsant	Carbamazepine and primidone
Antihyperlipidemics	Lipid regulators	Gemfibrozil, clofibric acid, and fenofibric acid
Non-steroidal anti-inflammatory drugs	Anti-inflammatory	Diclofenac, ibuprofen, ketoprofen, and naproxen
Synthetic hormones	Hormone	Estrone, 17a-estradiol, 17a-ethinylestradiol, and estriol
Antimicrobials	Antibiotic	Erythromycin, sulfamethoxazole, tetracycline and amoxicillin
	Antiseptic	Triclosan, biphenylol, and
Polycyclic musks	Fragrances	Hexahydrohexamethyl-
	Insect repellent	N,N-Diethyl-meta-toluamide (DEET)
Other	Fragrances	Acetophenone
	Stimulant	Caffeine
Endocrine disruptive chemicals (EDCs)		
Steroids	Natural human estrogen	17b-estradiol
	Metabolite	Estrone
Alkylphenols	Manufacture of household and industrial products	Nonylphenol and octylphenol
Polyaromatic compounds		Polychlorinated biphenyls and brominated flame retardants
Organic oxygen compounds	Plasticizers	Phthalates
	Industrial production of polycarbonates and epoxy	Bisphenol A
Pesticides	Insecticides, herbicides,	Atrazine, chlordane, and trifluralin
Others	By-products of various industrial and combustion	Dioxins and furans

Classes	Use/Function	Examples
Fire Retardants (FRs)		
Halogen-containing flame retardants	Fire Retardants	Brominated bisphenols and phenols
Phosphorus-based FRs		Elemental red phosphorus and inorganic phosphates
Melamine FRs		Melamine cyanurate
Inorganic hydroxides		Aluminum hydroxide and magnesium hydroxide
Borate FRs		Sodium borate and boric acid
Silicon FRs		
Pesticides		
Carbamates	Herbicides, insecticides, and fungicide	Carbendazim, benomyl, and carbaryl
Chloroacetanilides	Preemergent herbicides	Metolachlor and alachlor
Chlorophenoxy acids	Herbicides	Bentazone and triclopyr
Organochlorines	Insecticides	DDT, dieldrin, endrin, and endosulfan
Organophosphates	Insecticides	Diazinon, malathion, and chlorpyrifos
Pyrethroids	Insecticides	Biphenthrin, cypermethrin, and
Triazines	Herbicides	Atrazine, cyanazine, and simazine
Artificial sweeteners		
	Sugar substitutes	Acesulfame
		Sucralose
		Saccharin
		Cyclama
		Aspartame
		Neotame
		Neohesperidine dihydrochalcone

2.1.2. Amoxicillin

Amoxicillin (AMX), with chemical formula $C_{16}H_{19}N_3O_5S$ (**Figure 1**) was initially discovered by researchers at Beecham Research Laboratories in the 1970s, and was initially sold under the brand name "Amoxil". Today, amoxicillin is one of the most widely sold and prescribed antibiotics in the world, having gained widespread use due to its broad-spectrum effectiveness against a variety of bacterial infections, including skin infections, pneumonia, angina, and urinary tract infections [28–30].

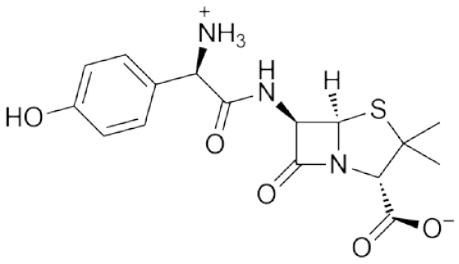

Figure 1. Amoxicillin structure in zwitterionic form

Research has demonstrated that a significant portion, over 80%, of AMX is eliminated from the human body via urine within 2 hours of consumption. Hence, its presence poses a potential risk as it can lead to the development of antimicrobial-resistant bacteria, which can be transmitted from animals to humans [31]. As such, AMX has been listed on the second and third EU "watch list" based on the Decision 2018/840/EU and 2020/1161/EU, respectively [18,19].

Due to the low metabolism rate of AMX in the body, it is likely to persist in the aquatic environment in its original form or as transformed compounds (i.e., hydrolysis byproducts etc.). In the first stage of metabolism, AMX is transformed into other substances through chemical processes such as the addition of functional groups, hydrolysis, reduction, and oxidation reactions. In the second stage, the products formed in the first stage, as well as the original AMX, are combined with endogenous conjugating molecules like sulfuric acid, glutathione, acetic acid, and glucuronic acid, resulting in hydrophilic derivatives that are more easily excreted or more readily degraded enzymatically [28,32,33]. Hence, the proposed aquatic transformation is shown in **Figure 2** and occurrence of AMX all over the world is summarized in **Table 2**.

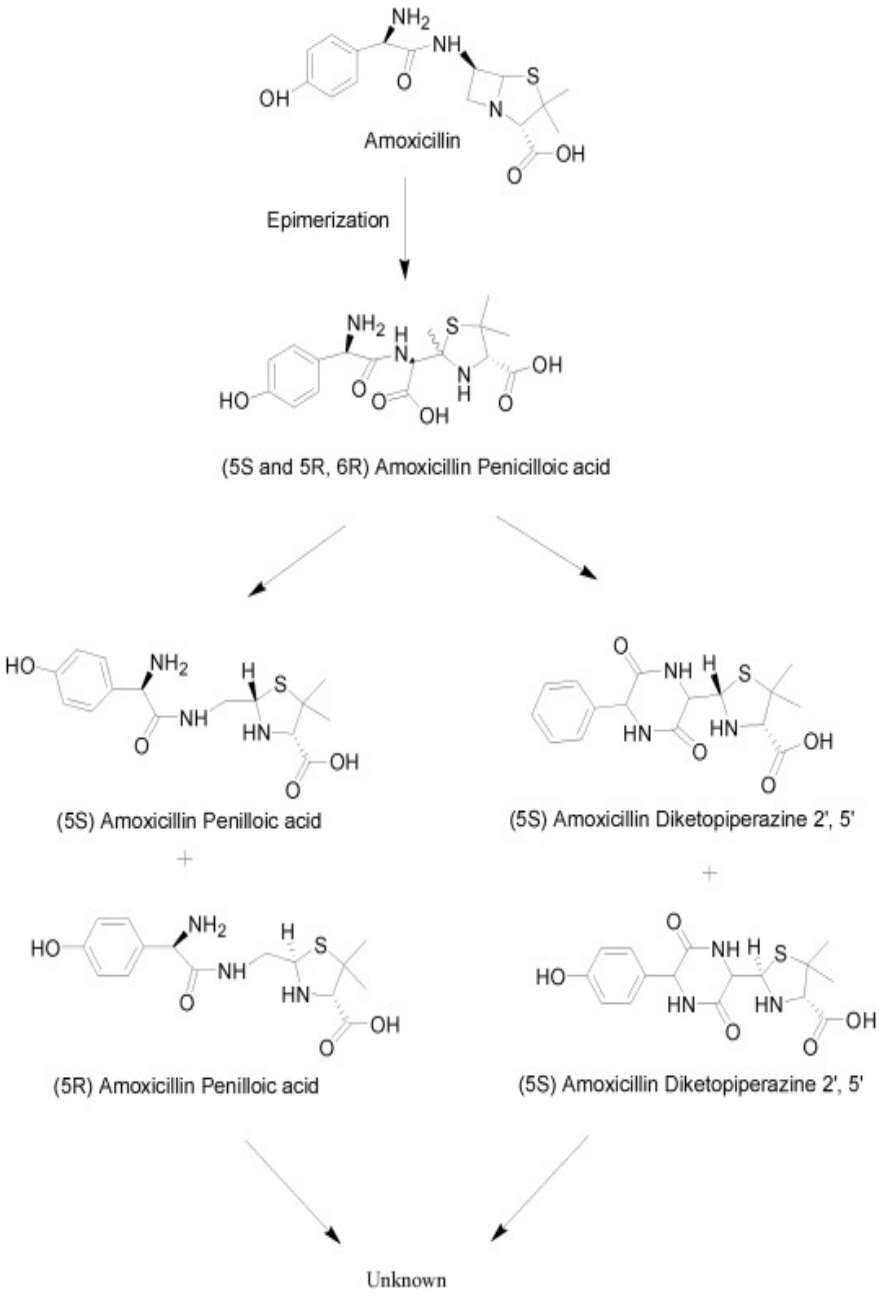

Figure 2. Proposed transformation of AMX in water (Adapted from [28,34])

Table 2. Occurrence of amoxicillin all over the world (Adapted from [35])

Country	Detected in	Concentration	Reference
Australia	Hospital effluent	900 $ng \cdot L^{-1}$	[36]
Australia	Raw sewage	280 $ng \cdot L^{-1}$	[36]
Australia	Effluent of conventional treatment plant	20 $ng \cdot L^{-1}$	[36]
China	Urban sewage	3380 $ng \cdot L^{-1}$	[37]
China	Estuary	786.40 $ng \cdot L^{-1}$	[38]
China	Bay	90.97 $ng \cdot L^{-1}$	[38]
India	Aquifers, surface	0.18 ± 0.16 $\mu g \cdot L^{-1}$, 0.18 ± 0.20 $\mu g \cdot L^{-1}$	[39]
Italy	WWTPs	15 $ng \cdot L^{-1}$	[40]
Italy	Effluent of sewage treatment plants	120 $ng \cdot L^{-1}$	[36]
Italy	WWTPs	25 $ng \cdot L^{-1}$	[40]
Kenya	WWTPs	4.6 $\mu g \cdot L^{-1}$	[41]
Kenya	Influent	1.58 $\mu g \cdot L^{-1}$	[41]
Spain	Surface water	200 $ng \cdot L^{-1}$	[36]
United Kingdom	WWTPs	56–60 $ng \cdot L^{-1}$	[40]
United Kingdom	WWTPs	39−49 $ng \cdot L^{-1}$	[40]
United Kingdom	WWTPs	198–245 $ng \cdot L^{-1}$	[40]
United Kingdom	Surface water	120 $ng \cdot L^{-1}$	[36]

2.2. Conventional wastewater treatment

The first step in a wastewater treatment facility (**Figure 3**) is aimed at removing large objects from the influent to protect the facility's equipment. The next step is to remove grit by flowing the influent through a grit chamber. Solids, also known as organics or sludge, are then separated out and pumped to a sludge digester or processing area to be dried and removed, along with the sludge from the clarifier. After grit removal, the influent enters primary clarifiers that separate out a portion of the solids. These solids, called sludge, are regularly removed to prevent them from impacting the separation process. The sludge is often used as fertilizer (depending on the quality), or it is classified as waste and, in such case, is landfilled or incinerated. Air is then added to the aeration tank to encourage the conversion of NH_4^+ to NO_3^- and to provide oxygen for bacteria to continue to propagate. The bacteria remove oxygen from the nitrate molecules and the nitrogen is given off as N_2 (in case of denitrification) This process is managed to offer the best conditions for bacteria which are directly related to Biochemical Oxygen Demand (BOD). BOD is a surrogate indicator for the amount of organic material present and is used to determine the effectiveness of organic material breakdown. The treated wastewater is then pumped into a secondary clarifier to allow any remaining sediment to settle out. Any remaining small solids at this stage are originated from aeration step, where biological treatment with activated sludge occurred. Hence, settled activated sludge after secondary clarifier is returned to the aeration tank to increase the mixed liquor suspended solids (MLSS).

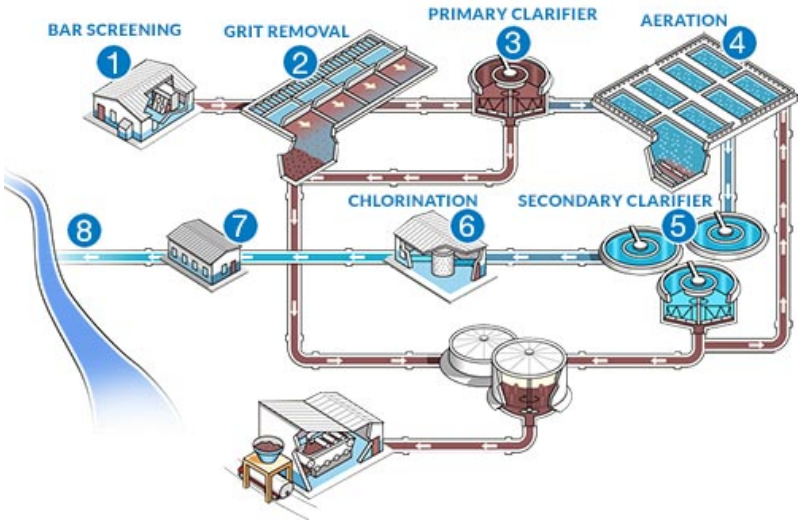

Figure 3. Wastewater treatment plant's general scheme (nitrification only) [42]

As a tertiary treatment, (nano- or ultra-) filtration, chlorine, ozone, UV or any form of advanced oxidation process is then performed to remove any remaining bacteria. The final step is water analysis and testing to ensure proper pH level, ammonia, nitrates, phosphates, dissolved oxygen, and residual chlorine levels. The effluent can then be disposed of and reintroduced to the environment [42].

However, wastewater treatment plants (WWTPs) have been found to be the main point for spreading of chemical compounds such as CECs, which ended in municipal wastewaters due to human activities, in the aquatic environment despite their attempts to remove them [22,23]. Previous research has shown that conventional WWTPs are of limited effectiveness in removing majority CECs and that they can still enter water systems [23,43]. The final effluent is often discharged into surface waters, but the remaining sludge may be disposed of in landfills or incinerated, which can lead to the contamination of groundwater or even surface waters, or can be used as fertilizer on agricultural areas, which poses a risk of run-off into water bodies [24,25]. WWTP effluents have a significant impact on the presence of CECs in water systems, particularly in recipients with low water flow or recipients that receive wastewater from multiple or large WWTPs [26]. New approaches must be integrated into conventional WWTPs to provide efficient removal of CECs.

2.3. Advanced oxidation processes

Advanced oxidation processes (AOPs) have gained much research attention due to their innate ability to provide effective oxidation of a wide variety of organic pollutants persistent to conventional WW treatment methods [44]. AOPs effectiveness rely on highly reactive and non-selective species, that can be formed either *in-situ* or via added oxidants (hydrogen peroxide, persulfate salts, percarbonates). Those are primarily hydroxyl radicals (HO•), although various other radical species might be formed depending also on the present oxidants and/or water matrix constituents: HO_2•, $O_2^{\bullet-}$, Cl•, $CO_3^{\bullet-}$, $NO_3^{\bullet}$, $SO_4^{\bullet-}$ etc [9]. The nature of HO•, including a combination of reactivity and non-selectivity, makes it suitable for the degradation of a wide range of organic and inorganic pollutants, while generating low amounts, or even no secondary waste at all [45]. Therefore, it is fairly obvious why AOPs have gained so much attention from the scientific community and water professionals, which lead to a rapid development and application of AOPs during the last several decades, but will continue to do so in the forthcoming years. AOPs can oxidize/mineralize organic pollutants to CO_2, H_2O and/or respective mineral salts (i.e., chlorides, nitrates, phosphates), depending on the structure of the starting pollutant(s). For example AOPs can sufficiently oxidize 2,4-dinitrophenol (2,4-DNP), a common industrial wastewater pollutant, to nitrates and byproducts which are rendered non-toxic to *Daphnia magna* [46]. However, complete mineralization of the target pollutants is rarely pursued, as it is resource/energy intense and unnecessary if the degradation byproducts are biodegradable. Therefore, AOPs are not intended to replace current wastewater technologies, rather supplement them by addressing their shortcomings either as a pretreatment to reduce the toxicity of influents and increase biodegradability [47,48] and/or as a tertiary post-treatment after biological oxidation [49]. Complete mineralization is also in part difficult to achieve, due to the scavenging effect of low molecular weight carboxylic acids that are common byproducts, which is the case if natural organic matter (NOM) is present in the system [50].

Radical species employed in AOPs can be generated by numerous means, including chemical, electrical, mechanical or radiation energy, hence AOPs can be categorized according to the means of radical production and process operating conditions, **Table 3**.

Table 3. Categorization of AOPs according to primary source of hydroxyl radicals: (Adapted from [51])

Atmospheric pressure and temperature		
Energy source	**Parent process**	**Modified processes**
chemical	Fenton (Fe^{2+}/H_2O_2)	photo-Fenton
		electro-Fenton
		sono-Fenton
		zero valent iron (Fe^0)
		non-ferrous based
	ozone (O_3)	peroxone
		catalytic ozonation
		photo-ozonation
		sono-ozonation
electrical	corona	Fenton-corona
		high pressure plasma
mechanical	ultrasound (US)	sono-Fenton
		sono-ozonation
		sono-photocatalysis
UV and visible photon	ultraviolet (UV)	photolysis
		photooxidation
	solar	solar-Fenton
		photocatalysis
high energy radiation	radiolysis	gamma
		electron-beam
Above normal conditions		
chemical	wet air oxidation (WAO)	catalytic wet air oxidation (CWAO)
		catalytic wet peroxidation (CWPO)

2.4. Semiconductor Photocatalysis

The general mechanism of semiconductor photocatalysis (**Figure 4**) is composed of three main steps: 1.) e^-/h^+ pairs are generated on the surface of the semiconductor under illumination with the required wavelength or energy; then, 2.) photogenerated charges (i.e., e^-/h^+) migrate to the surface of the semiconductor; and lastly, 3.) e^- and h^+ induce redox reactions on the surface that facilitate improved degradation of organic pollutants [52,53].

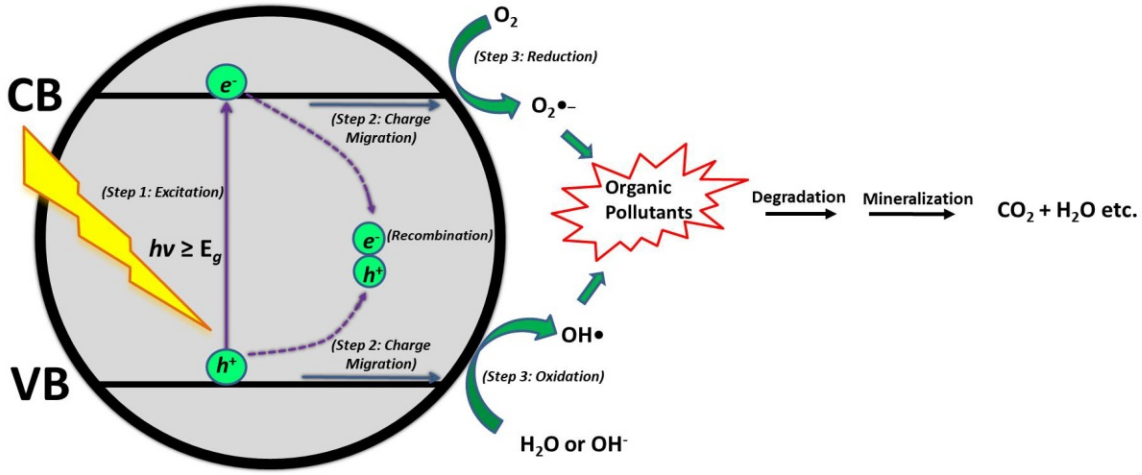

Figure 4. Photocatalytic reaction mechanism over semiconductor material [5]

2.4.1 Titanium Dioxide (TiO_2)

Titanium dioxide (TiO_2) is a polymorphic compound having three polymorphous structures (**Figure 5**): rutile phase (tetragonal), anatase phase (tetragonal), and the brookite phase (orthorhombic). Rutile is the most stable form among the three phases. Nevertheless, anatase is the most extensively studied among the three. TiO_2 is renowned for its chemical stability (photostability), superhydrophilicity, non-toxic, and for its low-cost production. However, TiO_2 suffers from fast e^-/h^+ pair recombination and large band gap (E_g= 3.0–3.2 eV), which can only be excited under UV light irradiation [5]. The strategy for improving these issues includes band gap engineering by doping with non-metals and/or transition metals, or coupling with graphene oxide or other conducting materials. Among them, semiconductor-coupling presents a viable structure-properties engineering solution for the enhancement of TiO_2 photocatalytic activity due to the simultaneously reduced e^-/h^+ recombination rate and enhanced visible light absorption [54].

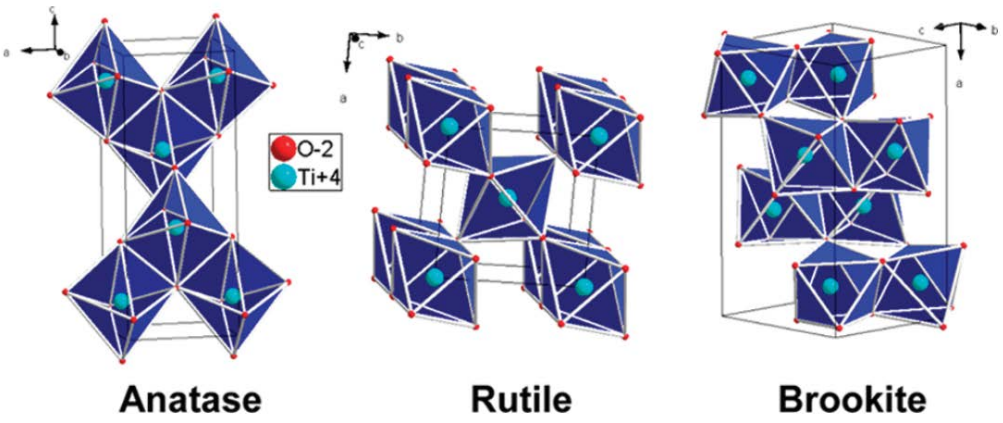

Figure 5. Representations of the TiO_2 anatase, rutile, and brookite forms [55]

2.5 Heterojunction Structures

Three main types of heterojunction architectures are reported for TiO_2/semiconductor composites [56] (**Figure 6**). In Type I heterojunction, the conduction band (CB) of TiO_2 is higher in energy (more negative potential) when compared to the CB of semiconductor 2 and the valence band (VB) of TiO_2 is lower in energy (more positive potential) as compared to the VB of semiconductor 2 [57,58]. This leads to the accumulation of photogenerated h^+ and e^- in semiconductor 2. In Type II heterojunction (where TiO_2 can be semiconductor 1 or 2), the CB of semiconductor 2 is higher than the CB position of semiconductor 1 leading to facile transfer of photogenerated e^- from CB of semiconductor 2 to CB of semiconductor 1 [59]. Meanwhile, photogenerated h^+ in VB of semiconductor 1 can travel to the VB of semiconductor 2, which facilitates efficient charge separation. Type III heterojunction (also known as broken gap situations) [60] shares the same charge transfer mechanism, like Type II heterojunction. In this case, the CB and VB of semiconductor 2 are higher than CB and VB of TiO_2 [61,62].

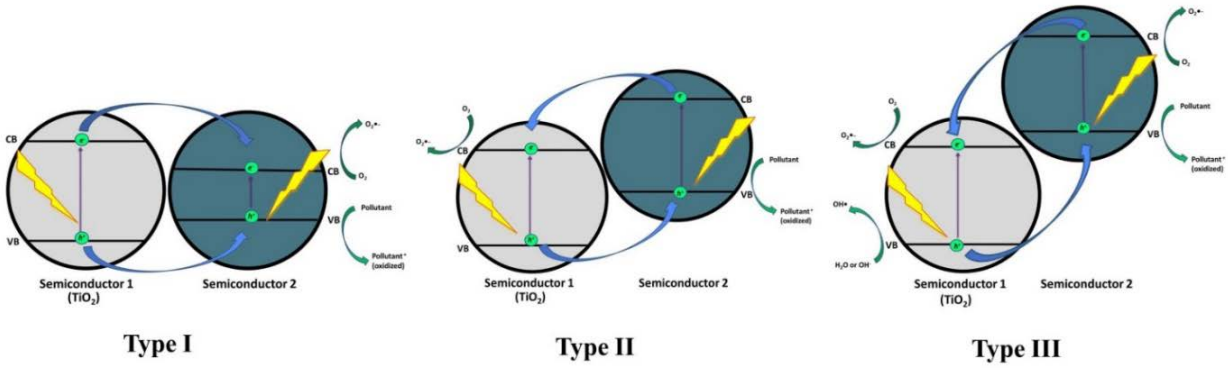

Figure 6. Type I, II, and III band alignment of TiO_2-based heterojunctions [5]

2.5.1 Coupling of TiO_2 with Metal Oxides

2.5.1.1 TiO_2/WO_3

Tungsten oxide (WO_3), which is a visible light active photocatalyst with band gap of 2.4–2.8 eV, is a promising candidate for photocatalytic applications, due to its oxidative properties, nontoxicity, low cost, and stability in acidic solutions. In addition, WO_3 directly matches the band positions of TiO_2 to form a heterojunction (*Type II Heterojunction*) [63–66]. Several authors studied the application of TiO_2/WO_3 composites for the degradation of various CECs; either pesticides or pharmaceuticals (**Table 4**). Hence, Macias et al. [58] studied the photocatalytic degradation of herbicide 2,4-dichlorophenoxyacetic acid (2,4-D)

while using TiO_2/WO_3 composites under natural sunlight. They reported the rather high effectiveness of the studied system: 94.6% degradation of 2,4-D and 88.6% mineralization of overall organic content under two and four hours of natural sunlight irradiation, respectively. Besides, they studied the mechanisms that are responsible for forming reactive species within the system and, based on their findings, proposed that, upon forming e^-/h^+ pairs under solar irradiation, photogenerated e^- from CB of TiO_2 are transferred to CB of WO_3. Consequently, W^{6+} was first reduced to W^{5+} on WO_3 surface, while the W^{5+} ions are then oxidized to W^{6+} by adsorbed O_2 producing superoxide anion radical ($O_2^{\bullet-}$). The photogenerated h^+ in VB of WO_3 are transferred to VB of TiO_2 where they reacted with water (or hydroxyl ions, HO^-) forming hydroxyl radicals (HO•) (**Figure 7**). The generated reactive oxygen species (ROS) promoted the degradation of 2,4-D and its intermediates, eventually yielding rather high mineralization extents, while their occurrence in the system was confirmed through tests with common scavenging agents (e.g., tert-butanol (TB) for HO•, formic acid (FA) for h^+, and *p*-benzoquinone (BQ) for $O_2^{\bullet-}$) [58].

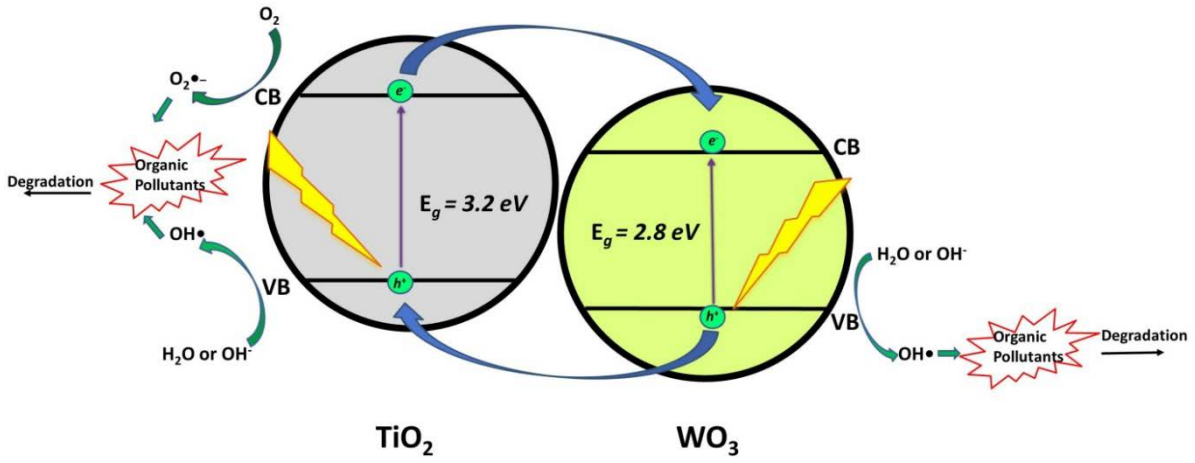

Figure 7. Photocatalytic degradation mechanism over TiO_2/WO_3 composite [5]

The same composite type was used in the degradation of pharmaceuticals. Hence, Mugunthan et al. [64] treated diclofenac (DCF) while using TiO_2/WO_3 composites under 4 hrs of visible light irradiation and reported a maximum of 92% mineralization of overall organic content. They also elucidated the DCF degradation pathway by LC-MS measurements, which included C-N cleavage in the DCF molecule forming benzene-ring based intermediates at the first stage, and open-ring intermediates at the later stage, which were eventually mineralized. Such findings were quite similar to other studies employing HO• based processes in the degradation of DCF [67,68], thus implying the important role of formed ROS, primarily HO•, in the case of TiO_2/WO_3 solar driven photocatalysis as well.

Arce-Sarria et al. [69] studied the performance of TiO_2/WO_3 composite for the degradation of another pharmaceutical, amoxicillin (AMX), in a pilot scale reactor, where they achieved 64.4% degradation.

Besides "pure" TiO_2/WO_3 composite, several authors studied the performance of its enriched analogues (**Table 4**). Hence, Cordero-García et al. [66] studied DCF degradation by WO_3/C-doped TiO_2 and reported 100% DCF degradation and 82.4% mineralization of the overall organic content under 250 $kJ \cdot m^{-2}$ and 400 $kJ \cdot m^{-2}$ of solar-accumulated energy, respectively. They also stated that the WO_3/C-doped TiO_2 composite showed superior photocatalytic activity for the complete degradation and mineralization of DCF when compared to the pristine TiO_2, used as benchmark material. Based on the findings on elucidated mechanisms within the studied composite and DCF degradation pathway provided, the authors concluded that the incorporation of elemental carbon to TiO_2 crystal structure promoted the formation of a C 2*p*-hybridized valence band that lowered the band gap of TiO_2 by mixing with O 2*p* orbitals. As a result, upon visible light irradiation, TiO_2 generates e^-/h^+ pairs, where the photogenerated e^- are promoted to the Ti 3*d* states (VB), thus reducing Ti^{4+} to Ti^{3+}. Ti^{3+} can be easily oxidized by WO_3 due to the differences in the reduction potential between TiO_2 (−0.70V vs NHE) and WO_3 (−0.03V vs NHE). Subsequently, W^{6+} traps photogenerated e^- to form its reduced state W^{5+}, while the redox reaction occurs further by returning to its original oxidation state in reaction with adsorbed O_2 on the composite catalyst surface (similarly as discussed above in the case of "pure" TiO_2/WO_3), thus leading to improved charge separation and the formation of ROS, which contributed in DCF degradation and mineralization of formed intermediates.

Table 4. Photocatalytic degradation of CECs over TiO_2/WO_3 composites

Catalyst	Target pollutant	Initial concentration/ working volume ((mg·L^{-1}) /mL)	Experimental conditions	Reaction time	Removal extent (%)	Reference
TiO_2 - WO_3 (0.5 g·L^{-1})	2,4-dichlorophenoxy acetic acid	50 (in 250 mL)	Light Source: natural sunlight 11AM-4PM; pH= 4	120 min	94.6 (TOC= 88.6)	[58]
TiO_2 - WO_3 (0.6 g·L^{-1})	Diclofenac	25 (in 100 mL)	Light Source: 400 W Metal Halide Lamp; pH= 5	240 min	TOC= 91	[64]
TiO_2 - WO_3 (0.1 g·L^{-1})	Amoxicillin	100 (in 25,000 mL)	CPC Reactor with accumulated energy 550,000 J/m^2	NA	64.4 (@ 550 kJ·m^{-2})	[70]
(WO_3/TiO_2-C) (1.0 g·L^{-1})	Diclofenac	10 (in 300 mL)	Light Source: 1500 W Xenon Lamp with filter(λ > 290 nm) ; pH= 7	NA	100 (@ 250 kJ·m^{-2}) (TOC= 82.4 @ 400 kJ·m^{-2})	[66]
(WO_3/TiO_2-N) (1.0 g·L^{-1})	Diclofenac	10	Light Source: 1500 W Xenon Lamp with ID65 solar filter; pH= 6.5	NA	100 (@ 250 kJ·m^{-2}) (TOC= 100 @ 400 kJ·m^{-2})	[65]

The same authors studied the degradation of DCF with another enhanced WO_3/TiO_2 composite (N-doped TiO_2), and again reported high degradation and mineralization rates; 100% according to both indicators under 250 $kJ \cdot m^{-2}$ and 400 $kJ \cdot m^{-2}$ of solar-accumulated energy, respectively [65]. They stressed that the same mechanism that was responsible for the enhancement of photocatalytic activity in C-doped WO_3/TiO_2 composite [66] also improved the performance of N-doped WO_3/TiO_2 [66].

2.5.1.2 TiO_2/Fe_2O_3

Iron oxide (α-Fe_2O_3) is a promising candidate for photocatalytic applications, due to its abundance, nontoxicity, low cost, stability in aqueous solutions (pH > 3), and narrow band gap (2.0–2.2 eV), which directly matches the band positions of TiO_2 to form heterojunction (*Type I Heterojunction*) [57,71]. Several authors report the photocatalytic degradation of CECs using TiO_2/Fe_2O_3 composites (**Table 5**). Hence, Mirmasoomi et al. [72] used TiO_2/Fe_2O_3 as a catalyst for photocatalytic degradation of diazinon (DZ). The authors reported an optimized system with maximum degradation of DZ equal to 95.07% within 45 min under visible light irradiation. In another study by Moniz et al. [57], photocatalytic degradation of 2,4-D while using TiO_2/Fe_2O_3 composites was investigated, reporting 100% 2,4-D degradation and 100% mineralization of overall organic content within 2 h and 3 h, respectively, using irradiation from a 300 W Xenon Lamp. The authors found out that, when compared to the benchmark TiO_2 (P25), the TiO_2/Fe_2O_3 composite shows superior photocatalytic activity. Based on photoluminescence and photocurrent studies, the TiO_2/Fe_2O_3 composite exhibits enhanced separation of e^-/h^+ pairs due to the formed heterojunction. The proposed mechanism was supported with DFT studies, which firstly involved the transfer of photogenerated e^- from TiO_2 CB to Fe_2O_3 CB. In addition, Fe_2O_3 binds strongly with (dissolved) oxygen, thus aiding the photoelectron transfer. This *in-situ* second stage mechanism facilitates the facile migration of h^+ from the VB of TiO_2 [57].
Macías et al. [58] studied the same system, TiO_2/Fe_2O_3 composites for photocatalytic degradation of 2,4-D, but while using natural sunlight. The authors reported 96.8% 2,4-D degradation and 90.0% mineralization of overall organic content less than two hours and four hours, respectively. Contrary to the presented mechanism of Moniz et al. [57], Macias et al. [58] proposed that the incorporation of Fe_2O_3 causes the photogenerated e^- in CB of TiO_2 to be transferred to CB of Fe_2O_3, promoting the reduction of Fe^{3+} to Fe^{2+}. Photogenerated h^+ in VB of TiO_2 is transferred to VB of Fe_2O_3, which leads to the regeneration of Fe^{3+} and avoids

the recombination of e^-/h^+ pairs at TiO_2 surface. In addition, Fe_2O_3 (E_g = 2.0-2.2 eV) can be excited by visible light irradiation producing photogenerated e^-/h^+ pairs. Photogenerated e^- in CB of Fe_2O_3 can be transferred to O_2 dissolved in water to form $O_2^{\bullet-}$, while photogenerated h^+ in VB of Fe_2O_3 can facilitate generation of HO• eventually contributing to the degradation of present organics [58] (**Figure 8**). The formation of mentioned ROS and their involvement in degradation of targeted pollutant was confirmed through common scavenging tests using TB, FA, and BQ.

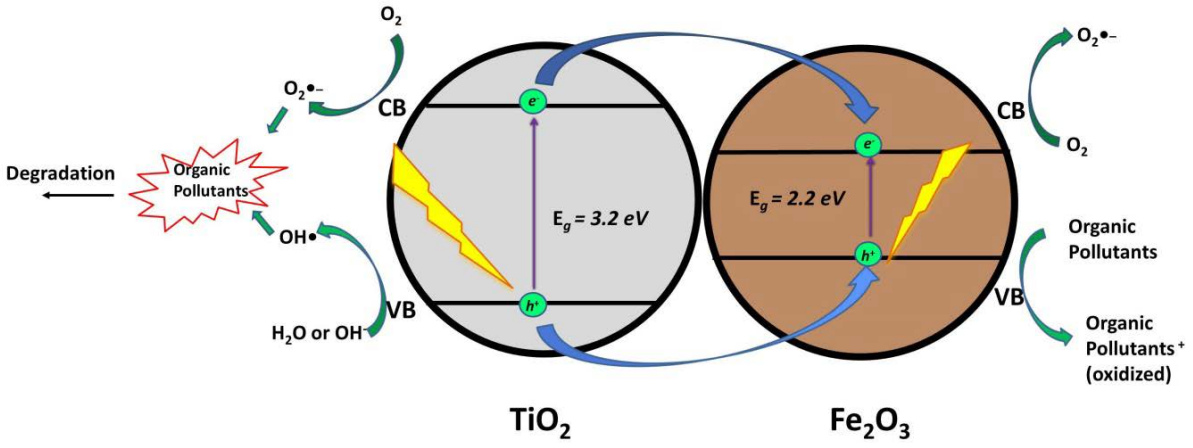

Figure 8. Photocatalytic degradation mechanism over TiO_2/Fe_2O_3 composite [5]

The photocatalytic degradation of the pharmaceutical tetracycline (TC) and its derivatives, such as oxytetracycline (OTC), using TiO_2/Fe_2O_3 materials has also been reported. Hence, it was found out that, under visible light irradiation (λ = 400–750 nm), α-Fe_2O_3 was activated and generated e^-/h^+ pairs, and then photogenerated e^- from CB of α-Fe_2O_3 moved to TiO_2 trapping sites for atmospheric O_2 to form $O_2^{\bullet-}$, which was proven to largely contribute to the degradation of OTC. On the other hand, the photogenerated h^+ from VB of α-Fe_2O_3 primarily reacted with OH^-, resulting in the generation of HO•, which also contributed to the degradation of OTC. When compared to TiO_2 reference material, the TiO_2/Fe_2O_3 composite exhibited an enhanced photocatalytic activity under visible light due to efficient e^-/h^+ separation, as stated above [73].

The same authors [73,74] also studied the degradation mechanism of OTC while using LC-MS-TOF analysis and, based on the formed intermediates, established the OTC degradation pathway, and concluded that HO• mainly mediated degradation. Besides, "pure" TiO_2/Fe_2O_3, enriched analogue with carbon nanotubes (CNTs) was also studied (**Table 5**). Hence, TiO_2/Fe_2O_3/CNTs was used as the catalyst for photocatalytic degradation of

TC**,** under visible light illumination [75]. It was found that the effectiveness of photocatalytic degradation of TC within 90 min treatment using TiO_2/Fe_2O_3/CNTs was almost twice higher when compared to that achieved by benchmark TiO_2; 89.41% and 47.64%, respectively. The authors attributed the improved photocatalytic efficiency to the presence of the CNT, which acted as a photogenerated e^- acceptor, thereby suppressing e^-/h^+ recombination [75]. In another study, the core-shell structured α-Fe_2O_3 (with TiO_2 shell of around 15 nm) exhibited 100% TC removal in 90 min [76]. The degradation improvement was ascribed to the addition of H_2O_2 in the system, which generated more ROS than by the common photocatalytic mechanisms described above [76]. Hence, the contribution of H_2O_2 in such a system can be described through restraining e^-/h^+ recombination and increasing HO• generation in the system, as in **Equation (1)** [77]:

$$H_2O_2 + e^- + H^+ \rightarrow H_2O + HO\bullet \quad (1)$$

Table 5. Photocatalytic degradation of CEC's over TiO_2/Fe_2O_3 composites

Catalyst	Target pollutant	Initial concentration/ working volume ((mg·L^{-1}) /mL)	Experimental conditions	Reaction time	Removal extent (%)	Reference
TiO_2/Fe_2O_3 (0.1 g·L^{-1})	Diazinon	10 (in 300 mL)	Light Source: 60 W Philips Visible lamp; pH= natural	45 min	95.07	[72]
TiO_2/Fe_2O_3 (10 mg)	2,4-dichlorophenoxy acetic acid	50 (in 100 mL)	Light Source: 300 W Xenon Lamp; pH= natural	120 min	100 (TOC= 100 @ 150 min)	[57]
TiO_2/Fe_2O_3 (0.5 g·L^{-1})	2,4-dichlorophenoxy acetic acid	50 (in 250 mL)	Light Source: natural sunlight 11AM-4PM; pH= 4	120 min	96.8 (TOC=90 @ 240 min)	[58]
TiO_2/Fe_2O_3 (70 mg)	Oxytetracycline Hydrochloride	60 (in 70 mL)	Light Source: 300 W Iodine Tungsten Lamp; pH= 5.5	300 min	75.6	[73]
TiO_2/Fe_2O_3 (1.0 g·L^{-1})	Oxytetracycline	60	Light Source: 300 W Iodine Tungsten Lamp; pH= 5.5	300 min	~80	[74]
TiO_2/Fe_2O_3/CNT (100mg)	Tetracycline	20 (in 100mL)	Light Source: 300 W Xenon Lamp; pH= natural	90 min	89.41	[75]
TiO_2-coated α-Fe_2O_3 core-shell (100mg)	Tetracycline Hydrochloride	50 (in 200 mL)	Light Source: 300 W Xenon Lamp (λ > 420 nm) ; pH= 5. 45 Oxidant= 120 µL (30% H_2O_2)	90 min	100	[76]

2.5.1.3 TiO_2/Spinel Ferrite

Spinel ferrites (MFe_2O_4) are metal oxides, where M is a divalent ion (i.e., Mg^{2+}, Ca^{2+}, Sr^{2+}, Ni^{2+}, Zn^{2+}, etc.), serving as promising candidates for photocatalytic applications due to their narrow band gap range (1.3–2.2 eV) and magnetic properties [78,79]. Spinel ferrites band positions match TiO_2, thus possessing compatibility to form a heterojunction (*Type II*

Heterojunction) [80–83].

The literature provides applications of MFe_2O_4/TiO_2 materials as photocatalysts in treatment of CECs, as in the case of previously discussed TiO_2-based composites. However, it should be noted that authors within such composites used modified TiO_2 (**Table 6**). Hence, Chen et al. [80] studied photocatalytic degradation of TC and its derivatives using N-doped $TiO_2/CaFe_2O_4$/diatomite, and reported 91.7% removal of TC within 150 min under visible light irradiation. The authors studied the composite stability and reusability; the results obtained after five cycles indicate that employed composite is rather stable, enabling 89.2% removal of TC. They also proposed the photocatalytic mechanism occurring within the composite; the excitation of both N-TiO_2 and $CaFe_2O_4$ by visible light leads to the formation of e^-/h^+ pairs (**Figure 9**). The photogenerated e^- in CB of N-TiO_2 can directly react to adsorbed O_2 generating $O_2^{\bullet-}$, while photogenerated h^+ in VB of N-TiO_2 directly react with H_2O and OH^- producing HO•. Simultaneously, photogenerated e^- in CB of $CaFe_2O_4$ can undergo the same mechanism (i.e., reaction with O_2 to produce $O_2^{\bullet-}$). In addition, the formed heterojunction helps the migration of e^- from CB of $CaFe_2O_4$ to CB of N-TiO_2, and h^+ from VB of N-TiO_2 to VB of $CaFe_2O_4$ (**Figure 9**). Such a transfer of charge carriers between the two semiconductors hinders the recombination process and enhances the photocatalytic activity of the composite, thus leading to more efficient generation of ROS ($O_2^{\bullet-}$ and HO•); the existence of formed ROS was confirmed through scavenging tests while using isopropyl alcohol (IPA), ammonium oxalate (AO), and BQ for HO•, h^+ and $O_2^{\bullet-}$, respectively [80].

Such behavior is confirmed by studying the degradation pathway of TC; it was found that the TC intermediates match those that formed through radical driven reactions undergoing in the first step demethylation and hydroxylation. The second step considered the removal of functional groups (amino, hydroxyl, and methyl) and further ring opening reactions that are mainly mediated by photogenerated h^+, yielding small fragments that were eventually mineralized [80]. Such a pathway confirmed the dual role of photogenerated h^+, as a promoter HO• generation and as sites for the direct oxidation of adsorbed organics.

There are several other studies investigating the application of different MFe_2O_4/TiO_2 materials (N-doped-$TiO_2/SrFe_2O_4$ diatomite [82]; Ce/N-co-doped $TiO_2/NiFe_2O_4$/ diatomite and $ZnFe_2O_4/TiO_2$ [83]) for the photocatalytic degradation of CECs, such as TC, OTC, and bisphenol A (BPA). Interestingly, the same mechanisms responsible for charge transfer and consequent generation of ROS were reported, regardless of the different M type within the spinel ferrite part of composite and/or TiO_2 (non-doped or doped with metal and/or non-metal ions).

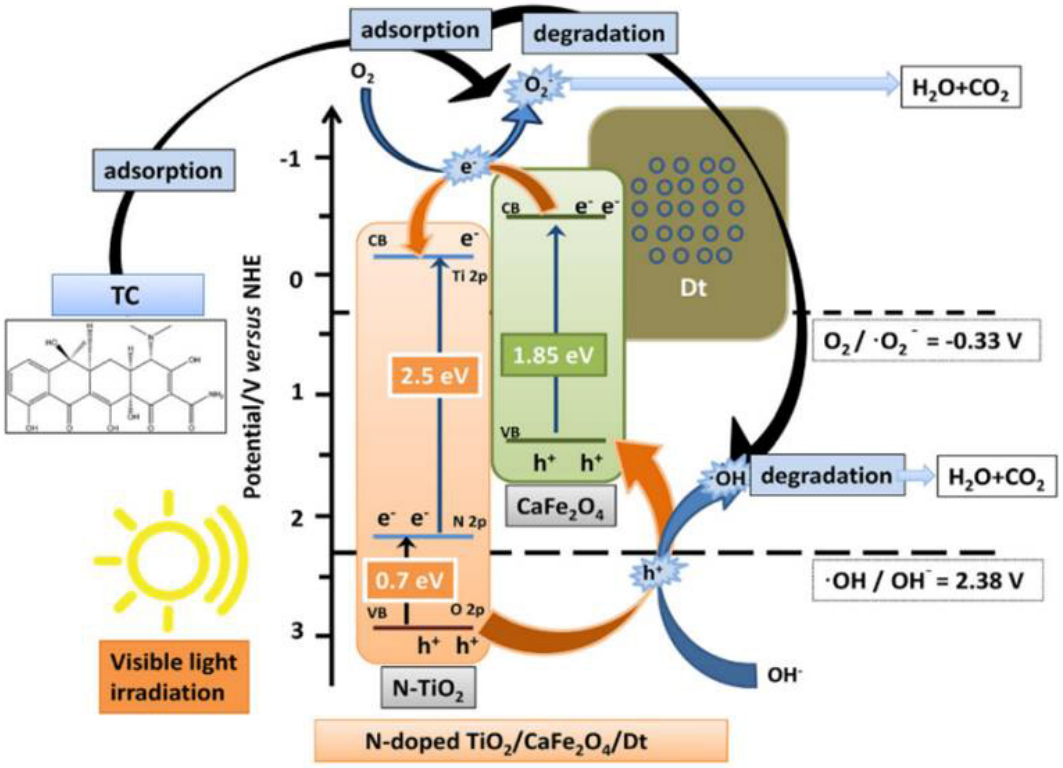

Figure 9. Proposed mechanism for the TC photodegradation process using N-doped $TiO_2/CaFe_2O_4$/diatomite [80]

Table 6. Photocatalytic degradation of CEC's over TiO_2/MFe_2O_4 composites

Catalyst	Target pollutant	Initial concentration/ working volume ((mg· L^{-1}) /mL)	Experimental conditions	Reaction time	Removal extent (%)	Reference
N-TiO_2/ $CaFe_2O_4$ /diatomite (2.0 g·L^{-1})	Tetracycline	10 (in 200 mL)	Light Source: 150 W Xenon Lamp with UV light filter	150 min	91.7 (TOC =~80 @ 2h)	[80]
N-TiO_2/ $SrFe_2O_4$ /diatomite (2.0 g·L^{-1})	Tetracycline	10 (in 200 mL)	Light Source: 150 W Xenon Lamp with UV light filter	150 min	92 (TOC= ~80 @ 2h)	[81]
Ce/N co-doped TiO_2 / $NiFe_2O_4$ diatomite (0.5 g·L^{-1})	Tetracycline	20 (in 200 mL)	Light Source: 150 W Xenon Lamp with UV light filter	180 min	98.2 (TOC= ~95)	[82]
$ZnFe_2O_4$ / TiO_2 (1.0 g·L^{-1})	Bisphenol A	10 (in 200 mL)	Light Source: 300 W Xenon Lamp pH= 7	30 min	100	[83]

2.5.1.4 TiO_2/Cu_2O

Cu_2O, a *p*-type semiconductor (E_g = 2.0–2.2 eV), is also a good candidate for making heterojunctions with TiO_2 (*Type II Heterojunction*). Hence, the photocatalytic degradation of various CECs (TC [84], and tetrabromodiphenyl ethers [85]) using TiO_2/Cu_2O composite materials was reported under solar light irradiation (**Table 7**). Based on the findings in the

mentioned studies, the photocatalytic mechanism of TiO_2/Cu_2O under solar light illumination involves the activation of both Cu_2O and TiO_2 to generate e^-/h^+ pairs (**Figure 10**). Photogenerated e^- in CB of Cu_2O then can migrate to CB of TiO_2 and, along with photogenerated e^- in CB of TiO_2, react with O_2 to form $O_2^{\bullet-}$. Simultaneously, photogenerated h^+ in VB of Cu_2O can be directly involved in the oxidation of adsorbed organics, while photogenerated h^+ in VB of TiO_2 can directly oxidize adsorbed organics or react with H_2O (i.e., OH^-) and generate HO•. Besides, these h^+ can also directly migrate to the VB of Cu_2O, thus leading to effective charge separation that improves the overall photocatalytic activity of the composite [84].

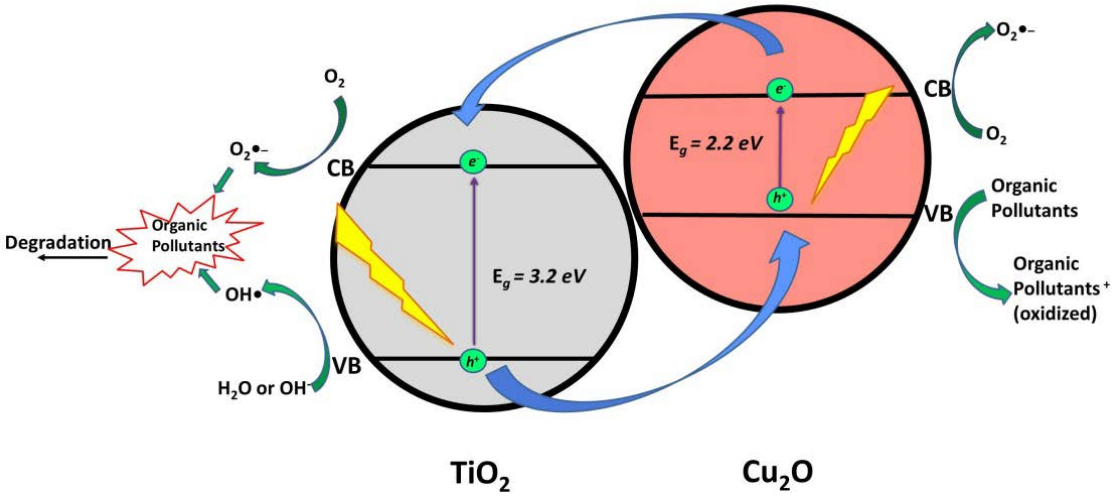

Figure 10. Photocatalytic degradation mechanism over TiO_2/Cu_2O composite [5]

Table 7. Photocatalytic degradation of CEC's over TiO_2/Cu_2O composites

Catalyst	Target pollutant	Initial concentration/ working volume ((mg· L^{-1}) /mL)	Experimental conditions	Reaction time	Removal Extent (%)	Reference
Cu_2O-TiO_2 supported palygorskite (1.0 g·L^{-1})	Tetracycline Hydrochloride	30 (in 50mL)	Light Source: 500 Xe Lamp; pH= 8.7	240 min	88.81	[84]
TiO_2-Cu_2O film	Tetrabromodiphenyl Ethers	5 (in 100 mL)	Light Source: 300 W Xenon Lamp; pH= natural solvent CH_3OH:H_2O (50:50 v/v)	150 min	90	[85]

2.5.1.5 TiO_2/Bi_2O_3

Bi_2O_3, a semiconductor with band gap range in the visible region (2.5–2.8 eV), is also a good candidate for making heterojunctions with TiO_2 (*Type II Heterojunction*). Studies including its application in photocatalytic degradation of CECs (quinalphos [86] and ofloxacin [87]) under solar light irradiation (**Table 8**) revealed the occurring photocatalytic

mechanism. Both of the composite phases can be activated under solar irradiation generating e^-/h^+ pairs (**Figure 11**). Accordingly, photogenerated h^+ in VB of TiO_2 are involved in the production of HO• (through reactions with H_2O, i.e., OH^-) as of e^-/h^+ pairs. In addition, h^+ in VB of Bi_2O_3 can be transferred to VB of TiO_2 that contributes to the direct oxidation of adsorbed organics or the generation of HO• [87].

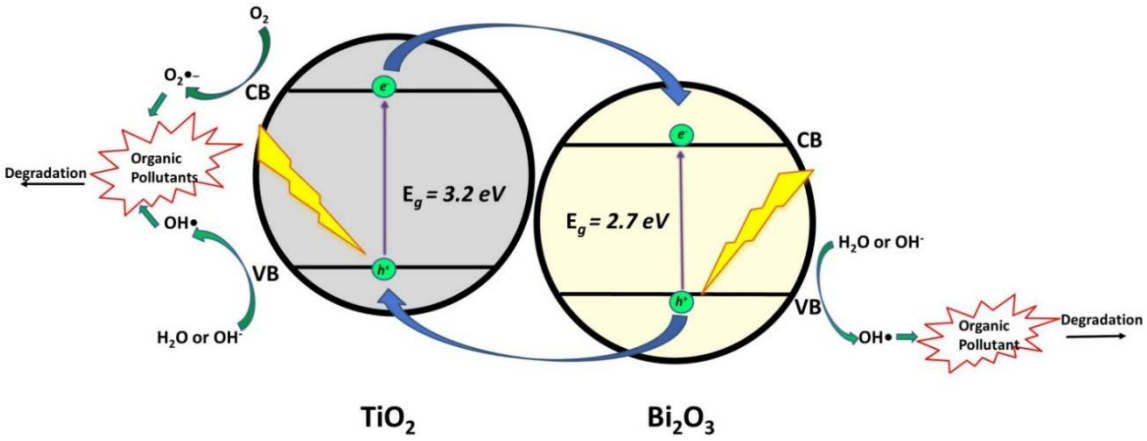

Figure 11. Photocatalytic degradation mechanism over TiO_2/Bi_2O_3 composite [5]

Table 8. Photocatalytic degradation of CEC's over TiO_2/Bi_2O_3 composites

Catalyst	Target pollutant	Initial concentration/ working volume ((mg· L^{-1}) /mL)	Experimental conditions	Reaction time	Removal extent (%)	Reference
Bi_2O_3–TiO_2 (50 mg)	Quinalphos	25 (in 50 mL)	Light Source: Visible light with 1.56 µmol•m^{-2}•s^{-1}; pH= 8	100 min	92	[86]
Bi_2O_3–TiO_2 (0.5 g·L^{-1})	Ofloxacin	25	Light Source: 70.3 K lux; pH= 7	120 min	92	[87]

2.5.2 Coupling of TiO_2 with Metal Sulfides

Cadmium sulfide (CdS), a metal sulfide semiconductor with a visible light range band gap (E_g = 2.1–2.4 eV), has been proven to be compatible with TiO_2, due to its higher position of CB than that of TiO_2 (*Type II Heterojunction*) (**Figure 12**) [59,88]. However, one should be aware that its application can lead to adverse effects due to its instability, resulting in the leaching of toxic Cd^{2+} during treatment [89]. Although its CB and VB positions are thermodynamically favorable for photocatalytic application, CdS as a photocatalytic material faces serious problems. Next to the above-mentioned promotion of toxic effects, issues, like poor stability due to photocorrosion and limited separation efficiency of photogenerated charge carriers, do not speak in favor of CdS application [90,91]. Photocorrosion is not only related to the photogenerated h^+ in semiconductor itself that oxidizes S^{2-} and release Cd^{2+} to

the solution, but also with newly formed O_2, where higher solubility in water leads to more dramatic levels of photocorrosion of CdS [90,92]. However, CdS was widely investigated in photocatalytic purposes, even in recent studies that focused on the degradation of CECs (ofloxacin, ciprofloxacin, tetracycline, and 17α-ethynylestradiol), where it was used in various forms (nano-rods, nano-belts) [59,88,93,94] (**Table 9**). Generally, upon visible light illumination, CdS is excited and generates the e^-/h^+ pair, where photogenerated e^- in CB of CdS migrates to CB of TiO_2 and is consumed in reactions with O_2 to produce $O_2^{\bullet-}$, while h^+ remain in the VB of CdS.

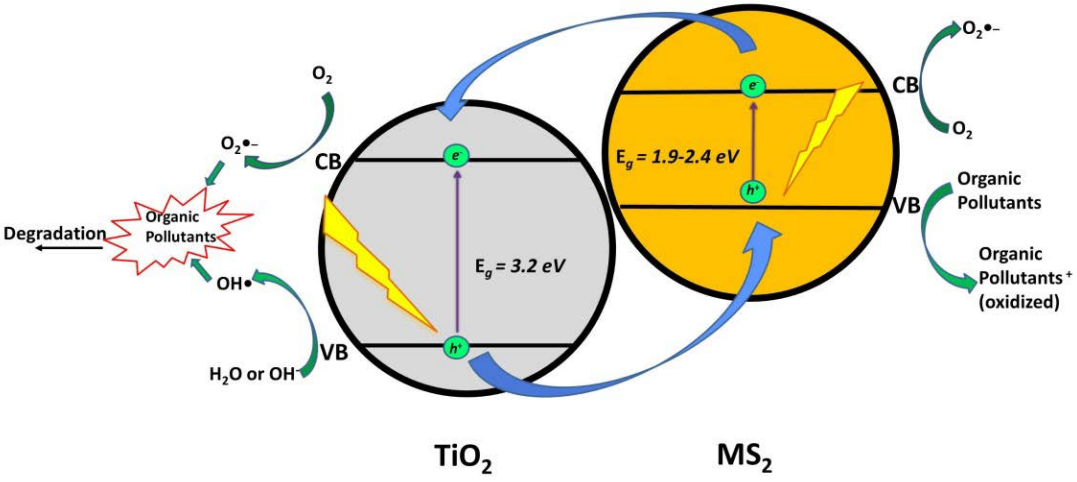

Figure 12. General photocatalytic degradation mechanism over TiO_2/MS (M=Cd or Cu) or MS_2 (M=Mo and Sn) composite [5]

Copper sulfide (CuS), which is another metal sulfide semiconductor with narrow band gap of 2.0 eV, has also been reported to be coupled with TiO_2 (*Type II Heterojunction*) [95,96]. Jiang et al. [95] reported a 85.5% degradation of enrofloxacin and 27.7% mineralization of overall organic content using immobilized CuS/TiO_2 nanobelts (**Table 9**). They elucidated the mechanisms occurring in the composite upon excitation by solar irradiation. Hence, such broad wavelengths excited both composite phases (CuS and TiO_2) and resulted in e^-/h^+ pairs, while the transfer of charges was analogous, as in the case of the CdS/TiO_2 composite. Photogenerated e^- in CB (−0.33 eV) of CuS underwent transfer to CB (−0.19 eV) of TiO_2 and were consumed in reactions with O_2 forming $O_2^{\bullet-}$. Photogenerated h^+ in VB of CuS remained there and present potential active sites for direct degradation of organics that were adsorbed at the CuS surface, since they cannot be involved in generation of HO• due to too high energy band positioning. On the other hand, photogenerated h^+ in VB of TiO_2 can directly react with adsorbed organics and OH^- generating HO•.

Chen et.al [96], incorporated Au nanoparticles to CuS/TiO_2 nanobelts structure to enhance the photocatalytic degradation ability of the composite by capturing e^- and, consequently, suppressing the recombination of photogenerated charges. As a result, they obtained 96% degradation of OTC and 68% mineralization of the overall organic content within one hour under artificial sunlight illumination. Accordingly, the mechanism of such enriched CuS/TiO_2 composite involves, besides the above discussed mechanism, the path considering the transfer of e^- to Au, which leads to enhanced charge separation, thus delaying recombination. In such a case scenario, photogenerated h^+ would have higher probability to react either with adsorbed organics or with HO^- in order to generate HO• (exclusively those in VB of TiO_2), thus contributing to the overall system efficiency. The involvement of formed ROS into reaction mechanisms for OTC degradation was confirmed by scavenging tests using TB, AO, and BQ.

Molybdenum disulfide (MoS_2), a two-dimensional (2D) layered metal chalcogenide with an indirect band gap of 1.1 eV and 1.9 eV direct band gap in monolayered form, with unique structure, low-cost, high thermal stability, and electrostatic integrity, is also a suitable candidate for forming heterojunction with TiO_2 (*Type II Heterojunction*) [97–99]. Hence, Kumar et al. [100] reported its application in the photocatalytic degradation of paracetamol. Furthermore, Irandost et al. [97] applied the modified MoS_2/TiO_2 composite (they used N,S-co-doped TiO_2) in the photocatalytic degradation of DCF under visible LED lamp irradiation (**Table 9**). Hence, the synergistic effect of dopants in TiO_2 promoted its visible light activity, yielding the formation of e^-/h^+ pairs in both composite phases. The mechanism of charge formation and consequent transfer was similar, as described above for CuS/TiO_2, which was excited by solar irradiation. Hence, photogenerated e^- in CB of N,S-co doped TiO_2 and CB of MoS_2 were able to undergo reactions with O_2 forming $O_2^{\bullet-}$, while h^+ in VB of TiO_2 promoted HO• formation in reactions with HO^- and provide the direct oxidation of adsorbed organics, while, again, h^+ in MoS_2 were able to do only the latter. The importance of HO• and h^+ in DCF degradation was confirmed by trapping agents used in scavenging tests: TB and potassium iodide (KI), respectively.

Tin sulfide (SnS_2), which is a metal sulfide semiconductor with band gap of 2.2 eV [101], has also been reported to be coupled with TiO_2 (*Type II Heterojunction*) [102,103]. Hence, Kovačić et al. [102] reported improved the degradation of 17β-estradiol (E2), for 51%, using SnS_2/TiO_2 when compared to the benchmark material (P25) TiO_2 under solar irradiation. A similar improvement was obtained by comparing performances of the same materials in the case of DCF degradation [103] (**Table 9**). The reason for such improvement

relies on the potential of photogenerated e^- in CB of SnS_2 to migrate to CB of TiO_2, while h^+ remained at the VB of SnS_2. In such case, the efficient separation of charges is achieved, thus facilitating the improved redox reactions, enabling effective degradation of adsorbed organics directly on the surface by h^+, in spite of the limited ability of such a composite to generate •OH. Accordingly, the adsorption has been shown as an important step in the effectiveness of the SnS_2/TiO_2 composite. Kovačić et al. [103] utilized DFT calculations to study the surface interaction of polar compound (DCF) and non-polar compound (memantine) at SnS_2/TiO_2 composite and found that DCF was more efficiently degraded due to much higher adsorption ability in comparison to memantine, which is one of its structure feature limitations (amine functionality).

Table 9. Photocatalytic degradation of CEC's over TiO_2/Metal sulfide composites

Catalyst	Target pollutant	Initial concentration/ working volume ((mg· L^{-1}) /mL)	Experimental conditions	Reaction time	Removal extent (%)	Reference
CdS –TiO_2 (50 mg)	Tetracycline Hydrochloride	50 (in 50mL)	Light Source: 500 W Xenon Lamp with filter (λ>400 nm); pH= natural	480 min	87.0	[94]
Au-CdS/TiO_2 nanowire (20 mg)	Ciprofloxacin	20	Average solar light intensity=100, 000	60 min	99	[93]
CdS/TiO_2 (450 mg)	Ofloxacin	10 (in 100mL)	Light Source: 85 W Oreva bulb with 4150 lumens (λ= 450-650 nm); pH= natural	180 min	86	[88]
CdS nano-rod/TiO_2 nano-belt (0.50 g·L^{-1})	17α-ethynylestradiol	3 (in 10 mL)	Light Source: 500 W Xenon Lamp with filter (λ>420 nm); pH= natural	120 min	92	[59]
CuS/TiO_2 nanobelts	Enrofloxacin	5 (in 35 mL)	Light Source: 35 W Xenon Lamp; pH= natural	120 min	85.5 (TOC= 27.7)	[95]
Au-CuS-TiO_2 nanobelts	Oxytetracycline	5 (in 35 mL)	Light Source: 35 W Xenon Lamp; pH= natural	60 min	96 (TOC= 68)	[96]
MoS_2/TiO_2 (25 mg·L^{-1})	Acetaminophen	302	Light Source: Sunlight; pH= natural	25 min	40	[100]
N,S co-doped TiO_2@MoS_2 (0.98 g·L^{-1})	Diclofenac	0.15 (in 100 mL)	Light Source: 60 W LED lamp; pH= 5.5	150 min	98	[97]
TiO_2/SnS_2 films	17β-estradiol	1.36 (in 90 mL)	Light Source: 450 W Xenon Arc Lamp	90 min	51.0	[102]
TiO_2/SnS_2 films	Diclofenac	31.8 (in 90mL)	Light Source: 450 W Xenon Arc Lamp; pH= 4	60 min	76.21	[103]

2.5.3 Coupling of TiO_2 with Silver-Based Semiconductors

Silver phosphate (Ag_3PO_4), a promising semiconductor with narrow band gap ($E_g \geq$ 2.4 eV), showed good photocatalytic performance in the degradation of organic pollutants

under visible light irradiation [104,105]. Namely, Ag_3PO_4 exhibits a quantum efficiency of up to 90% [104] and it can absorb wavelengths that are shorter than ~530 nm [105]. Despite the qualities of Ag_3PO_4 as a potential photocatalyst, it still suffers from limitations, such as photocorrosion, small but not negligible solubility in water ($K_{sp} = 1.6 \times 10^{-16}$), and particle agglomeration upon synthesis [106]. To overcome these limitations, constructing a heterojunction between Ag_3PO_4 and a compatible semiconductor has attracted attention due to the increase in charge separation and production of more ROS [107]. The positions of VB and CB in TiO_2 directly match the Ag_3PO_4 band positions, thus providing the compatibility to form a heterojunction. Hence, Wang et al. [108] investigated the performance of TiO_2 nanotubes/Ag_3PO_4 quantum dots for the degradation of TC under visible light illumination, and reported a high removal rate within a short treatment period; 90% TC removal within 8 min (**Table 10**).

The conventional heterojunction transfer mechanism (**Figure 13A**) explains that the photogenerated h^+ in the composite would be promoted from the VB of Ag_3PO_4 to VB of Ti^{3+}-doped TiO_2 nanotubes, where can react with H_2O or HO^- forming HO•. Simultaneously, photogenerated e^- from the Ti^{3+}-doped TiO_2 nanotubes CB can react with O_2 forming $O_2^{\bullet-}$ or may transfer to the CB of Ag_3PO_4. However, $O_2^{\bullet-}$ are not formed in Ag_3PO_4, due to the fact that the position of its CB is lower than the standard reduction potential of $O_2^{\bullet-}/O_2$. Wang et al. [108] concluded that TC was primarily degraded by $O_2^{\bullet-}$ and photogenerated h^+ based on the results of the conducted electron trapping experiments. Accordingly, they have extended the study by proposing a Z-scheme heterojunction transfer mechanism (**Figure 13B**). Under this mechanism, Ag(0) acts as recombination center, "collecting" photogenerated e^- from CB of Ag_3PO_4, where they undergo recombination with the photogenerated h^+ from VB of Ti^{3+}-doped TiO_2 nanotubes. In such case, photogenerated h^+ on VB of Ag_3PO_4 might participate in the direct oxidation reactions with adsorbed organics, while the photogenerated e^- in the CB of Ti^{3+}-doped TiO_2 nanotubes can be involved in forming desired ROS, $O_2^{\bullet-}$, thus contributing to the enhanced performance of composite photocatalyst. Du et al. [109] applied an analogue TiO_2/Ag_3PO_4 composite employing TiO_2 nanotube arrays for the degradation of ciprofloxacin (CIP) under solar irradiation and reported 85.3% removal of CIP within 60 min. was facilitated through the above-mentioned mechanisms. Furthermore, Liu et al. [110] reported 95% degradation of BPA in 16 min using TiO_{2-X}/Ag_3PO_4 under visible light irradiation (**Table 10**). They reported that both composite phases, TiO_{2-X} and Ag_3PO_4, were excited and generated e^-/h^+ pairs. Hence, photogenerated h^+ in VB of TiO_{2-X} are promoted to VB of Ag_3PO_4 and contribute to the direct oxidation of adsorbed organics, similarly as

reported in the study by Wang et al. [108]. Photogenerated e^- from the CB of Ag_3PO_4 are transferred to oxygen vacancies (V_o) of TiO_2 and contributed in reactions with adsorbed O_2 generating $O_2^{\bullet-}$ (**Figure 14**). They also investigated the role of these species in the degradation of BPA and found, based on monitoring BPA degradation pathway by LC-MS analysis, that intermediates are formed through two pathways: 1) hydroxylation, through reactions with $O_2^{\bullet-}$ yielding BPA-*o*-catechol; and, 2) direct oxidation by h^+ forming isopropenylphenol and phenol, which was further oxidized by h^+ yielding hydroquinone and its dehydrated form benzoquinone.

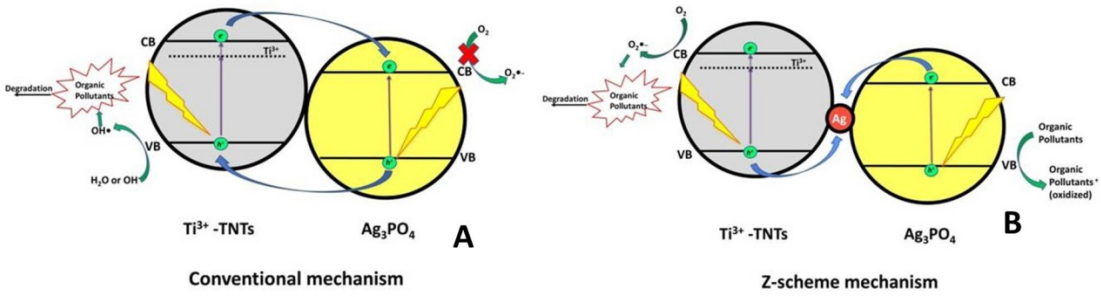

Figure 13. Photocatalytic mechanism Ti^{3+}-TNT/Ag_3PO_4 (**A**) conventional heterojunction, (**B**) Z-scheme heterojunction [5]

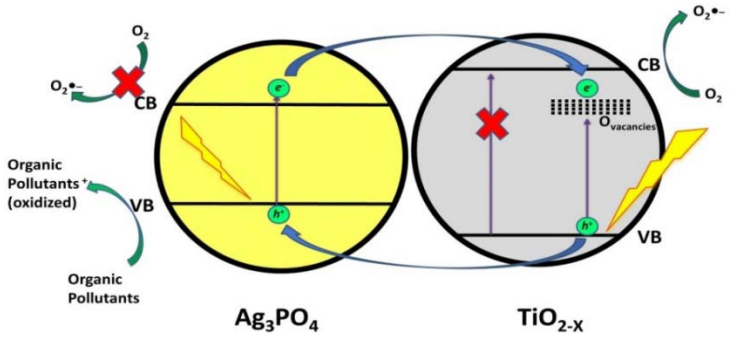

Figure 14. Photocatalytic reaction mechanism of TiO_{2-x} /Ag_3PO_4 under visible light irradiation [5]

Silver oxide (Ag_2O), a visible light active photocatalyst with a band gap of 1.2 eV, is another silver-based compound with semiconducting properties. Based on the band positions (VB and CB), it represents a promising matching candidate to form heterojunctions with TiO_2 (*Type III Heterojunction*). Hence, photocatalytic degradation of levofloxacin (LEV) using Ag_2O/TiO_2 quantum dots is reported with the maximum of 81% LEV degradation within 90 min of visible light irradiation [61]. Based on the proposed mechanism under visible light illumination (**Figure 15**), upon excitation of Ag_2O, e^-/h^+ pairs are formed,

whereas TiO_2 is not activated due to its wide band gap. Photogenerated e^- in the CB of Ag_2O were transferred to CB of TiO_2 and involved in reactions with adsorbed O_2 forming $O_2^{\bullet-}$ that participated in LEV degradation. In addition, photogenerated h^+ in VB of Ag_2O yielded the formation of HO•, through reactions with OH^-, and participated in LEV degradation as well. The authors employed LC-MS analysis to elucidate the LEV degradation pathway and, as such, establish the role of formed ROS. Hence, parent compound LEV underwent decarboxylation of the acetyl group; hydroxylation resulting in the formation of quinolone moieties; demethylation and the subsequent addition of hydrogen atom generating modifications at piperazine ring; while successive HO• attack resulted in multi-hydroxylated intermediates. Such findings confirmed the dominant role of HO• in LEV degradation.

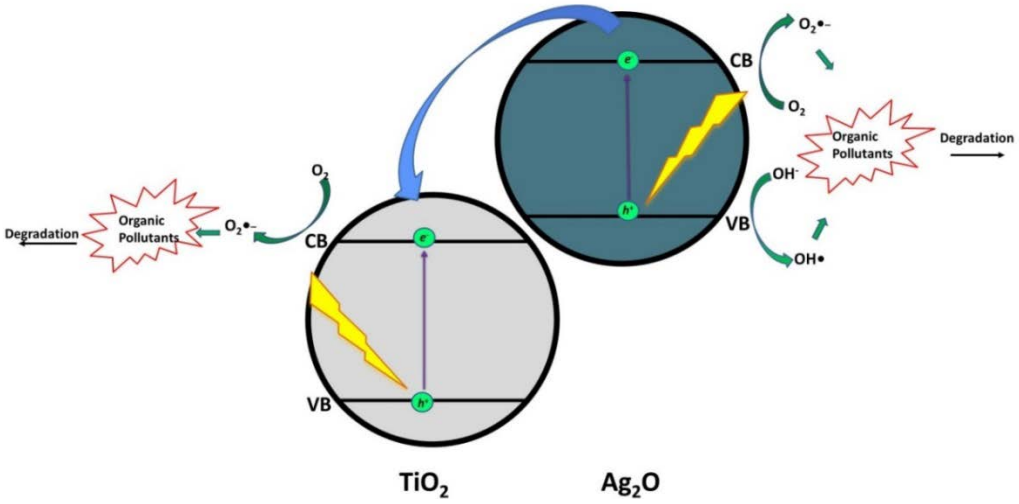

Figure 15. Photocatalytic degradation mechanism over TiO_2/Ag_2O composite [5]

Table 10. Photocatalytic degradation of CEC's over TiO_2/Ag-based composite

Catalyst	Target pollutant	Initial concentration/ working volume ((mg· L^{-1}) /mL)	Experimental conditions	Reaction time	Removal extent (%)	Reference
Ti^{3+}-doped TiO_2 nanotubes/ Ag_3PO_4 quantum dots (0.5 g·L^{-1})	Tetracycline	10 (NA)	Light Source: 400 W Xenon Lamp; pH= natural	8 min	90	[108]
TiO_2 nanotube/ Ag_3PO_4 nanoparticles (40 mg)	Ciprofloxacin	10 (in 40 mL)	Light Source: 300 W Xenon Lamp	60 min	85.3	[109]
TiO_{2-x} /Ag_3PO_4 (100 mg)	Bisphenol A	10 (in 100 mL)	Light Source: 500 W Xenon Lamp with filter (λ=420 nm); pH= natural	16 min	95	[110]
Ag_2O/ TiO_2 quantum dots (0.25 g·L^{-1})	Levofloxacin	10 (in 100 mL)	Light Source: 85 W Oreva CFL (4150 lumens) (λ=380-700 nm) pH=4	90 min	81	[61]
Ag_2O /TiO_2 – zeolite (50 mg)	Norfloxacin	5 (in 100 mL)	Light Source: 35 W Xenon Lamp	60 min	98.7 (TOC=83.1)	[62]

In another study, Gou et al. [62] investigated the application of Ag_2O/TiO_2/zeolite composite for solar-driven degradation of norfloxacin (NOR) (**Table 10**). Besides high effectiveness (98.7% NOR degradation and 83.1% mineralization of organic content within 60 min. treatment), they elucidated the NOR degradation pathway, involving in the initial stage decarboxylation, defluorination or hydroxylation of parent compound (NOR), which confirmed the involvement of both formed ROS ($O_2^{\bullet -}$ and HO•).

2.5.4 Coupling of TiO_2 with Graphene and Graphene-Like Materials

2.5.4.1 TiO_2 / Graphene Composites

Graphene is a zero bandgap semiconductor with a sheet-like structure (i.e., it is considered as a 2D monolayer material) consisting of sp^2 hybridized carbon atoms with excellent thermal conductivity, optical transmittance, high mechanical strength, large surface area (2600 $m^2 \cdot g^{-1}$), and appreciable charge carrier transport [111]. Under light illumination, it can achieve a reverse saturation state with high density ($\sim 10^{13}$ cm^2) of hot electrons above the Fermi level, which can be used as a powerful agent in redox reactions [112]. It was also found that the incorporation of graphene-based materials (i.e., graphene oxide and its reduced form; GO and rGO, respectively) with TiO_2 might suppress e^-/h^+ pairs recombination. As such, TiO_2/graphene-based composites were employed in the photocatalytic degradation of CECs (**Table 11**).

2.5.4.2 TiO_2 /Semiconductor/ Graphene Composites

As described in above sections, the coupling of TiO_2 with other semiconductors promotes efficient charge transfer, eventually yielding improved photocatalytic activity. However, in most cases, the recombination is still an existing issue that needs to be suppressed. Such a double effect can be obtained by combining a composite concept involving two semiconductors (even "pure" TiO_2, which cannot be active under visible light) with graphene-based materials. For instance, Hao et al. [113] reported 93.2% degradation of BPA in seven hours of sunlight irradiation while using the TiO_2/WO_3/GO composite. The mechanism occurring in such a combined composite involved the excitation of both TiO_2 and WO_3 under solar light irradiation (TiO_2 utilized UV-A fraction), yielding the generation e^-/h^+ in both semiconductors. Hence, photogenerated e^- in CB of TiO_2 can directly react with absorbed O_2, producing $O_2^{\bullet -}$, or it can be transferred to CB of WO_3, and then further migrate to GO enhancing charge separation. Since the amount of adsorbed O_2 is quite limited, the tendency of e^- to recombine with h^+ is rather favored; ~90% of pairs

recombine rapidly after excitation [3]. Hence, the charge separation represents an important factor in the evaluation of photocatalyst performance. Accordingly, in the case of effective separation and recombination suppression, as in the case with GO, photogenerated h^+ in VB of activated composite components, e.g., of TiO_2 and WO_3 in the case of TiO_2/WO_3/GO, can be involved in a larger amount, either directly or indirectly (through formation of HO•) in the degradation of present organics. It should be noted that, in composites with two semiconductors, GO could also act as a redox site, attracting photogenerated e^- and h^+, thus promoting improved surface migration of charges [113]. **Table 11** summarizes several works regarding TiO_2/semiconductor/GO composites employed for the degradation of CECs with analogous mechanisms, as mentioned above.

Table 11. Photocatalytic degradation of CEC's over TiO_2/Semiconductor/graphene composites

Catalyst	Target pollutant	Initial concentration/ working volume ((mg·L^{-1}) /mL)	Experimental conditions	Reaction time	Removal extent (%)	Reference
TiO_2/WO_3/GO (2 mg)	Bisphenol A	20 (in 50 mL)	Light Source: sunlight pH= 7	7 h	93.2	[113]
Graphene-WO_3 /TiO_2 nanotube (photoelectrodes)	Dimethyl Phthalate	10 (in 40 mL)	Light Source: 150W Xe lamps	120 min	75.9	[114]
TiO_2/ZnO/GO (0.5 g·L^{-1})	Bisphenol A	10 (in 50 mL)	Light Source: 18 UV lamps (λ=365 nm) ;Visible metal halide lamps(λ= 400-800 nm) pH= 6	120 min (UV) 180 min (Vis)	99.7 (UV) 94.9 (Vis)	[115]
TiO_2/ZnO/GO (0.5 g·L^{-1})	Ibuprofen	10 (in 50 mL)	Light Source: 18 UV lamps (λ=365 nm) ;Visible metal halide lamps(λ= 400-800 nm) pH= 6	120 min (UV) 180 min (Vis)	98.5 (UV) 79.6 (Vis)	[115]
TiO_2/ZnO/GO (0.5 g·L^{-1})	Flurbiprofen	10 (in 50 mL)	Light Source: 18 UV lamps (λ=365 nm) ;Visible metal halide lamps(λ= 400-800 nm) pH= 6	120 min (UV) 180 min (Vis)	98.1(UV) 82.2 (Vis)	[115]
$ZnFe_2O_4$/rGO/TiO_2 (0.1 g)	Fulvic Acid	20 (in 50 mL)	Light Source: 300 W (λ=420 nm); Vol $_{H2O2}$ =0.8 mL, pH= 7	180 min	95.4%	[116]
TiO_2 /MoS_2/rGO (0.5 g·L^{-1})	Bisphenol A	10 (in 50 mL)	Light Source: 20 W (λ=254 nm);	300 min	62.4	[117]
$TiO_2/BiVO_4$/rGO	Tetracycline	10 µg·L^{-1} (NA)	Light Source: 1000 W Xe Lamp (λ=420 nm) with filter	120 min	96.2	[118]
$TiO_2/BiVO_4$/rGO	Chlorotetracycline	10 µg·L^{-1} (NA)	Light Source: 1000 W Xe Lamp (λ=420 nm) with filter	120 min	97.5	[118]
$TiO_2/BiVO_4$/rGO	Oxytetracycline	10 µg·L^{-1} (NA)	Light Source: 1000 W Xe Lamp (λ=420 nm) with filter	120 min	98.7	[118]
$TiO_2/BiVO_4$/rGO	Doxycycline	10 µg·L^{-1} (NA)	Light Source: 1000 W Xe Lamp (λ=420 nm) with filter	120 min	99.6	[118]

2.5.4.3 TiO_2/g-C_3N_4

Graphitic carbon nitride (g-C_3N_4) is a two-dimensional, metal-free polymeric π-conjugated semiconductor material, which has attracted a lot of attention [119–127] since the pioneering work of Wang et al. [128] in 2009, due to its high stability, visible light response with the bandgap of 2.7 eV and non-toxicity [129]. It can be easily synthesized through the direct pyrolysis of nitrogen-rich precursors, such as melamine, cyanamide, dicyandiamide, and urea, but its practical application and principle drawback is low specific surface area and high rate of electron-hole recombination [119,130,131]. Therefore, g-C_3N_4 modification to address shortcomings are needed, e.g., as an excellent candidate to form heterojunction with TiO_2 (*Type II Heterojunction*), due to their matched band positions (VB and CB). Hence, several studies employing g-C_3N_4/TiO_2 were focused on photocatalytic degradation of CECs (**Table 12**). For instance, Yang et al. [132] reported 88.1% degradation of CIP within 180 min. under visible light irradiation. The authors ascribed the improved photocatalytic activity to multiple effects: (i) an increase in the surface area of the composite; (ii) good dispersity of TiO_2 in g-C_3N_4 enabling the intimately coupling of composite phases; and, (iii) extension of light absorption of the composite due to low band gap of g-C_3N_4. Trapping experiments that were conducted revealed that photogenerated h^+ were the major reactive site involved in CIP degradation.

In another study, Li et al. [133] reported the 100% degradation of acyclovir in 90 min using g-C_3N_4/TiO_2 under visible light irradiation. However, after seven hours of continuous irradiation, any TOC removal was not noticed, implying the formation of rather recalcitrant intermediates with high resistance to degradation by ROS that were formed within the studied system. Trapping experiments for formed reactive species elucidated that g-C_3N_4/TiO_2 under visible light irradiation only produced h^+ and $O_2^{\bullet-}$, and not the most reactive HO•, explaining limited oxidation capability and no TOC removal in the case of acyclovir degradation. This significant contribution proves that the use of g-C_3N_4/TiO_2 under visible light irradiation must undergo careful laboratory tests regarding the susceptibility of targeted organics and their intermediates to degradation by h^+ and $O_2^{\bullet-}$ prior to considering real scale application [133].

Several studies also showed that the tailoring of composite morphology promotes improved photocatalytic efficiency. For instance, Yu et al. [134] prepared a mesoporous g-C_3N_4/TiO_2 that was applied to polysulfone ultrafiltration membranes for sulfamethoxazole (SMX) removal. It was found that mpg-C_3N_4/TiO_2 exhibit 69% SMX degradation within 30

hours of sunlight irradiation. On the other hand, TiO_2 nanosheets with exposed facets (001) (core)-g-C_3N_4 (shell) composite exhibit a higher degradation rate of 2.2 mg·min^{-1}, which is 36% faster when compared to TiO_2 and g-C_3N_4 physically-mixed composite. The improved effect is ascribed to the close interaction of TiO_2 and g-C_3N_4 core-shell structure, whereas, in physically mixed composite the formed heterojunction is random and non-uniform [135].

The use of support materials, such as clays [136] and polymers [137] has been also utilized for improved adsorption capacity and the stability of g-C_3N_4/TiO_2 composites. For instance, Chen et al. [137] used g-C_3N_4–shielding polyester fiber (PET)/TiO_2 for photocatalytic degradation of sulfaquinoxaline and thiamethoxam. Interestingly, the composite removal efficiency for sulfaquinoxaline reached 97%, after 10 consequent cycles. Furthermore, the introduction of kaolinite with g-C_3N_4/TiO_2 improved the surface area and adsorption capacity of the composite, leading to 92% degradation of CIP in 240 min. of visible light irradiation [136].

An additional approach considers doping of metals and non-metals in TiO_2, enhancing its light absorption capacity from UV absorption to visible light absorption. Thus, incorporating doped TiO_2 with g-C_3N_4 structures has also attracted great attention for the degradation of CECs. For instance, S-Ag/TiO_2@g-C_3N_4 [138] was employed for the degradation of triclosan (TS) and yielded 92.3% degradation of TS within 60 min. under visible light irradiation. Song et al. [139] fabricated a nanofibrous Co-TiO_2 coated with g-C_3N_4, which was applied to TC removal; the authors reported a consistent stability of composite photocatalyst during five consecutive cycles.

Besides doping, sensitization with dyes [140] and carbon dots [141] was also found to enhance the light absorption capacity of g-C_3N_4/TiO_2 composite. For example, D35 organic dye was applied next to g-C_3N_4/TiO_2 and it was found that the light absorption range was enhanced up to 675 nm [140]. On the other hand, Su et al. [141] studied the application of C dots decorated/g-C_3N_4/TiO_2 for the degradation of enrofloxacin under visible light and assigned the observed enhancement to the upconversion photoluminescence properties of C dots, which convert near-infrared light wavelength into visible light wavelength [142]. As effective solutions for improving g-C_3N_4/TiO_2 performance, the incorporation of graphene quantum dots [143] and another semiconductor (i.e., MoS_2 [144], WO_3 [145]) is also reported; such systems resulted in enhanced separation of charges and the suppression of their recombination, thus leading to improved photocatalytic activity in the degradation of CECs.

Table 12. Photocatalytic degradation of CEC's over TiO_2/g-C_3N_4 composites

Catalyst	Target pollutant	Initial concentration/ working volume ((mg· L^{-1}) /mL)	Experimental conditions	Reaction time	Removal extent (%)	Reference
g-C_3N_4/TiO_2 (30 mg)	Ciprofloxacin	10 (in 80 mL)	Light Source: 300 W Xe Lamp with filter (λ>400 nm) pH= natural	180 min	88.1	[132]
g-C_3N_4/TiO_2 (30 mg)	Acyclovir	10 (in 100 mL)	Light Source: 300 W Xe Lamp with filter (λ>420 nm) pH= natural	90 min	100	[133]
mpg-C_3N_4/TiO_2 (membrane)	Sulfamethoxazole	10 (in 50 mL)	Light Source: 300 W Xe Lamp pH=natural Flow rate=13 mL/min Membrane flux=918 L /m^2 h	1800 min	69	[134]
TiO_2@g-C_3N_4 core-shel (100 mg)	Tetracycline	20 (in 100 mL)	Light Source: Xenon Lamp with full spectrum pH=natural	9 min	(2.2 mg· min^{-1})	[135]
g-C_3N_4 –shielding polyester/ TiO_2 (130 mg)	sulfaquinoxaline	2 x 10^{-5} mol·L^{-1} (30 mL)	Light Source: Q-Sun Xe-1 test, pH= 7	90 min	97	[137]
g-C_3N_4 –shielding polyester/ TiO_2 (130 mg)	thiamethoxam	2 x 10^{-5} mol·L^{-1} (30 mL)	Light Source: Q-Sun Xe-1 test, pH= 7	180 min	~95	[137]
g-C_3N_4/TiO_2/kaolinite (200 mg)	Ciprofloxacin	10 (in 100 mL)	Light Source: Ave. light intensity =90 mW/cm^2 ; Xe Lamp with filter (λ>400 nm), pH= natural	240 min	92	[136]
S-Ag/ TiO_2 @ g-C_3N_4 (0.20 g·L^{-1})	Triclosan	10 (in 100 mL)	Light Source: 250 W Xe Lamp with filter (λ>420 nm), pH= 7.8	60 min	92.3 (Detoxification Efficiency= 64.3± 3.9)	[138]
Co-TiO_2 @g-C_3N_4 (5 mg ; 2 × 2 cm^2 membranes)	Tetracycline Hydrochloride	20 (in 10 mL)	Light Source: 300 W Xe Lamp with filter (λ>420 nm), pH= 7	60 min	90.8	[139]
D35-TiO_2/g-C_3N_4 (0.5 g·L^{-1})	Bisphenol A	10 (in 100 mL)	Light Source: 300 W Metal Halide pH=7, Oxidant= 2mM Persulfate	15 min	100 (TOC= 50)	[140]
C dots decorated g-C_3N_4/TiO_2 (1.0 g·L^{-1})	Enrofloxacin	4 (in 50 mL)	Light Source: 350 W Xe Lamp with filter (λ> 420 nm) pH= natural	60 min	91.6	[141]
graphene quantum dots Mn-N-TiO_2 /g-C_3N_4 (45 mg)	Ciprofloxacin	10 (in 80 mL)	Light Source: 300 W Xe Lamp (320≤λ≤780 nm), pH= 7	120 min	89	[143]
graphene quantum dots Mn-N-TiO_2 /g-C_3N_4 (45 mg)	Diethyl Phthalate	10 (in 80mL)	Light Source: 300 W Xe Lamp (320≤λ≤780 nm), pH= 7	120 min	70.4	[143]
MoS_2 supported TiO_2/g C_3N_4 (30 mg)	Atrazine	10 (in 100 mL)	Light Source: 500 W Xe Lamp (λ>420 nm), pH= 7	300 min	86.5	[144]
WO_3–TiO_2 @g-C_3N_4	Acetylsalicylate	10 (in 100 mL)	Light Source: 500 W Metal Halide pH=natural	90 min	98	[145]
WO_3–TiO_2 @g-C_3N_4	Methyl-theobromine	10 (in 100 mL)	Light Source: 500 W Metal Halide pH=natural	90 min	97	[145]

2.6 Analytical methods for CEC identification and quantification

2.6.1 High Performance Liquid Chromatography

High performance liquid chromatography (HPLC) is a suitable technique for separating and identifying polar organic compounds in an aqueous mixture. The main components of an HPLC system include a solvent reservoir, pump, column, and detector [146].

In liquid chromatography (**Figure 16**), the mobile phase is the liquid that is used to separate and identify the compounds. This can be a single solvent, a combination of solvents, or a changing mixture of solvents over time, known as a gradient. The sample is dissolved in a mobile phase. This mobile phase is then forced through an immiscible stationary phase, which is fixed in place in a column. The two phases are chosen so that components of the sample distribute themselves between the mobile and stationary phases to varying degrees. Those components strongly retained by the stationary phase move only slowly with the flow of the mobile phase. In contrast, components that are weakly held by stationary phase travel rapidly. Reversed-phase chromatography (RPC) is the most commonly used form of HPLC, where the stationary phase is typically a nonpolar hydrophobic material, while the mobile phase is a polar solvent or a mixture of polar solvents and an organic modifier. This creates a hydrophobic environment in the stationary phase, which can interact with analytes based on their hydrophobicity and polarity. In RPC, more polar analytes will have a stronger attraction to the polar mobile phase and will elute faster, while less polar analytes will have a stronger interaction with the nonpolar stationary phase (i.e., C_{18} or C_8 alkyl chains bounded to silica particles) and will elute more slowly. Meanwhile, the use of high pressure technology for HPLC applications led to the creation of ulra-high performance liquid chromatography (UHPLC) which are commonly used nowadays due to its faster separation times and increased resolution [147].

The pump in an HPLC system provides a consistent and reproducible supply of mobile phase to the column. The mobile phase is mixed in a mixer to ensure consistent separation and elution from the column, especially when more than one solvent is used. The mixed mobile phase is then passed through a valve, where the sample is loaded into a loop. The valve opens, allowing the mobile phase to carry the sample into the column [146].

The analyte elutes from the column and passes through a detector, depending on the mobile phase and the analyte. The column is specifically designed to retain the analyte, and

compounds mainly elute based on their polarity. The elution time and intensity at the detector determine the analyte's identity and concentration. The solution may then pass through another detector or be discarded. A column oven is used to maintain a controlled temperature during the separation process and improves resolution, peak shape and elution time [146].

The detector is chosen based on the method and what characteristics of the analytes are being measured. The most commonly used detectors for environmental analysis are UV absorbance, fluorescence, and mass spectrometry. A UV detector can be used to measure organic compounds with aromatic or at least pi-conjugation systems, as it measures any compound that absorbs light at a selected wavelength [146]. The main disadvantage of HPLC-UV system is that it is restricted to limited analysis of compounds (i.e., not suitable for multi-residue analysis). Nevertheless, the combination of HPLC with mass spectrometry (MS), is a technique of choice nowadays since it provides better selectivity and sensitivity.

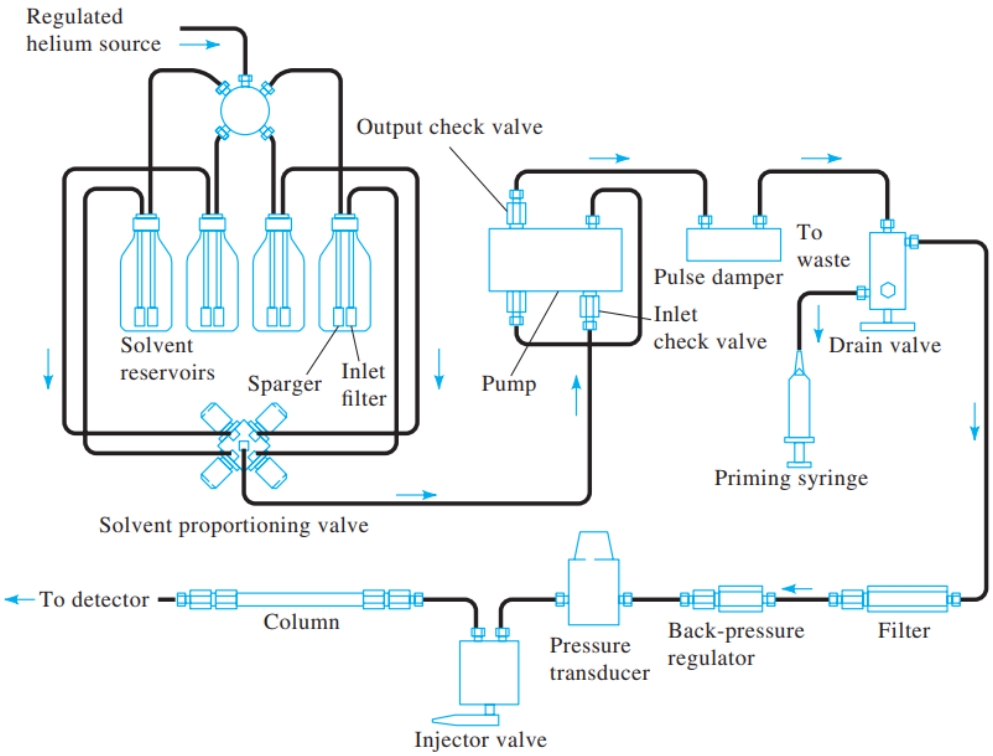

Figure 16. Diagram showing components of a typical apparatus for HPLC. Adapted from [147]

2.6.2 High Performance Liquid Chromatography-Mass Spectrometry (LC-MS)

In HPLC-MS (**Figure 17**), the HPLC and MS are connected through an interface. As the eluent flows into the interface, the solvent is evaporated and the analyte molecules are

vaporized and ionized, which is necessary as the mass spectrometer can only detect and measure gas phase ions [148].

The process of generating analyte ions at atmospheric pressure in the interface is known as atmospheric pressure ionization (API) and the interface is referred as the API source. The most common sources used in LC-MS analysis are electrospray ionization (ESI) and atmospheric pressure chemical ionization (APCI) [148]. ESI involves the formation of ions through the application of a high voltage to a solution containing the analyte. The solution is typically a mixture of the analyte and a volatile solvent (i.e., methanol or acetonitrile). The high voltage causes the solvent to evaporate, leaving behind a highly charged droplet of the analyte. This droplet then undergoes a series of desolvation and ionization events, resulting in the formation of gas-phase ions that can be detected by the mass spectrometer. APCI, on the other hand, involves the ionization of analytes in the presence of a corona discharge. The corona discharge creates a stream of charged particles that react with the analyte molecules to form ions. Unlike ESI, which requires a volatile solvent, APCI can ionize analytes in a wider range of solvents and matrices, including nonpolar solvents (i.e., hexane). One key difference between ESI and APCI is the type of analytes they can ionize. ESI is typically better suited for the ionization of polar and charged analytes, while APCI is better suited for the ionization of nonpolar and neutral analytes [147].

Once the analyte ions are generated, they are drawn into the mass spectrometer where they are subjected to electric and/or magnetic fields, which alter their flight paths and separates them based on their mass-to-charge ratio (*m/z*). These separated ions can then be detected by a variety of mass detectors, of which the most common is the electron-multiplier. When the ions hit the surface of the electron-multiplier, secondary electrons are released. These secondary electrons are amplified by cascading them through a series of dynodes, generating a measurable current that corresponds to the ion concentrations in the mass spectrometer [148]. In HPLC-MS, compounds are mostly analyzed by selected ion monitoring (SIM) mode.

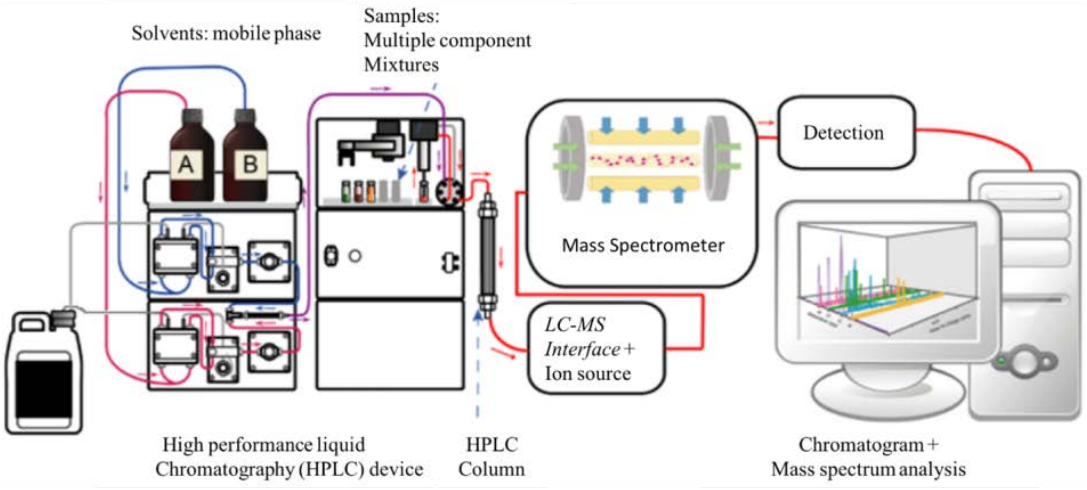

Figure 17. Diagram showing components of a typical apparatus for HPLC-MS [148]

In general, HPLC can be coupled to a single mass spectrometer or to tandem mass spectrometry (**Figure 18**). The main difference between LC-MS and LC-MS/MS is the addition of a collision cell and second mass analyzer [149]. Usually, a single mass spectrometer may not provide accurate or thorough information when it is difficult to separate compounds using both chromatography and *m/z* (such as with isomers). This is especially true when analyzing complex samples with trace amounts of target compounds [149].

To address these limitations, tandem mass spectrometry MS/MS is used, using triple quadrupole or hybrid instruments (i.e., quadrupole-linear ion trap or quadrupole-time of flight instruments). Triple quadrupole instruments involve two quardupole mass analyzers of the same type) or hybrid mass spectrometry (mass analyzers of different types) MS/MS is often used. This method involves two mass analyzers connected in sequence, with a fragmentation cell in between. The ions are first selected in the first mass analyzer (MS1), then enter the fragmentation cell and break apart into smaller ions called product ions, which are then separated and detected in the second mass analyzer (MS2). MS/MS is a more versatile and powerful tool for many applications, such as drug discovery and development, structural analysis of polysaccharides and proteins, and metabolomics research. It provides detailed mass information, reduces matrix interferences and background, resulting in superior selectivity and sensitivity [149].

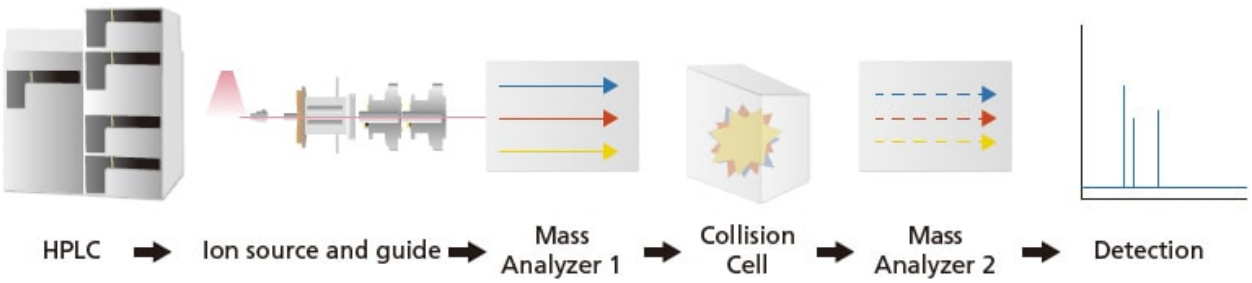

Figure 18. Basic instrumentation of LC-MS/MS. Adapted from [149]

CID, or collision-induced dissociation, is the go-to technique for breaking apart ions in a collision cell. This process generates specific information about the fragment ions through fragmentation of the precursor ions. As shown in **Figure 19**, the collision cell is where this fragmentation takes place [149].

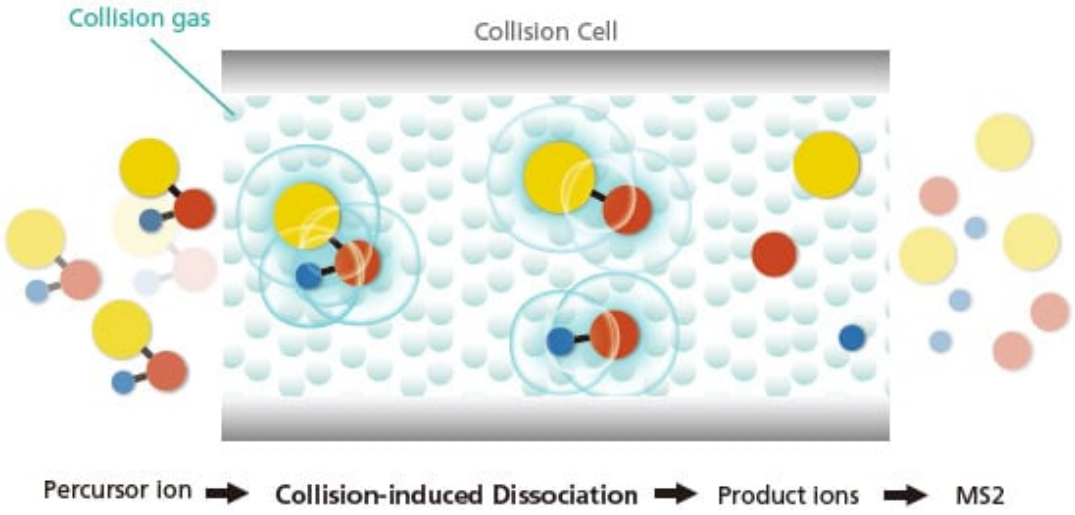

Figure 19. CID illustration in the collision cell of MS/MS system [149]

Precursor ions of a specific mass-to-charge ratio (*m/z*) selected by MS1, are introduced into a collision cell filled with a chemically inert gas, such as helium, argon, xenon or nitrogen. The precursor ions then collide with the inert gas particles by applying an oscillatory field, this process is also known as "shaking". These collisions convert kinetic energy into molecular excitation, which leads to the breaking of chemical bonds and the formation of product ions. The degree of fragmentation and the specific product ions that are formed depend on the amount of energy supplied, as some bonds require more energy to break than others. As shown in **Figure 20**, at a collision energy of 0 volts, the molecular ion of oseltamivir (*m/z* = 313) is the most abundant and no product ions are formed. As the collision energy increases, the abundance of the molecular ion decreases and fragmentation occurs, resulting in a variety of product ions. At even higher collision energies, the degree of

fragmentation becomes more extensive, resulting in the mass spectrum showing no molecular ion and higher abundances of product ions of lower *m/z*. While CID is the most common method of fragmentation, there are other alternatives such as electron capture/transfer dissociation, surface-induced dissociation, and photodissociation [149].

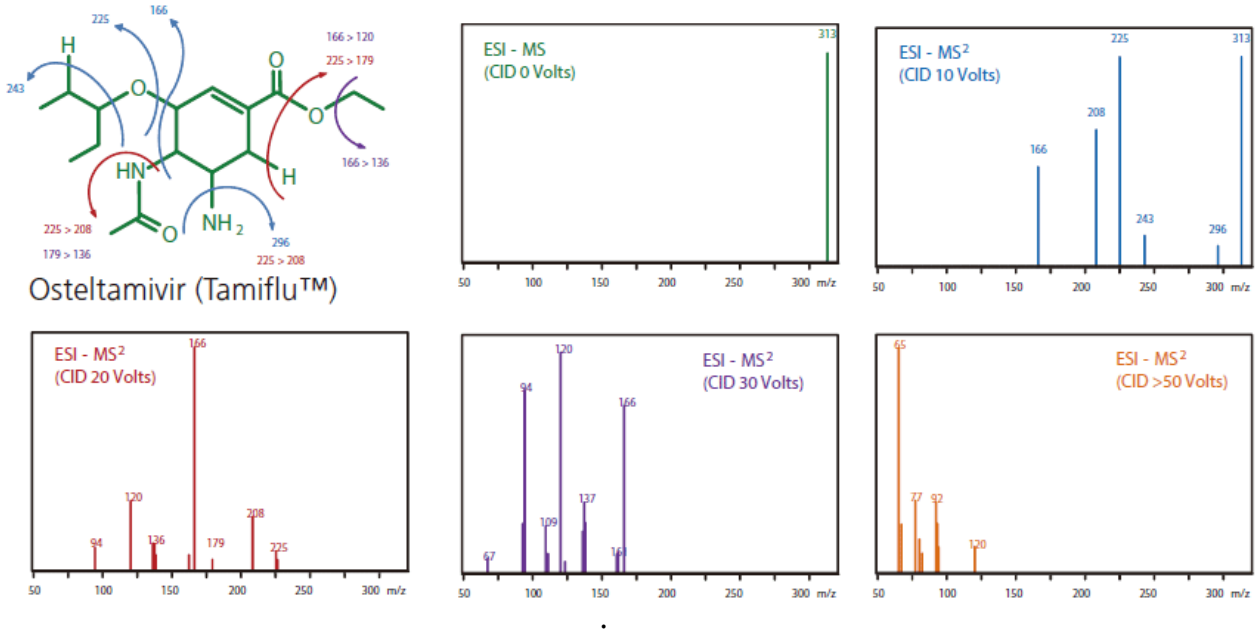

Figure 20. CID of oseltamivir at various collision energies [149]

MS/MS systems can operate either under scan or SIM (fixed) mode whereas MS/MS methods use selected reaction monitoring (SRM) or multiple reaction monitoring (MRM) mode. Before MRM, a product ion scan is typically done to find the most abundant product ion. Overall, MS/MS can selectively target certain ions for more specific and sensitive analysis by removing noise and interference [149].

As such, in MS/MS techniques, four different operational modes can be used as follows: (**Figures 21-24**)

Product Ion Scan

MS1 is set at a specific *m/z* while the MS2 scans for all product ions resulting from the fragmentation of a selected precursor ion. The mass spectrum shows the intensity and m/z of all the captured product ions [149].

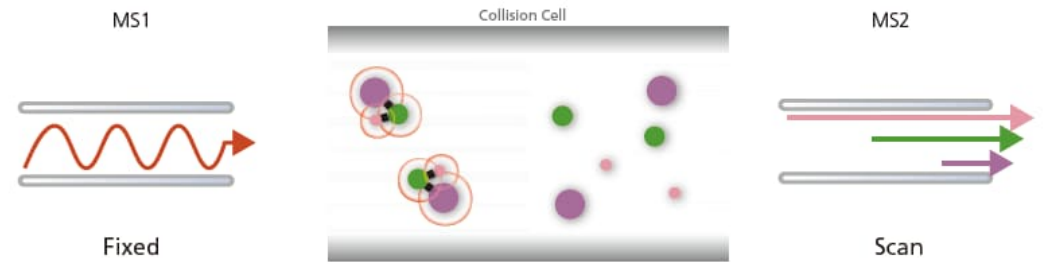

Figure 21. Product ion scan scheme [149].

Precursor Ion Scan

MS1 scans for ions while the MS2 is set to a specific *m/z* product ion formed by CID (collision-induced dissociation) in the collision cell. This mode is helpful for identifying the precursor ions that produce fragment ions of a specific *m/z* [149].

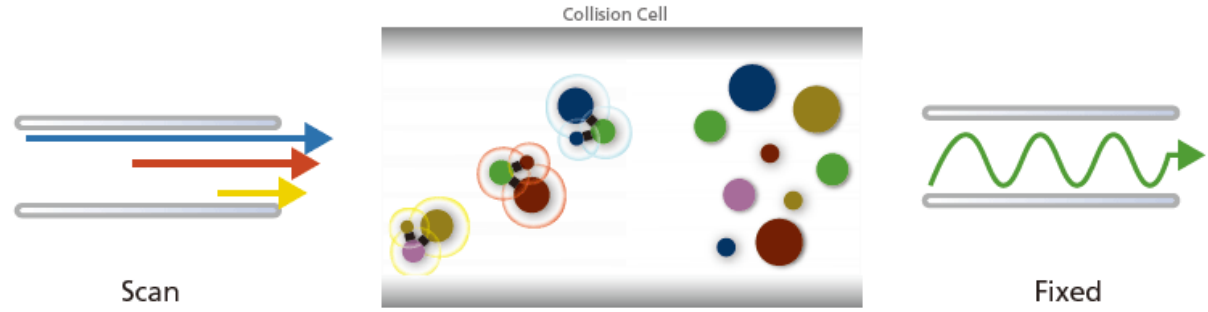

Figure 22. Precursor ion scan scheme [149].

Neutral Loss Scan

Both MS1 and MS2 are in scan mode and set to look for a specific *m/z* difference. This scan helps identify precursor ions that lose a specific neutral molecule, such as a hydroxyl group or phosphate group, during fragmentation [149].

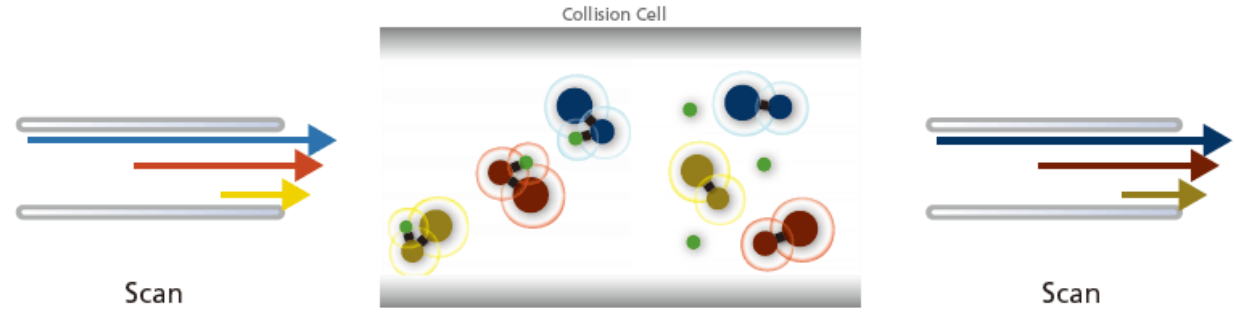

Figure 23. Neutral loss scan scheme [149]

Selected Reaction Monitoring (SRM)/Multiple Reaction Monitoring (MRM)

The process of observing the transition from a chosen precursor ion to a specific product ion is monitored while MS1 and MS2 are fixed at their respective specific *m/z* values [149]. As such, due to enhance selectivity and sensitivity, SRM is the most widely used target analysis and multiresidue methods.

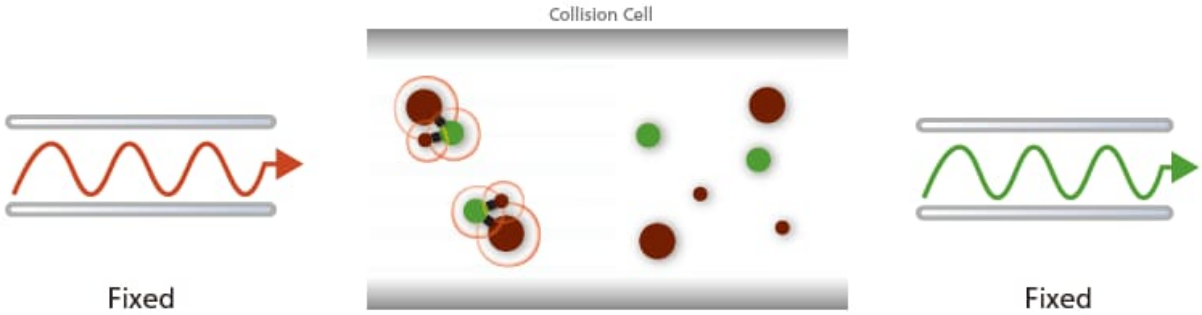

Figure 24. SRM/MRM scheme[149].

2.6.3 High Performance Liquid Chromatography-High Resolution-Mass Spectrometry (LC-MS-Orbitrap)

Orbitrap is a high-resolution mass analyzer, which can operate as a single detector or in combination with a quadrupole mass analyzer [150]. The Q Exactive hybrid quadrupole-Orbitrap mass spectrometer (an example of Orbitrap system, **Figure 25**) consists of several components. It mainly includes an ion source, a stacked-ring ion guide (S-lens), a quadrupole mass filter, a curved linear trap (C-trap), a Higher Energy Collisional Dissociation (HCD) cell, and an Orbitrap mass analyzer. Samples can be introduced into the ion source through various methods, and the injection flatapole transfers ions from the source to the quadrupole. The quadrupole rod assembly acts as an ion transmission device that can filter transmitted ions based on their mass-to-charge ratios. The ions are then transferred into the C-Trap and injected into the Orbitrap mass analyzer to obtain mass spectra. Additionally, ions can be passed through the C-Trap into the HCD cell to conduct MS/MS experiments in combination with the quadrupole mass filters [150]. As of today, it is the most advanced HPLC-MS system, capable of generating up to five decimal places in terms of *m/z*.

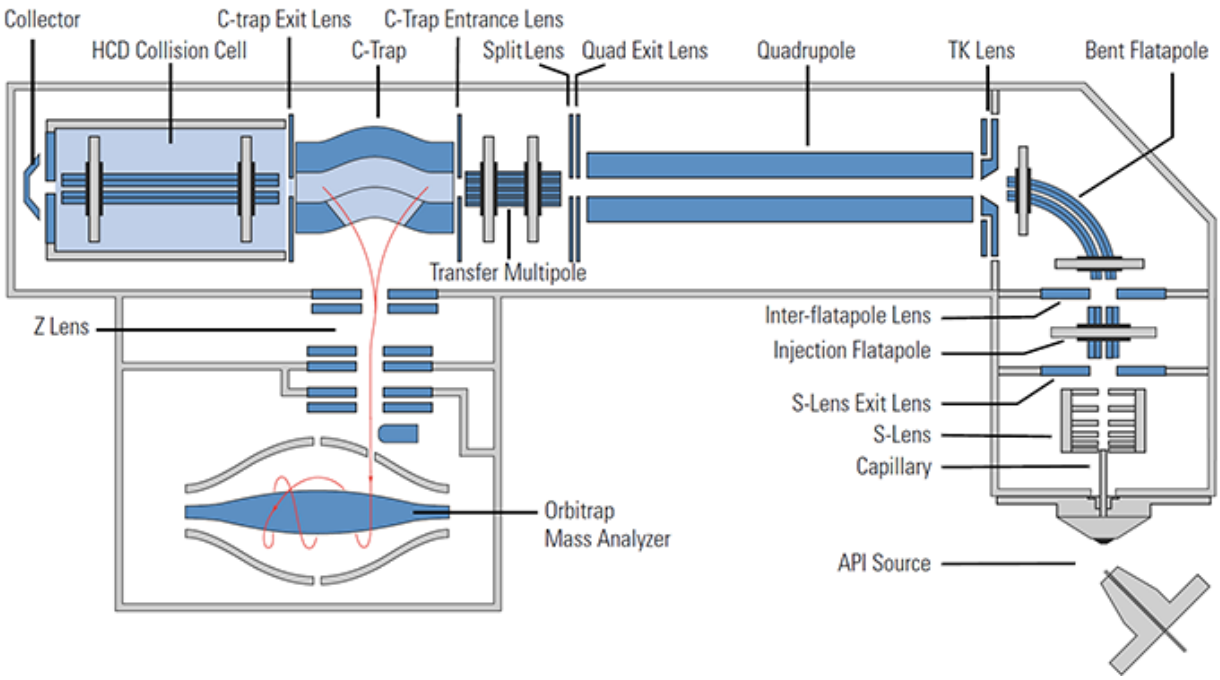

Figure 25. Scheme of Q Exactive Mass Spectrometer (Orbitrap) [150]

2.7 Ecotoxicity

Ecotoxicity refers to the ability of a chemical or physical agent to cause harm to both the environment and living organisms, such as fish, insects, microorganisms, wildlife, and plants [151]. Assessing the toxicity of environmental samples is a crucial aspect of monitoring pollution and assessing risks, as well as to evaluate the feasibility of water treatments applied. Traditional chemical testing methods are accurate and sensitive for specific molecules being analyzed, but do not provide information about the biological effects on the ecosystem. These methods also fail to account for the synergistic effects of multiple compounds and may underestimate the toxic potential of a sample. Using rapid, simple, and cost-effective methods to evaluate biological effects can provide information about the overall effects of a sample and include these important toxicity parameters in regulatory frameworks [152].

A bioluminescence inhibition assay is an important method for evaluating toxicity quickly and cost-effectively. This method uses a marine gram-negative bacterium called *Aliivibrio fischeri* (previously known as *Vibrio fischeri*) as the test species. Bioluminescence produced by the bacterial population is directly proportional to its metabolic activity and any inhibition of enzymatic activity due to toxicity or cell death results in a corresponding decrease in light production by the colony. Test samples are exposed to rehydrated bacteria for a pre-determined period, and the degree of light inhibition is compared to a negative control. In this way, the assay provides a measure of sub-lethal response as well as lethality through the degree of inhibition. The *Vibrio fischeri* test is a fast and easy way to obtain results, the test organisms are available in freeze-dried and liquid-dried form and can easily be reconstituted for use, and the test has been validated and widely used for wastewater and environmental monitoring. These factors make assays that use *Aliivibrio fischeri* a good choice for continuous remote initial screening [152–154].

Another commonly used test species is *Daphnia magna* (*D. magna*), which is an aquatic invertebrate that belongs to the crustacean group. *D. magna* is widely used in ecotoxicological studies on manufactured nanomaterials (MNs), degradation products, and pollutants [155,156].

Toxicity against *Vibrio fischeri* and *Daphnia magna* is usually measured as the half maximal effective concentration (EC_{50}), which is a measure of the concentration of a substance that produces a response halfway between the baseline and maximum after a specific exposure time. In a dose-response curve, the EC_{50} represents the concentration at

which 50% of the maximal effect is observed. It is also the point of inflection on the sigmoidal curve [157].

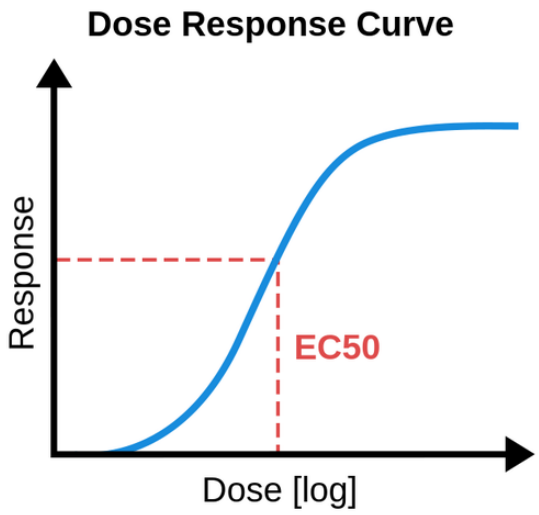

Figure 26. Determination of the EC_{50} from a dose response curve [157]

One of the challenges faced by advanced oxidation processes is the formation of undesired (more toxic) degradation products than the corresponding parent compound. For instance, Li et al. [133] reported the 100% degradation of acyclovir in 90 min using g-C_3N_4/TiO_2 under visible light irradiation. However, after seven hours of continuous irradiation, no TOC removal was observed anymore, implying the formation of rather recalcitrant intermediates with high resistance to degradation by ROS that were formed within the studied system. As such, P3 becomes much more toxic than its parent compound acyclovir (**Figure 27 A** and **B**). Based on "ecological structure-activity relationship" program (ECOSAR), the aquatic toxicity of the third intermediate P3, guanine, was more than double that of acyclovir, although most toxicity values still fell in the same toxic class except for the chromic impact on daphnia (i.e., acyclovir is harmful, and the guanine intermediate is toxic) (**Figure 27B**).

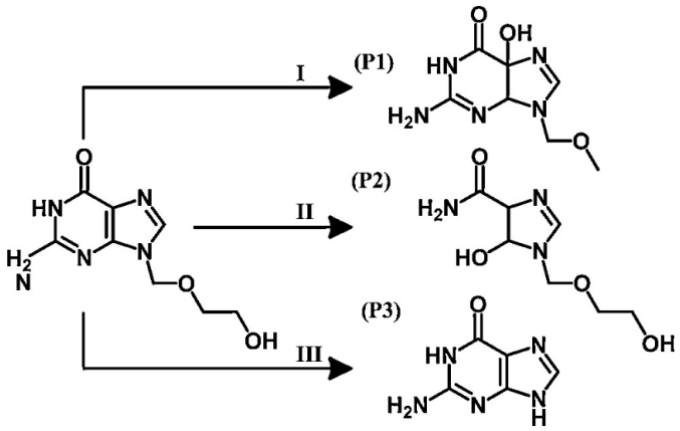

Figure 27A. Proposed visible-light driven photocatalytic degradation pathway of acyclovir in water using g-C_3N_4/TiO_2 [133]

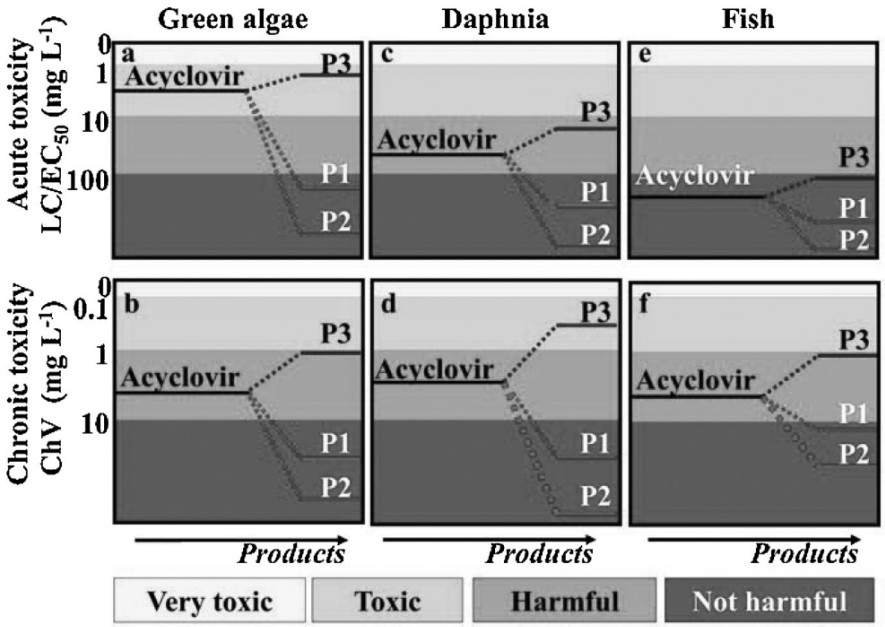

Figure 27B. (ECOSAR)-Theoretical calculated data of aquatic toxicity of acyclovir and its degradation intermediates [133]

2.8 Current challenges and opportunities of TiO_2-based/semiconductor composites

TiO_2-based/semiconductor composites for water treatment generated a vast literature, with its efficacy in degrading CECs as demonstrated in subsection 2.5. However, several knowledge gaps were needed to be addressed regarding TiO_2-based/semiconductor composites application in real environmental conditions, including the following:

(i) *Unequal distribution of solar energy around Earth's surface.* Most applications of TiO_2-based/semiconductor composites for CEC removal are reported under solar irradiation [8]. In fact, solar light is composed of 3% UV light, 44% visible light, and 53% infrared light [11,12]. The UV light portion within solar irradiation plays an important role for the activation of the overall photocatalytic composite (i.e., TiO_2-based/semiconductor composites), and its absence may result in different mechanisms [13]. It must also be noted that UV distribution at the Earth's surface is unequal and influenced by several factors [14]. As such, focusing on the utilization of visible light is favorable for such environmental applications.

(ii) *Toxicity assessment*. Transformation and/or degradation byproducts of CECs after photocatalytic processes (i.e., TiO_2-based/semiconductor composites) are scarcely reported. Clearly, the formation of more toxic byproducts has already been reported using different TiO_2-based/semiconductor composites, as described in section 2.7 [15]. Accordingly, such potential treatment drawbacks must receive well-deserved attention since they can impose additional risk to the environment.

(iii) *Photocatalyst recovery*. Immobilization in various supports is scarcely reported and is usually applied in powder form, thus requiring secondary treatment to remove fine nano-sized composite particles. Immobilization of photocatalysts provides a potential decrease in operating costs for the water treatment process by avoiding in-treatment agglomeration and post-treatment separation issues [1,3,9,16,17].

Despite the success of different TiO_2-based/semiconductor composites as presented in subsection 2.5, Fe_2O_3 was chosen as the main partner of TiO_2 in this dissertation due to the following reasons [71]:

(i) *Abundance and low-cost*. Iron oxide is one of the most abundant minerals on Earth and is readily available, making it a low-cost option for photocatalytic applications.

(ii) *Stability*. Iron oxide is highly stable under both acidic and basic conditions and can withstand high temperatures, making it a durable and long-lasting photocatalyst.

(iii) *Photoactivity*. Iron oxide has a wide bandgap, which allows it to absorb visible light and UV radiation, and its valence band (VB) and conduction band (CB) are aligned with TiO_2 to make a suitable heterojunction.

To fill up the knowledge gaps as mentioned above and to take advantage of Fe_2O_3 properties, immobilized Fe_2O_3/TiO_2 composite was employed for the removal of amoxicillin under solar and visible irradiation, while evaluating the toxicity of the formed byproducts.

3. EXPERIMENTAL PART

3.1 Materials and Methods

The list of chemicals used in the preparation of this work is presented in **Table 13**.

Table 13. List of chemicals used for the present work.

Substance	CAS number	Purity	Supplied by
Target CEC			
Amoxicillin	26787-78-0	>96%	Acros Chemicals
Photocatalyst preparation			
Aeroxide P25- TiO_2	12188-41-9	/	Evonik (Degussa)
Iron(III) nitrate nonahydrate	7782-61-8	≥98%	Fluka
Titanium (IV) butoxide	5593-70-4	>97%	Acros Organics
Iron(III) oxide nanopowder, <50	1309-37-1	/	Sigma-Aldrich
Acetic Acid	64-19-7	p.a	Fluka
Photocatalyst immobilization			
Titanium (IV) isopropoxide	546-68-9	>97%	Acros Organics
Tetraethyl orthosilicate	78-10-4	99%	Sigma-Aldrich
Hydrochloric acid	7647-01-0	>98%	Kemika
Perchloric acid	7601-90-3	60%,p.a	Kemika
Ethanol	64-17-5	96%,p.a	Carlo Erba Reagent
Levasil 200/30	/	/	Obermeier
Isopropanol	67-63-0	HPLC	Fisher Scientific
Nafion 117	31175-20-9	5%	Sigma-Aldrich
Chromatographic Analysis			
Acetonitrile	75-05-08	HPLC	J. T. Baker
Formic acid	64-18-6	HPLC	Sigma-Aldrich
Ammonium acetate	631-61-8	HPLC	J. T. Baker
Water matrix compounds			
Sodium chloride	7647-14-5	p.a.	Kemika
Sodium nitrate	7631-99-4	p.a.	Kemika
Sodium carbonate	497-19-8	p.a.	Kemika
Disodium hydrogen phosphate	10028-24-7	p.a.	Kemika
Humic acids	/	/	Suwannee river, International Humic Substance Society
Scavengers			

Substance	CAS number	Purity	Supplied by
Methanol	67-56-1	HPLC	J.T. Baker
Formic Acid	64-18-6	98%	Fluka
Tert-butanol	75-65-0	99%	Lach-Ner
1,4-benzoquinone	106-51-	98%	Fluka
Others			
Sodium persulfate	7775-27-1	≥99%	Sigma-Aldrich
Hydrogen peroxide	7722-84-1	30%	Kemika
Sodium hydroxide	1310-73-2	p.a.	Kemika
Sulfuric acid	7664-93-9	p.a	Kemika
Potassium Iodide	7681-11-0	p.a	Kemika
Iron(II) sulfate heptahydrate	7782-63-0	≥99%	Fluka
1,10-phenanthroline	5144-89-8	p.a	Kemika
Sodium acetate	127-09-03	p.a	Kemika
Potassium thiocyanate	333-20-0	p.a	Gram-mol

3.1.1 Preparation of Layered Photocatalysts

Commercial photocatalyst nanopowders were immobilized on round glass substrates (r = 37.5 mm) using a low-temperature method [16]. The procedure involved the preparation of a titania sol and silica sol. The titania-sol was prepared by $HClO_4$ catalyzed hydrolysis of TTIP in EtOH under reflux for 48 h. The silica sol was prepared by hydrolysis of TEOS in water catalyzed by HCl, conducted under constant stirring until a clear sol was obtained. Thereafter, the obtained titania sol, silica sol, Levasil 200/30, and EtOH were mixed to form a binder sol. Approximately, 1.0 g of commercial photocatalyst (TiO_2-P25 or α-Fe_2O_3) was added to binder sol and the mixture was homogenized in an ultrasonic bath for 10 min prior to the coating. The photocatalyst-binder sol mixture was deposited on round glass substrates by spin coating at 1500 rpm for 30 s using a KW-4A spin coater (Chemat Technology, USA). The single-layer immobilized photocatalysts were heat-treated in an oven at 200°C for 2 h. The same procedure was repeated for preparing 2 catalyst layers, while between a coatings of layers, the heating cycles (200°C for 2 h) were applied. Configurations of the layered films were as follows: pure TiO_2 (double layer), pure α-Fe_2O_3 (double layer), TiO_2 layer over α-Fe_2O_3 (i.e., TiO_2@α-Fe_2O_3), α-Fe_2O_3 layer over TiO_2 (i.e., α-Fe_2O_3@TiO_2), and physically mixed 50% (*w/w*) of TiO_2/Fe_2O_3 composite (double layer).

3.1.2 Preparation of Fe_2O_3/ TiO_2 nanocomposites

The appropriate amount of TiO_2–P25 (0.300 g) was dispersed in 80 mL of EtOH under sonication (Bandelin Sonorex RK 510 H, Berlin, Germany) for 5 min. Then, the appropriate amount of $Fe(NO_3)_3 \times 9H_2O$ dissolved in 20 mL of EtOH was slowly added dropwise to the TiO_2 P25 suspension whilst under sonication. After the sonication process was carried out for 30 minutes, a mixture that was brownish-white in color was observed. The suspension was then continuously stirred for 6 h at room temperature, before drying at 60 °C for 12h. The collected powder was calcined at 350 °C for 2 h in air using a muffle furnace (LP-08, Instrumentaria, Zagreb, Croatia) to obtain the final product. Different contents of $Fe(NO_3)_3 \times 9H_2O$ were added to form final Fe_2O_3/TiO_2 nanocomposites with a theoretical content (*w/w*) of 1%, 3%, 5%, 10%, and 20% (Fe_2O_3 to TiO_2 P25). Pure α-Fe_2O_3 was obtained by performing the same procedure without the presence of TiO_2 P25. Images of the prepared nanocomposites are shown in **Figure S1**, Appendix

3.1.3 Immobilization of Fe_2O_3/ TiO_2 nanocomposites

Immobilization procedure was similar to subsection 3.1.1 except that three layers were prepared instead of sandwich (i.e., two) layers. The same procedure was repeated for heating cycles (200°C for 2 h) between coating layers.

3.2 Characterization

X-ray diffractograms (XRD) of the prepared nanocomposites were recorded using an X-ray diffractometer MiniFlex 600 (Rigaku, Tokyo, Japan), using Cu $K_{\alpha 1}$ (λ = 1.54059Å) radiation from 3° to 70° with a step width of 0.02° and scan speed of 2.00°·min^{-1}.

Raman spectra of the samples were measured using an Alpha300 (Oxford Instruments-Witec, Ulm, Germany) equipped with a microscope and attached atomic force microscope (AFM). The excitation source wavelength was set to 532 nm, while the integration time was set to 5 s with an average of 20 scans taken.

Scanning electron microscopy (SEM) images were obtained using an Ultra Plus SEM (Zeiss, Jena, Germany). Energy-dispersive spectroscopy spectra (EDS) were recorded with an X-max silicon drift detector (Oxford Instruments, Abingdon, UK).

X-ray photoelectron spectroscopy (XPS) measurements were performed using a PHI VersaProbe III (Version AD) (PHI, Chanhassen, USA) equipped with a hemispherical analyzer and a monochromatic Al Kα X-ray source. Survey spectra were measured using a pass energy of 224 eV and step of 0.8 eV, while Fe *2p* core-level spectra were measured at a pass energy of 27 eV and step of 0.1 eV. The data were acquired using ESCApe 1.4 software. Fitting of Fe and Ti *2p* core-level spectra were performed using CasaXPS software.

Diffuse reflectance spectra (DRS) of the prepared nanocomposites were measured using a UV-2600i UV/Vis spectrophotometer (Shimadzu, Kyoto, Japan), equipped with an integrating sphere. The obtained reflectance versus wavelength spectra of pure components and nanocomposites were transformed into the Kubelka–Munk function (KM) versus photon energy (hv) in order to calculate bandgap (E_g) values. The bandgap (E_g) values of studied photocatalytic materials were calculated from the onsets of the absorption edge using the formula presented in **Equation (2)** [158].

$$\lambda_g = \frac{1240}{E_g} \quad (2)$$

where λ_g is the bandgap wavelength.

Photoluminescence (PL) spectra were recorded at room temperature using a Varian Cary Eclipse fluorescence spectrophotometer (Agilent, Sta.Clara, CA, USA) with an excitation wavelength of 325 nm.

The Brunauer–Emmett–Teller (BET) single-point and multipoint surface area wasdetermined from N_2 adsorption/desorption isotherms using Gemini 2380 instrument (Micrometrics, Norcross, GA, USA). The nanocomposites were characterized in powdered

form in all above-stated characterization techniques.

Photoelectrochemical (PEC) measurements

Prepared nanocomposites were immobilized on 1 cm^2 area of fluorine-doped tin oxide (FTO, Sigma-Aldrich, St. Louis, MO, USA) glass (2.2 mm thick; resistivity of 7 Ω sq^{-1}; overall dimension: 2 cm × 1 cm) using the method described by Elbakkay et al. [159]. Prior to the coating, FTO glass slides were sonicated for 10 min sequentially in EtOH, acetone, and ultrapure water and then dried at room temperature. Thereafter, 2 mg of prepared nanocomposite was dispersed in 400 μL of 2-propanol and 10 μL of Nafion (Sigma- Aldrich, 5% (*w/w*)) under sonication for 30 min. Finally, 30 μL of catalyst suspension was immediately drop-casted on 1 cm^2 area of clean FTO glass and then dried in an oven at 80 °C for 30 min to form a working electrode.

Transient photocurrent responses and electrochemical impedance spectra (EIS) were obtained using a potentiostat/galvanostat PalmSens4 (PalmSensBV, Houten, Netherlands) equipped with a standard three-electrode system and an LED light source (spectrum shown in **Figure S2**, Appendix). Ag/AgCl electrode, Pt wire, as prepared nanocomposite-coated FTO glass (1 cm^2), and 0.1 M Na_2SO_4 solution were used as the reference electrode, counter electrode, working electrode, and electrolyte solution, respectively.

3.3 Photocatalytic Activity Evaluation

3.3.1 Layered Photocatalysts

Photocatalytic treatment experiments with 0.050 mM AMX water solution (**Table S1**, Appendix) were carried out in a water-jacketed (V = 0.09 L, T = 25.0 ± 0.2 °C) batch photo-reactor illuminated by a solar simulator (Oriel Arc source, Newport; 450 W Xe lamp, Osram), equipped with a collimator and air mass filter (AM 1.5G) [17]. The immobilized photocatalytic material was placed at the bottom of the reactor in contact with the AMX solution under constant mixing (90 rpm) by an orbital shaker DOS-20 (NeoLab, Germany). The solution was continuously mixed for 30 min in the dark in order to achieve adsorption-desorption equilibrium, denoted as (-30), and thereafter was exposed to the simulated solar illumination. The onset of illumination was denoted as (0). During the experiments, 700 μL aliquots of samples were collected at designated time intervals and filtered through a 0.45 μm Chromafil XTRA RC (Macherey-Nagel) syringe filter and were immediately quenched with 100 μL of methanol prior to HPLC analysis as described in subsection 3.4. Preliminary experiments were carried out at AMX solution natural pH (5.5) for an illumination period of 30 min. Further study on the effect of initial pH and PS concentration was based on a full factorial experimental (FFD) plan as described in **Table 14A** and **Table S2.1**, Appendix, where coded parameters X_1 and X_2 represent pH (ranging from 4 to 8) and concentration of PS (ranging from 0.05 to 0.5 mM), respectively. The chosen minimum and maximum concentrations of PS correspond to a AMX:PS molar ratios of 1:1 to 1:10 respectively. The obtained optimal conditions for degradation of AMX based on FFD experiments and response surface modeling (RSM) performed were utilized for the investigation of environmental parameters (i.e., mineralization, biodegradability, and toxicity), degradation by-products, scavenging studies, and the influence of water matrix parameters. Identification of reactive oxidizing species (ROS) was carried out using *t*-BuOH (5 mM), FA (5 mM), BQ (5 mM), and MeOH (5 mM) which were used as scavengers for HO•, h^+, O_2•−, and both HO• and sulfate radical ($SO_4^{\bullet-}$), respectively. Studies on the influence of water matrix parameters were carried out by spiking AMX solution with an exact concentration of the following: γ(Cl−) = 100 mg·L^{-1}, γ(CO_3^{2-}) =100 mg·L^{-1}, γ(NO_3^-) = 2 mg·L^{-1}, γ(PO_4^{3-}) = 2 mg·L^{-1}, and γ(HA) = 5 mg·L^{-1}. In order to test the stability of Fe_2O_3/TiO_2 layered composite films, the glass plates with immobilized catalysts showing the best performance were air-dried after the treatment and reused in four consecutive runs, employing the conditions found as optimal

within the investigated range. All experiments were conducted in triplicates and average values were reported; the reproducibility of experiments was ≥96.5%.

Table 14A. Experimental range and levels of process/variables

Process parameters	Model variables / coded values	level / range		
		-1	0	1
pH	X_1	4	6	8
$[S_2O_8^{2-}]$ (mM)	X_2	0.050	0.275	0.500

3.3.2 As-prepared Photocatalysts

Photocatalytic treatment experiments with 0.050 mM AMX water solution were carried out in a water-jacketed (V = 0.09 L, T = 25.0 ± 0.2 °C) batch photoreactor illuminated by a simulated solar irradiation produced by Oriel Arc source (Newport; 450 W Xe lamp, Osram, Irvine, CA, USA), which was equipped with a collimator and air mass filter (AM 1.5 G), as well as an additional UV cutoff filter (λ > 400 nm) to provide only visible-light illumination [17]. In preliminary experiments a slurry system was used; 0.045 g of photocatalyst powder was dispersed with AMX solution (natural pH = 5.5) under constant stirring (300 rpm). The solution was continuously mixed for 30 min in the dark in order to achieve adsorption/desorption, denoted as (−30), and thereafter exposed to visible-light illumination. The onset of illumination is denoted as (0). During the experiments, 700 μL aliquots of samples were collected at designated time intervals (15, 30, 45, 60, 75, and 90 min), filtered through a 0.45 μm Chromafil XTRA RC (Macherey-Nagel, Duren, Germany) syringe filter, and immediately quenched with 100 μL of MeOH prior to HPLC analysis, as described in Section 3.4. The photocatalyst powder which possessed the highest photocatalytic activity was selected for immobilization onto glass plates as described in Section 3.1.3. The glass plates with immobilized photocatalytic material were placed at the bottom of the reactor in contact with AMX solution under constant mixing (90 rpm) by an orbital shaker DOS-20 (NeoLab, Heidelberg, Germany) and were subjected to a similar treatment procedure as described above for the slurry system, except for the illumination time intervals (15, 30, 45, 60, 75, 90, 120, and 150 min). A full factorial design (FFD) was utilized to study the effect of initial pH and PS concentration on AMX degradation (**Tables 14B** and **Table S2.2**, Appendix). The coded parameters X_1 and X_2 represent pH (ranging from 4 to 8)

and concentration of PS (ranging from 0.500 mM to 3.0 mM), respectively. The chosen minimum and maximum concentrations of PS corresponded to AMX:PS molar ratios of 1:10 to 1:60, respectively. The obtained optimal conditions for the degradation of AMX based on FFD experiments and response surface modeling were utilized as the basis for H_2O_2 conditions, which were later used and compared for the investigation of toxicity, transformation byproducts, and scavenging studies. Identification of reactive oxidizing species (ROS) was carried out using *t*-BuOH (5 mM), FA (5 mM), BQ (0.5 mM), and MeOH (5 mM) as scavengers for HO•, h^+, O_2•−, and both HO• and sulfate radical ($SO_4^{\bullet-}$), respectively. The experiments were conducted in triplicate, and average values are reported; the reproducibility of experiments was ≥95.5%.

Table 14B. Experimental range and levels of process/variables

Process parameters	**Model variables / coded values**	**level / range**		
		-1	0	1
pH	X_1	4	6	8
$[S_2O_8^{2-}]$ (mM)	X_2	0.500	1.750	3.000

3.4 Analytical Methods

Measurements of pH were performed using a Handylab pH/LF portable pH-meter (Schott Instruments GmbH, Mainz, Germany). AMX concentration was monitored using an HPLC, Series 10, (Shimadzu, Kyoto, Japan) equipped with a UV-DAD detector (SPD M10AVP, Shimadzu) and a reversed-phase (RP) C18 column (250 mm × 4.6 mm, 5 μm, Macherey-Nagel Nucleosil, Duren, Germany). Isocratic elution was carried out with a mobile phase consisting of 90% aqueous 50 mM FA and 10% acetonitrile at an overall flow of 1 $mL \cdot min^{-1}$, whereas AMX was monitored at 272 nm. AMX degradation by-products (for by-products formed using layered composites-solar activated) were analyzed using ultrahigh-performance chromatography, tandem with triple quadrupole mass spectrometry on an LCMS-8045 (Shimadzu, Japan). The samples were diluted fivefold with HPLC-grade water prior to the injection. Chromatographic separation of AMX and its degradation intermediates were achieved on an RP C18 column (150 mm ×2.1 mm Shim-pack GIST column 3 μm, Shimadzu, Japan). Gradient elution of 15 mM formic acid (A phase) and 15 mM formic acid in acetonitrile (B phase) was utilized, under the following gradient program: 0–3 min 5% B, 3–13 min 95% B, then maintained 95% B for 3 min (13–16 min) and 8 min post-run time back to the initial mobile composition (95%A/5%B). Total organic carbon (TOC) was measured using a TOC-VCPN analyzer (Shimadzu, Japan). Meanwhile, AMX transformation products (TPs) formed using synthesized nanocomposite-visible light activated were analyzed using an ultrahigh-performance chromatograph (Thermo Scientific Vanquish system) in tandem with a high-resolution mass spectrometer (Orbitrap ExplorisTM 120, Thermo Scientific, Waltham, MA, USA), in positive and negative ionization mode. The samples were diluted fivefold with HPLC-grade water prior to the injection. Chromatographic separation of AMX and its transformation products was achieved on an RP C18 column (50 mm × 2.1 mm Hypersil GOLDTM, pore size 1.9 μm, Thermo Scientific, Vilnius, Lithuania). Gradient elution of water with 0.1% FA (A phase) and acetonitrile (B phase) was utilized, at a flow rate of 0.400 $mL \cdot min^{-1}$ under the following gradient program: 0–0.200 min, 2% B; 0.200–4.750 min, 98% B; 98% B maintained for 1.250 min (4.750–6.000 min); back to the initial mobile phase composition 3 min post run time (98% A/2% B). Ammonium acetate was used for negative mode instead of FA. The conditions for high-resolution mass spectrometry with an electrospray ionization source were the following: capillary, 3500 V; ion transfer tube temperature, 325 °C; vaporizer temperature, 350 °C; sheath gas pressure (Arb), 50; auxiliary gas pressure (Arb), 10; scan

modes, full MS (resolution 60,000) and ddMS2 (resolution 15,000); scan range, *m/z* 100–1000. Raw MS data files of the control, blank matrix, and AMX samples were imported into Compound Discoverer^{TM} (v.3.3 SP1 Thermo Scientific, Waltham, MA, USA) software for transformation product identification. Fragment ion search (FISh) coverage function in Compound Discoverer^{TM} was utilized for structure elucidation and chemical transformations involved for each chromatographic peak. Expected compounds were measured within ±2 ppm of mass error; with maximum area $\geq 10^5$ and FISh coverage score ≥43.50. Total organic carbon (TOC) was measured using a TOC-VCPN analyzer (Shimadzu, Japan). A Lambda EZ 201 UV/VIS spectrophotometer (Perkin Elmer, USA) was used for spectrophotometric monitoring of PS [160], ferrous (Fe^{2+}), and ferric (Fe^{3+}) ions concentrations [161]. Chemical oxygen demand (COD) and biochemical oxygen demand (BOD_5) in the samples were determined by colorimetric methods using a HACH DR2800 spectrophotometer (Hach-Lange, USA) and commercially available reagent kits, that is, LCK1414 and LCK554 (Hach-Lange) respectively. Biodegradability was expressed as BOD_5/COD ratio. Aquatic toxicity of treated samples was evaluated with commercial bioassays, based on *Daphnia magna* (DM) immobilization according to ISO 6341:2012 standard (Daphtoxkit F magna, Microbiotests, Belgium) and based on inhibition of the luminescence emitted by *Vibrio fischeri* (VF) according to ISO 11348-3:2007 measured on a BiofixLumi-10 luminometer (Macherey-Nagel, Germany). The results were expressed as effective concentrations causing a 50% reduction in bioluminescence (EC_{50}) and converted into toxicity units (TU = $100/EC_{50}$).

3.5 Calculations

Response surface methodology (RSM) was utilized to determine the effectiveness of solar light and visible-light-driven photocatalytic treatment of AMX dependent on initial pH and PS concentration. The values of process parameters are represented by independent variables: X_1 and X_2 (**Table 14A** and **14B**). Experimental space was described using a 3^2 full factorial design (FFD) for the solar-TiO_2@Fe_2O_3/PS and vis-(5% (*w/w*) Fe_2O_3/TiO_2)/PS system. The AMX conversion rate constants were chosen as process responses. The combined influence of studied parameters on process performance was described by a quadratic polynomial equation representing the RSM model, which was evaluated using a standard statistical test, i.e., analysis of variance (ANOVA), considering the following statistical parameters: Fisher *F*-test value (*F*), its probability value (*p*), regression coefficients (pure: R^2 ; adjusted: R_{adj}^2), and *t*-test value. Moreover, graphical-based analysis was conducted on the so-called "residual diagnostic" (RD) using a normal probability test, Levene's test, and a constant variance test. The calculations were performed using the Statistica 13.5 (Tibco, Palo Alto, CA, USA) and Design-Expert 10.0 (StatEase, Minneapolis, MN, USA) software packages. The calculation of PS anion highest occupied molecular orbital (HOMO) and lowest occupied molecular orbital (LUMO) molecular orbital energy levels, with included effects of water as the solvent by the self-consistent reaction field (SCRF) method, was done using the DFT method implemented in Gaussian 16 rev.C01 [162].

Ab initio density functional theory (DFT) method implemented in Gaussian 16 rev. C01 electronic structure software was used to optimize the structure of PS anion and to calculate the energies of the HOMO and LUMO molecular orbitals of PS [162]. The calculations were performed using the hybrid density functional B3LYP [163,164] with the augmented triple-ζ basis set (aug-CC-pVTZ) developed by Dunning and coworkers [165]. The polarizable continuum model (PCM) within the self-consistent reaction field (SCRF) method implemented in Gaussian 16 was used in order to simulate the effects of water on PS.

4. RESULTS AND DISCUSSION

4.1 Layered Photocatalysts

4.1.1 Characterization

SEM images showing the thickness of the layers within the sandwich composites (**Figure 28**), deposited layers are rather thin (1.06 ± 0.20 μm), allowing the transmission of emitted light through the upper layer **Figure 28**. UV-DRS of pure components and layered composites are shown in **Figure 29A** whereas KM transformed spectra for the calculation of bandgap values are shown in **Figure 29B**. As shown in **Table 15**, calculated bandgap values of commercial TiO_2 and Fe_2O_3 powders were in agreement with the literature [166,167]. For composites TiO_2@α-Fe_2O_3 and α-Fe_2O_3@TiO_2 the top layer contributes mostly to the total bandgap value of the composite. Moreover, the reflectance-identity of each layer can be noted in the layered, sandwich composites, that is, the distinct steep linear regions corresponding to individual semiconductor components can be identified. The semi-transparence of the top layer in both cases enables simultaneous photo-activation of top and bottom layers. The physically mixed 50% (*w/w*) of TiO_2/α-Fe_2O_3 exhibited almost the same reflectance identity and bandgap value as that of pure α-Fe_2O_3 (**Table 15**), indicating the formation of an in situ heterojunction between TiO_2 and α-Fe_2O_3, promoted by the binding action of the immobilization.

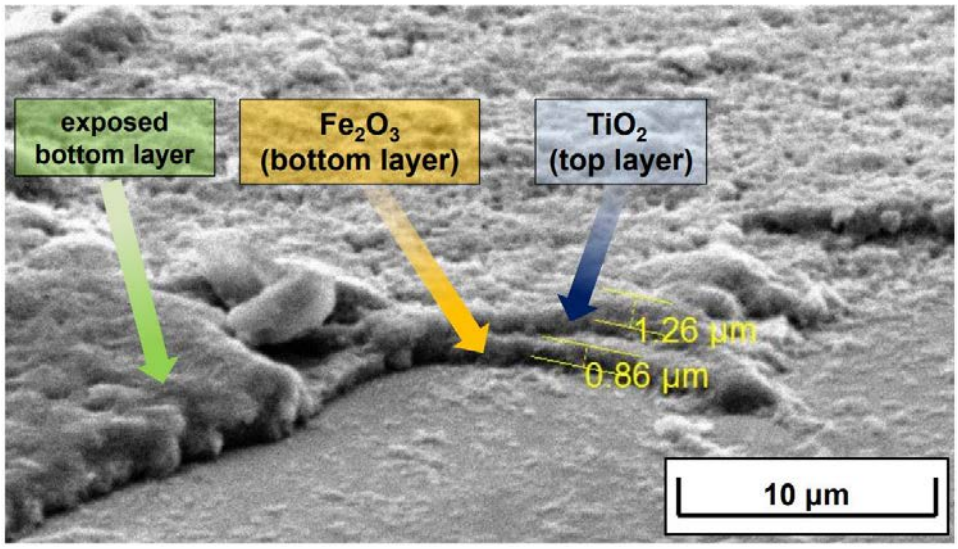

Figure 28. SEM image of TiO_2@Fe_2O_3

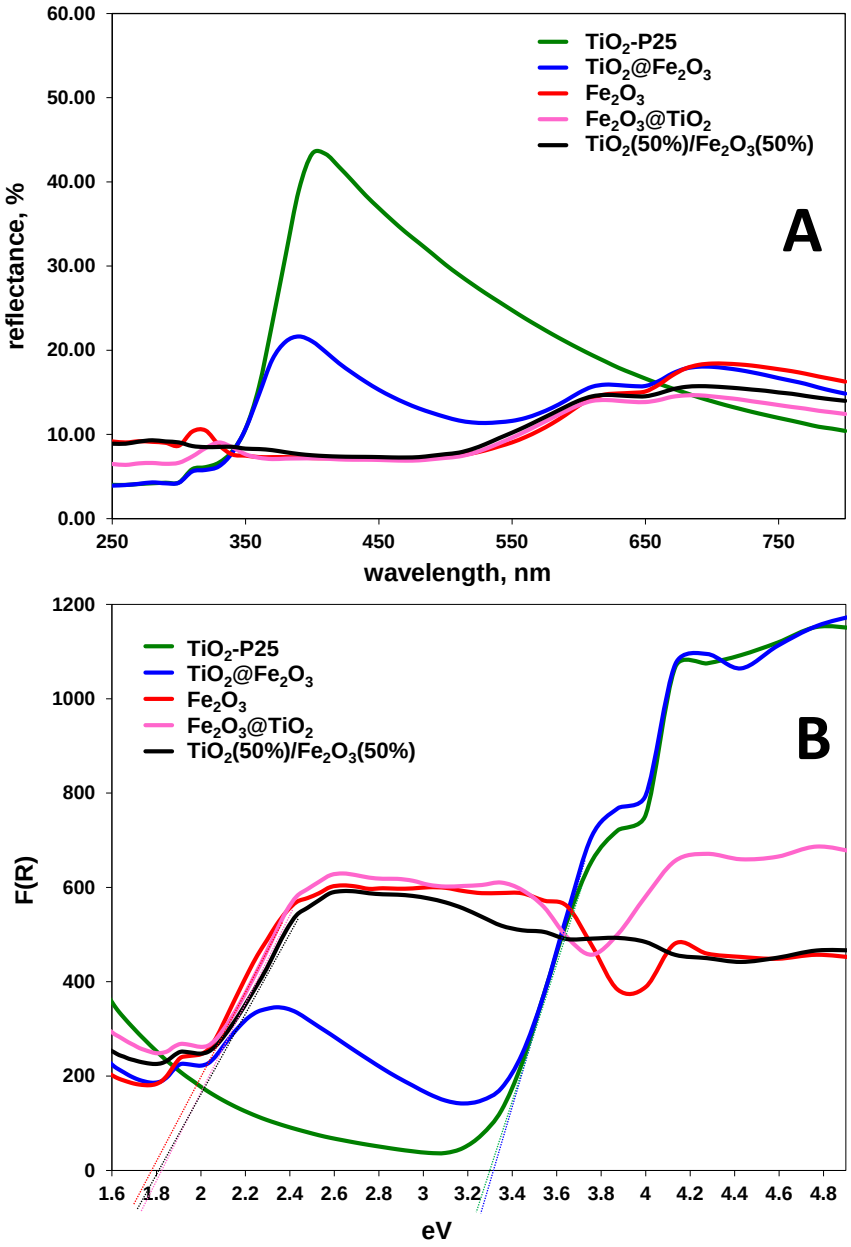

Figure 29. (A) Diffuse reflectance spectra of coated plates; and (**B**) corresponding plots of transformed Kubelka-Munk function versus the energy of light (eV)

Table 15. Photocatalyst bandgap values estimated using Kubelka-Munk function.

Photocatalyst	TiO_2 (P25)	TiO_2@α-Fe_2O_3	α-Fe_2O_3	α-Fe_2O_3@TiO_2	TiO_2(50%)/α-Fe_2O_3 (50%)
Band Gap (eV)	3.27	3.30	1.75	1.80	1.78

4.1.2 Photocatalytic Degradation Experiments

Preliminary investigations of the stability of AMX towards hydrolysis, photolysis, and direct PS oxidation have shown no effect on AMX concentration (**Figure 30**). The initial evaluation of photocatalytic effectiveness of the pure components and sandwich-type composites towards AMX degradation was carried out at the natural pH of AMX solution (pH 5.5), for an illumination period of 30 min after the initial dark period of 30 min, allowing the achievement of the adsorption/desorption equilibrium at the photocatalyst surface. In all cases the initial adsorption extents achieved during the dark period were miniscule (<3%), hence all observed removal extents of AMX were approximated as the equivalent to the direct degradation extents. The obtained results were normalized to the degradation extent achieved by TiO_2-P25, considered herein as the benchmark photocatalysts (**Figure 30**).

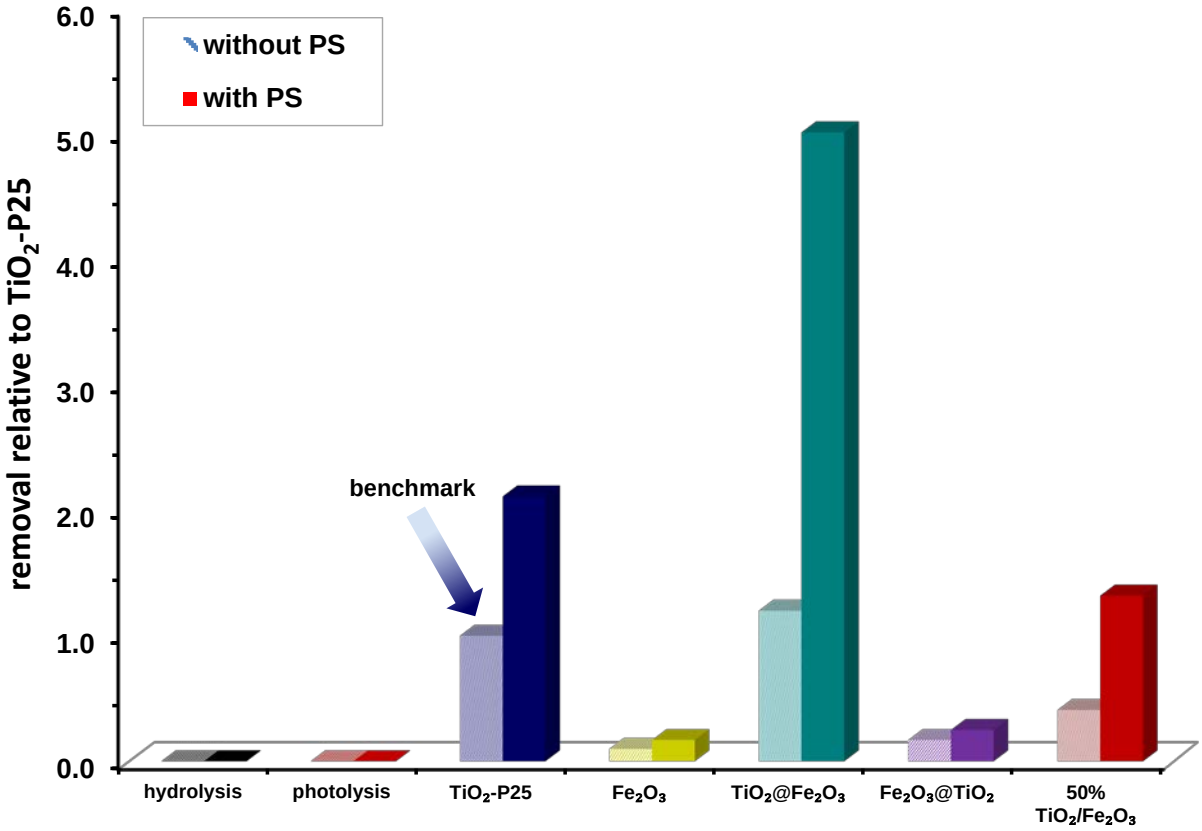

Figure 30. Photocatalytic degradation of AMX (0.050 mM) using different configurations of TiO_2–Fe_2O_3 layered composite under solar irradiation with and without PS compared relatively to benchmark TiO_2-P25 (experimental conditions: initial pH=natural pH, 5.5; treatment time under solar irradiation, t=30 min)

The highest degradation extent without the addition of PS was achieved by TiO_2@α-Fe_2O_3, that is, 1.39-fold relative to that of TiO_2-P25 (i.e., 8% AMX total degradation for TiO_2-P25 and 11.12% AMX total degradation for TiO_2@Fe_2O_3). Such marked improvement of photocatalytic activity indicates beneficial inhibition of photogenerated e^-/h^+ recombination within TiO_2 by allowing inter-sandwich layer e^- migration towards Fe_2O_3. Such a hypothesis is further supported by the ineffectiveness of sole α-Fe_2O_3 towards AMX degradation without the presence of PS. Fe_2O_3 is innately unable to react directly with H_2O/OH^-, due to inadequate band edge positions of the valence and conduction bands [5], thereby preventing the formation of HO• or other less reactive ROS, such as superoxide radical (O_2•−). According to the low adsorption extents achieved during the initial dark period, the observed degradation extents can be primarily ascribed to the reaction of ROS with AMX within the photocatalyst/solution boundary layer. Therefore, a potentially misleading synergistic effect due to the total achieved AMX degradation caused by the sum of individual contributions of TiO_2 and α- Fe_2O_3 is effectively ruled out, strongly supporting the notion of effective charge separation by TiO_2@α-Fe_2O_3 composite, yielding the improvement comparing to the benchmark TiO_2-P25 (**Figure 30**).

On the other hand, α-Fe_2O_3@TiO_2 sandwich composite has demonstrated inferior effectiveness in comparison to the benchmark TiO_2-P25, however, it is seemingly an improvement over sole α-Fe_2O_3. However, the observed AMX degradation can be contributed to that achieved by TiO_2, which can potentially form HO• radicals, through AMX solution interface contact achieved by surface imperfections in the top α-Fe_2O_3 layer, as can be observed on SEM micrographs (**Figure 28**). Physically admixed 50% (*w/w*) TiO_2/Fe_2O_3 has achieved an improvement considering the effectiveness of Fe_2O_3@TiO_2. However, the AMX degradation after 30 min treatment was only 41%-relative (i.e., AMX total degradation is 3.28%) of that achieved by TiO_2-P25. Despite showing promising optical properties, in the context of filling electron states within the bandgap of TiO_2, α-Fe_2O_3 hinders total effectiveness as it does not contribute to the formation of radicals directly, thereby effectively diluting the surface concentration of ROS formation sites. A similar effect was reported by Monfort et al., [168] showing that TiO_2 (top)–$BiVO_4$ (bottom) photocatalyst layers exhibited superior activity for solar photodegradation of Rhodamine B compared to the pure TiO_2, $BiVO_4$, and $BiVO_4$ (top)–TiO_2 (bottom) layers. They concluded that such enhanced effect observed can be assigned to the formation of both O_2•−and HO• as main oxidative species over TiO_2 (top) surface when irradiated with sunlight compared to $BiVO_4$ (top) which is limited to holes (h^+) only, having ability to form only HO•. The addition of PS has proven to

be highly beneficial for TiO_2@α-Fe_2O_3 composite, as a fivefold increase in AMX degradation (i.e., ~40%, AMX total degradation for solar-TiO_2@Fe_2O_3/PS system vs 8% AMX total degradation for solar-TiO_2/no PS system (benchmark)) was noted. The LUMO of PS is able to accept the photogenerated e^- from TiO_2, which then leads to the generation of SO_4•− and may lead to the formation of additional HO• [161]. However, such a charge transfer from α-Fe_2O_3 to PS is either thermodynamically or kinetically unfavorable, as can be observed by negligible improvement in photocatalytic activity of α-Fe_2O_3 with the addition of PS (**Figure 30**). The molecular orbital configuration of PS anion obtained by DFT calculation, along with included solvation (SCRF) effects, indicates that the LUMO energy level of PS anion in the ground state is equal to −0.49 eV (**Table 16**). Since the calculated LUMO of PS is significantly more negative than that of α-Fe_2O_3 [5], such a result supports the notion that photogenerated electron transfer from pristine α-Fe_2O_3 to PS is thermodynamically unfavorable. Therefore, as photocatalytic activation of PS by immobilized α-Fe_2O_3 and direct degradation of AMX are not observed, it can be concluded that α-Fe_2O_3 serves solely as a sink for h^+ and e^- photogenerated within TiO_2 thereby enhancing its activity.

Table 16. HOMO and LUMO orbital level of the PS anion calculated using B3LYP/aug-CC-pVTZ level theory and SCRF method

Molecular orbital	E, eV	$\Delta E_{HOMO\text{-}LUMO}$, eV
HOMO	-0.494	0,24
LUMO	-0.734	

Ismail et al. [169] suggested that there is a competition between the present pollutant, PS, and dissolved O_2 towards the reaction with photogenerated e^- in the CB of TiO_2. Similarly, Wang et al. [170] observed that the addition of PS in the UV/TiO_2 system showed a non-synergistic effect for 2-chlorobiphenyl degradation. Hence, in order to elucidate the effects of operating conditions, that is, pH and PS concentration, an experimental design and RSM approach was utilized to elucidate the performance of TiO_2@α-Fe_2O_3 in combination with PS for AMX degradation kinetics. As can be seen from the kinetic profiles of AMX degradation obtained by solar-TiO_2@Fe_2O_3/PS system (experiment performed at conditions set by 3^2 FFD, **Table 14A** and **Table S2.1**, Appendix), the degradation during the period under solar irradiation obey zero-order kinetics and can be

displayed with **Equation (3)**, representing the functional dependence of AMX degradation versus treatment time, implying a surface reaction mechanism for the activation of PS [171–173], where c = variable concentration, c_0 = initial concentration, k_{obs} = rate constant and t = time.

$$c - c_0 = -k_{obs} \times t \quad (3)$$

By applying RSM modeling, misleading information obtained from conventional "one-parameter-at-the-time" approach would be avoided [1] FFD matrix is summarized in **Table S2.1**, Appendix, along with the obtained AMX degradation rate constants after 50 min of exposure to simulated solar irradiation (k_{obs}), which were used as system responses. It should be noted that photocatalytic experiments were run including 30 min dark period to establish adsorption equilibrium (**Figure S3**). However, the adsorbed amount of AMX during the dark period was negligible in all cases (<0.9%). Such results can be assigned to point zero surface charge of TiO_2-P25 (pH_{pzc} =6.5–6.7) [174–176] and pK_a values of AMX (pK_{a1} = 2.4; pK_{a2} = 7.4; pK_{a3} = 9.6) [177]. Hence, in our applied pH range (from 4 to 8) AMX exists in two speciation forms. For pH 4 and 6, AMX is present mostly in neutral form pK_{a1} (2.4) < pH < pK_{a2} (7.4) [177], while TiO_2 net surface charge is positive, thus leading to less attraction between two moieties. Furthermore, at pH 8, the net charge of TiO_2 and AMX are both negative implying repulsion between two moieties and leads to poor adsorption. Such a low adsorption in all cases allowed us to use zero-order k_{obs} as treatment responses. Hence, the multiple regression analysis was applied on FFD matrix and k_{obs} (AMX) values calculated for the treatment period under simulated solar irradiation (**Table S2.1**, Appendix), yielding a polynomial equation, that is, and RSM model **Equation (4)**:

$$Y=5.13-2.06\times X_1+0.10\times X_1^2+0.88\times X_2-1.61\times X_2^2+0.037\times X_1\times X_2 \quad (4)$$

The obtained model is characterized by ANOVA (**Table S3**, Appendix) and RD tools (**Figure S4**, Appendix). Basically, a model was found to be significant (p = 0.0089), and accurate (R^2 = 0.981 and R_{adj}^2 = 0.949), while RD revealed that (i) there are no violations in the assumptions that errors are normally distributed and independent of each other, (ii) the error variances are homogeneous, and (iii) residuals are independent. Accordingly, such a model can be used hereinafter as a tool to enlighten the influence of studied parameters (initial pH and PS concentration) on AMX degradation.

The ANOVA analysis also revealed that model terms corresponding to both studied process parameters are significant,that is, possess $p < 0.05$ (**Table S3**, Appendix); thus, the

changes in both initial pH and PS concentration significantly contributes to the effectiveness of solar-TiO_2@Fe_2O_3/PS system to AMX degradation. Such behavior can be clearly seen from the 3D surface and contour representation of the influence of initial pH and PS concentration on AMX degradation rate (k_{obs}), provided in **Figure 31**. Acidic pH values are favorable for AMX degradation, thus it can be ascribed to the high concentration of $SO_4^{\bullet-}$ (*E*o = 2.5–3.1 V vs NHE) [178] which has higher oxidation potential than HO• (*E*o = 1.89–2.72 V vs NHE) [178]. AMX degradation rate strongly decreases with the increase of initial pH, regardless of the PS concentration in the system.

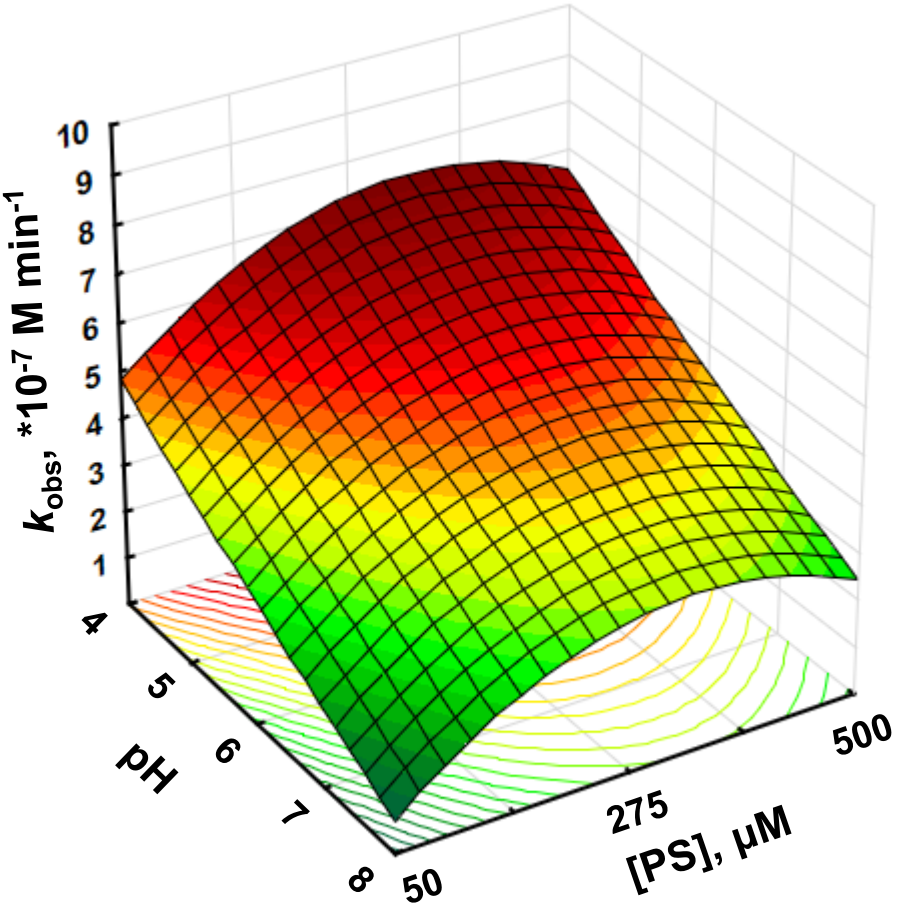

Figure 31. 3D surface and contour plots presenting mutual interactions of initial pH and [PS] on AMX degradation by solar-TiO_2@Fe_2O_3/PS

Such behavior can be also assigned to the predominant species existing in the system, which is also a pH depending effect. For instance, at acidic pH (pH 4 and 6) sulfate radicals are dominant as described by **Equations (5) and (6)** [179,180]. On the other hand, at basic pH, $SO_4^{\bullet-}$ is converted to HO• as described by **Equation (7)** [181]**.**

$$S_2O_8{}^{2-} + H^+ \rightarrow HS_2O_8{}^- \quad (5)$$

$$HS_2O_8^- \rightarrow SO_4^{\bullet-} + HSO_4^{\bullet} \quad (6)$$

$$SO_4^{\bullet-} + OH^- \rightarrow HO\bullet + SO_4^{2-} \quad (7)$$

On the other hand, PS concentration effect is two fold; by an increase of PS concentration, process effectiveness (i.e., AMX degradation) increases up to the certain point where further increase has a negative influence. The increase of PS concentration can be beneficial for the decrease of recombination rate and generation of sulfate radicals in the system. However, at too high concentration of PS, its scavenging nature toward present radical species comes forth **(Equations (8) and (9))** [161]:

$$S_2O_8^{2-} + SO_4^{\bullet-} \rightarrow S_2O_8^{\bullet-} + SO_4^{2-} \quad (8)$$

$$S_2O_8^{2-} + HO\bullet \rightarrow HSO_4^- + SO_4^{\bullet-} + 0.5O_2 \quad (9)$$

Besides, too high concentration of radical species may promote their termination, as presented by **Equations (10)** and **(11)** [161]:

$$SO_4^{\bullet-} + SO_4^{\bullet-} \rightarrow S_2O_8^{2-} \quad (10)$$

$$SO_4^{\bullet-} + HO\bullet \rightarrow HSO_4^- + 0.5O_2 \quad (11)$$

Accordingly, as can be seen in **Figure 31**, the most beneficial conditions for AMX degradation are pH 4 and PS concentration of approx. 0.330 mM, which was accurately calculated to be 0.334 mM by maximizing the polynomial **Equation (4)**, thus predicting AMX degradation at the zero-order rate of 7.4×10^{-7} M·min^{-1}. Such conditions were further utilized during the investigation of AMX degradation mechanism, pathway, and related changes in biodegradability and toxicity, as well as the influence of common water matrix constituents.

4.1.3 Degradation Mechanism

In order to study the degradation mechanism of AMX by solar-TiO_2@Fe_2O_3/PS system, the experiments were performed at previously established optimal conditions within the investigated range of studied process parameters and in the presence of common ROS scavengers. Hence, the quantification of the levels of oxidation by ROS was performed using the following scavengers: MeOH and *t*-BuOH to differentiate the contributions of $SO_4^{\bullet-}$ and HO•. Namely, MeOH reacts with both $SO_4^{\bullet-}$ and HO• ($k = 1.1 \times 10^7$ M^{-1} s^{-1} and $k = 9.7 \times 10^8$ M^{-1} s^{-1}, respectively). Meanwhile, *t*-BuOH reacts with HO• at a much higher rate, even three orders of magnitude ($k = (3.8–7.6) \times 10^8$ M^{-1} s^{-1}) compared to that for $SO_4^{\bullet-}$ ($k = (4.0–9.1) \times 10^5$ M^{-1} s^{-1}), thus exhibiting effective scavenging effect for HO• [182]. BQ reacts with $O_2^{\bullet-}$ (*k*

= (0.9–1.0) × 10^9 M^{-1} s^{-1}) and with HO• (k = 6.6 × 10^9 M^{-1} s^{-1}) [183], while FA was used for photogenerated h^+ scavenging. **Figure 32** shows AMX degradation and kinetic profiles achieved by solar-TiO_2@Fe_2O_3/PS in the presence and absence of ROS scavengers. It can be observed that the highest inhibition of AMX degradation occurred in the presence of FA. AMX degradation was reduced from 70% (no scavengers) to only 12% (with FA). This indicates that photogenerated h^+ plays the main role in AMX degradation, despite the fact that AMX adsorption is minor, thus direct AMX oxidation by h^+ can be neglected. Accordingly, such results can be assigned to the suppression of recombination of charges by the presence of PS as well as the generation of ROS at h^+, both contributing to the overall AMX degradation. Meanwhile, it was observed that AMX degradation was reduced from 70% (no scavengers) to 39 and 54% in presence of MeOH and *t*-BuOH, respectively. Such results indicate that $SO_4^{\bullet-}$ plays a more significant role than HO• in the overall AMX degradation. The presence of BQ reduced AMX degradation to 64% from 70%, suggesting that $O_2^{\bullet-}$ had a minor role in overall AMX degradation. Thus, the arrangement of ROS in decreasing order of its role for AMX degradation by solar-TiO_2@Fe_2O_3/PS process is the following: h^+> $SO_4^{\bullet-}$ > HO• > $O_2^{\bullet-}$. Similar ordering was observed by Sabri et al. [184] for another TiO_2-iron-PS system (vis-TiO_2/FeOCl/$S_2O_8^{2-}$).

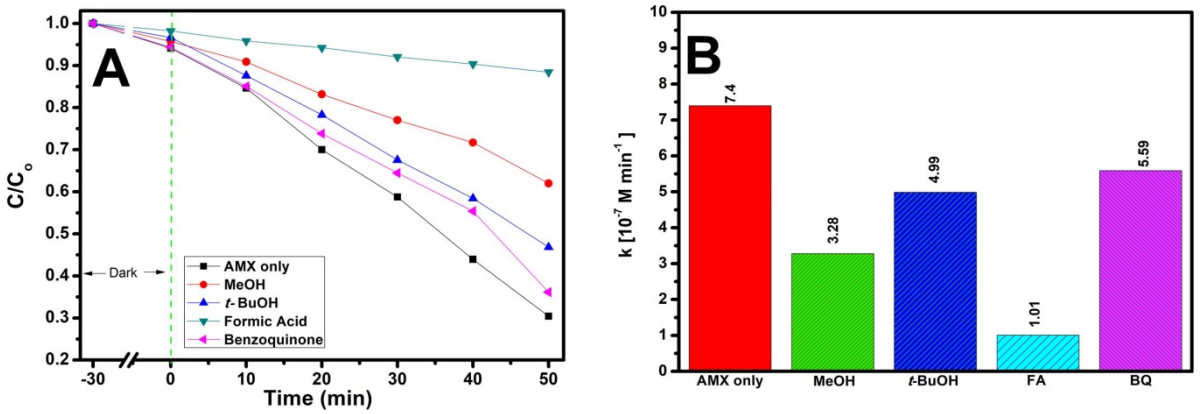

Figure 32. (**A**) Photocatalytic degradation of AMX under solar irradiation in the presence of scavengers; and (**B**) corresponding zero-order rate constants (k_{obs}). (experimental conditions: [AMX] = 0.050 mM; initial pH=4; [PS]=0.334 mM; [MeOH]=5 mM; [*t*-BuOH]=5 mM; [FA]=5 mM; [BQ]=5 mM; treatment time, *t*=50 min)

4.1.4 AMX Degradation Pathway and Environmental Aspects

In order to study the degradation pathway and the influence of formed by-products on the environmental aspects, that is, changes in biodegradability and toxicity, the experiments were performed for a longer period (480 min) at conditions established as optimal within the range of studied process parameters (initial pH 4 and [PS] = 0.334 mM). As can be seen from **Figure 33**, after 75 min >90% of AMX was degraded, while total AMX degradation was achieved within 180 min of treatment. The mineralization of organic content occurred at a much lower rate; after 75 min treatment, only 5% was mineralized, while at the treatment point where AMX was completely degraded, ≈25% of overall organic content was mineralized. It should be noted that total mineralization extent achieved after 480 min amounts to 52.2% (**Figure 33A**). Accordingly, the most part of the overall organic content during AMX treatment pertained to formed intermediates (e.g., after 30 min of treatment, where >50% of AMX was degraded, overall organic content is almost unchanged). Degradation of AMX is accompanied by the changes in pH (**Figure 33A**), which can be associated with the transformation of aromatics into aliphatic acids [185,186]. However, the decrease in pH from an initial value of 4 was only moderate due to the low strength of formed organic acids.

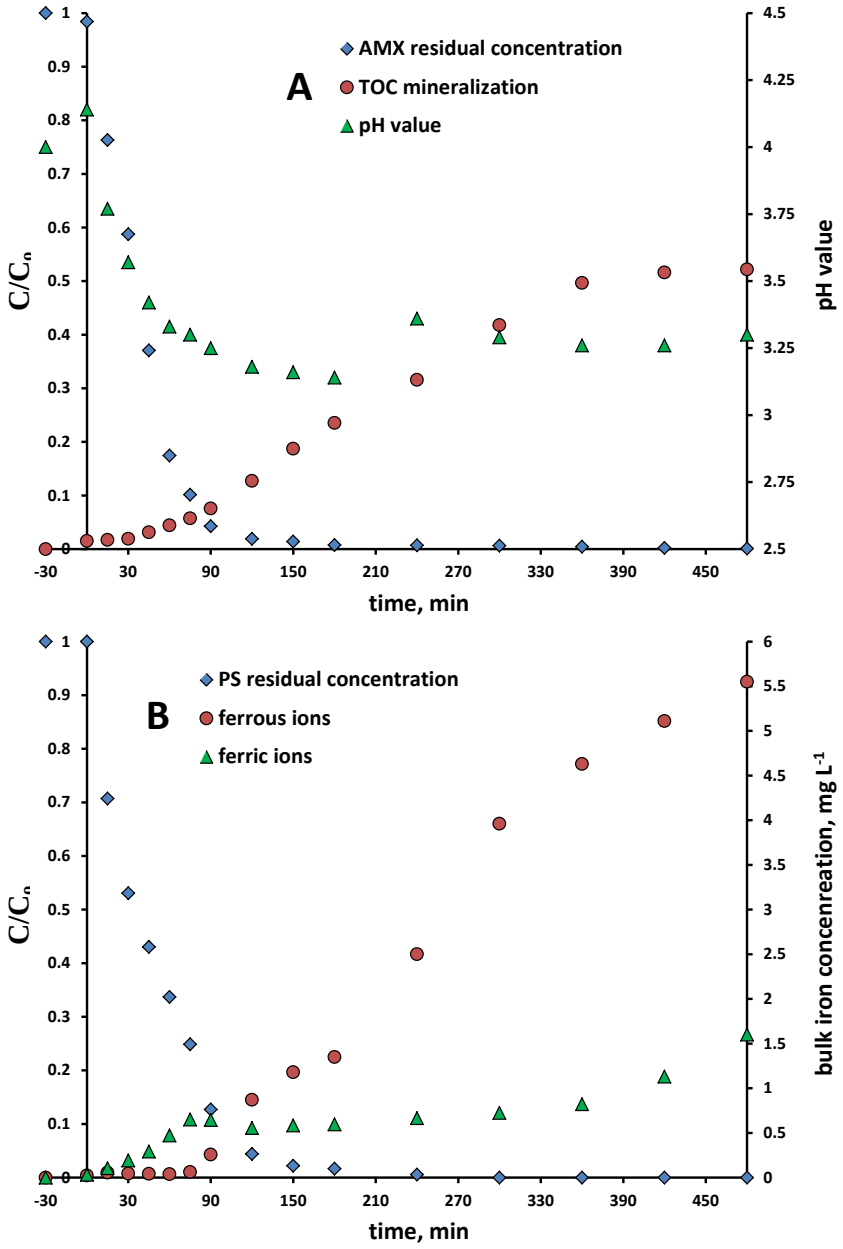

Figure 33. (**A**) AMX degradation and total organic content mineralization kinetics, and changes of pH; and (**B**) concentration of PS and iron species (ferrous/ferric ions), during AMX treatment by solar-TiO_2@Fe_2O_3/PS (experimental conditions: initial pH=4 and [PS]=0.334 mM)

Nevertheless, recorded pH changes (**Figure 33A**) display a typical pattern for degradation of organics, whereas initial decrease of pH values, associated with the formation of aliphatic acids, is followed by the slight increase as the transformation of the intermediates progresses towards final mineralization products [187]. AMX degradation and PS consumption followed similar treatment time profiles, as can be seen from **Figure 33A** and **B**. It is worth noting that PS was completely consumed up to 240 min of treatment while the

mineralization continued to proceed with a similar rate. The consumption of PS may be associated with the increased concentration of iron species in the system, due to the fact that its presence most likely suppressed the recombination of photogenerated charges as well as hematite photocorrosion. The increased concentration of iron species may lead to the generation of HO• in the bulk through **Equation (12)** [161]:

$$Fe^{III}(OH)^{2+} \overset{hv}{\rightarrow} Fe^{2+} + HO\bullet \quad (12)$$

which additional quantity empowers the oxidative ability of the solar-TiO_2@Fe_2O_3/PS system over HO• mechanism. The fact that iron leaches from hematite in a form of ferric ions, and recorded profiles of ferric and ferrous ions, presented in **Figure 33B**, support such an assumption.

The degradation pathway of AMX by solar-TiO_2@Fe_2O_3/PS was proposed in **Figure 34**; it indicates three possible degradation pathways via hydroxylation of aromatic structures and/or heteroatom(s) (N or S) involving moieties within the AMX molecule. Three intermediates were detected by LC-MS/MS with molecular ion peak of (*m/z* = 382) and base peak (*m/z* = 365). All of the detected intermediates are ascribed to monohydroxylation of AMX [188,189]. Accordingly, DP1 was formed via attack of $SO_4^{\bullet-}$ and/or HO• to the sulfur atom of thioether moiety by electron transfer mechanism and was confirmed by molecular orbital calculations [188]. Thereafter, DP1 can proceed with further hydroxylation in the aromatic ring moiety yielding intermediate with *m/z* = 398 [188]. Meanwhile, DP2 was formed via attack of HO• to the aromatic ring of AMX. Subsequently, DP2 would undergo further hydroxylation and deamination to yield intermediate with *m/z* = 383, and further degradation leads to smaller by-products such as *m/z* = 176. DP3 was formed by hydroxylation of secondary amine moiety of AMX, and was further hydroxylated to form *m/z* = 412 then subsequently degraded to form *m/z* = 176. However, ion chromatography results revealed that there are no free N-containing ions (i.e., NO_3^-, NO_2^-, NH_4^+) during the entire treatment time of 480 min, suggesting that degradation products contain N-functionality. Accordingly, it seems that DP2 underwent hydroxylation step, but not an elimination of amino moiety. As compared to the literature, solar photo-Fenton and UV/PS treatment of AMX degradation proceeds via hydroxylation, hydrolysis, and decarboxylation. However, it must be noted that three monohydroxylated by-products were not detected simultaneously by the previous studies. For instance, Trovo et al. [189] only detected DP2 and DP3, while Zhang et al. [188] only detected DP1 and DP2.

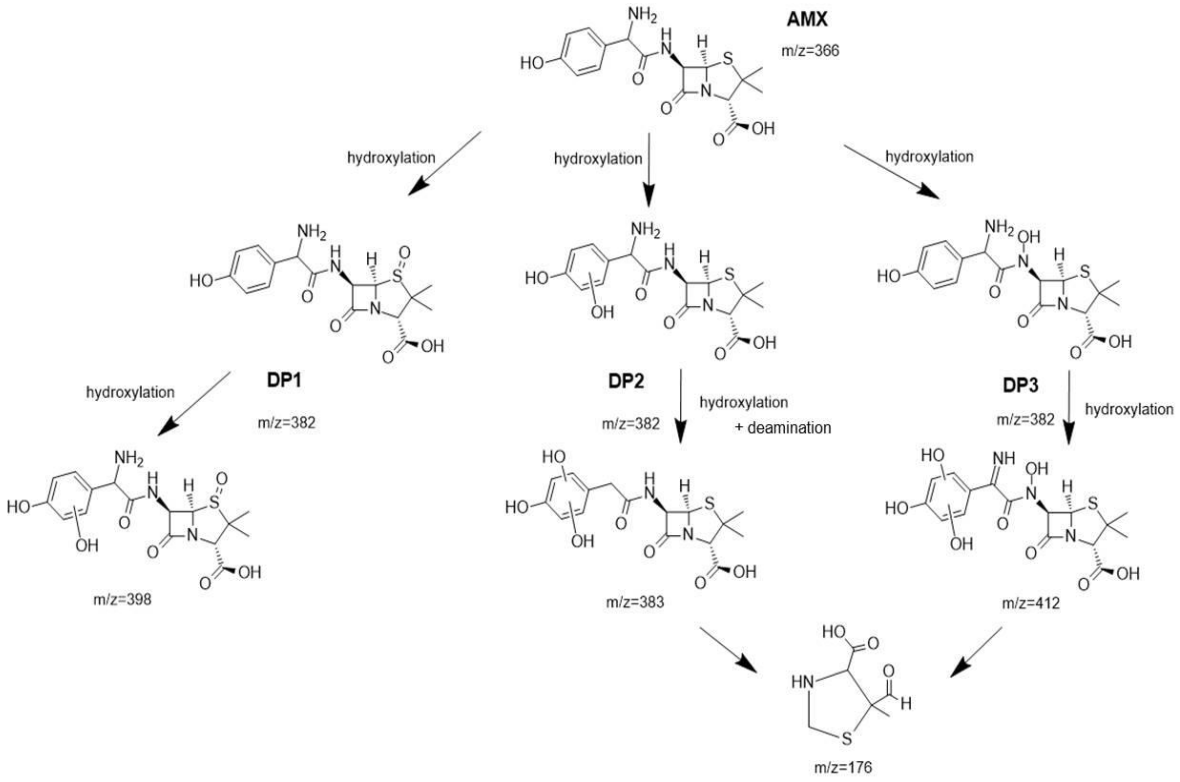

Figure 34. Proposed degradation pathway of AMX by solar-TiO_2@Fe_2O_3/PS system based on identified AMX intermediates and literature data (experimental conditions: initial pH=4; [PS] = 0.334 mM; (*m/z*) were expressed as $[M+H]^+$ and results are obtained from LC-MS/MS)

The evolution and degradation profiles of DP1, DP2, and DP3 are presented in **Figure 35A** and were correlated with the changes in biodegradability (**Figure 35B**) and toxicity (**Figure 35C**). As it can be seen, all three identified AMX by-products followed a similar evolution/degradation pattern. Hence, their concentrations increased continuously up to 45th (for DP2 and DP3) and 60th (DP1) minute or treatment, while after those periods, their degradation rates prevailed over evolution rates, thus their concentration started to decrease during further treatment period, and eventually completely disappeared from the system after 480 min treatment (**Figure 35A**). Despite that, TOC value amounted after 480 min treatment to 47.8% of the initial value (**Figure 33A**, indicating that other unidentified AMX organic by-products were still present to a large extent. As can be seen from the proposed pathway, identified DP1, DP2 and DP3 are consequences of hydroxylation of AMX molecule (either at benzene moiety or present heteroatoms, **Figure 34**), while their further degradation undergoes a similar pattern, that is, via hydroxylation at benzene moiety. Accordingly, after

the cleavage of C_{10}-C_{11} bond (**Table S1**), such (poly)-hydroxylated benzene ring would then undergo degradation as phenolic-like compounds over ring-open products and would be eventually mineralized [190]. This is supported by the fact that no free N-containing ions were detected with the progress of mineralization.

As it can be seen from **Figure 35B**, the initial AMX solution can be characterized as non-biodegradable; $BOD_5/COD = 0.017$. As it is known from the literature [191], wastewater with $BOD_5/COD < 0.3$ are characterized as non-biodegradable, while those with $0.3 < BOD_5/COD < 0.4$ are partially biodegradable; and those with $BOD_5/COD > 0.4$ can be characterized as biodegradable. Treatment of AMX solution by solar-TiO_2@Fe_2O_3/PS resulted in an increase in BOD_5/COD ratio. Comparing BOD_5/COD and mineralization profiles presented in **Figure 35B** and **Figure 35A** respectively, one may conclude that improved biodegradability is a consequence of mineralization, that is, decreases in organic content. However, that is not quite correct. Although TOC, COD, and BOD_5 are used as the main sum parameters to quantify the organic load, they possess different biases. Namely, TOC and COD encompass the entire organic content regardless of their structural characteristics as they measure the amount of carbon bound to organic compound and the amount of organic compound which is chemically oxidized to CO_2. On the other hand, susceptibility of organics to biochemical transformation encompassed in BOD is influenced by its chemical structures. Hence, COD and TOC can only decrease during applied photocatalytic treatment, while BOD_5 values can either decrease or increase depending on the nature (i.e., structure) of the degradation byproducts formed. The decrease can be associated with either the formation of less biodegradable compounds or the decrease in overall organic content, while the increase in BOD_5 value can be only due to the formation of compounds, degradation intermediates, which are more biodegradable than the parent compound [191]. Although these profiles are similar, biodegradability increase is not the only consequence of decreased organic content. Namely, the partially biodegradable values were reached at treatment period (180 min) aligned with the complete AMX degradation and disappearance of the majority of DP1, DP2, and DP3 from the system (they were present at <10% of their maximum detected concentration detected). Considering the proposed pathway and assumption that the majority of mineralization underwent over (poly)-hydroxylated benzene moiety, which are known to be non-biodegradable [190], the improvement of biodegradability can be associated with the degradation of such hydroxylated structures. More clear correlation between formed DP1, DP2, and DP3 can be observed from toxicity changes, presented in **Figure 35C**.

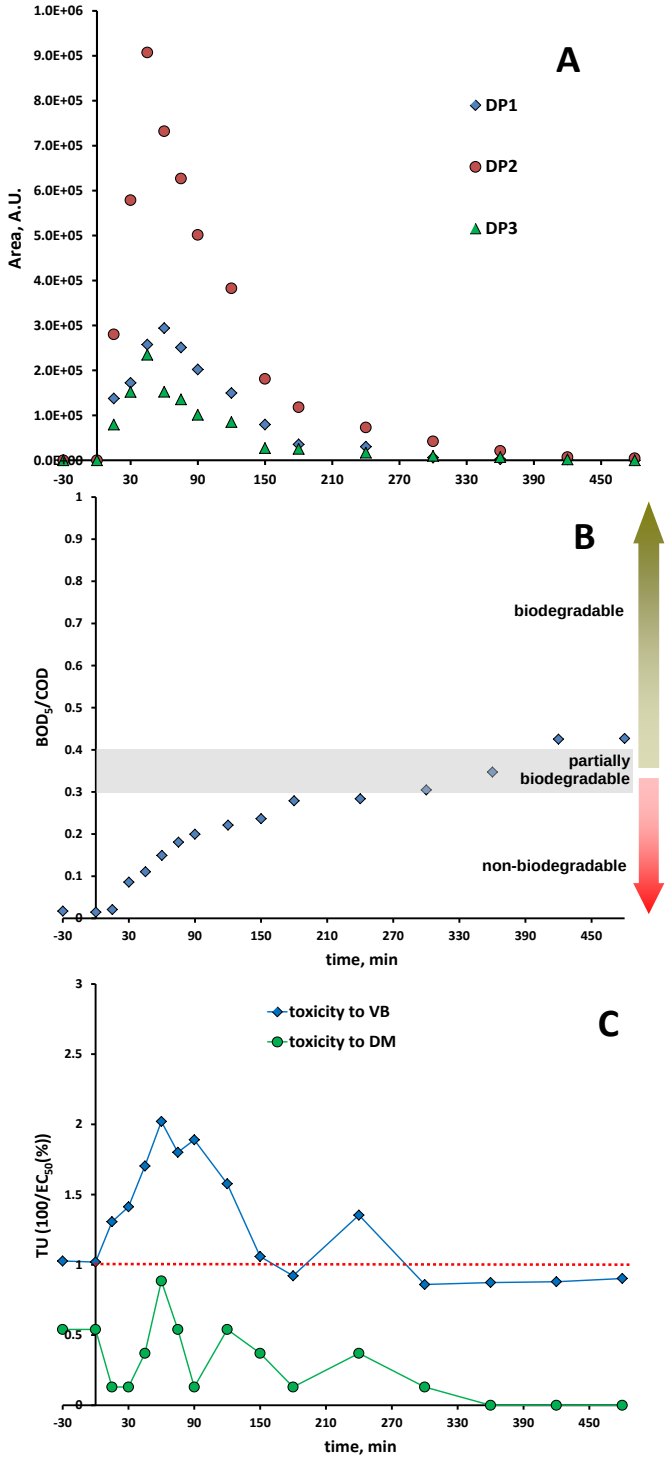

Figure 35. (**A**) Evolution and degradation of identified AMX by-products; (**B**) changes in biodegradability; and (**C**) toxicity toward VB and DM, during AMX treatment by solar-TiO_2@Fe_2O_3/PS (experimental conditions: initial pH=4 and [PS]=0.334 mM)

It should be noted that according to the toxicity categories established by the guidelines [192], the initial AMX solution can be classified as "harmful to aquatic microorganisms"; EC_{50}(VB) =17.79 mg·L^{-1} and EC_{50}(DM) = 33.83 mg·L^{-1}. Such results are

generally in accordance with the literature data, which are, rather scarce; only several sources were found referring to AMX toxicity toward VB and/or DM [189]. However, these studies did not present toxicity over common parameters such as EC_{50} or TU (presentation was done over single inhibition numbers), thus it is hard to compare the results from this study and available literature. The toxicity changes recorded toward both bioassays follow more or less the same trend; during the treatment period where AMX and its initial by-products DP1, DP2, and DP3 prevail in the reaction mixture (i.e., up to 180th minute of treatment), toxicity underwent sinusoidal increases and decreases, reaching the maximums aligned with the maximal recorded concentrations of identified by-products (i.e., at 45th and 60th min). After that period toxicity value mostly decreased, the exception is a slight increase recorded in 240th minute of treatment by both bioassays, which can be associated with the appearance of characteristic by-products toxic for both VB and DM. However, after that treatment period toxicity decreased <1 (in TU) and to 0 in the cases of VB and DM bioassays, respectively (**Figure 35C**). The obtained results indicate the strong correlation between the evolution and degradation of hydroxylated aromatic structures and the observed changes in toxicity profiles.

4.1.5 Influence of Water Matrix

In order to get an insight into the efficiency of solar-TiO_2@Fe_2O_3/PS system for the degradation of AMX in the presence of common water matrix constituents such as: carbonates, chlorides, phosphates, nitrates, and NOM in a form of HA, experiments were performed to investigate their individual and mutually combined effects.

As shown in **Figure 36A**, AMX degradation was inhibited in all cases. The obtained results can be plausibly explained with the fact that added substances may react with the formed $SO_4^{\bullet-}$ and HO•, forming specific radicals which seem to be less reactive toward AMX than $SO_4^{\bullet-}$ and HO•, thus, consequently inhibiting AMX degradation through such competitive reactions. The inhibitory effect strongly depends on the reaction rates and concentrations of added substances with $SO_4^{\bullet-}$ and HO•. According to the literature[193,194], AMX reaction rate constants with SO_4•− and HO• are $k(SO_4^{\bullet-}) = 2.79 \times 10^9$ M^{-1} s^{-1} and k(HO•) = 6.64 ± 1.40 × 10^9 M^{-1} s^{-1}. The highest inhibitory effect toward AMX degradation was observed in the case of carbonates; k_{obs} decreased by 86.0% compared to the case-referent case without water matrix constituents presence (1.04×10^{-7} M·min^{-1}<< 7.40×10^{-7} M·min^{-1}) (**Figure 36B**). Taking into account that both CO_3^{2-} and HCO_3^- reacts rather rapidly with $SO_4^{\bullet-}$ k ($SO_4^{\bullet-}$ /HCO_3^-) =1.6 × 10^6 M^{-1} s^{-1} and k ($SO_4^{\bullet-}$ /CO_3^{2-})= 6.1 ×

10^6 $M^{-1}s^{-1}$) [195] and HO• k (HO•/HCO_3^-) = 8.5 × 10^6 $M^{-1}s^{-1}$ and k (HO•/CO_3^{2-})= 3.9 × 10^8 $M^{-1}s^{-1}$) [183], as well as the fact that carbonates concentration was 33.3 times higher than that of AMX, the inhibitory effect was not surprising. Similar is valid for chlorides as well, where k_{obs} has also been diminished significantly (for 61.4%) (**Figure 36B**). Besides reactions with formed radical species k(HO•/Cl^-) = 4.3 × 10^9 $M^{-1}s^{-1}$ and k($SO_4^{\bullet-}$ /Cl^-) = 3.1 × 10^8 $M^{-1}s^{-1}$) [183,196] chlorides adsorption on the surface of TiO_2 layer may hinder the adsorption and consequently reactive sites for PS activation [197]. Namely, in solar-TiO_2@Fe_2O_3/PS process, persulfate activation occurs at the surface of the photocatalyst, thus the adsorption step is essential for the overall AMX degradation. The observed inhibitory effects in the case of nitrates and phosphates can be assigned to combined adsorption and competitive reactions, as in the case of chlorides [197]. However, as can be seen from **Figure 36B**, inhibitory effects were much lower than in the case of chlorides; k_{obs} diminished 14.5% (with nitrates) and 31.4% (with phosphates). The plausible explanation can be found in the concentrations of added nitrates and phosphates that were 80 and 130 times lower, respectively, compared to chlorides. Their concentrations definitely affected the competitive reactions with AMX as well; nitrates and phosphates were present in 1.5 and 2.4 times lower concentrations, respectively, than AMX. The presence of NOM, represented by HA, inhibited AMX degradation rather significantly; k_{obs} diminished for 44.6% (4.1 × 10^{-7} M·min^{-1} < 7.4 × 10^{-7} M·min^{-1} (**Figure 36B**). It should be noted that HA, besides reacting with present radical species in the system, is susceptible to photodegradation under solar irradiation, thus introducing additional radical species that are capable of reacting with targeted organics. Accordingly, HA may also provide synergistic or inhibitory effects on the removal rate of targeted compounds by photo-AOPs [198–200]. As can be concluded from the obtained results in our study, the inner filter effect of HA (which promotes the reduction of incident irradiation flux activation of photocatalytic material) occurred, thus lowering AMX degradation rate. Moreover, HA is rich in electrons and could also scavenge HO• and $SO_4^{\bullet-}$ rapidly [201,202], thus contributing to the observed inhibitory effect (**Figure 36B**). In addition, HA promotes the increase in a negative charge in the surface of TiO_2 [203], thus leading to the inhibition of PS activation, consequently lowering the overall AMX degradation rate (**Figure 36B**). Hence, it seems that in our case multiple negative effects of HA presence prevailed over the above-stated synergistic effect related to the formation of additional NOM-based radical species. Finally, we have also studied combined effects of all substances investigated separately and found out that inhibitory effect is quite significant (k_{obs}

diminished for 81.2%, (**Figure 36B**), most likely as a consequence of above-explained separate effects.

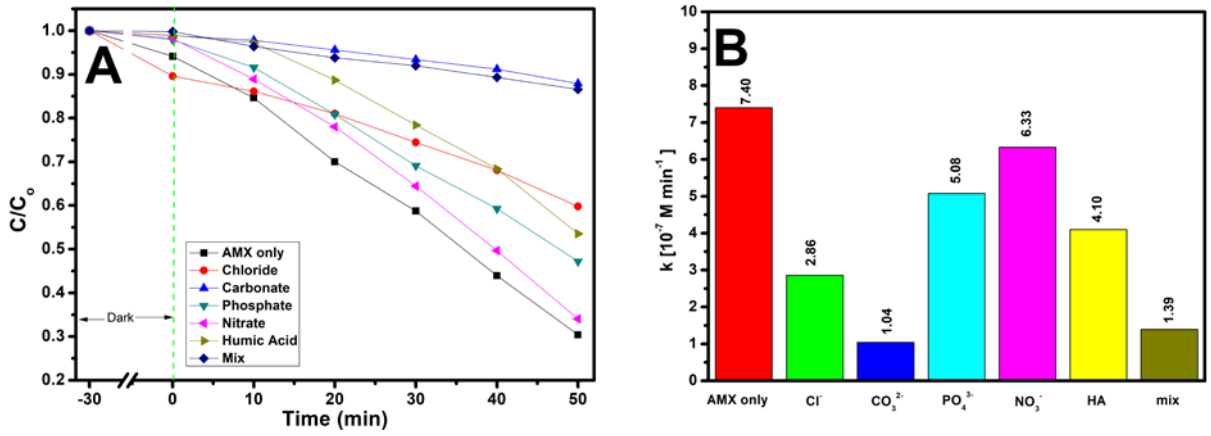

Figure 36. (**A**) Photocatalytic degradation of AMX under solar irradiation in the presence of water matrix constituents; and (**B**) corresponding zero-order rate constants (k_{obs}). (experimental conditions: [AMX]=0.050 mM; pH=4; [PS]=0.334 mM; [Cl^-]=100 mg·L^{-1}, [CO_3^{2-}]=100 mg·L^{-1}, [NO_3^-]=2 mg·L^{-1}, [PO_4^{3-}]=2 mg·L^{-1}, and [HA]=5 mg·L^{-1}, treatment time=50 min)

4.1.6 *Stability Test*

In order to confirm the stability of immobilized photocatalyst, TiO_2@Fe_2O_3 composites were utilized for four consecutive degradation experiments employing optimal conditions within the studied range of parameters obtained in subsection 4.1.2.

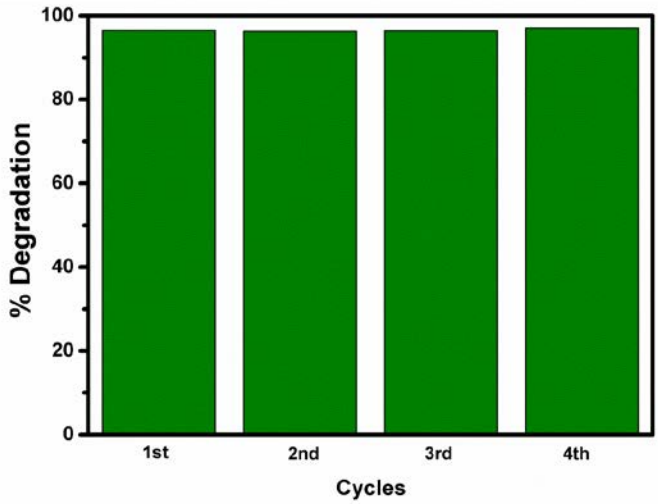

Figure 37. AMX removal by solar-TiO_2@Fe_2O_3/PS at multiple regeneration cycles. (experimental conditions: initial pH=4, [PS]=0.334 mM and irradiation time=120 min)

As shown in **Figure 37**, AMX removal of >96% was achieved in each cycle. Gravimetric analysis revealed negligible weight loss (<0.008%), confirming excellent stability and potential to be reused. In addition, no significant changes in appearance between fresh (**Figure 38A**) and reused (**Figure 38B**) TiO_2@Fe_2O_3 immobilized composites were observed in **Figure 38**.

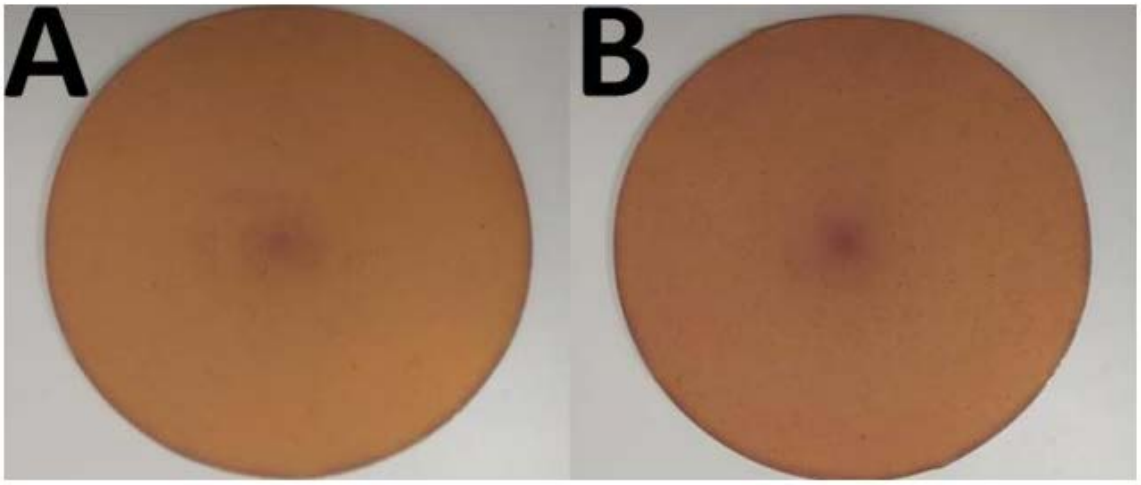

Figure 38. TiO_2@Fe_2O_3 plates fresh (**A**) and after four cycles of use (**B**)

4.1.7 Visible-light Experiments (Layered Composites)

The layered composites were subjected to photocatalytic degradation experiments using visible light irradiation instead solar irradiation (**Figure 39**). The results revealed that the prepared layered composites performed well under solar irradiation. Under visible light, TiO_2@Fe_2O_3 (TiO_2(*top*) and Fe_2O_3(*bottom*)), TiO_2 cannot be excited (formation of photogenerated e^-/h^+) due to its band gap restriction. On the other hand, it must be noted that Fe_2O_3 (bottom) can still be excited by visible light. Nevertheless, the results are all inferior against the performance of TiO_2 and TiO_2@Fe_2O_3. Monfort et al. [168] suggests that the *top layer* of sandwich composites (i.e., TiO_2 based composites) plays the superior role in determining photocatalytic efficiency.

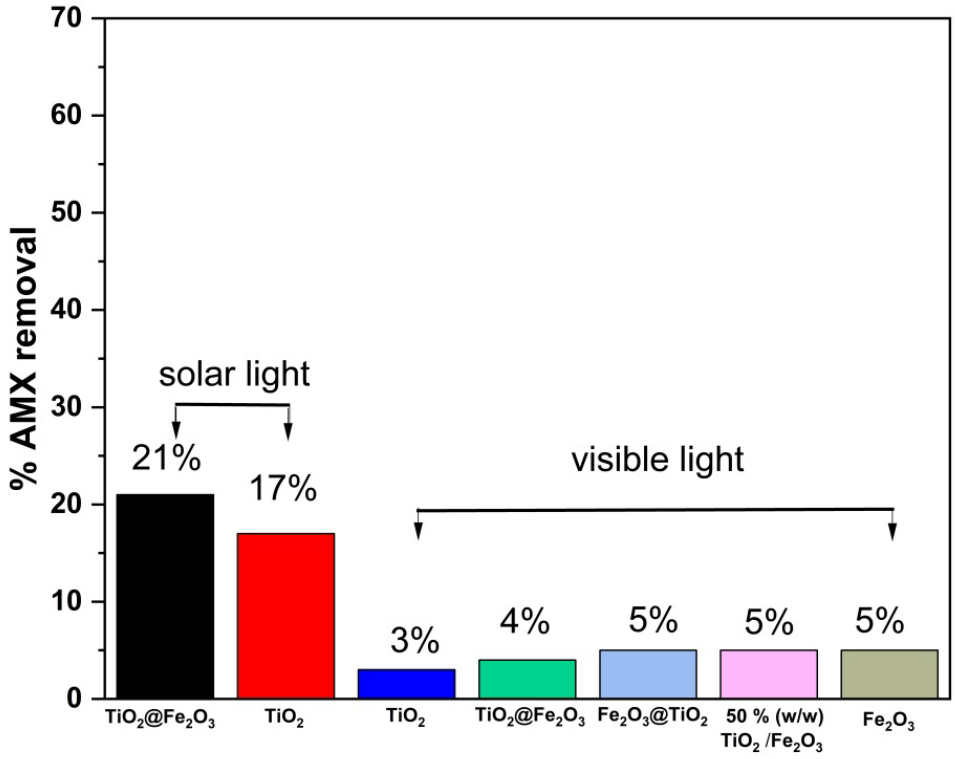

Figure 39. Comparison of photocatalytic performance of layered composites under solar and visible light irradiation. (experimental conditions: [AMX] = 0.050 mM; pH=natural pH (5.5); treatment time: 45 min; no oxidant)

4.2 Fe_2O_3 /TiO_2 nanocomposite

4.2.1 Characterization

The X-ray diffractograms of the as-prepared Fe_2O_3/TiO_2 nanocomposite materials are shown in **Figure 40**.

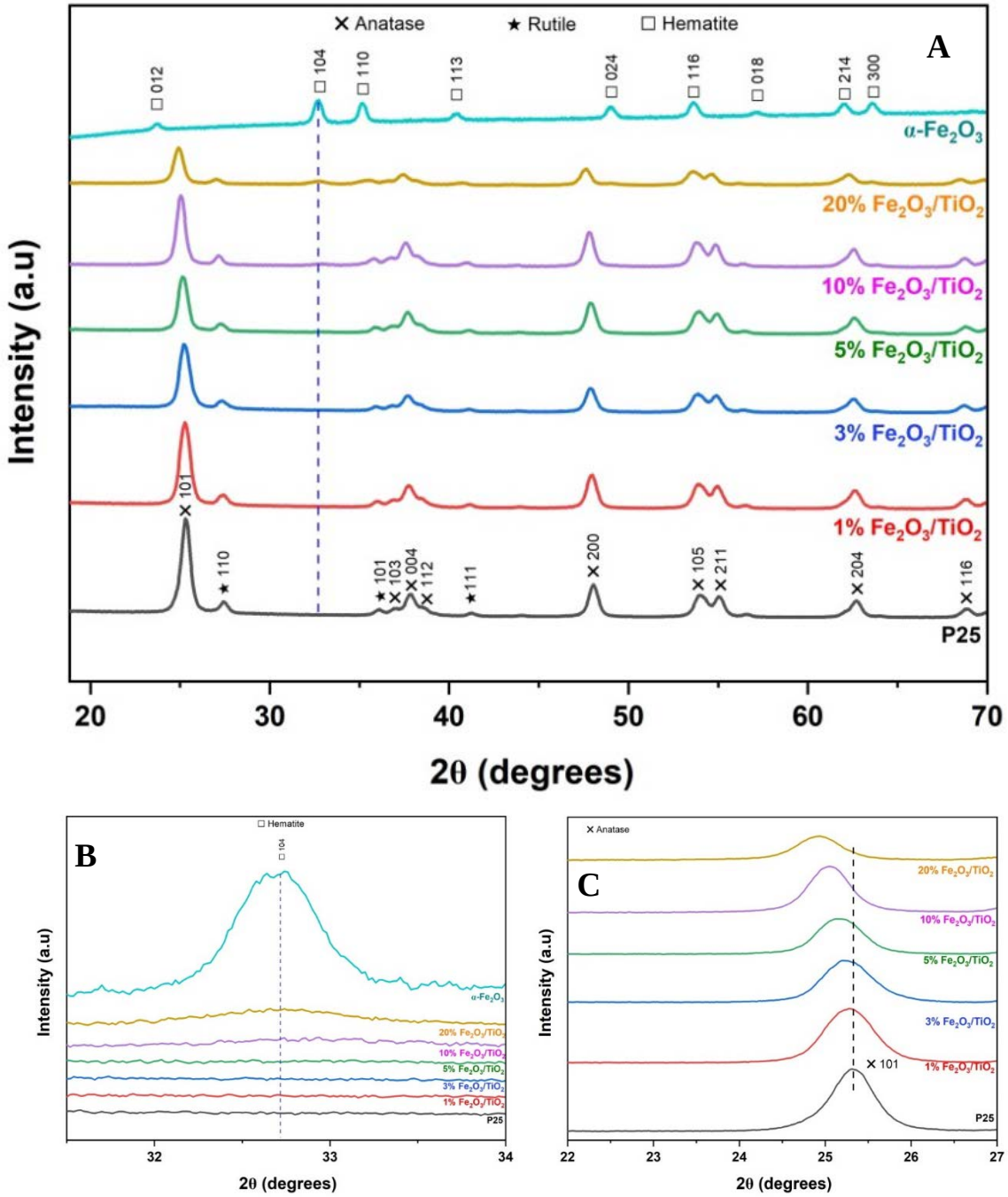

Figure 40. (**A**) XRD pattern of prepared Fe_2O_3/TiO_2 nanocomposites, (**B**) partial magnification around (104) plane of hematite, and (**C**) partial magnification around (101) plane of anatase

The crystalline structure of the as-prepared photocatalytic materials were investigated by XRD. In **Figure 40A**, the peaks observed in the diffractograms at 2θ = 25.30°, 37.00°, 37.84°, 38.72°, 48.02°, 53.94°, 54.94°, 62.72° and 68.92° were indexed into lattices (101), (103), (004), (112), (200), (105), (211), (204) and (116) which is in good agreement with anatase (ICDD PDF card 21-1272), while 2θ = 27.44°, 36.14° and 41.22° were indexed into lattices (110), (101) and (111) which corresponds to rutile (ICDD PDF card 21-1276) [57,204]. Meanwhile, preparation using only pure iron precursor yielded diffractogram peaks at 2θ = 23.72°, 32.74°, 35.20°, 40.40°, 49.06°, 53.02°, 57.10°, 62.08° and 63.62° were indexed into lattices (012), (104), (110), (113), (024), (116), (018), (214) and (300) which corresponds to pure hematite (ICDD PDF card 33-0664) [205,206]. Partial magnification around (104) plane (**Figure 40B**) of hematite revealed that only 20% (*w/w*) Fe_2O_3/ TiO_2 provides noticeable additional peak confirming the successful inclusion of α-Fe_2O_3, while no traces of hematite are detected to all of the remaining nanocomposites due to XRD detection limit [204]. In **Figure 40C**, partial magnification around 25.30°((101)-anatase plane), revealed peak shift to lower angle upon increasing addition of Fe_2O_3 which is attributed to lattice distortion on the TiO_2 surface [204].

Raman spectra of the prepared nanocomposites and pure α-Fe_2O_3 are shown in **Figure 41**. All of the prepared nanocomposites showed distinct phonon modes of TiO_2 such as E_g (143, 196 and 641 cm^{-1}), A_{1g} (516 cm^{-1}), and B_{1g} (396 cm^{-1}) [207,208]. Meanwhile, α-Fe_2O_3 showed two A_{1g} phonon modes (227 and 496 cm^{-1}) and four E_g phonon modes (245, 294, 410 and 613 cm^{-1}) [205,209–212]. No vibrational modes of other iron related species (i.e., maghemite or magnetite) were detected, which indicates high purity of the obtained α-Fe_2O_3. It must be noted that only 10% and 20% (*w/w*) Fe_2O_3/TiO_2 provide noticeable α-Fe_2O_3 vibrational modes (A_{1g} (227 cm^{-1}), E_g (294 cm^{-1})), confirming the successful inclusion of α-Fe_2O_3 in the composite, as it is also in agreement with XRD results.

Scanning electron microscopy (SEM) images and EDX spectra of prepared nanocomposite photocatalysts are shown in **Figure 42**. The formation of agglomerated TiO_2–P25 (Aeroxide) particles is a consequence of the impregnation-calcination method. It must be noted that Fe_2O_3 content loading is low and did not cause any distortion on the overall appearance of the nanocomposite. As such, it can be denoted that small Fe_2O_3 particles are formed around TiO_2-P25 to promote heterojunction between the semiconductor (i.e., TiO_2 and Fe_2O_3), which may improve charge transfer mobility in the overall nanocomposite [204]. EDX spectra revealed the presence of small Fe amount among the prepared nanocomposites,

which later proved the incorporation of Fe_2O_3. These results are in agreement with the obtained XRD and Raman results, as discussed above.

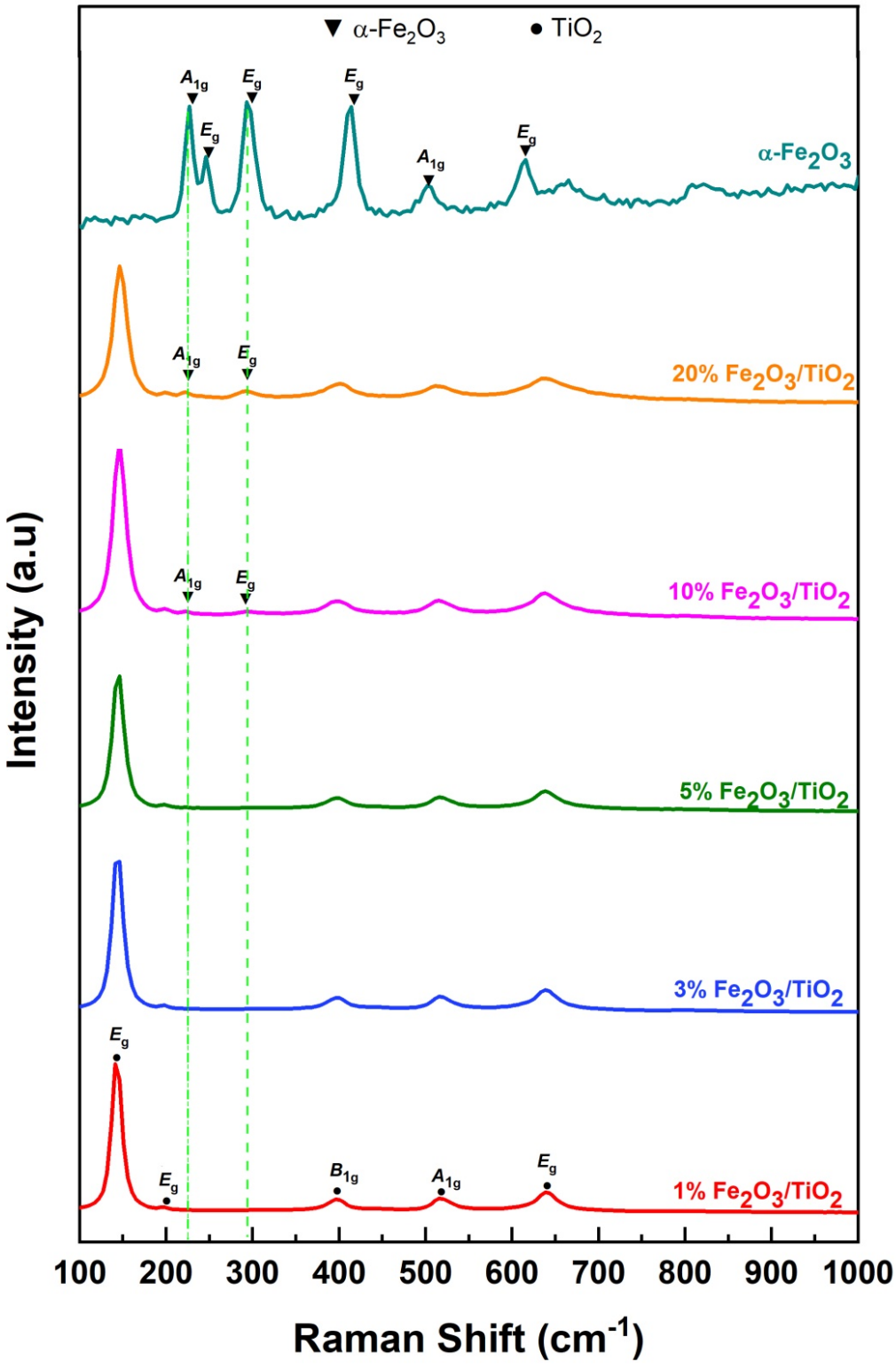

Figure 41. Raman spectra of Fe_2O_3/TiO_2 nanocomposites and pure α-Fe_2O_3

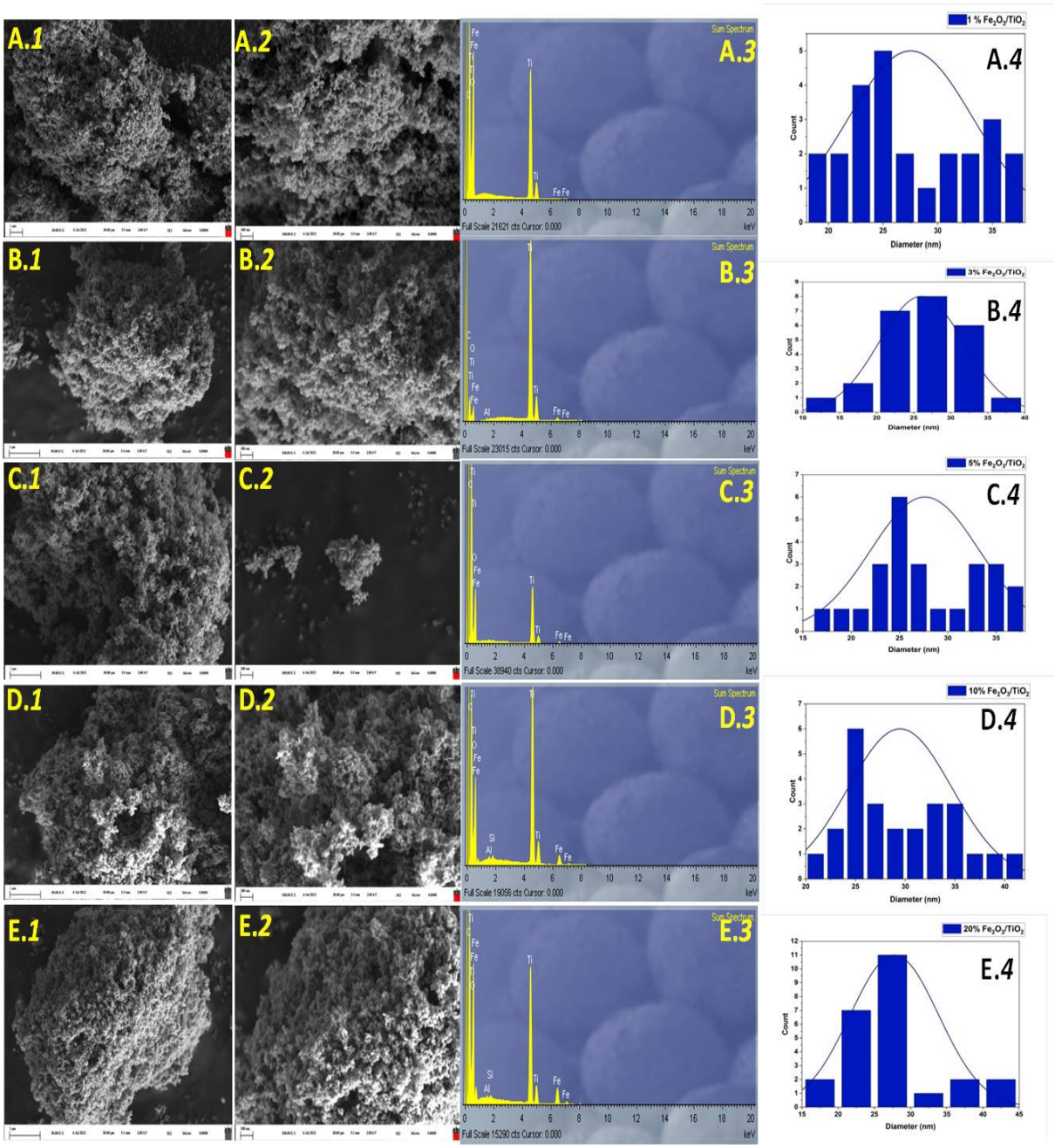

Figure 42. SEM images (50,000 x (*1*); 100,000 x (*2*); EDX spectrum (*3*); particle size distribution (*4*) of (**A**) 1% (*w/w*) Fe_2O_3/TiO_2; (**B**) 3% (*w/w*) Fe_2O_3/TiO_2; (**C**) 5% (*w/w*) Fe_2O_3/TiO_2; (**D**) 10% (*w/w*) Fe_2O_3/TiO_2 and (**E**) 20% (*w/w*) Fe_2O_3/TiO_2 nanocomposite

X-ray Photoelectron Spectroscopy (XPS) was further used to determine the surface chemical composition and oxidation states of 5% (*w/w*) Fe_2O_3/TiO_2 nanocomposites. XPS full survey spectrum (**Figure 43A**) showed distinct signal of Fe 2*p*, Ti 2*p* and O 1*s*, confirming the successful inclusion of α-Fe_2O_3 on the surface of TiO_2 [213], while C 1*s* peak

is attributed to adventitious carbon contamination originating from air exposure of samples [214].

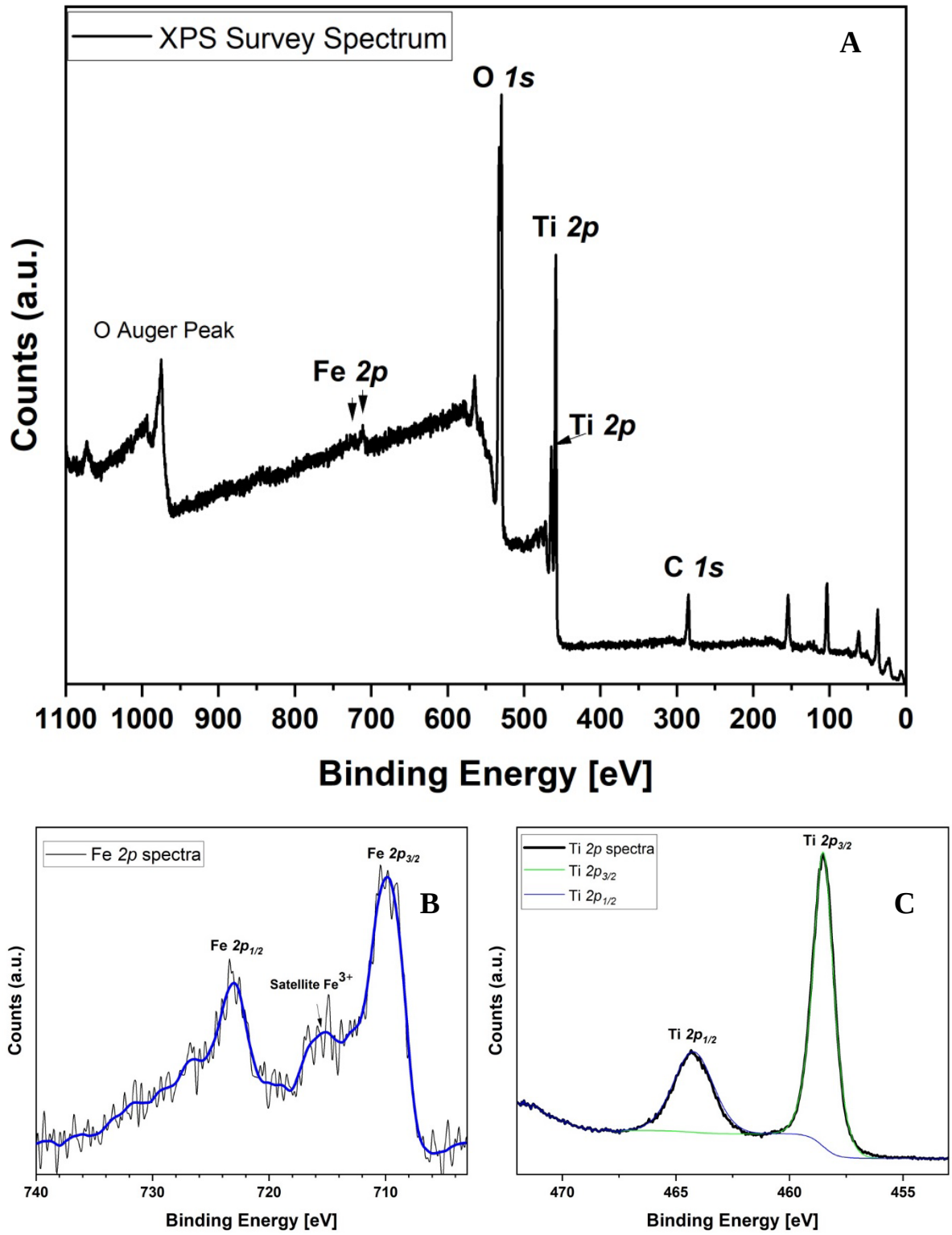

Figure 43. (**A**) XPS survey analysis of 5% (*w/w*) Fe_2O_3/TiO_2, (**B**) Fe 2*p* core level spectrum of 5% (*w/w*) Fe_2O_3/TiO_2, and (**C**) Ti 2*p* core level spectrum of 5% (*w/w*) Fe_2O_3/TiO_2

In **Figure 43B**, the core level XPS spectrum of Fe 2*p* showed two peaks at binding energy (B.E) values of 723.50 and 709.85 eV, corresponding to Fe $2p_{1/2}$ and Fe $2p_{3/2}$, respectively and a satellite signal at around 715 eV that are all characteristic of Fe^{3+} in Fe_2O_3 [204,213,215] . Moreover, the difference in core energy level of Fe 2*p*, Δ(B.E)= ($2p_{1/2}$-$2p_{3/2}$)= 13.65 eV, also proved the presence of α-Fe_2O_3 [213,215]. **Figure 43C**, core level XPS spectrum of Ti 2*p* showed Ti^{4+} characteristic peaks at B.E values of 464.33 and 458.53 eV, corresponding to Ti $2p_{1/2}$ and Ti $2p_{3/2}$, respectively [204,213]. Similarly, Ti 2*p*, Δ(B.E)= ($2p_{1/2}$-$2p_{3/2}$)= 5.8 eV, indicates normal state of Ti^{4+} in TiO_2–anatase, which is nearly similar to the results reported in literature [213,216,217].

UV-diffuse reflectance spectra of pure components and prepared nanocomposites are shown in **Figure 44A**, whereas Kubelka-Munk transformed spectra for the calculation of band gap values are presented in **Figure 44B**. As shown in **Table 17**, calculated band gap values of TiO_2-P25 and α-Fe_2O_3 powders are in agreement with the values provided in the literature [166,167]. An increasing visible light absorption (**Figure 44A**) and overall decrease in band gap values (**Table 17**) of the Fe_2O_3/TiO_2 nanocomposites were observed upon increasing Fe_2O_3 content.

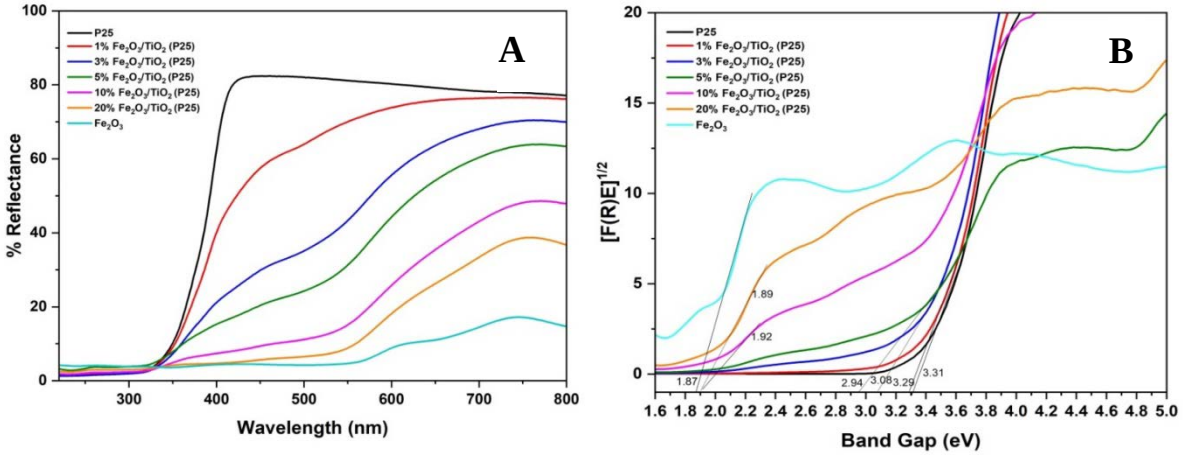

Figure 44. (A) UV-visible DRS spectrum of Fe_2O_3/ TiO_2 nanocomposites, and (**B**) Kubelka-Munk functions $[F(R)E]^{1/2}$ versus photon energy (eV)

Table 17. Photocatalyst bandgap values estimated using Kubelka-Munk function

Photocatalyst	**TiO_2 (P25)**	**1%Fe_2O_3/TiO_2**	**3%Fe_2O_3/TiO_2**	**5%Fe_2O_3/TiO_2**	**10%Fe_2O_3/TiO_2**	**20%Fe_2O_3/TiO_2**	**α-Fe_2O_3**
Band Gap (eV)	3.31	3.29	3.08	2.94	1.92	1.89	1.87

Photoluminescence (PL) spectroscopy was used to study the separation of photogenerated e^-/h^+ pairs in the as-prepared nanocomposites. As can be seen in **Figure 45**, all Fe_2O_3/TiO_2 nanocomposites showed a specific emission peak at around 444 nm as

similarly reported by Sayed et al. [218]; however, with different intensities. Materials containing 1% and 3% (*w/w*) Fe_2O_3 exhibited higher PL intensity compared to pristine TiO_2. Such low Fe_2O_3 loading (i.e. 1 and 3% (*w/w*)) may suppress the defects concentration and thus promote the increase in e^-/h^+ recombination rate [219,220]. Similarly, further increase of Fe_2O_3 loading (i.e., 20% (*w/w*)) exhibited the highest PL intensity among all the prepared nanocomposites and moreover, higher than pristine TiO_2. As such, an optimal level of 5% Fe_2O_3 loading exhibited the lowest PL intensity, suggesting strongly suppressed e^-/h^+ recombination rate [221] and it would be considered with the highest photocatalytic activity among all of the prepared nanocomposites.

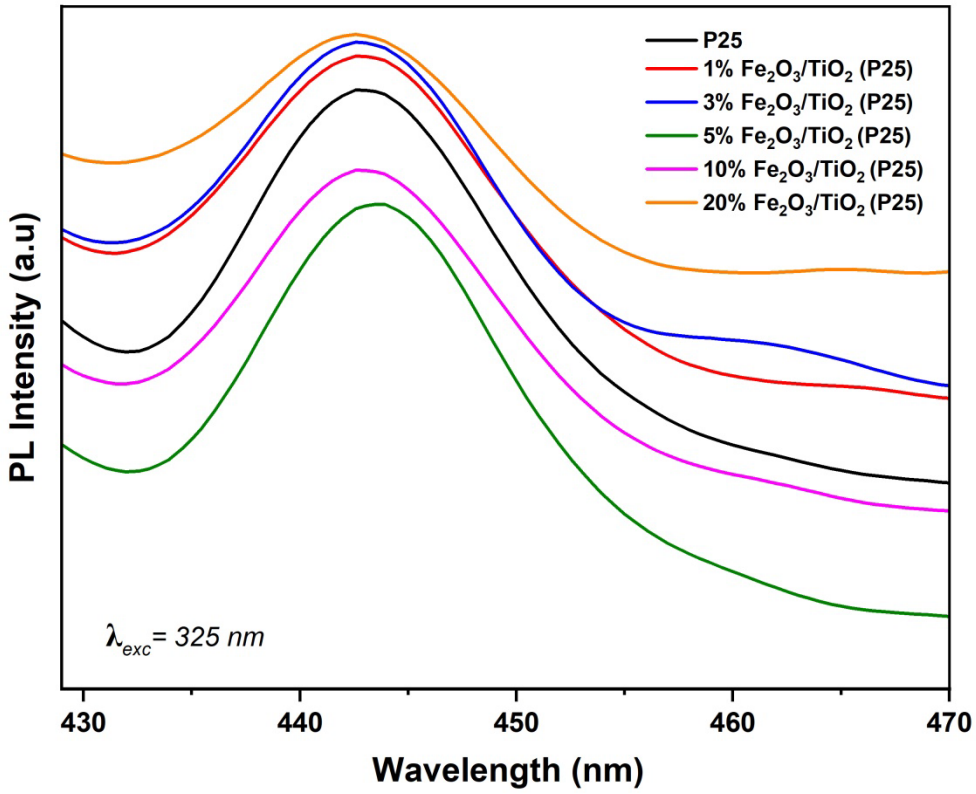

Figure 45. Photoluminescence (PL) spectra of pristine TiO_2 and Fe_2O_3/TiO_2 nanocomposites

To further explore the photogenerated charge carrier separation efficiency of the prepared nanocomposite, photoelectrochemical studies (i.e. transient photocurrent responses and EIS) were conducted. Photocurrent density responses of photocatalyst are directly related to its photocatalytic activity [222,223]. Transient photocurrent responses of TiO_2, α-Fe_2O_3 and 5% (*w/w*) Fe_2O_3/TiO_2 are shown in **Figure 46A**. 5% (*w/w*) Fe_2O_3/TiO_2 exhibited the highest response (0.55 μA cm^2) compared to individual parts of the composite (i.e. TiO_2 and Fe_2O_3). The improved separation efficiency was attributed to successful heterojunction

formation. It must be noted that photocurrent density of 5% (*w/w*) Fe_2O_3/TiO_2 was reduced in the second cycle (light on-light off) to 0.45 µA cm^2, which may be attributed to the leaching of Fe_2O_3 [223]. Electron impedance spectroscopy (EIS) was used to study the interfacial charge transfer mechanism in the prepared samples [224]. In **Figure 46B**, EIS Nyquist plots of pure TiO_2 and 5% (*w/w*) Fe_2O_3/TiO_2 were measured in dark and light irradiation. In EIS, the radius of the semi-circle corresponds to the overall charge transfer resistance [175,223,224]. Under visible light irradiation, all samples showed less charge transfer resistance than in dark, while 5% (*w/w*) Fe_2O_3/TiO_2 has smaller radius than pure TiO_2 indicating efficient charge transfer mechanism between Fe_2O_3 and TiO_2 due to successful heterojunction formation.

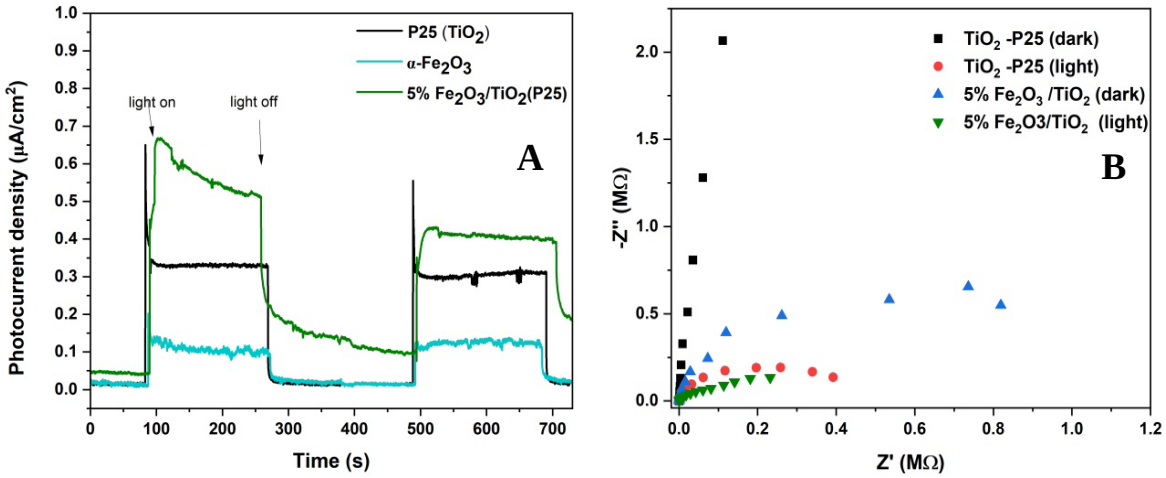

Figure 46. (**A**) Transient photocurrent responses of TiO_2-P25, α-Fe_2O_3, and 5% (*w/w*) Fe_2O_3/TiO_2 nanocomposites, and (**B**) EIS Nyquist plots of TiO_2-P25 and 5% (*w/w*) Fe_2O_3/TiO_2 in dark and light conditions

4.2.2 Photocatalytic Activity Tests

Preliminary experiments revealed negligible effect of hydrolysis and photolysis on AMX concentration within 90 min period of visible light (**Figure 47A**). Initial adsorption extents of AMX onto the prepared photocatalysts during the dark period (-30 to 0 min) were found to be infinitesimally small (< 1.5%), thus observed removal extents of AMX during photocatalytic treatment were mainly approximated to the conversion extents. Such results were ascribed to pK_a of values of AMX (pK_{a1} = 2.4; pK_{a2} = 7.4; and pK_{a3} = 9.6) [177] and point of zero charge of TiO_2-P25 (pH_{pzc} = 6.5-6.7) [174,176,225], α-Fe_2O_3(pH_{pzc} = 6.2) [226], and Fe_2O_3/TiO_2 (pH_{PZC}=5.8-6.8) [218,227,228]. Hence, at pH 5.5, AMX is mostly present in its neutral form/zwitterionic form (pK_{a1} = 2.4) < pH < pK_{a2} = 7.4 [177] and all prepared

photocatalysts net surface charged are positive, thus leading to less interaction between two moieties. Single and multi-point B.E.T surface areas of the prepared photocatalysts are presented in **Table 18**. Incorporation of α-Fe_2O_3 with TiO_2-P25 generally decreases the surface area of the prepared nanocomposites. However, such changes in surface area did not affect the adsorption behavior of the prepared photocatalysts since electrostatic interaction (i.e. pK_a and pH_{pzc}) plays a major role in this scenario.

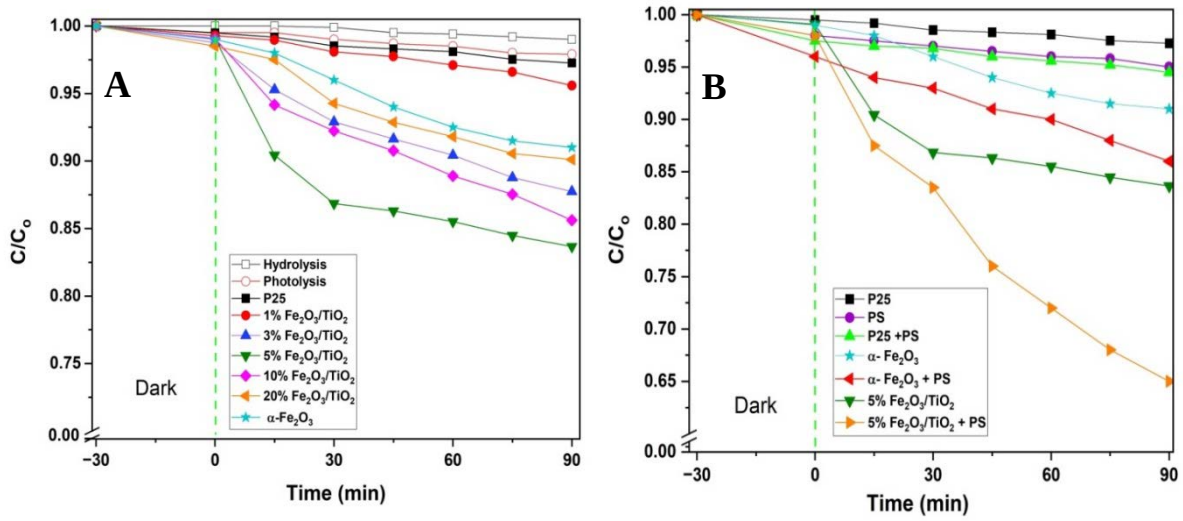

Figure 47. Photocatalytic removal of AMX using prepared photocatalysts under visible light irradiation without oxidant (**A**) and (**B**) with [PS] = 0.3 mM. (*Conditions:* [catalyst dosage] = 0.5 g/L; [AMX] = 0.050 mM; initial pH = natural pH (5.5); catalyst used in powdered form)

Table 18. Single point and multipoint B.E.T surface area of samples

Photocatalyst	**Single Point B.E.T ($m^2 \cdot g^{-1}$)**	**Multi Point B.E.T ($m^2 \cdot g^{-1}$)**
TiO_2-P25	46.6112	47.3512 ± 0.1206
α-Fe_2O_3	25.2897	25.4548 ± 0.2408
1% (*w/w*) Fe_2O_3/TiO_2	49.7926	51.2769 ± 0.4552
3% (*w/w*) Fe_2O_3/TiO_2	39.3548	39.6042 ± 0.3677
5% (*w/w*) Fe_2O_3/TiO_2	40.4217	40.985 ± 0.2412
10% (*w/w*) Fe_2O_3/TiO_2	42.5486	43.4856 ± 0.1723
20% (*w/w*) Fe_2O_3/TiO_2	34.4068	34.7489 ± 0.3532

The highest photocatalytic activity was achieved by 5% (*w/w*) Fe_2O_3/TiO_2, exhibiting 16.3% AMX conversion within 90 min period, which is significantly higher than any of the nanocomposites and pure components (i.e., TiO_2-P25 and α-Fe_2O_3) (**Figure 47A**). Such

improvement of photocatalytic activity were ascribed to the suppression of recombination of photogenerated e^-/h^+ within the composite, which is also proved and supported by PL spectroscopy (**Figure 45**) and photoelectrochemical experiments (**Figure 46**). Accordingly, 5% (*w/w*) Fe_2O_3/TiO_2 was selected as the photocatalyst to be immobilized onto glass support due to its superior photocatalytic activity compared to other prepared nanocomposites.

Parallel photocatalytic studies have been conducted using the same of prepared composites under solar irradiation (**Figure S5.1**). Results revealed that increasing % (*w/w*) Fe_2O_3 on the overall composite leads to decrease in overall photocatalytic activity. As such, the results implied an opposite trend compared to visible-light assisted experiments. Lee et al. [229] reported the same phenomenon when using Fe_2O_3/TiO_2 composite for photocatalytic degradation of 2,4-dichlorophenoxyacetic acid. In addition, Li.et al. [230] showed that TiO_2 have superior photocatalytic activity over prepared Fe_2O_3/TiO_2 when photodegrading oxytetracycline under UV light. Nevertheless, it must be noted that most of the reported literature for Fe_2O_3/TiO_2 suggest that incorporation of Fe_2O_3 into TiO_2 promotes solar activity [231]. As such, it is critically implied that synthetic technique on the prepared Fe_2O_3/TiO_2 composite plays a crucial role in the overall activity. For this dissertation, a special focus on visible light –activation of photocatalysts have been employed due to limited studies. As such, studies under visible light have been continued with the addition of PS to improve AMX removal.

In **Figure 47B**, the presence of [PS] = 0.3 mM with 5% (*w/w*) Fe_2O_3/TiO_2, showed significant increase in AMX conversion (35%). Such results are ascribed to additional $SO_4^{\bullet-}$ (and potentially $HO^{\bullet}$) produced from PS, which serves as an electron acceptor and suppressor for e^-/h^+ recombination [9]. Determination of excess [PS] was shown in **Figure S5.2**, Appendix. For further optimization, 5% (*w/w*) Fe_2O_3/TiO_2 was immobilized on glass support (**Figure S6**) and RSM modeling was applied to avoid misleading information obtained from conventional "one-parameter-at-time" approach [1]. As can be seen from **Figure S7**, kinetic profiles of AMX conversions for vis-(5% (*w/w*) Fe_2O_3/TiO_2)/PS system operated at conditions set by 3^2 FFD (**Table 14B** and **Table S2.2**, Appendix), the obtained results obey zero-order kinetics. Accordingly, AMX conversion rate constants (k_{obs}) for period of treatment under visible irradiation were calculated using **Equation (3)**, representing functional dependence of AMX conversion versus treatment time, implying surface reaction mechanism for activation of PS [171–173]. Such calculated k_{obs} were used as system responses in RSM.

It must be noted that all photocatalytic experiments include 30 min dark period to ensure adsorption-desorption equilibrium (**Figure S7**, Appendix). For pH 4 and 6, the net surface charge of 5% (*w/w*) Fe_2O_3/TiO_2 is positive, while AMX mostly exists in neutral form. As a result AMX absorbed amount is less than 1.5%, which is a consequence of less attraction between two moieties. For pH 8, it is expected that AMX absorbed amount will be less as well, since 5% (*w/w*) Fe_2O_3/TiO_2 and AMX net charge are both negative and repulsion of negative charges is expected to be dominant. However, AMX removal was observed to be 37-40% within 30 min dark period which can be associated with base activation of persulfate [232,233]. In this case, base catalyzed hydrolysis of persulfate yields hydroperoxide anion and sulfate ion **Equation (13)**. Thereafter, additional persulfate ion reacts with hydroperoxide anion to yield sulfate radical and superoxide radical **Equation (14)**. Lastly, sulfate radicals can react with hydroxide ions to produce hydroxyl radicals **Equation (15)** [232,233]. Hence, it must be noted that the AMX removal associated with base catalyzed persulfate is not included in RSM modeling since its process is characterized as non-photochemical reaction. As such, only the photocatalytic treatment (i.e., 0 to 150 min) is included and is expressed as AMX conversion rate constant, (k_{obs}).

$$S_2O_8{}^{2-} + 2H_2O \xrightarrow{OH^-} 2SO_4{}^{2-} + HOO^- + 3H^+ \quad (13)$$

$$S_2O_8{}^{2-} + HOO^- \rightarrow SO_4{}^{\bullet-} + SO_4{}^{2-} + O_2{}^{\bullet-} + H^+ \quad (14)$$

$$SO_4{}^{\bullet-} + OH^- \rightarrow OH\bullet + SO_4{}^{2-} \quad (15)$$

Accordingly, multiple regression analysis was applied on FFD matrix and AMX (k_{obs}) values calculated for the treatment period under visible light irradiation (**Table S2.2**, Appendix), yielding polynomial equation, that is RSM model, **Equation (16)**:

$$Y=1.41-0.2967\times X_1+0.2467\times X_1{}^2+0.0433\times X_2-0.1367\times X_2{}^2+0.0275\times X_1\times X_2 \quad (16)$$

The obtained model is characterized by ANOVA (**Table S4**, Appendix) and RD tools (**Figure S8**, Appendix), and was found to be significant (p = 0.0010), and accurate (R^2 =0.9956 and $R_{adj}{}^2$=0.9883), while RD revealed that i) there are no violations in the assumptions that errors are normally distributed and independent of each other, ii) the error variances are homogenous, and iii) residuals are independent. ANOVA analysis also revealed that model terms corresponding to both process parameters (i.e. pH and [PS]) are significant, (p = < 0.05). (**Table S4**, Appendix). Therefore, the model can be used as a tool to clearly discuss the influence of studied parameters on AMX conversion. 3D surface and contour

representation of the influence of initial pH and [PS] on AMX conversion rate (k_{obs}), are shown in **Figure 48**.

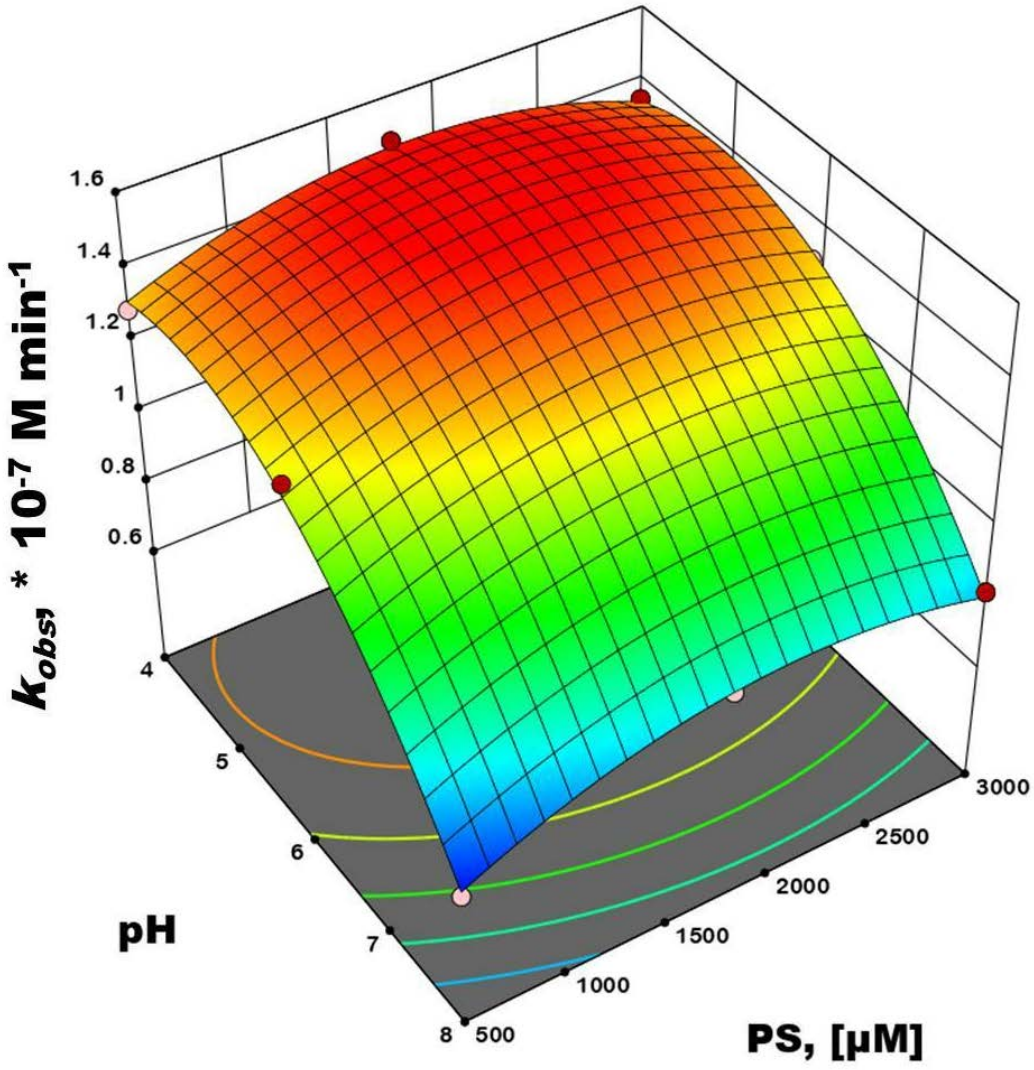

Figure 48. 3D surface and contour plots presenting mutual interactions of initial pH and [PS] on photocatalytic AMX conversion by vis-(5% (*w/w*) Fe_2O_3/TiO_2)/PS (catalyst used in immobilized form)

As can be observed from **Figure 48**, acidic pH (pH 4 to 6) are favorable for AMX conversion, which can be associated with high concentration of SO_4•− (E_o = 2.5-3.1 V vs NHE) that has higher oxidation potential than HO• (E_o = 2.5-3.1 V vs NHE) [178]. In addition, sulfate radicals are also dominant in acidic pH (pH 4 to 6) as described by **Equations (5) and (6)** [179,180]. An increase in pH towards basic range decreases the AMX conversion rate, which can be described by **Equation (15)** [181].

An increase in PS concentration is directly proportional to enhancement of AMX conversion rate up to the point where further increase promotes negative effect. Such decrease in AMX conversion rate can be attributed to excess PS concentration that promotes scavenging and terminating the formed radical species, as described in **Equations (8-11)** [161].

Based on the results presented in **Figure 48**, the optimum conditions for AMX conversion are pH 4.808 and PS concentration of approx. 1873 μM (1.873mM), which are accurately calculated by maximizing polynomial **Equation 16**, thus the predicted AMX conversion rate is 1.51 $\times 10^{-7}$ M min^{-1}. Accordingly, the obtained optimum conditions were further used as the basis for H_2O_2 assisted photoconversion experiments, which was later compared for the investigation of AMX conversion mechanism, transformation by-products and toxicity studies.

As shown in **Figure 49**, three photocatalytic processes (i.e., photocatalysis, photocatalysis + H_2O_2, photocatalysis + PS) are compared on the basis of their AMX conversion profiles upon reaching <99%. Photocatalysis + PS has shown to be the fastest, reaching the full %AMX conversion within 380 min. Photocatalysis + H_2O_2 also showed improved full AMX conversion (within 720 min) compared to the photocatalysis alone (3900 min). Photocatalysis only relies on photogenerated h^+, $O_2^{\bullet-}$, and HO• as ROS for AMX conversion (**Equations 17-20**). Accordingly, 5% (*w/w*) Fe_2O_3/TiO_2 will be excited using visible light to yield photogenerated e^-/h^+ (**Equation 17**). Thereafter, photogenerated e^- will react with O_2 (dissolved in water) to form $O_2^{\bullet-}$ (**Equation 18**) [13,234,235]. Photogenerated h^+ accumulated in valence band (VB) of Fe_2O_3 may react with OH^- to form HO• (**Equation 19**) [234], and lastly photogenerated h^+ may directly react with AMX (adsorbed at the catalyst surface) producing transformation by-products (**Equation 20**).

$$5\%\ (w/w)\ Fe_2O_3\ /TiO_2\ + hv\ (visible\ light) \rightarrow e^-_{CB} + h^+_{VB} \quad (17)$$

$$e^-_{CB}\ + O_2 \rightarrow\ O_2{}^{\bullet-} \quad (18)$$

$$h^+_{VB}\ + OH^- \rightarrow HO\bullet \quad (19)$$

$$h^+_{VB}\ + AMX \rightarrow AMX\ (products) \quad (20)$$

The improved AMX conversion by photocatalytic processes with oxidants are ascribed the reactions of photogenerated e^- with H_2O_2 and PS to form HO• and SO_4•−, respectively (**Equation 21-22**) [182].

$$e^-_{CB}\ +\ H_2O_2 \rightarrow OH^- +\ HO\bullet \quad (21)$$

$$e^-_{CB} + S_2O_8{}^{2-} \rightarrow SO_4{}^{2-} + SO_4{}^{\bullet-} \quad (22)$$

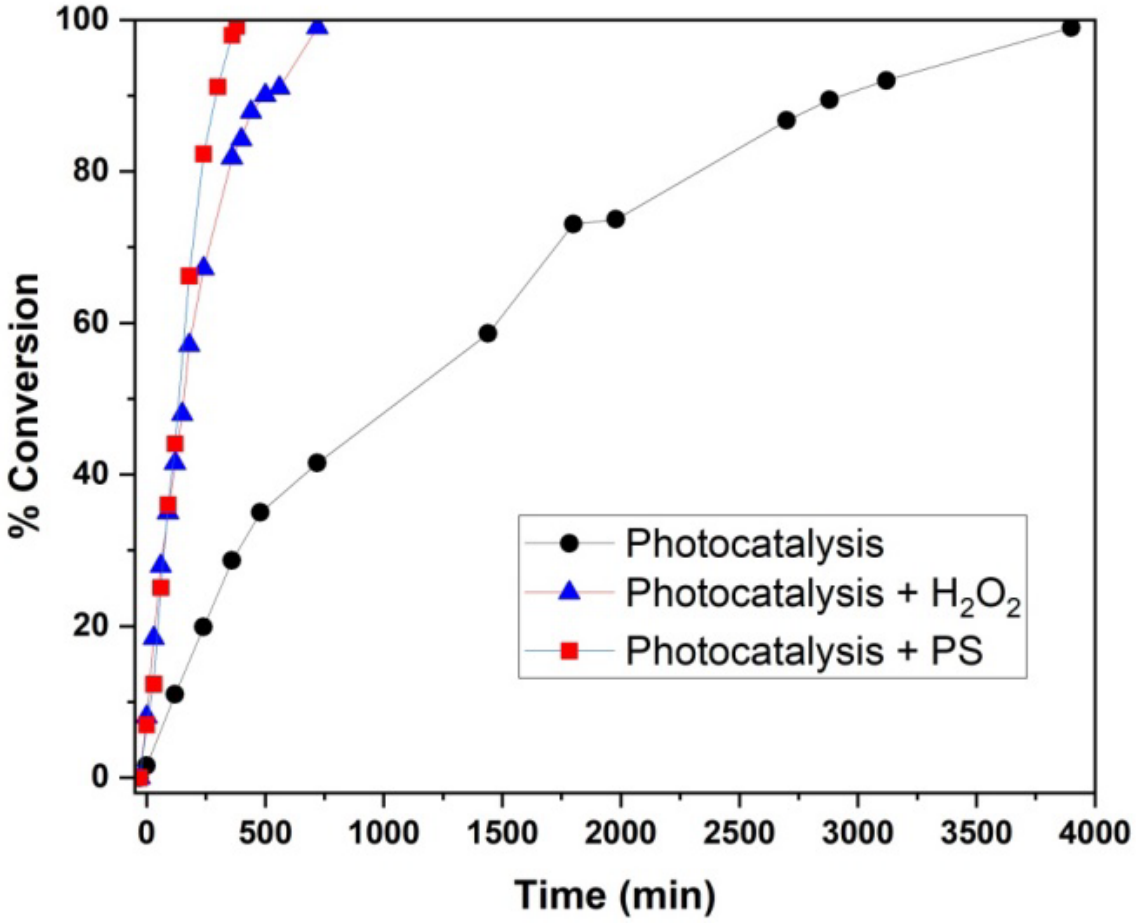

Figure 49. %AMX conversion with photocatalysis, photocatalysis + H_2O_2 and photocatalysis + PS (Experimental Conditions: pH = 4.808; [PS] = [H_2O_2] = 1.873 mM; catalyst = immobilized 5% (*w/w*) Fe_2O_3/TiO_2; [AMX] = 0.050 mM)

4.2.3 Mechanism

AMX conversion mechanisms by photocatalysis, photocatalysis + H_2O_2 and photocatalysis + PS systems were studied in the presence of ROS scavengers (**Figure 50)**. FA was used for scavenging of photogenerated h^+, while BQ was used to scavenge $O_2{}^{\bullet-}$ (k = (0.9-1.0) × 10^9 M^{-1} s^{-1}) [183,236]. MeOH and *t*-BuOH were used to differentiate the contributions of $SO_4{}^{\bullet-}$ and HO•. In such case, MeOH reacts with both $SO_4{}^{\bullet-}$ and HO• (k = 1.1 × 10^7 M^{-1} s^{-1} and k = 9.7 × 10^8 M^{-1} s^{-1}, respectively) [237,238]. Conversely, *t*-BuOH reacts three orders of magnitude higher with HO• (k = 9.7 × 10^8 M^{-1} s^{-1}, than with $SO_4{}^{\bullet-}$ k = (4.0-9.1) × 10^5 M^{-1} s^{-1} [182]) , thus making *t*-BuOH as an efficient scavenger for HO•.

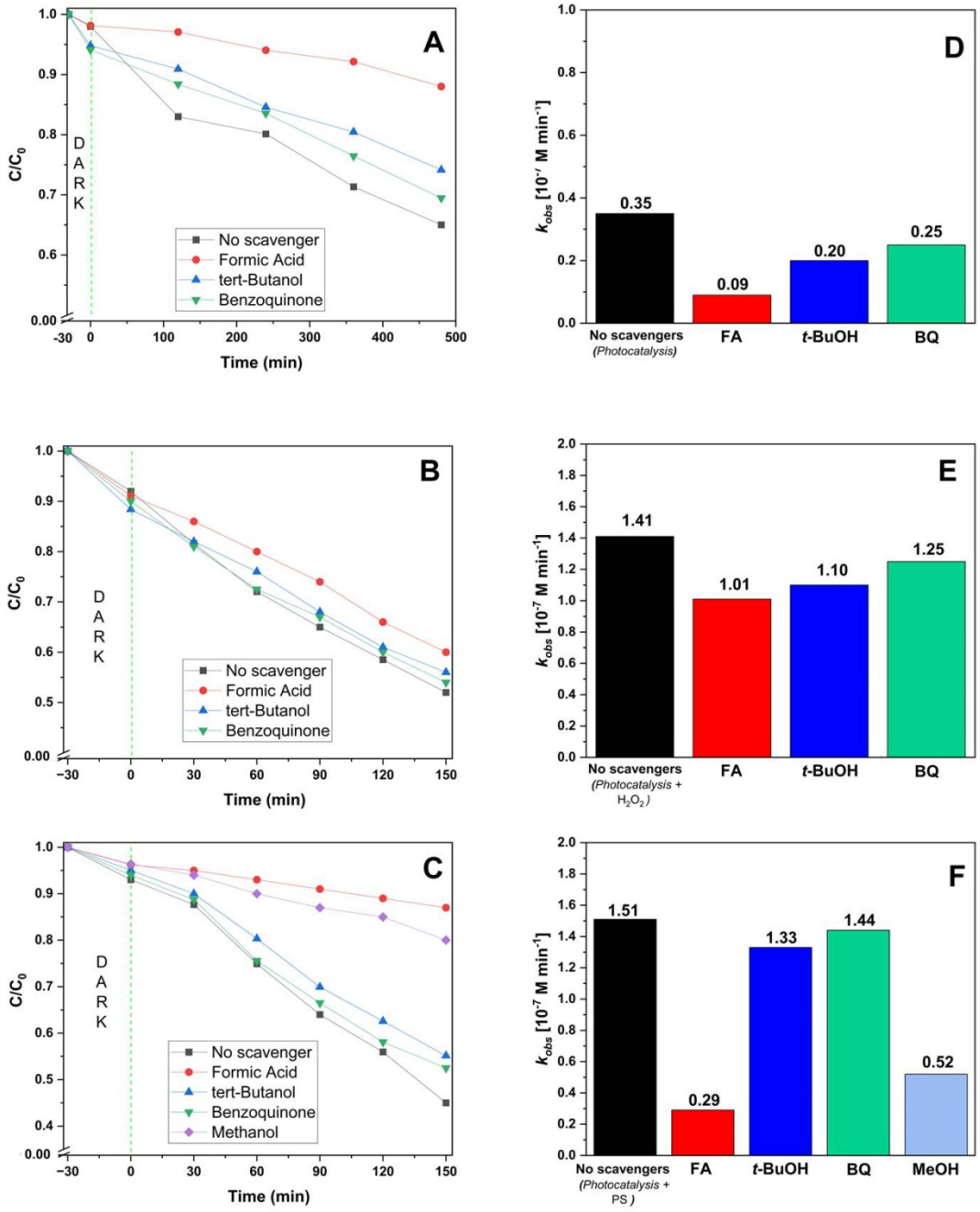

Figure 50. AMX conversion under photocatalysis (**A**), photocatalysis + H_2O_2 (**B**), photocatalysis + PS (**C**) in presence of scavengers and; (**D**-**F**) corresponding zero-order rate constants for each process. (Experimental conditions: [AMX] = 0.050 mM; initial pH = 4.808; [PS]=[H_2O_2]= 1.873 mM; [FA]= [MeOH]=[*t*-BuOH]= 5 mM; [BQ]= 0.5 mM; catalyst = immobilized 5% (*w/w*) Fe_2O_3/TiO_2

AMX conversion and kinetic profiles achieved by photocatalysis in the presence of ROS scavengers are shown in **Figure 50A and 50D**, respectively. The highest inhibition of AMX conversion occurred in presence of FA, resulting in only 12% of AMX degradation (compared to 35% obtained in the absence of any scavenger). This indicated that photogenerated h^+ plays the main role in AMX photocatalytic conversion. Similarly, Zhu et al. reported that Fe_2O_3-TiO_2/fly-ash-cenosphere composite's main active species for degradation of methylene blue are also photogenerated h^+ [239]. Besides, it was observed that AMX conversion was reduced to 31% and 26% in the presence of BQ and *t*-BuOH, respectively. Such results indicated that HO• play a more significant role than $O_2^{\bullet-}$. Hence, the order of ROS in decreasing contribution under photocatalysis process is the following: h^+ > HO• > $O_2^{\bullet-}$.

AMX conversion and kinetic profiles achieved by photocatalysis + H_2O_2 in the presence of ROS scavengers are shown in **Figure 50B and 50E**, respectively. Highest inhibition of AMX conversion occurred in presence of FA, resulting with 8% reduction compared to the case without scavengers (40 and 48% of AMX degradation, respectively). This indicates that photogenerated h^+ plays a major role in AMX conversion. Similarly, Monteagudo et al. reported the dominant role of h^+ in solar-TiO_2/H_2O_2 system for degradation of aniline [182]. AMX conversion in presence of *t*-BuOH was reduced to 44%. It is important to note that even h^+ plays the major role, $HO^{\bullet}$ contribution is nearly the same as shown in comparison of their rate constants (**Figure 50B**). Lastly, the presence of BQ reduces AMX conversion only to 46%, showing that superoxide radical has a minor role in the overall process. Hence, the order of ROS in decreasing contribution in photocatalysis + H_2O_2 process is the following: $h^+ \geq$ HO• > $O_2^{\bullet-}$.

AMX conversion and kinetic profiles achieved with photocatalysis + PS in the presence of ROS scavengers are showed in **Figure 50C and 50F**, respectively. FA promotes the greatest inhibition among all scavengers used yielding AMX conversion of only 13% (compared to 55 % in the case with no scavenger), implying that photogenerated h^+ plays a major role in AMX conversion. Similar results were obtained upon performing persulfate-activation related processes such as solar/TiO_2/$S_2O_8^{2-}$ [182], solar-TiO_2@Fe_2O_3/PS [9] and vis-TiO_2/FeOCl/PS [184], which all reported that photogenerated h^+ is the main oxidative species. On the other hand, AMX conversion was reduced to 20% and 45%, in presence of MeOH and *t*-BuOH, respectively. Accordingly, $SO_4^{\bullet-}$ plays more significant role than $HO^{\bullet}$, as expected due to acidic conditions applied. Presence of BQ resulted with rather low inhibition, up to 47.5% of AMX degraded, suggesting that $O_2^{\bullet-}$ contributes only with a minor

role. Therefore, the overall order of ROS in decreasing contribution by photocatalysis + PS is the following: $h^+ > SO_4^{\bullet-} > HO\bullet > O_2^{\bullet-}$.

The combined mechanism depiction of the three photocatalytic systems is shown in **Figure 51**. Conventionally, combination of TiO_2 and Fe_2O_3 leads to formation of *Type 1 heterojunction* [5], where the valence band(VB) and conduction band (CB) of Fe_2O_3 are in between the VB and CB of TiO_2, (**Figure 51**, *Before Contact*). However, such heterojunction formation is unfavorable for effective separation of photogenerated charges (e^-/h^+) due to the migration-accumulation to Fe_2O_3. Xia et al. [234], Liu et al. [235], and Mei et al.[223] proposed that in order to achieve greater charge separation between Fe_2O_3 and TiO_2, the fermi level of each semiconductor must be equalized. Thereafter, photogenerated electrons can now flow from CB of Fe_2O_3 to CB of TiO_2 under visible light irradiation (**Figure 52**, *After Contact*). Additionally, photogenerated e^- can react to O_2, H_2O_2 and $S_2O_8^{2-}$ yielding $O_2^{\bullet-}$, HO• and $SO_4^{\bullet-}$, respectively, while photogenerated holes reacts directly to AMX and HO^- forming HO•.

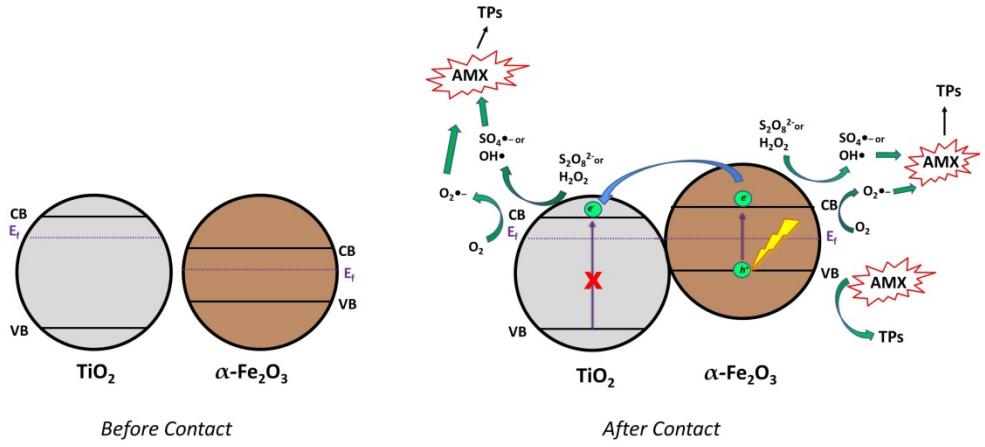

Figure 51. Proposed charge transfer mechanism between Fe_2O_3 and TiO_2 heterojunction before and after contact, under visible light irradiation

4.2.4 AMX Transformation Byproducts and Toxicity Evaluation

The transformation products (TPs) of AMX in photocatalysis, photocatalysis + H_2O_2, and photocatalysis + PS systems were investigated and identified using LC-HRMS-Orbitrap in positive and negative modes. The TPs detected and their corresponding mass spectra are presented in ***Table S5 and Figures S9-S16***, Appendix, respectively. Annotated Δmass (error)

between experimental mass-to-charge ratio (*m/z*) and theoretical values (*m/z*) of all proposed chemical formula are less than ± 2 ppm and with FISh coverage score ≥ 43.50, which allows accuracy in the assignment of elemental composition and fragment ion elucidation, respectively. It must be noted that only results from positive modes are elucidated, since all results from negative modes showed FISh coverage score ≤ 40 %. As shown in **Figure 52**, three TPs (TP 384 (H1), TP 384 (H2) and TP 366) were detected in all processes studied. TP 384 (H1) and TP 384 (H2) correspond to penicilloic acid ($C_{16}H_{21}N_3O_6S$) (a.k.a. hydrolysis by-product of AMX), which were formed by the reaction of H_2O molecule to the strained four-membered *β*-lactam ring of AMX [188,189]. TP 366 corresponds to amoxicillin 2',5'-diketopiperazine ($C_{16}H_{19}N_3O_5S$), which is formed via loss of H_2O and then further condensation of TP 384 (H1) or TP 384 (H2) [240].

TP 367 was detected in both photocatalysis and photocatalysis + H_2O_2 treatments, and is attributed to two-step successive transformation (i.e., 1. oxidative deamination, and 2. reduction to alcohol) of AMX (**Figure S17**). Oxidative deamination by-products formation of *β*-lactam derivatives were ascribed to the abstraction of α-hydrogen atoms leading to the formation of a carbonyl derivative [241]. In such a case, >CH-NH_2 moiety of AMX could be transformed to imine moiety >CH=NH, and then further cleavage of carbon-nitrogen double bond occurs, yielding C=O moiety, TP (*m/z*) = 365. However, it must be noted that the intermediate TP (*m/z*)=365 was not detected in any of the photocatalytic processes studied since its carbonyl moiety was further reduced to alcohol, forming the detected derivative, TP 367. The involved reduction reaction may be attributed to photocatalytic hydrogenation of TP 365 with the assistance of AMX as "self" hydrogen donor (H^+) and sacrificial agent. Similarly, Wei et al. reported simultaneous hydrogen production and degradation of AMX using Bi spheres-g-C_3N_4 [242] and MoS_2@$Zn_xCd_{1-x}S$ [243], supporting the assumption that persistent organic pollutants can be used as sacrificial electron donors. Conventionally, low C-atom alcohols (i.e. methanol, ethanol, isopropanol, triethanolamine etc.) and low C-atom carboxylic acids (i.e. lactic acid) are used as sacrificial electron donor for photocatalytic hydrogenation and H_2 production [5,244]. In this case, it can be assumed that AMX and its by-products (i.e., low C-atom species) mimic the role of lower C-atom alcohols in photocatalytic hydrogenation/hydrogen forming reactions.

Three oxidation TPs (TP 382 (S-O), TP 382 (E1) and TP 382 (E2)) were detected in both photocatalysis + H_2O_2 and photocatalysis + PS treatment processes. Accordingly, TP 382 (S-O) was formed via attack of $SO_4^{\bullet-}$ and/or HO• to the sulfur atom of thioether moeity by electron transfer mechanism and was confirmed by molecular orbital calculations [188].

TP 382 (E1) and TP 382 (E2) are ascribed to monohydroxylation of AMX. AMX reaction centers that are susceptible to HO• attack are illustrated in **Figure 52**. Based on MS2 results, hydroxylation on the methyl (C_{3a} and C_{3b}) and aromatic ring ($C_{11\text{-}14}$), are all ruled out due to detection of fragments (*m/z*) 131.01610, and 107.04916, respectively (**Figure S10.1**). Moreover, the fragment proposed by Trovo et al. $C_7H_{13}N_2O_3S$ (*m/z* =189.0686) and other related fragments [189], which accounts for hydroxylation in N_8 position (**Figure 52**) are not detected in this study. Instead, (*m/z* = 189.06583) fragment was detected, which accounts to $C_{10}H_9N_2O_2$ as proposed by Compound Discoverer^{TM} (**Figure S10.1**). Both $SO_4^{\bullet-}$ and HO• are expected to attack the sulfur atom of AMX to generate sulfur centered radical cation via electron transfer mechanism [188]. Thereafter, this radical cation can be deprotonated to generate α-thioether radical, which are susceptible for hydroxylation (**Figure 53**). As such, TP 382 (E1) and TP 382 (E2) are proposed since hydroxylation can occur on the positive/negative lobe of the α-thioether radical's vacant p-orbital [245].

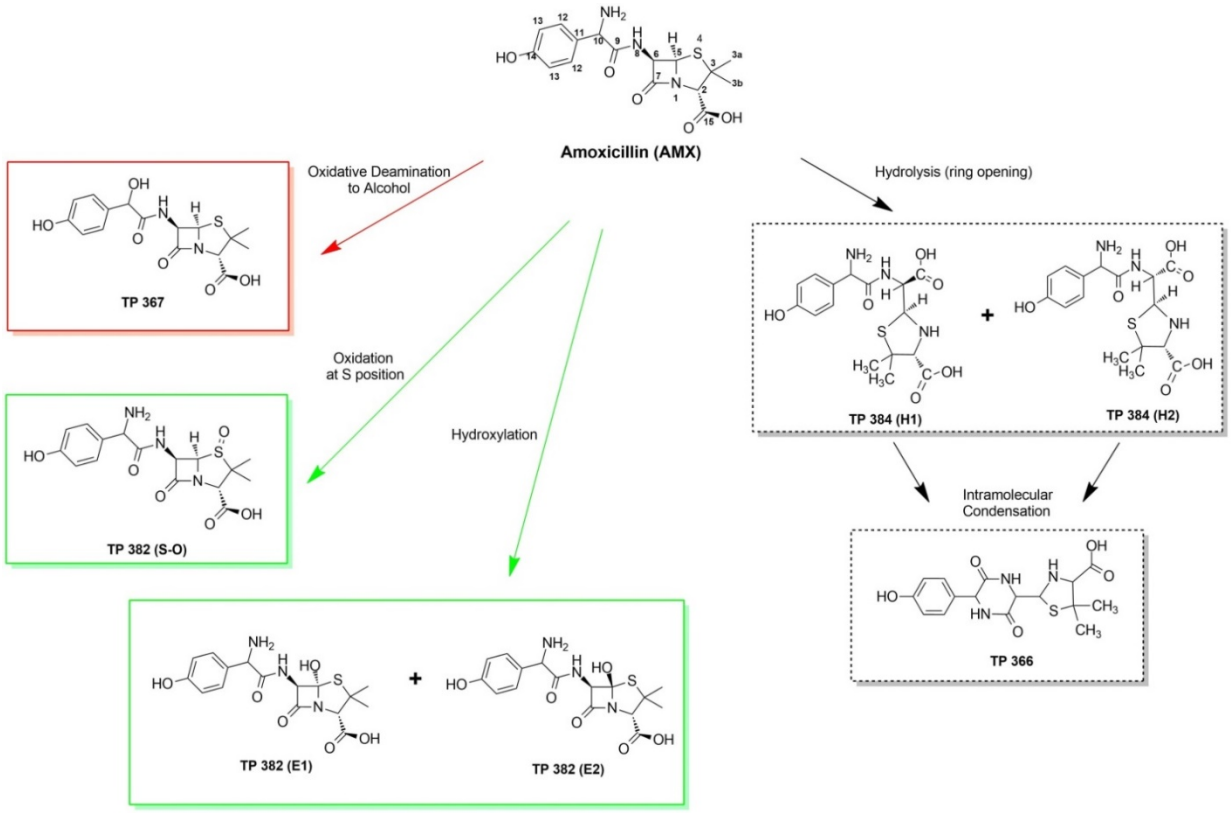

Figure 52. Proposed transformation by-products of AMX under different photocatalytic treatment processes. Black boxes indicated transformation by-products obtained in all processes; red boxes indicated transformation products obtained under photocatalysis and photocatalysis + H_2O_2; green boxes indicated transformation by-products obtained under photocatalysis + H_2O_2 and photocatalysis+ persulfate and (*m/z*) were expressed as $[M+H]^+$ and results are obtained from LC-MS-Orbitrap)

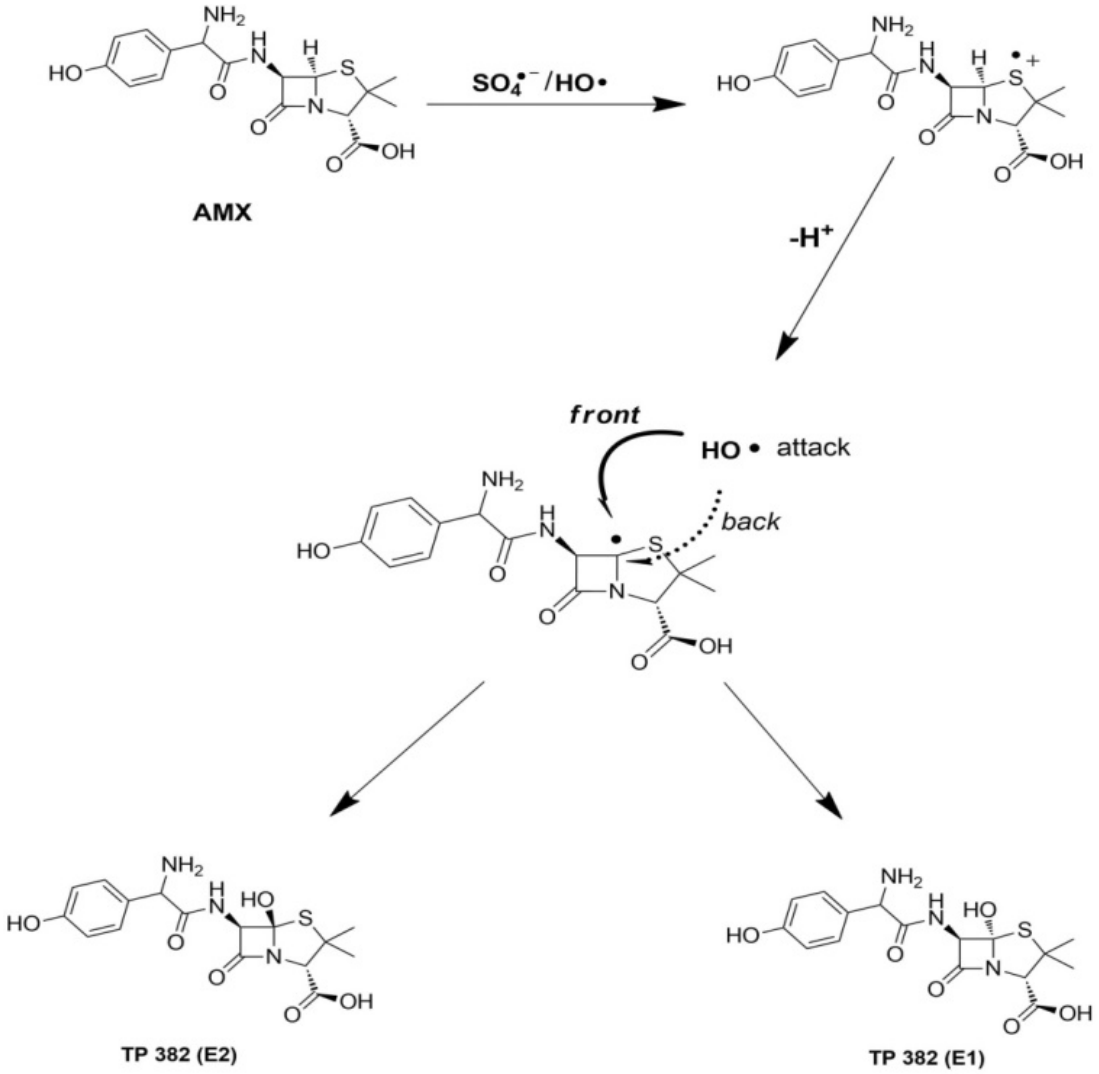

Figure 53. Proposed mechanism for the formation of TP 382 (E1 and E2)

Evolution and conversion profiles of TPs obtained from three different photocatalytic processes are presented in **Figure 54-56** respectively. As can be seen in **Figure 54A** (photocatalysis), four by-products are detected; TP 366, TP367, and the hydrolysis by-products TP 384 (H1) and (H2). As compared to process toxicity profile (**Figure 54B**), it can observed that the sample reached the maximum 4.15 toxicity units (more toxic than initial level) at 25% AMX conversion. This result can be ascribed to TP 366 evolution which also reached its maximum area at the same point (i.e. 25% AMX conversion). Namely, TP 366 is amoxicillin 2',5'-diketopiperazine, a known by-product of AMX, which is already detected in Israel water effluents [240] and Spain river water samples [34]. Nevertheless, it must be noted that toxicity units dropped to 1.12 after reaching 50% AMX conversion which coincides with the decrease in TP 366 concentration as well. Although TP 384 (H2) is the

dominant by-product in photocatalysis process, it showed minor contribution to the overall toxicity. TP 367 also showed minor contribution to overall toxicity, despite increasing formation (between 50-99% AMX conversions extents). Clearly, the spike up in toxicity units is directly linked to TP 366 formation.

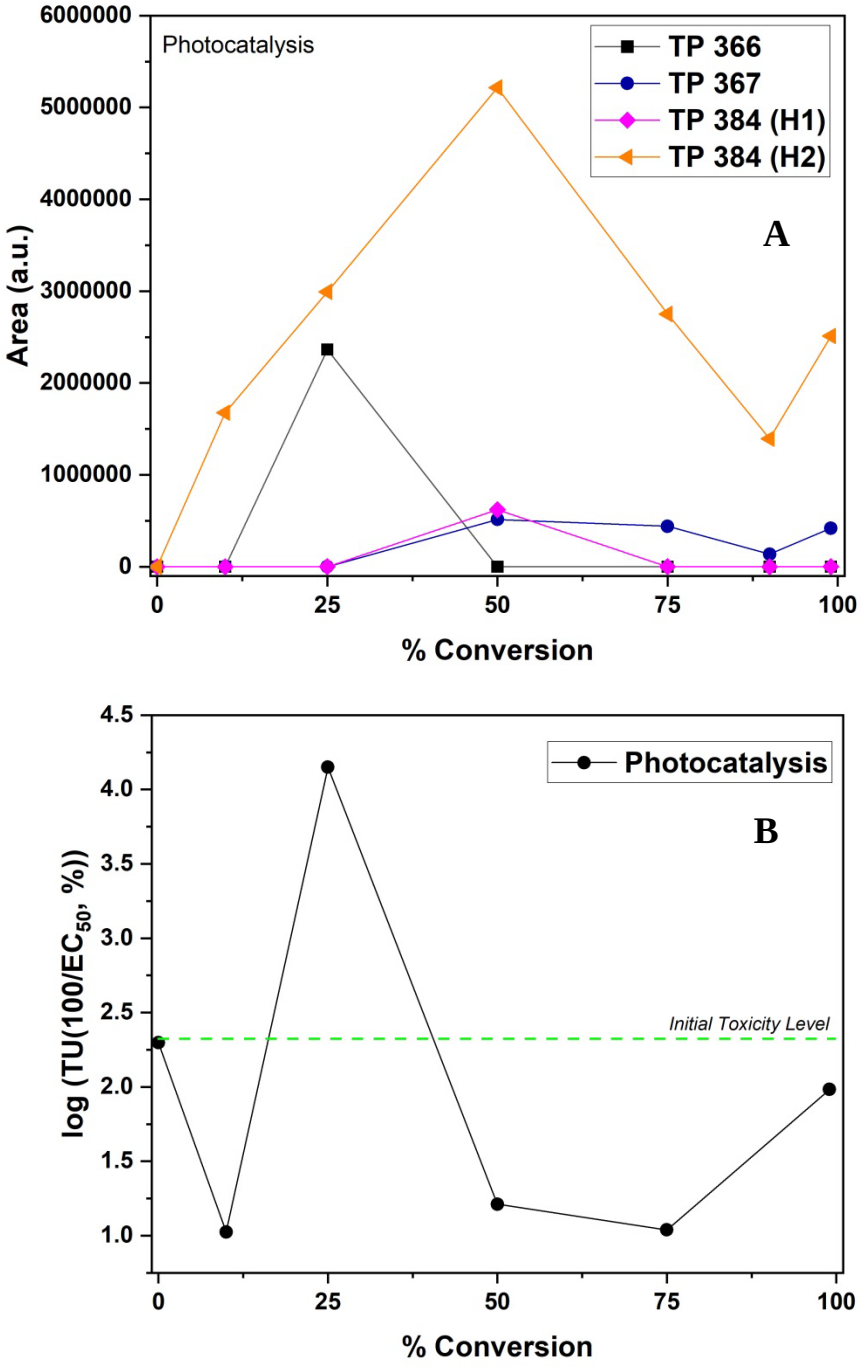

Figure 54. Evolution and conversion of identified AMX transformation by-products for photocatalysis (**A**), photocatalysis and corresponding toxicity towards *V. fischeri* (**B**); catalyst = immobilized 5% (*w/w*) Fe_2O_3/TiO_2

As shown in **Figure 55A** (photocatalysis+ H_2O_2), seven by-products are detected; TP 366, TP 367, TP 382 (E1 and E2), TP 382 (S-O) and TP 384 (H1 and H2).

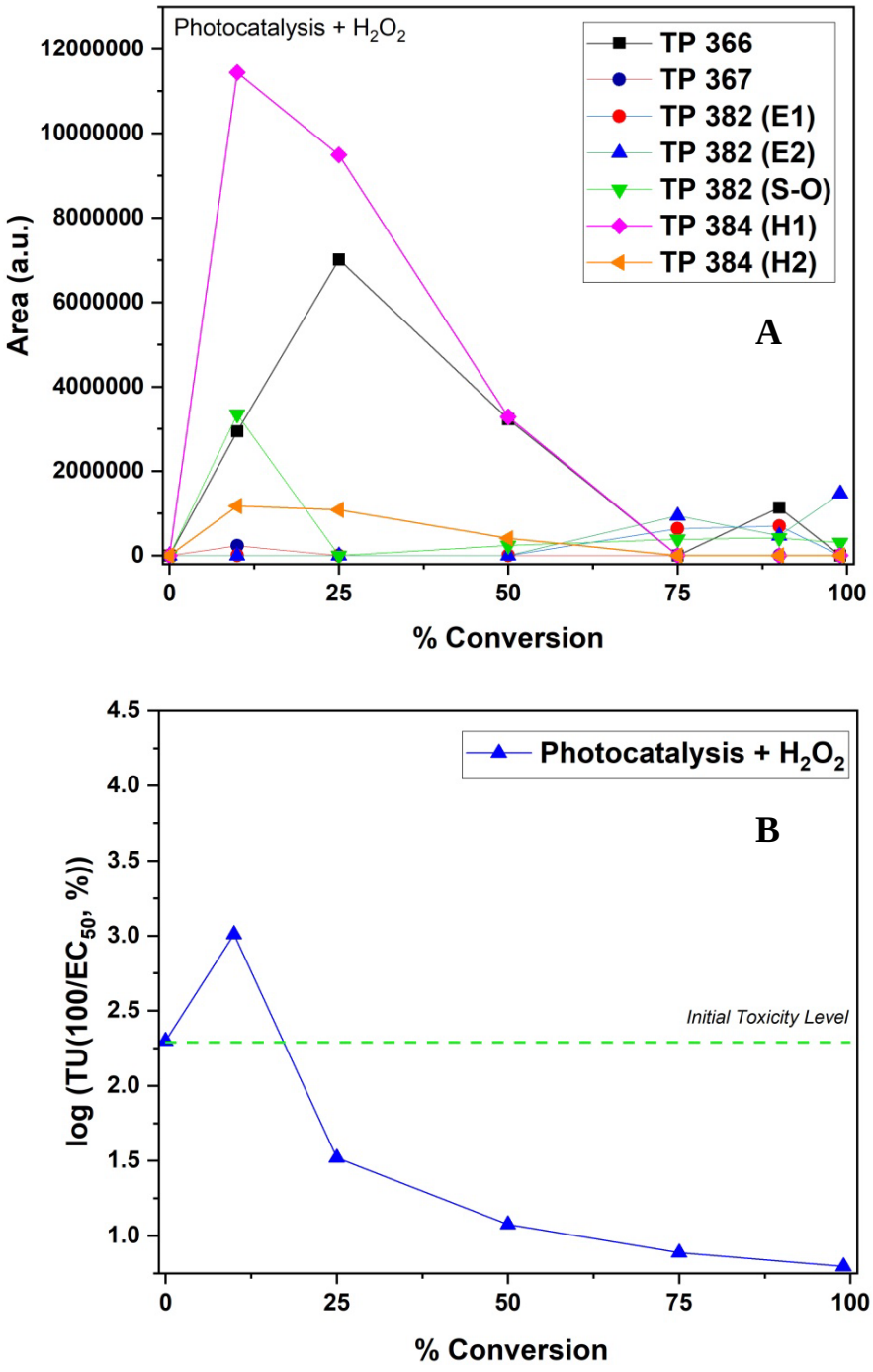

Figure 55. Evolution and conversion of identified AMX transformation by-products for photocatalysis (**A**), photocatalysis + H_2O_2 and corresponding toxicity towards *V. fischeri* (**B**); catalyst = immobilized 5% (*w*/*w*) Fe_2O_3/TiO_2

As compared to process toxicity profile (**Figure 55B**), it can observed that the sample reached the maximum of 3.01 toxicity units (more toxic than initial level), at 10% AMX conversion.

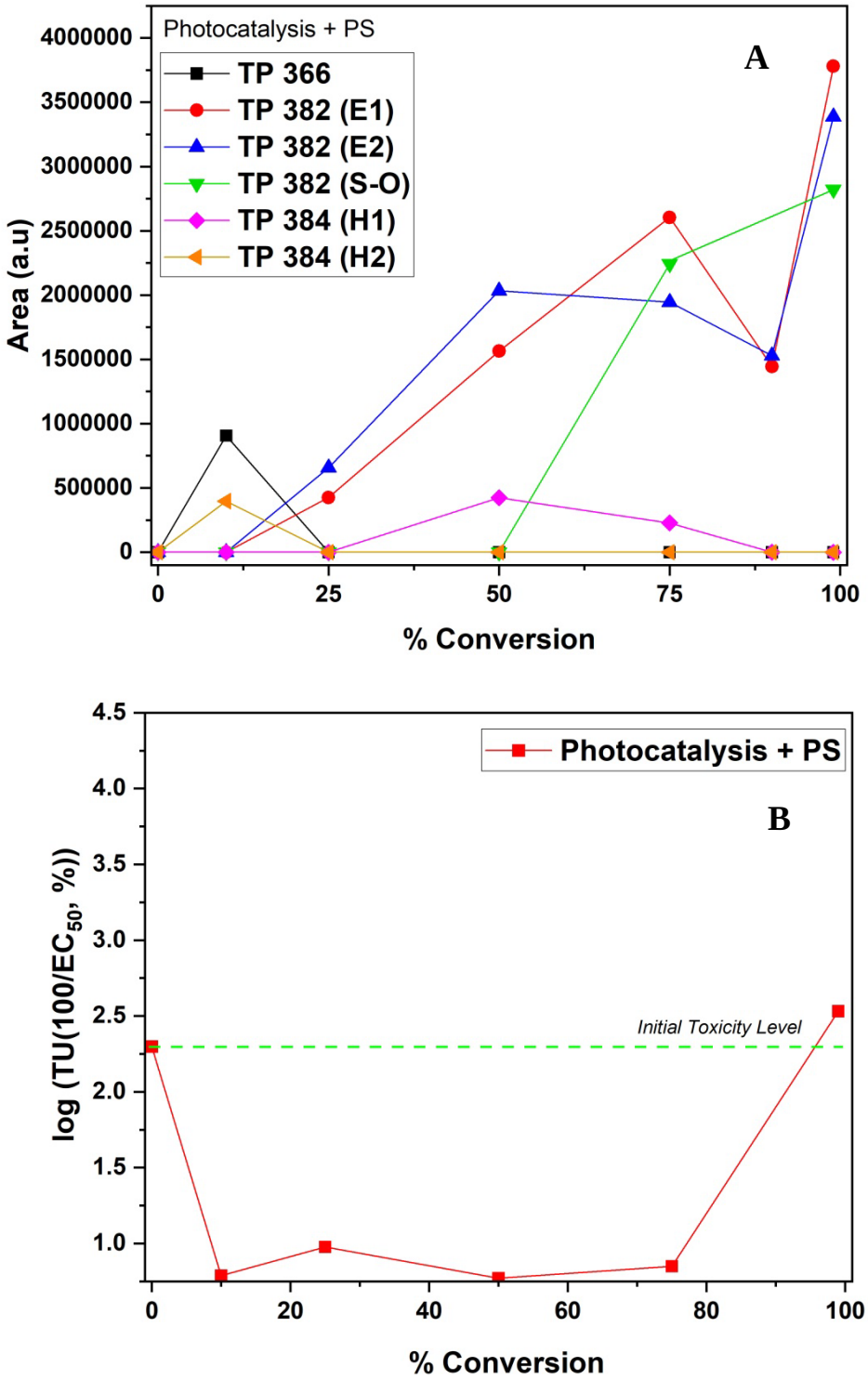

Figure 56. Evolution and conversion of identified AMX transformation by-products for photocatalysis (**A**), photocatalysis + PS and corresponding toxicity towards *V.fischeri* (**B**); catalyst = immobilized 5% (*w/w*) Fe_2O_3/TiO_2

This result can be ascribed to combined toxicity of TP 382 (S-O) with TP 366 and TP 384 (H1). It must be noted that TP 382 (S-O) also reached its maximum area at the same point (i.e. 10% AMX conversion). As reported in literature, TP 382 (S-O) was found to be a contributor to the overall toxicity of persulfate-treated AMX aqueous solution[9]. Accordingly, toxicity units dropped down to 1.52 upon reaching 25% AMX conversion, which coincides with the decrease in TP 382 (S-O) concentration. The maximum of TP 366 was reached at 50% of AMX conversion, exhibiting no abrupt effect on the toxicity of the sample. Such results may be ascribed to the "antagonistic" effect of other TPs, such as the presence TP 384 (H1), which may eventually result in the reduced toxicity of TP 366 [246].

In **Figure 56A** (photocatalysis + PS), six byproducts were detected: TP 366, TP 382 (E1) and (E2), TP 382 (S–O), and TP 384 (H1 and H2). As compared to the process toxicity profile (**Figure 56B**), it can be observed that the sample reached the maximum of 2.53 toxicity units (more toxic than initial level) at <99% AMX conversion. This result can be ascribed to the increased formation of TP 382 (E1) and (E2), as well as TP 382 (S–O), which also reached their maximum concentrations at the same point (i.e. <99% AMX conversion). All remaining TPs (i.e. TP 366, TP 367, and TP 384 (H1 and H2)) showed no synergistic and/or antagonistic effect on the overall toxicity.

4.2.5 Stability Test

Stability tests were performed for three consecutive cycles using the immobilized 5% (*w/w*) Fe_2O_3/TiO_2 photocatalyst with the optimum conditions obtained in section 4.2.2. As shown in **Figure 57**, AMX conversion of <99% was achieved in three consecutive cycles of photocatalytic experiments containing PS and H_2O_2. However, 95% and 85% AMX conversions were achieved in the second and third cycles, respectively, of the sole photocatalysis process. The loss of activity of the immobilized photocatalyst during photocatalysis (*without oxidant*) in consecutive cycles was mainly due to overexposure (3900 min/cycle) compared to other processes containing PS and H_2O_2 (380 and 720 min/cycle, respectively).

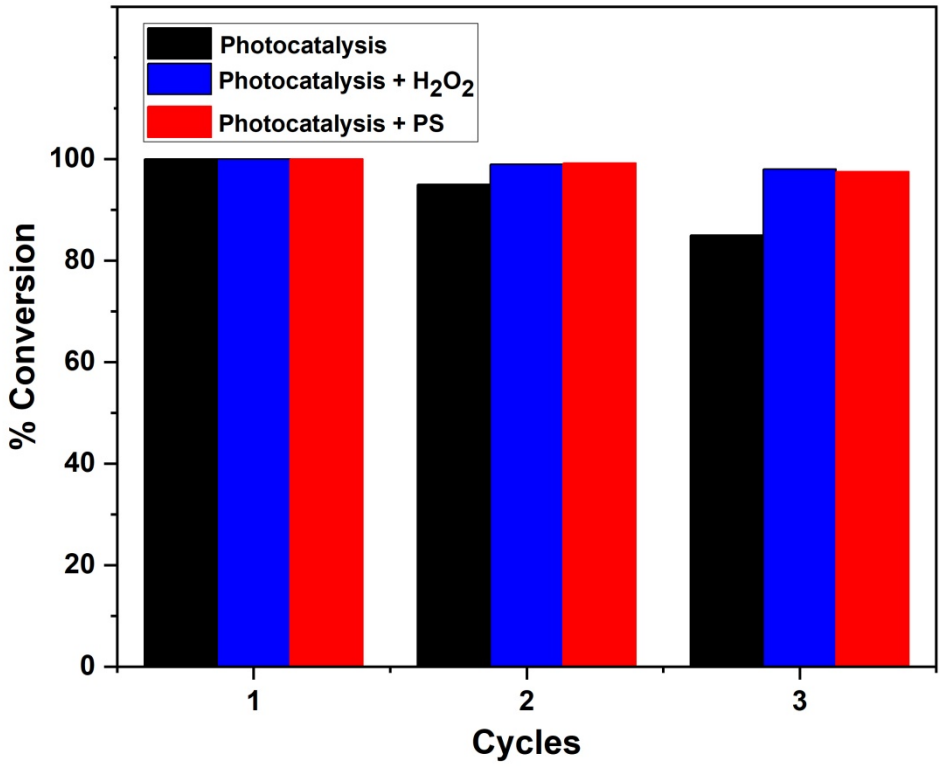

Figure 57. %AMX conversion by photocatalysis, photocatalysis +H_2O_2 and photocatalysis + PS during three consecutive cycles. (Experimental conditions: [AMX] = 0.050 mM; initial pH =4.808; [PS] = [H_2O_2] = 1.873 mM; reaction time: photocatalysis (3900 min·cycle^{-1}); photocatalysis + H_2O_2 (720 min·cycle^{-1}); photocatalysis + PS (380 min·cycle^{-1});
catalyst = immobilized 5% (*w/w*) Fe_2O_3/TiO_2

4.3 Comparison of solar and visible light activated processes

The process solar-TiO_2@Fe_2O_3/PS (as described in section 4.1) showed superior performance in terms of AMX removal compared to the processes described in section 4.2 (i.e., vis-(5% (*w/w*) Fe_2O_3/TiO_2, vis-(5% (*w/w*) $Fe_2O_3/TiO_2/H_2O_2$ and vis-(5% (*w/w*) Fe_2O_3/TiO_2/PS) as shown in **Table 19**. This superior performance is mainly due to the ability of TiO_2 to be activated during solar irradiation. Moreover, it worthy to mention that the overall toxicity of the treated water containing AMX is less toxic compared to its original state, under solar-TiO_2@Fe_2O_3/PS process. Nevertheless, it must be noted that TiO_2@Fe_2O_3 exhibits poor performance in visible light (**Figure 39**), which is attributed for inactivity of TiO_2 in visible light irradiation.

On the other hand, 5% (*w/w*) Fe_2O_3/TiO_2 showed improved photocatalytic activity compared to TiO_2 (**Figure 47**) under visible light irradiation. The improved activity is mainly due to the exposed Fe_2O_3 in the composite and to the heterojunction formation. Meanwhile, it is noteworthy to mention that 5% (*w/w*) Fe_2O_3/TiO_2 showed less photocatalytic activity compared to TiO_2 under solar light (**Figure S5.1**). In a similar study, Li.et al. [230] results showed that TiO_2 have superior photocatalytic activity over prepared Fe_2O_3/TiO_2 when photodegrading oxytetracycline under UV light. Nevertheless, it must be noted that most of the reported literature for Fe_2O_3/TiO_2 suggest that incorporation of Fe_2O_3 into TiO_2 promotes solar activity [231]. As such, it is critically implied that synthetic technique on the prepared Fe_2O_3/TiO_2 composite plays a crucial role in the overall activity. Meanwhile, vis-(5% (*w/w*) $Fe_2O_3/TiO_2/H_2O_2$ and vis-(5% (*w/w*) Fe_2O_3/TiO_2/PS, showed superior performance compared to vis-(5% (*w/w*) Fe_2O_3/TiO_2-without oxidant, which results account mainly to the presence of oxidants.

Table 19. Comparison of photocatalytic processes in this dissertation

Process	**Rate Constant, $\times10^{-7}$ ($M\cdot min^{-1}$)**	**AMX Removal (%)**	**Removal time (min)**
solar-TiO_2@Fe_2O_3/PS	7.40	<99	120
vis-Fe_2O_3/TiO_2	0.35	<99	3900
vis-$Fe_2O_3/TiO_2/H_2O_2$	1.41	<99	720
vis-Fe_2O_3/TiO_2/PS	1.51	<99	380

5. CONCLUSIONS

The sandwich-type composites made of commercial TiO_2-P25 and α-Fe_2O_3 with different layer configurations were successfully prepared by spin coating, and thereafter tested for photocatalytic activity in the presence and absence of PS under simulated solar irradiation using pharmaceutical AMX as targeted CECs.

SEM analysis showed that prepared layers within sandwich-type composites are rather thin (1.06±0.20 μm), while DRS analysis revealed the semi-transparence of the top layer enabling simultaneous photo-activation of both top and bottom layers. Such property is shown to be beneficial particularly for the activity of TiO_2@Fe_2O_3 composite, particularly in the presence of PS. Namely, TiO_2@Fe_2O_3 showed superior activity under simulated solar irradiation and PS presence among all studied composite combinations and their pure components. Such marked improvement of photocatalytic activity was due to the successful suppression of the recombination of photogenerated charges (e^-/h^+) within TiO_2 by allowing inter-sandwich layer migration of photogenerated e^- towards α-Fe_2O_3. Additionally, as revealed by DFT calculations, LUMO of PS is able to accept photogenerated e^- from TiO_2, which then led to the generation of SO_4•$^-$, yielding the improved AMX degradation. RSM modeling demonstrated that acidic conditions are favorable for AMX degradation by solar-TiO_2@Fe_2O_3/PS process. The experiments using common ROS scavengers showed that AMX degradation was mainly driven over SO_4•$^-$ and HO•, clearly emphasizing the important role of photogenerated h^+ as a result of effective suppression of charge recombination, yielding enhanced ROS generation at both h^+ and e^-. Biodegradability of AMX solution was significantly improved, while the changes observed during the treatment can be correlated mostly with mineralization kinetics, that is, decrease in overall organic content by progressed mineralization of benzene moiety of AMX molecule via hydroxylation pathway similar to that of phenolic compounds. Toxicity changes of AMX solution during solar-TiO_2@Fe_2O_3/PS treatment are correlated with (poly)-hydroxylated by-products evolution/degradation; their disappearance from the system yielded a significant toxicity decrease of treated solution.

Fe_2O_3/TiO_2 nanocomposites were successfully prepared using an impregnation/calcination technique of TiO_2-P25 and $Fe(NO_3)_3 \cdot 9H_2O$. XRD and RS analyses revealed that the obtained iron oxide was hematite, α-Fe_2O_3. Moreover, XRD, RS, XPS, and SEM/EDXS showed successful incorporation of α-Fe_2O_3 with TiO_2. DRS results showed improved visible-light absorption and a decrease in overall bandgap values of Fe_2O_3/TiO_2 nanocomposites upon increasing α-Fe_2O_3 content. Electrochemical experiments (EIS and photocurrent responses) revealed improved charge separation (e^-/h^+) of the

obtained nanocomposite compared to its individual components (i.e., TiO_2 and α-Fe_2O_3). Specifically, 5% (*w/w*) Fe_2O_3/TiO_2 showed the highest photocatalytic activity based on preliminary photocatalytic experiments, as well as on the PL spectroscopy results. The results obtained from RSM modeling showed optimum conditions of [PS] = 1.873 mM and pH 4.808. Photocatalysis + PS achieved fastest AMX conversion, possessing a higher zero-order rate constant ($k = 1.51 \times 10^{-7}$ M·min^{-1}) compared to photocatalysis + H_2O_2 ($k = 1.41 \times 10^{-7}$ M·min^{-1}) and photocatalysis only ($k = 0.35 \times 10^{-7}$ M·min^{-1}). ROS scavenging showed that photogenerated h^+ played the major role for AMX conversion in all processes. Toxicity changes of AMX solution were associated with TP 366 during photocatalysis, TP 382 (S–O) during photocatalysis + H_2O_2, and hydroxylated TPs (i.e., TP 382 (S–O) and TP 382 (E1 and E2)) during photocatalysis + PS. It is important to note that these AMX TPs greatly affected the toxicity of AMX solution during treatment in general.

Overall, removal of AMX was superior by using $TiO_2@Fe_2O_3$ under solar irradiation over the as-prepared Fe_2O_3/TiO_2 under visible light irradiation (via impregnation-calcination). Different synthetic techniques must be focused in order to improve Fe_2O_3/TiO_2 photocatalytic activity over solar and visible light irradiation. A careful monitoring of TPs must be made specifically when using photocatalysis in water treatment processes.

6. REFERENCES

1. Chong, M.N.; Jin, B.; Chow, C.W.K.; Saint, C. Recent developments in photocatalytic water treatment technology: A review. *Water Res.* **2010**, *44*, 2997–3027.
2. Pichat, P. *Photocatalysis and Water Purification: From Fundamentals to Recent Applications*; Wiley Berlin Germany, **2013**;
3. Schneider, J.; Matsuoka, M.; Takeuchi, M.; Zhang, J.; Horiuchi, Y.; Anpo, M.; Bahnemann, D.W. Understanding TiO_2 photocatalysis: Mechanisms and materials. *Chem. Rev.* **2014**, *114*, 9919–9986.
4. Pelaez, M.; Nolan, N.T.; Pillai, S.C.; Seery, M.K.; Falaras, P.; Kontos, A.G.; Dunlop, P.S.M.; Hamilton, J.W.J.; Byrne, J.A.; O'Shea, K.; et al. A review on the visible light active titanium dioxide photocatalysts for environmental applications. *Appl. Catal. B Environ.* **2012**, *125*, 331–349.
5. Perović, K.; dela Rosa, F.M.; Kovačić, M.; Kušić, H.; Štangar, U.L.; Fresno, F.; Dionysiou, D.D.; Bozic, A.L. Recent achievements in development of TiO_2-based composite photocatalytic materials for solar driven water purification and water splitting. *Materials (Basel).* **2020**, *13*.
6. Li, J.; Chu, D. *Energy band engineering of metal oxide for enhanced visible light absorption*; Elsevier Ltd., **2018**; ISBN 9780081019788.
7. Lanzl, C.A.; Baltrusaitis, J.; Cwiertny, D.M. Dissolution of hematite nanoparticle aggregates: Influence of primary particle size, dissolution mechanism, and solution pH. *Langmuir* **2012**, *28*, 15797–15808.
8. Fawzi Suleiman Khasawneh, O.; Palaniandy, P. Removal of organic pollutants from water by Fe_2O_3/TiO_2 based photocatalytic degradation: A review. *Environ. Technol. Innov.* **2021**, *21*, 101230.
9. dela Rosa, F.M.; Papac, J.; Garcia-Ballesteros, S.; Kovačić, M.; Katančić, Z.; Kušić, H.; Božić, A.L. Solar Light Activation of Persulfate by TiO_2/Fe_2O_3 Layered Composite Films for Degradation of Amoxicillin: Degradation Mechanism, Matrix Effects, and Toxicity Assessments. *Adv. Sustain. Syst.* **2021**, *2100119*.
10. García-Muñoz, P.; Zussblatt, N.P.; Pliego, G.; Zazo, J.A.; Fresno, F.; Chmelka, B.F.; Casas, J.A. Evaluation of photoassisted treatments for norfloxacin removal in water using mesoporous Fe_2O_3-TiO_2 materials. *J. Environ. Manage.* **2019**, *238*, 243–250.
11. Battula, V.R.; Jaryal, A.; Kailasam, K. Visible light-driven simultaneous H_2 production by water splitting coupled with selective oxidation of HMF to DFF catalyzed by porous carbon nitride. *J. Mater. Chem. A* **2019**, *7*, 5643–5649.
12. He, Y.; Qian, J.; Wang, P.; Wu, J.; Lu, B.; Tang, S.; Gao, P. Acceleration of levofloxacin degradation by combination of multiple free radicals via MoS_2 anchored in manganese ferrite doped perovskite activated PMS under visible light. *Chem. Eng. J.* **2022**, *431*, 133933.
13. Sakar, M.; Prakash, R.M.; Do, T.-O. Insights into the TiO_2-Based Photocatalytic Systems and Their Mechanisms. *Catalysts* **2019**, *9 (8)*, 680.
14. Herman, J.R.; Krotkov, N.; Celarier, E.; Larko, D.; Labow, G. Distribution from of UV radiation at the Earth ' s surface from TOMS-measure UV-backscattered radiances. *J. Geophys. Res.* **1999**, *104*, 12059-12076.
15. Li, G.; Nie, X.; Gao, Y.; An, T. Can environmental pharmaceuticals be photocatalytically degraded and completely mineralized in water using g-C_3N_4/TiO_2 under visible light irradiation?-Implications of persistent toxic intermediates. *Appl. Catal. B Environ.* **2016**, *180*, 726–732.
16. Kete, M.; Pavlica, E.; Fresno, F.; Bratina, G.; Štangar, U.L. Highly active photocatalytic coatings prepared by a low-temperature method. *Environ. Sci. Pollut. Res.* **2014**, *21*, 11238–11249.
17. Kovacic, M.; Kopcic, N.; Kusic, H.; Bozic, A.L. Solar driven degradation of 17β-estradiol using composite photocatalytic materials and artificial irradiation source: Influence of process and water matrix parameters. *J. Photochem. Photobiol. A Chem.* **2018**, *361*, 48–61.
18. Decision 2018/840 of 5 June 2018 establishing a watch list of substances for Union-wide monitoring in the field of water policy pursuant to Directive 2008/105/EC of the European Parliament and of the Council and repealing Comm. *Off. J. Eur. Union* **2018**, *L 141*, 9–12.
19. Decision 2020/1161/EU Commission Implementing Decision (EU) 2020/1161. *Off. J. Eur. Union* **2020**, *257*, 32–35.
20. https://www.oecd.org/g20/topics/energy-environment-green-growth/ (Accessed in April 1 2023)
21. Joseph Alcamo; Moreno, J.M.; Nováky, B.; Marco Bindi; Corobov, R.; Robert Devoy; Giannakopoulos, C.; Martin, E.; Olesen, J.E.; Shvidenko, A. 2007: Europe. *Clim. Chang. 2007 Impacts, Adapt. Vulnerability. Contrib. of Working Gr. II to Fourth Assess. Rep. Intergov. Panel Clim. Chang.* **2007**, 541–580.
22. Golovko, O.; Örn, S.; Sörengård, M.; Frieberg, K.; Nassazzi, W.; Lai, F.Y.; Ahrens, L. Occurrence and removal of chemicals of emerging concern in wastewater treatment plants and their impact on receiving water systems. *Sci. Total Environ.* **2021**, *754*, 142122.
23. Sörengård, M.; Campos-Pereira, H.; Ullberg, M.; Lai, F.Y.; Golovko, O.; Ahrens, L. Mass loads, source apportionment, and risk estimation of organic micropollutants from hospital and municipal wastewater in recipient catchments. *Chemosphere* **2019**, *234*, 931–941.

24. Luo, Y.; Guo, W.; Ngo, H.H.; Nghiem, L.D.; Hai, F.I.; Zhang, J.; Liang, S.; Wang, X.C. A review on the occurrence of micropollutants in the aquatic environment and their fate and removal during wastewater treatment. *Sci. Total Environ.* **2014**, *473–474*, 619–641.
25. Yang, Y.; Ok, Y.S.; Kim, K.H.; Kwon, E.E.; Tsang, Y.F. Occurrences and removal of pharmaceuticals and personal care products (PPCPs) in drinking water and water/sewage treatment plants: A review. *Sci. Total Environ.* **2017**, *596–597*, 303–320.
26. Blum, K.M.; Andersson, P.L.; Ahrens, L.; Wiberg, K.; Haglund, P. Persistence, mobility and bioavailability of emerging organic contaminants discharged from sewage treatment plants. *Sci. Total Environ.* **2018**, *612*, 1532–1542.
27. Salimi, M.; Esrafili, A.; Gholami, M.; Jonidi Jafari, A.; Rezaei Kalantary, R.; Farzadkia, M.; Kermani, M.; Sobhi, H.R. Contaminants of emerging concern: a review of new approach in AOP technologies. *Environ. Monit. Assess.* **2017**, *189*.
28. Aryee, A.A.; Han, R.; Qu, L. Occurrence, detection and removal of amoxicillin in wastewater: A review. *J. Clean. Prod.* **2022**, *368*, 133140.
29. Yazidi, A.; Atrous, M.; Edi Soetaredjo, F.; Sellaoui, L.; Ismadji, S.; Erto, A.; Bonilla-Petriciolet, A.; Luiz Dotto, G.; Ben Lamine, A. Adsorption of amoxicillin and tetracycline on activated carbon prepared from durian shell in single and binary systems: Experimental study and modeling analysis. *Chem. Eng. J.* **2020**, *379*.
30. Ighalo, J.O.; Igwegbe, C.A.; Aniagor, C.O.; Oba, S.N. A review of methods for the removal of penicillins from water. *J. Water Process Eng.* **2021**, *39*, 101886.
31. Amarasiri, M.; Sano, D.; Suzuki, S. Understanding human health risks caused by antibiotic resistant bacteria (ARB) and antibiotic resistance genes (ARG) in water environments: Current knowledge and questions to be answered. *Crit. Rev. Environ. Sci. Technol.* **2020**, *50*, 2016–2059.
32. Patel, M.; Kumar, R.; Kishor, K.; Mlsna, T.; Pittman, C.U.; Mohan, D. Pharmaceuticals of emerging concern in aquatic systems: Chemistry, occurrence, effects, and removal methods. *Chem. Rev.* **2019**, *119*, 3510–3673.
33. Tillement, J.P.; Tremblay, D. Clinical pharmacokinetic criteria for drug research. *Compr. Med. Chem. II* **2006**, *5*, 11–30.
34. Pérez-Parada, A.; Agüera, A.; Gómez-Ramos, M. del M.; García-Reyes, J.F.; Heinzen, H.; Fernández-Alba, A.R. Behavior of amoxicillin in wastewater and river water: identification of its main transformation products by liquid chromatography/electrospray quadrupole time-of-flight mass spectrometry. *Rapid Commun. Mass Spectrom.* **2011**, *25*, 731–742.
35. Sodhi, K.K.; Kumar, M.; Singh, D.K. Insight into the amoxicillin resistance, ecotoxicity, and remediation strategies. *J. Water Process Eng.* **2021**, *39*, 101858.
36. Elizalde-Velázquez, A.; Gómez-Oliván, L.M.; Galar-Martínez, M.; Islas-Flores, H.; Dublán-García, O.; SanJuan-Reyes, N. Amoxicillin in the Aquatic Environment, Its Fate and Environmental Risk. *Environ. Heal. Risk - Hazard. Factors to Living Species* **2016**.
37. Jia, J.; Guan, Y.; Cheng, M.; Chen, H.; He, J.; Wang, S.; Wang, Z. Occurrence and distribution of antibiotics and antibiotic resistance genes in Ba River, China. *Sci. Total Environ.* **2018**, *642*, 1136–1144.
38. Lu, S.; Lin, C.; Lei, K.; Wang, B.; Xin, M.; Gu, X.; Cao, Y.; Liu, X.; Ouyang, W.; He, M. Occurrence, spatiotemporal variation, and ecological risk of antibiotics in the water of the semi-enclosed urbanized Jiaozhou Bay in eastern China. *Water Res.* **2020**, *184*.
39. Velpandian, T.; Halder, N.; Nath, M.; Das, U.; Moksha, L.; Gowtham, L.; Batta, S.P. Un-segregated waste disposal: an alarming threat of antimicrobials in surface and ground water sources in Delhi. *Environ. Sci. Pollut. Res.* **2018**, *25*, 29518–29528.
40. Lamm, A.; Gozlan, I.; Rotstein, A.; Avisar, D. Detection of amoxicillin-diketopiperazine-2′, 5′ in wastewater samples. *J. Environ. Sci. Heal. Part A* **2009**, *44*, 1512–1517.
41. Kairigo, P.; Ngumba, E.; Sundberg, L.R.; Gachanja, A.; Tuhkanen, T. Occurrence of antibiotics and risk of antibiotic resistance evolution in selected Kenyan wastewaters, surface waters and sediments. *Sci. Total Environ.* **2020**, *720*, 137580.
42. https://www.coleparmer.com/tech-article/eight-stages-of-wastewater-treatment-process.
43. Gago-Ferrero, P.; Gros, M.; Ahrens, L.; Wiberg, K. Impact of on-site, small and large scale wastewater treatment facilities on levels and fate of pharmaceuticals, personal care products, artificial sweeteners, pesticides, and perfluoroalkyl substances in recipient waters. *Sci. Total Environ.* **2017**, *601–602*, 1289–1297.
44. Parsons, S. *Advanced Oxidation Processes for Water and Wastewater Treatment*; IWA Publishing: London , UK, 2005;
45. Gogate, P.R.; Pandit, A.B. A review of imperative technologies for wastewater treatment I: Oxidation technologies at ambient conditions. *Adv. Environ. Res.* **2004**, *8*, 501–551.
46. Goi, A.; Trapido, M. Comparison of Advanced Oxidation Processes for the Destruction of 2,4-

Dinitrophenol. *Proc. Est. Acad. Sci. Chem.* **2001**, *50*, 5.
47. Kajitvichyanukul, P.; Lu, M.C.; Liao, C.H.; Wirojanagud, W.; Koottatep, T. Degradation and detoxification of formaline wastewater by advanced oxidation processes. *J. Hazard. Mater.* **2006**, *135*, 337–343.
48. Mantzavinos, D.; Psillakis, E. Enhancement of biodegradability of industrial wastewaters by chemical oxidation pre-treatment. *J. Chem. Technol. Biotechnol.* **2004**, *79*, 431–454.
49. Carra, I.; Sánchez Pérez, J.A.; Malato, S.; Autin, O.; Jefferson, B.; Jarvis, P. Performance of different advanced oxidation processes for tertiary wastewater treatment to remove the pesticide acetamiprid. *J. Chem. Technol. Biotechnol.* **2016**, *91*, 72–81.
50. Agbaba, J.; Jazić, J.M.; Tubić, A.; Watson, M.; Maletić, S.; Isakovski, M.K.; Dalmacija, B. Oxidation of natural organic matter with processes involving O_3, H_2O_2 and UV light: Formation of oxidation and disinfection by-products. *RSC Adv.* **2016**, *6*, 86212–86219.
51. Kovacic, M.; Kusic, H.; Loncaric Bozic, A.; Dionysiou, D.D. Advanced Oxidation Processes. *Encycl. Water* **2019**, 1–15.
52. Tong, H.; Ouyang, S.; Bi, Y.; Umezawa, N.; Oshikiri, M.; Ye, J. Nano-photocatalytic materials: Possibilities and challenges. *Adv. Mater.* **2012**, *24*, 229–251.
53. Pasternak, S.; Paz, Y. On the similarity and dissimilarity between photocatalytic water splitting and photocatalytic degradation of pollutants. *ChemPhysChem* **2013**, *14*, 2059–2070.
54. Wang, H.; Zhang, L.; Chen, Z.; Hu, J.; Li, S.; Wang, Z.; Liu, J.; Wang, X. Semiconductor heterojunction photocatalysts: Design, construction, and photocatalytic performances. *Chem. Soc. Rev.* **2014**, *43*, 5234–5244.
55. Dambournet, D.; Belharouak, I.; Amine, K. Tailored preparation methods of TiO_2 anatase, rutile, brookite: Mechanism of formation and electrochemical properties. *Chem. Mater.* **2010**, *22*, 1173–1179.
56. Moniz, S.J.A.; Shevlin, S.A.; Martin, D.J.; Guo, Z.X.; Tang, J. Visible-light driven heterojunction photocatalysts for water splitting-a critical review. *Energy Environ. Sci.* **2015**, *8*, 731–759.
57. Moniz, S.J.A.; Shevlin, S.A.; An, X.; Guo, Z.X.; Tang, J. Fe_2O_3-TiO_2 nanocomposites for enhanced charge separation and photocatalytic activity. *Chem. - A Eur. J.* **2014**, *20*, 15571–15579.
58. Macías-Tamez, R.; Villanueva-Rodríguez, M.; Ramos-Delgado, N.A.; Maya-Treviño, L.; Hernández-Ramírez, A. Comparative Study of the Photocatalytic Degradation of the Herbicide 2,4-D Using WO_3/TiO_2 and Fe_2O_3/TiO_2 as Catalysts. *Water. Air. Soil Pollut.* **2017**, *228*.
59. Luo, L.; Long, J.; Zhao, S.; Dai, J.; Ma, L.; Wang, H.; Xia, L.; Shu, L.; Jiang, F. Effective visible-light-driven photocatalytic degradation of 17α-ethynylestradiol by crosslinked CdS nano-rod/TiO_2 (B) nano-belt composite. *Process Saf. Environ. Prot.* **2019**, *130*, 77–85.
60. Marschall, R. Semiconductor composites: Strategies for enhancing charge carrier separation to improve photocatalytic activity. *Adv. Funct. Mater.* **2014**, *24*, 2421–2440.
61. Kaur, A.; Salunke, D.B.; Umar, A.; Mehta, S.K.; Sinha, A.S.K.; Kansal, S.K. Visible light driven photocatalytic degradation of fluoroquinolone levofloxacin drug using Ag_2O/TiO_2 quantum dots: A mechanistic study and degradation pathway. *New J. Chem.* **2017**, *41*, 12079–12090.
62. Gou, J.; Ma, Q.; Deng, X.; Cui, Y.; Zhang, H.; Cheng, X.; Li, X.; Xie, M.; Cheng, Q. Fabrication of Ag_2O/TiO_2-Zeolite composite and its enhanced solar light photocatalytic performance and mechanism for degradation of norfloxacin. *Chem. Eng. J.* **2017**, *308*, 818–826.
63. Dong, P.; Hou, G.; Xi, X.; Shao, R.; Dong, F. WO_3-based photocatalysts: morphology control, activity enhancement and multifunctional applications. *Environ. Sci. Nano* **2017**, *4*, 539–557.
64. Mugunthan, E.; Saidutta, M.B.; Jagadeeshbabu, P.E. Visible light assisted photocatalytic degradation of diclofenac using TiO_2-WO_3 mixed oxide catalysts. *Environ. Nanotechnology, Monit. Manag.* **2018**, *10*, 322–330.
65. Cordero-García, A.; Turnes Palomino, G.; Hinojosa-Reyes, L.; Guzmán-Mar, J.L.; Maya-Teviño, L.; Hernández-Ramírez, A. Photocatalytic behaviour of WO_3/TiO_2-N for diclofenac degradation using simulated solar radiation as an activation source. *Environ. Sci. Pollut. Res.* **2017**, *24*, 4613–4624.
66. Cordero-García, A.; Guzmán-Mar, J.L.; Hinojosa-Reyes, L.; Ruiz-Ruiz, E.; Hernández-Ramírez, A. Effect of carbon doping on WO_3/TiO_2 coupled oxide and its photocatalytic activity on diclofenac degradation. *Ceram. Int.* **2016**, *42*, 9796–9803.
67. Pérez-Estrada, L.A.; Malato, S.; Gernjak, W.; Agüera, A.; Thurman, E.M.; Ferrer, I.; Fernández-Alba, A.R. Photo-fenton degradation of diclofenac: Identification of main intermediates and degradation pathway. *Environ. Sci. Technol.* **2005**, *39*, 8300–8306.
68. Salaeh, S.; Juretic Perisic, D.; Biosic, M.; Kusic, H.; Babic, S.; Lavrencic Stangar, U.; Dionysiou, D.D.; Loncaric Bozic, A. Diclofenac removal by simulated solar assisted photocatalysis using TiO_2-based zeolite catalyst; mechanisms, pathways and environmental aspects. *Chem. Eng. J.* **2016**, *304*, 289–302.
69. Arce-Sarria, A.; Machuca-Martínez, F.; Bustillo-Lecompte, C.; Hernández-Ramírez, A.; Colina-Márquez, J. Degradation and loss of antibacterial activity of commercial amoxicillin with TiO_2/WO_3-

assisted solar photocatalysis. *Catalysts* **2018**, *8*.
70. Arce-Sarria, A.; Machuca-Martínez, F.; Bustillo-Lecompte, C.; Hernández-Ramírez, A.; Colina-Márquez, J. Degradation and loss of antibacterial activity of commercial amoxicillin with TiO_3/WO_3-assisted solar photocatalysis. *Catalysts* **2018**, *8*, 1–14.
71. Mishra, M.; Chun, D.M. α-Fe_2O_3 as a photocatalytic material: A review. *Appl. Catal. A Gen.* **2015**, *498*, 126–141.
72. Mirmasoomi, S.R.; Mehdipour Ghazi, M.; Galedari, M. Photocatalytic degradation of diazinon under visible light using TiO_2/Fe_2O_3 nanocomposite synthesized by ultrasonic-assisted impregnation method. *Sep. Purif. Technol.* **2017**, *175*, 418–427.
73. Li, R.; Liu, J.; Jia, Y.; Zhen, Q. Photocatalytic degradation mechanism of oxytetracyclines using Fe_2O_3-TiO_2 nanopowders. *J. Nanosci. Nanotechnol.* **2017**, *17*, 3010–3015.
74. Li, R.; Jia, Y.; Wu, J.; Zhen, Q. Photocatalytic degradation and pathway of oxytetracycline in aqueous solution by Fe_2O_3-TiO_2 nanopowder. *RSC Adv.* **2015**, *5*, 40764–40771.
75. Lu, C.; Guan, W.; Zhang, G.; Ye, L.; Zhou, Y.; Zhang, X. TiO_2/Fe_2O_3/CNTs magnetic photocatalyst: A fast and convenient synthesis and visible-light-driven photocatalytic degradation of tetracycline. *Micro Nano Lett.* **2013**, *8*, 749–752.
76. Zheng, X.; Fu, W.; Kang, F.; Peng, H.; Wen, J. Enhanced photo-Fenton degradation of tetracycline using TiO_2-coated α-Fe_2O_3 core–shell heterojunction. *J. Ind. Eng. Chem.* **2018**, *68*, 14–23.
77. Pichat, P. *Photocatalysis and Water Purification:from Fundamentals to Recent Applications*; Wiley, Germany, **2013**;
78. Casbeer, E.; Sharma, V.K.; Li, X.Z. Synthesis and photocatalytic activity of ferrites under visible light: A review. *Sep. Purif. Technol.* **2012**, *87*, 1–14.
79. Garcia-Muñoz, P.; Fresno, F.; de la Peña O'Shea, V.A.; Keller, N. Ferrite Materials for Photoassisted Environmental and Solar Fuels Applications. *Top. Curr. Chem.* 2020, *378*.
80. Chen, Y.; Wu, Q.; Wang, J.; Song, Y. The fabrication of magnetic recyclable nitrogen-doped titanium dioxide/calcium ferrite/diatomite heterojunction nanocomposite for improved visible-light-driven degradation of tetracycline. *J. Chem. Technol. Biotechnol.* **2019**, *94*, 2702–2712.
81. Chen, Y.; Liu, K. Fabrication of magnetically recyclable Ce/N co-doped $TiO_2/NiFe_2O_4$/diatomite ternary hybrid: Improved photocatalytic efficiency under visible light irradiation. *J. Alloys Compd.* **2017**, *697*, 161–173.
82. Wu, Q.; Zhang, Z. The fabrication of magnetic recyclable nitrogen modified titanium dioxide/strontium ferrite/diatomite heterojunction nanocomposite for enhanced visible-light-driven photodegradation of tetracycline. *Int. J. Hydrogen Energy* **2019**, *44*, 8261–8272.
83. Nguyen, T.B.; Doong, R.A. Heterostructured $ZnFe_2O_4/TiO_2$ nanocomposites with a highly recyclable visible-light-response for bisphenol A degradation. *RSC Adv.* **2017**, *7*, 50006–50016.
84. Shi, Y.; Yang, Z.; Wang, B.; An, H.; Chen, Z.; Cui, H. Adsorption and photocatalytic degradation of tetracycline hydrochloride using a palygorskite-supported Cu_2O-TiO_2 composite. *Appl. Clay Sci.* **2016**, *119*, 311–320.
85. Hu, Z.; Wang, X.; Dong, H.; Li, S.; Li, X.; Li, L. Efficient photocatalytic degradation of tetrabromodiphenyl ethers and simultaneous hydrogen production by TiO_2-Cu_2O composite films in N_2 atmosphere: Influencing factors, kinetics and mechanism. *J. Hazard. Mater.* **2017**, *340*, 1–15.
86. Sud, D.; Syal, A. Investigations on the Phase Transformation, Optical Characteristics, and Photocatalytic Activity of Synthesized Heterostructured Nanoporous Bi_2O_3–TiO_2. *J. Chinese Chem. Soc.* **2016**, *63*, 776–783.
87. Sood, S.; Mehta, S.K.; Sinha, A.S.K.; Kansal, S.K. Bi_2O_3/TiO_2 heterostructures: Synthesis, characterization and their application in solar light mediated photocatalyzed degradation of an antibiotic, ofloxacin. *Chem. Eng. J.* **2016**, *290*, 45–52.
88. Kaur, A.; Umar, A.; Anderson, W.A.; Kansal, S.K. Facile synthesis of CdS/TiO_2 nanocomposite and their catalytic activity for ofloxacin degradation under visible illumination. *J. Photochem. Photobiol. A Chem.* **2018**, *360*, 34–43.
89. Kušić, H.; Leszczynska, D. Altered toxicity of organic pollutants in water originated from simultaneous exposure to UV photolysis and CdSe/ZnS quantum dots. *Chemosphere* **2012**, *89*, 900–906.
90. Ning, X.; Li, J.; Yang, B.; Zhen, W.; Li, Z.; Tian, B.; Lu, G. Inhibition of photocorrosion of CdS via assembling with thin film TiO_2 and removing formed oxygen by artificial gill for visible light overall water splitting. *Appl. Catal. B Environ.* **2017**, *212*, 129–139.
91. Pan, Y.X.; Zhou, T.; Han, J.; Hong, J.; Wang, Y.; Zhang, W.; Xu, R. CdS quantum dots and tungsten carbide supported on anatase-rutile composite TiO_2 for highly efficient visible-light-driven photocatalytic H_2 evolution from water. *Catal. Sci. Technol.* **2016**, *6*, 2206–2213.
92. Zhu, R.; Yang, R.; Hu, L.; Chen, B. Preparation of Z-Scheme system of CdS-RGO-$BiVO_4$ and its activity for hydrogen production. *Int. J. Hydrogen Energy* **2019**, *44*, 25119–25128.

93. Kandi, D.; Behera, A.; Martha, S.; Naik, B.; Parida, K.M. Quantum confinement chemistry of CdS QDs plus hot electron of Au over TiO_2 nanowire protruding to be encouraging photocatalyst towards nitrophenol conversion and ciprofloxacin degradation. *J. Environ. Chem. Eng.* **2019**, *7*, 102821.
94. Li, W.; Ding, H.; Ji, H.; Dai, W.; Guo, J.; Du, G. Photocatalytic degradation of tetracycline hydrochloride via a CdS-TiO_2 heterostructure composite under visible light irradiation. *Nanomaterials* **2018**, *8*.
95. Jiang, Y.; Zhang, M.; Xin, Y.; Chai, C.; Chen, Q. Construction of immobilized CuS/TiO_2 nanobelts heterojunction photocatalyst for photocatalytic degradation of enrofloxacin: synthesis, characterization, influencing factors and mechanism insight. *J. Chem. Technol. Biotechnol.* **2019**, *94*, 2219–2228.
96. Chen, Q.; Wu, S.; Xin, Y. Synthesis of Au-CuS-TiO_2 nanobelts photocatalyst for efficient photocatalytic degradation of antibiotic oxytetracycline. *Chem. Eng. J.* **2016**, *302*, 377–387.
97. Irandost, M.; Akbarzadeh, R.; Pirsaheb, M.; Asadi, A.; Mohammadi, P.; Sillanpää, M. Fabrication of highly visible active N, S co-doped TiO_2@MoS_2 heterojunction with synergistic effect for photocatalytic degradation of diclofenac: Mechanisms, modeling and degradation pathway. *J. Mol. Liq.* **2019**, *291*.
98. Wu, L.; Shi, S.; Li, Q.; Zhang, X.; Cui, X. TiO_2 nanoparticles modified with 2D $MoSe_2$ for enhanced photocatalytic activity on hydrogen evolution. *Int. J. Hydrogen Energy* **2019**, *44*, 720–728.
99. Du, J.; Wang, H.; Yang, M.; Zhang, F.; Wu, H.; Cheng, X.; Yuan, S.; Zhang, B.; Li, K.; Wang, Y.; et al. Highly efficient hydrogen evolution catalysis based on MoS_2/CdS/TiO_2 porous composites. *Int. J. Hydrogen Energy* **2018**, *43*, 9307–9315.
100. Kumar, N.; Bhadwal, A.S.; Mizaikoff, B.; Singh, S.; Kranz, C. Electrochemical detection and photocatalytic performance of MoS_2/TiO_2 nanocomposite against pharmaceutical contaminant: Paracetamol. *Sens. Bio-Sensing Res.* **2019**, *24*.
101. Deng, L.; Liu, H.; Gao, X.; Su, X.; Zhu, Z. SnS_2/TiO_2 nanocomposites with enhanced visible light-driven photoreduction of aqueous Cr(VI). *Ceram. Int.* **2016**, *42*, 3808–3815.
102. Kovacic, M.; Kopcic, N.; Kusic, H.; Bozic, A.L. Solar driven degradation of 17β-estradiol using composite photocatalytic materials and artificial irradiation source: Influence of process and water matrix parameters. *J. Photochem. Photobiol. A Chem.* **2018**, *361*, 48–61.
103. Kovacic, M.; Papac, J.; Kusic, H.; Karamanis, P.; Loncaric Bozic, A. Degradation of polar and non-polar pharmaceutical pollutants in water by solar assisted photocatalysis using hydrothermal TiO2-SnS_2. *Chem. Eng. J.* **2019**, 122826.
104. Yan, T.; Guan, W.; Li, W.; You, J. Ag_3PO_4 photocatalysts loaded on uniform SiO_2 supports for efficient degradation of methyl orange under visible light irradiation. *RSC Adv.* **2014**, *4*, 37095–37099.
105. Yi, Z.; Ye, J.; Kikugawa, N.; Kako, T.; Ouyang, S.; Stuart-Williams, H.; Yang, H.; Cao, J.; Luo, W.; Li, Z.; et al. An orthophosphate semiconductor with photooxidation properties under visible-light irradiation. *Nat. Mater.* **2010**, *9*, 559–564.
106. Ren, J.; Chai, Y.; Liu, Q.; Zhang, L.; Dai, W.L. Intercorrelated Ag_3PO_4 nanoparticles decorated with graphic carbon nitride: Enhanced stability and photocatalytic activities for water treatment. *Appl. Surf. Sci.* **2017**, *403*, 177–186.
107. Meng, S.; Ning, X.; Zhang, T.; Chen, S.F.; Fu, X. What is the transfer mechanism of photogenerated carriers for the nanocomposite photocatalyst Ag_3PO_4/g-C_3N_4, band-band transfer or a direct Z-scheme? *Phys. Chem. Chem. Phys.* **2015**, *17*, 11577–11585.
108. Wang, Y.; Yu, H.; Lu, Y.; Qu, J.; Zhu, S.; Huo, M. A nano-composite comprised of Ti^{3+}-doped TiO_2 nanotubes and Ag_3PO_4 quantum dots with enhanced photocatalytic activity under visible light. *Mater. Lett.* **2019**, *240*, 35–38.
109. Du, J.; Ma, S.; Yan, Y.; Li, K.; Zhao, F.; Zhou, J. Corn-silk-templated synthesis of TiO_2 nanotube arrays with Ag_3PO_4 nanoparticles for efficient oxidation of organic pollutants and pathogenic bacteria under solar light. *Colloids Surfaces A Physicochem. Eng. Asp.* **2019**, *572*, 237–249.
110. Liu, J.; Xie, F.; Li, R.; Li, T.; Jia, Z.; Wang, Y.; Wang, Y.; Zhang, X.; Fan, C. TiO_{2-x} /Ag_3PO_4 photocatalyst: Oxygen vacancy dependent visible light photocatalytic performance and BPA degradative pathway. *Mater. Sci. Semicond. Process.* **2019**, *97*, 1–10.
111. Police, A.K.R.; Chennaiahgari, M.; Boddula, R.; Vattikuti, S.V.P.; Mandari, K.K.; Chan, B. Single-step hydrothermal synthesis of wrinkled graphene wrapped TiO_2 nanotubes for photocatalytic hydrogen production and supercapacitor applications. *Mater. Res. Bull.* **2018**, *98*, 314–321.
112. Lu, Y.; Ma, B.; Yang, Y.; Huang, E.; Ge, Z.; Zhang, T.; Zhang, S.; Li, L.; Guan, N.; Ma, Y.; et al. High activity of hot electrons from bulk 3D graphene materials for efficient photocatalytic hydrogen production. *Nano Res.* **2017**, *10*, 1662–1672.
113. Hao, X.; Li, M.; Zhang, L.; Wang, K.; Liu, C. Photocatalyst TiO_2/WO_3/GO nano-composite with high efficient photocatalytic performance for BPA degradation under visible light and solar light illumination. *J. Ind. Eng. Chem.* **2017**, *55*, 140–148.

114. Wang, G.; Chen, Q.; Xin, Y.; Liu, Y.; Zang, Z.; Hu, C.; Zhang, B. Construction of graphene-WO_3/TiO_2 nanotube array photoelectrodes and its enhanced performance for photocatalytic degradation of dimethyl phthalate. *Electrochim. Acta* **2016**, *222*, 1903–1913.
115. Bilgin Simsek, E.; Kilic, B.; Asgin, M.; Akan, A. Graphene oxide based heterojunction TiO_2–ZnO catalysts with outstanding photocatalytic performance for bisphenol-A, ibuprofen and flurbiprofen. *J. Ind. Eng. Chem.* **2018**, *59*, 115–126.
116. Feng, J.; Wang, Y.; Hou, Y.; Li, L. Hierarchical structured $ZnFe_2O_4$@RGO@TiO_2 composite as powerful visible light catalyst for degradation of fulvic acid. *J. Nanoparticle Res.* **2017**, *19*.
117. Luo, L. jun; Li, J.; Dai, J.; Xia, L.; Barrow, C.J.; Wang, H.; Jegatheesan, J.; Yang, M. Bisphenol A removal on TiO_2–MoS_2–reduced graphene oxide composite by adsorption and photocatalysis. *Process Saf. Environ. Prot.* **2017**, *112*, 274–279.
118. Wang, W.; Han, Q.; Zhu, Z.; Zhang, L.; Zhong, S.; Liu, B. Enhanced photocatalytic degradation performance of organic contaminants by heterojunction photocatalyst $BiVO_4$/TiO_2/RGO and its compatibility on four different tetracycline antibiotics. *Adv. Powder Technol.* **2019**, *30*, 1882–1896.
119. Alcudia-Ramos, M.A.; Fuentez-Torres, M.O.; Ortiz-Chi, F.; Espinosa-González, C.G.; Hernández-Como, N.; García-Zaleta, D.S.; Kesarla, M.K.; Torres-Torres, J.G.; Collins-Martínez, V.; Godavarthi, S. Fabrication of g-C_3N_4/TiO_2 heterojunction composite for enhanced photocatalytic hydrogen production. *Ceram. Int.* **2020**, *46*, 38–45.
120. Liu, C.; Wu, P.; Wu, J.; Hou, J.; Bai, H.; Liu, Z. Effective protect of oxygen vacancies in carbon layer coated black TiO_{2-x}/CNNS hetero-junction photocatalyst. *Chem. Eng. J.* **2019**, *359*, 58–68.
121. Yang, Y.; Li, X.; Lu, C.; Huang, W. G-C3N4 Nanosheets Coupled with TiO_2 Nanosheets as 2D/2D Heterojunction Photocatalysts Toward High Photocatalytic Activity for Hydrogen Production. *Catal. Letters* **2019**, *149*, 2930–2939.
122. Kong, L.; Zhang, X.; Wang, C.; Xu, J.; Du, X.; Li, L. Ti^{3+} defect mediated g-C_3N_4/TiO_2 Z-scheme system for enhanced photocatalytic redox performance. *Appl. Surf. Sci.* **2018**, *448*, 288–296.
123. Wang, J.; Wang, G.; Wang, X.; Wu, Y.; Su, Y.; Tang, H. 3D/2D direct Z-scheme heterojunctions of hierarchical TiO_2 microflowers/g-C_3N_4 nanosheets with enhanced charge carrier separation for photocatalytic H_2 evolution. *Carbon N. Y.* **2019**, *149*, 618–626.
124. Pan, C.; Jia, J.; Hu, X.; Fan, J.; Liu, E. In situ construction of g-C_3N_4/TiO_2 heterojunction films with enhanced photocatalytic activity over magnetic-driven rotating frame. *Appl. Surf. Sci.* **2018**, *430*, 283–292.
125. Zou, Y.; Shi, J.W.; Ma, D.; Fan, Z.; Lu, L.; Niu, C. In situ synthesis of C-doped TiO_2@g-C_3N_4 core-shell hollow nanospheres with enhanced visible-light photocatalytic activity for H2 evolution. *Chem. Eng. J.* **2017**, *322*, 435–444.
126. Ma, J.; Zhou, W.; Tan, X.; Yu, T. Potassium ions intercalated into g-C_3N_4-modified TiO_2 nanobelts for the enhancement of photocatalytic hydrogen evolution activity under visible-light irradiation. *Nanotechnology* **2018**, *29*.
127. Pan, J.; You, M.; Chi, C.; Dong, Z.; Wang, B.; Zhu, M.; Zhao, W.; Song, C.; Zheng, Y.; Li, C. The two dimension carbon quantum dots modified porous g-C_3N_4/TiO_2 nano-heterojunctions for visible light hydrogen production enhancement. *Int. J. Hydrogen Energy* **2018**, *43*, 6586–6593.
128. Wang, X.; Maeda, K.; Thomas, A.; Takanabe, K.; Xin, G.; Carlsson, J.M.; Domen, K.; Antonietti, M. A metal-free polymeric photocatalyst for hydrogen production from water under visible light. *Nat. Mater.* **2009**, *8*, 76–80.
129. Corredor, J.; Rivero, M.J.; Rangel, C.M.; Gloaguen, F.; Ortiz, I. Comprehensive review and future perspectives on the photocatalytic hydrogen production. *J. Chem. Technol. Biotechnol.* **2019**, *94*, 3049–3063.
130. Wen, J.; Xie, J.; Chen, X.; Li, X. A review on g-C_3N_4-based photocatalysts. *Appl. Surf. Sci.* **2017**, *391*, 72–123.
131. Huang, H.; He, M.; Yang, X.; Tian, Z.; Hu, J.; Wen, B. One-pot hydrothermal synthesis of TiO_2/RCN heterojunction photocatalyst for production of hydrogen and rhodamine B degradation. *Appl. Surf. Sci.* **2019**, *493*, 202–211.
132. Yang, Z.; Yan, J.; Lian, J.; Xu, H.; She, X.; Li, H. g-C_3N_4/TiO_2 Nanocomposites for Degradation of Ciprofloxacin under Visible Light Irradiation. *ChemistrySelect* **2016**, *1*, 5679–5685.
133. Li, G.; Nie, X.; Gao, Y.; An, T. Can environmental pharmaceuticals be photocatalytically degraded and completely mineralized in water using g-C_3N4/TiO_2 under visible light irradiation?-Implications of persistent toxic intermediates. *Appl. Catal. B Environ.* **2016**, *180*, 726–732.
134. Yu, S.; Wang, Y.; Sun, F.; Wang, R.; Zhou, Y. Novel mpg-C_3N_4/TiO_2 nanocomposite photocatalytic membrane reactor for sulfamethoxazole photodegradation. *Chem. Eng. J.* **2018**, *337*, 183–192.
135. Wang, W.; Fang, J.; Shao, S.; Lai, M.; Lu, C. Compact and uniform TiO_2@g-C_3N_4 core-shell quantum heterojunction for photocatalytic degradation of tetracycline antibiotics. *Appl. Catal. B Environ.* **2017**,

217, 57–64.
136. Li, C.; Sun, Z.; Zhang, W.; Yu, C.; Zheng, S. Highly efficient g-C_3N_4/TiO_2/kaolinite composite with novel three-dimensional structure and enhanced visible light responding ability towards ciprofloxacin and S. aureus. *Appl. Catal. B Environ.* **2018**, *220*, 272–282.
137. Chen, Y.; Lu, W.; Shen, H.; Gu, Y.; Xu, T.; Zhu, Z.; Wang, G.; Chen, W. Solar-driven efficient degradation of emerging contaminants by g-C_3N_4-shielding polyester fiber/TiO_2 composites. *Appl. Catal. B Environ.* **2019**, *258*, 117960.
138. Xie, X.; Chen, C.; Wang, X.; Li, J.; Naraginti, S. Efficient detoxification of triclosan by a S-Ag/TiO_2@g-C_3N_4 hybrid photocatalyst: Process optimization and bio-toxicity assessment. *RSC Adv.* **2019**, *9*, 20439–20449.
139. Song, J.; Wu, X.; Zhang, M.; Liu, C.; Yu, J.; Sun, G.; Si, Y.; Ding, B. Highly flexible, core-shell heterostructured, and visible-light-driven titania-based nanofibrous membranes for antibiotic removal and E. coil inactivation. *Chem. Eng. J.* **2020**, *379*, 122269.
140. Yang, L.; Bai, X.; Shi, J.; Du, X.; Xu, L.; Jin, P. Quasi-full-visible-light absorption by D35-TiO_2/g-C_3N_4 for synergistic persulfate activation towards efficient photodegradation of micropollutants. *Appl. Catal. B Environ.* **2019**, *256*.
141. Su, Y.; Chen, P.; Wang, F.; Zhang, Q.; Chen, T.; Wang, Y.; Yao, K.; Lv, W.; Liu, G. Decoration of TiO_2/g-C_3N_4 Z-scheme by carbon dots as a novel photocatalyst with improved visible-light photocatalytic performance for the degradation of enrofloxacin. *RSC Adv.* **2017**, *7*, 34096–34103.
142. Wang, F.; Chen, P.; Feng, Y.; Xie, Z.; Liu, Y.; Su, Y.; Zhang, Q.; Wang, Y.; Yao, K.; Lv, W.; et al. Facile synthesis of N-doped carbon dots/g-C_3N_4 photocatalyst with enhanced visible-light photocatalytic activity for the degradation of indomethacin. *Appl. Catal. B Environ.* **2017**, *207*, 103–113.
143. Nie, Y.C.; Yu, F.; Wang, L.C.; Xing, Q.J.; Liu, X.; Pei, Y.; Zou, J.P.; Dai, W.L.; Li, Y.; Suib, S.L. Photocatalytic degradation of organic pollutants coupled with simultaneous photocatalytic H_2 evolution over graphene quantum dots/Mn-N-TiO_2/g-C_3N_4 composite catalysts: Performance and mechanism. *Appl. Catal. B Environ.* **2018**, *227*, 312–321.
144. Jo, W.K.; Adinaveen, T.; Vijaya, J.J.; Sagaya Selvam, N.C. Synthesis of MoS_2 nanosheet supported Z-scheme TiO_2/g-C_3N_4 photocatalysts for the enhanced photocatalytic degradation of organic water pollutants. *RSC Adv.* **2016**, *6*, 10487–10497.
145. Tahir, M.B.; Sagir, M.; Shahzad, K. Removal of acetylsalicylate and methyl-theobromine from aqueous environment using nano-photocatalyst WO_3-TiO_2@g-C_3N_4 composite. *J. Hazard. Mater.* **2019**, *363*, 205–213.
146. Shimadzu. https://www.ssi.shimadzu.com/industries/environment/high-performance-liquid-chromatography/index.html. (Accessed in April 1, 2023)
147. Skoog, D.; James Holler, F.; Crouch, S. *Principles of Instrumental Analysis, 7th edition*; 2016;
148. https://www.technologynetworks.com/analysis/articles/lc-ms-what-is-lc-ms-lc-ms-analysis-and-lc-msms-348238#D1. (Accessed in April 1, 2023)
149. Shimadzu https://www.shimadzu.com/an/service-support/technical-support/analysis-basics/fundamental/core_principles.html. (Accessed in April 1, 2023)
150. https://www.creative-proteomics.com/support/q-exactive-hybrid-quadrupole-orbitrap-mass-spectrometer.htm. (Accessed in April 1, 2023)
151. Roy, K.; Kar, S. In Silico Models for Ecotoxicity of Pharmaceuticals. In *In Silico Methods for Predicting Drug Toxicity*; Benfenati, E., Ed.; Springer New York: New York, NY, **2016**; pp. 237–304 ISBN 978-1-4939-3609-0.
152. https://www.biotoxicity.com/index.php/ebpi-toxicity-tests/aliivibrio-fischeri-toxicity-tests. (Accessed in April 1, 2023)
153. Faria, E.C.; Treves Brown, B.J.; Snook, R.D. Water toxicity monitoring using Vibrio fischeri: A method free of interferences from colour and turbidity. *J. Environ. Monit.* **2004**, *6*, 97–102.
154. 11348-3:2007, I. https://www.iso.org/standard/40518.html. (Accessed in April 1, 2023)
155. Xu, Z.; Liu, Y.; Wang, Y. Application of Daphnia magna for Nanoecotoxicity Study. In *Nanotoxicity: Methods and Protocols*; Zhang, Q., Ed.; Springer New York: New York, NY, **2019**; pp. 345–352 ISBN 978-1-4939-8916-4.
156. https://www.iso.org/obp/ui/#iso:std:iso:6341:ed-4:v1:en. (Accessed in April 1, 2023)
157. https://theory.labster.com/ec50/.(Accessed in April 1, 2023)
158. Andrews, D.; Lipson, R.; Nann, T. *Comprehensive Nanoscience and Nanotechnology*; David Andrews Thomas Nann Robert Lipson, Ed.; Elsevier B.V, **2019**; ISBN 978-0-12-812296-9.
159. Elbakkay, M.H.; El Rouby, W.M.A.; Mariño-López, A.; Sousa-Castillo, A.; Salgueiriño, V.; El-Dek, S.I.; Farghali, A.A.; Correa-Duarte, M.A.; Millet, P. One-pot synthesis of TiO_2/Sb_2S_3/RGO complex multicomponent heterostructures for highly enhanced photoelectrochemical water splitting. *Int. J. Hydrogen Energy* **2021**, *46*, 31216–31227.

160. Liang, C.; Huang, C.F.; Mohanty, N.; Kurakalva, R.M. A rapid spectrophotometric determination of persulfate anion in ISCO. *Chemosphere* **2008**, *73*, 1540–1543.
161. Kusic, H.; Peternel, I.; Ukic, S.; Koprivanac, N.; Bolanca, T.; Papic, S.; Bozic, A.L. Modeling of iron activated persulfate oxidation treating reactive azo dye in water matrix. *Chem. Eng. J.* **2011**, *172*, 109–121.
162. M.J. Frisch, G.W. Trucks, H.B. Schlegel, G.E. Scuseria, M.A. Robb, J.R. Cheeseman, G. Scalmani, V. Barone, G.A. Petersson, H. Nakatsuji, X. Li, M. Caricato, A. Marenich, J. Bloino, B.G. Janesko, R. Gomperts, B. Mennucci, H.P. Hratchian, J.V. Ortiz, A.F. I, D.J.F. Gaussian, Inc 2019.
163. Lee, C.; Yang, W.; Parr, R. Development of the Colle-Salvetti correlation-energy formula into a functional of the electron density. *Phys. Rev. B* **1988**, *37*, 36–39.
164. Becke, A.D. Density-functional thermochemistry. III. The role of exact exchange. *J. Chem. Phys.* **1993**, *98*, 5648–5652.
165. Dunning, T.H. Gaussian basis sets for use in correlated molecular calculations. I. The atoms boron through neon and hydrogen. *J. Chem. Phys.* **1989**, *90*, 1007–1023.
166. Strens, R.G.J.; Wood, B.J. Diffuse reflectance spectra and optical properties of some iron and titanium oxides and oxyhydroxides. *Mineral. Mag.* **1979**, *43*, 347–354.
167. Torrent, J.; Barron, V. Diffuse reflectance spectroscopy of iron oxides. *Encycl. Surf. Colloid Sci.* **2002**, 1438–1446.
168. Monfort, O.; Roch, T.; Gregor, M.; Satrapinskyy, L.; Raptis, D.; Lianos, P.; Plesch, G. Photooxidative properties of various $BiVO_4/TiO_2$ layered composite films and study of their photocatalytic mechanism in pollutant degradation. *J. Environ. Chem. Eng.* **2017**, *5*, 5143–5149.
169. Ismail, L.; Ferronato, C.; Fine, L.; Jaber, F.; Chovelon, J.M. Elimination of sulfaclozine from water with SO_4 radicals: Evaluation of different persulfate activation methods. *Appl. Catal. B Environ.* **2017**, *201*, 573–581.
170. Wang, Y.; Hong, C.S. Effect of hydrogen peroxide, periodate and persulfate on photocatalysis of 2-chlorobiphenyl in aqueous TiO_2 suspensions. *Water Res.* **1999**, *33*, 2031–2036.
171. Fang, G.; Wu, W.; Liu, C.; Dionysiou, D.D.; Deng, Y.; Zhou, D. Activation of persulfate with vanadium species for PCBs degradation: A mechanistic study. *Appl. Catal. B Environ.* **2017**, *202*, 1–11.
172. Matzek, L.W.; Carter, K.E. Sustained persulfate activation using solid iron: Kinetics and application to ciprofloxacin degradation. *Chem. Eng. J.* **2017**, *307*, 650–660.
173. Zhong, H.; Tian, Y.; Yang, Q.; Brusseau, M.L.; Yang, L.; Zeng, G. Degradation of landfill leachate compounds by persulfate for groundwater remediation. *Chem. Eng. J.* **2017**, *307*, 399–407.
174. Boncagni, N.T.; Otaegui, J.M.; Warner, E.; Curran, T.; Ren, J.; De Cortalezzi, M.M.F. Exchange of TiO_2 nanoparticles between streams and streambeds. *Environ. Sci. Technol.* **2009**, *43*, 7699–7705.
175. Jiang, W.; Zong, X.; An, L.; Hua, S.; Miao, X.; Luan, S.; Wen, Y.; Tao, F.F.; Sun, Z. Photocatalytic Membrane Reactor for the Removal of C.I. Disperse Red 73. *ACS Catal.* **2018**, *8*, 2209–2217.
176. Kritikos, D.E.; Xekoukoulotakis, N.P.; Psillakis, E.; Mantzavinos, D. Photocatalytic degradation of reactive black 5 in aqueous solutions : Effect of operating conditions and coupling with ultrasound irradiation. *Water Res.* **2007**, *41*, 2236–2246.
177. Zhao, J.; Sun, Y.; Wu, F.; Shi, M.; Liu, X. Oxidative Degradation of Amoxicillin in Aqueous Solution by Thermally Activated Persulfate. *J. Chem.* **2019**, *2019*, 1–10.
178. Olmez-Hanci, T.; Arslan-Alaton, I. Comparison of sulfate and hydroxyl radical based advanced oxidation of phenol. *Chem. Eng. J.* **2013**, *224*, 10–16.
179. Kolthoff, I.M.; Miller, I.K. The Chemistry of Persulfate. I. The Kinetics and Mechanism of the Decomposition of the Persulfate Ion in Aqueous Medium. *J. Am. Chem. Soc.* **1951**, *73*, 3055–3059.
180. Kolthoff, I.M.; Miller, I.K. The Chemistry of Persulfate. II. The Reaction of Persulfate with Mercaptans Solubilized in Solutions of Saturated Fatty Acid Soaps. *J. Am. Chem. Soc.* **1951**, *73*, 5118–5122.
181. Gao, H.; Chen, J.; Zhang, Y.; Zhou, X. Sulfate radicals induced degradation of Triclosan in thermally activated persulfate system. *Chem. Eng. J.* **2016**, *306*, 522–530.
182. Monteagudo, J.M.; Durán, A.; Martín, I.S.; Vellón, B. Photocatalytic degradation of aniline by solar / TiO_2 system in the presence of the electron acceptors $Na_2S_2O_8$ and H_2O_2. *Sep. Purif. Technol.* **2020**, *238*, 116456.
183. Buxton, G. V.; Greenstock, C.L.; Helman, W.P.; Ross, A.B. Critical Review of rate constants for reactions of hydrated electrons, hydrogen atoms and hydroxyl radicals (·OH/·O− in Aqueous Solution. *J. Phys. Chem. Ref. Data* **1988**, *17*, 513–886.
184. Sabri, M.; Habibi-Yangjeh, A.; Chand, H.; Krishnan, V. Activation of persulfate by novel TiO_2/FeOCl photocatalyst under visible light: Facile synthesis and high photocatalytic performance. *Sep. Purif. Technol.* **2020**, *250*, 117268.
185. Krebel, M.; Kusic, H.; Koprivanac, N.; Meixner, J.; Bozic, A.L. Treatment of Chlorophenols by UV-Based Processes: Correlation of Oxidation By-Products, Wastewater Parameters, and Toxicity. *J.*

Environ. Eng. **2011**, *137*, 639–649.
186. Cvetnić, M.; Tomić, A.; Sigurnjak, M.; Stankov, M.N.; Ukić, Š.; Kušić, H.; Bolanča, T.; Lončarić Božić, A. Structural features of contaminants of emerging concern behind empirical parameters of mechanistic models describing their photooxidative degradation. *J. Water Process Eng.* **2020**, *33*, 101053.
187. Brlenic, V.; Kusic, H.; Juretic, D.; Bozic, A.L. Comparative study on photooxidative treatment of diclofenac: Response surface and mechanistic modeling. *J. Water Process Eng.* **2016**, *10*, 78–88.
188. Zhang, Y.; Xiao, Y.; Zhong, Y.; Lim, T.T. Comparison of amoxicillin photodegradation in the UV/H_2O_2 and UV/persulfate systems: Reaction kinetics, degradation pathways, and antibacterial activity. *Chem. Eng. J.* **2019**, *372*, 420–428.
189. Trovó, A.G.; Pupo Nogueira, R.F.; Agüera, A.; Fernandez-Alba, A.R.; Malato, S. Degradation of the antibiotic amoxicillin by photo-Fenton process - Chemical and toxicological assessment. *Water Res.* **2011**, *45*, 1394–1402.
190. Juretic, D.; Kusic, H.; Dionysiou, D.D.; Bozic, A.L. Environmental aspects of photooxidative treatment of phenolic compounds. *J. Hazard. Mater.* **2013**, *262*, 377–386.
191. Farré, M.J.; Franch, M.I.; Ayllón, J.A.; Peral, J.; Domènech, X. Biodegradability of treated aqueous solutions of biorecalcitrant pesticides by means of photocatalytic ozonation. *Desalination* **2007**, *211*, 22–33.
192. Hernando, M.D.; Fernández-Alba, A.R.; Tauler, R.; Barceló, D. Toxicity assays applied to wastewater treatment. *Talanta* **2005**, *65*, 358–366.
193. Matta, R.; Younes, H.; Hanna, R.; Saab, J.; Abou-Khalil, R. Sulfate radicals mediated oxidation of amoxicillin: Optimization of key parameters. *J. Environ. Manage.* **2019**, *245*, 375–383.
194. Wojnárovits, L.; Tóth, T.; Takács, E. Critical evaluation of rate coefficients for hydroxyl radical reactions with antibiotics: A review. *Crit. Rev. Environ. Sci. Technol.* **2018**, *48*, 575–613.
195. Zuo, Z.; Cai, Z.; Katsumura, Y.; Chitose, N.; Muroya, Y. Reinvestigation of the acid-base equilibrium of the (bi)carbonate radical and ph dependence of its reactivity with inorganic reactants. *Radiat. Phys. Chem.* **1999**, *55*, 15–23.
196. Chawla, O.P.; Fessenden, R.W. Electron spin resonance and pulse radiolysis studies of some reactions of so4-. *J. Phys. Chem.* **1975**, *79*, 2693–2700.
197. Guillard, C.; Puzenat, E.; Lachheb, H.; Houas, A.; Herrmann, J.M. Why inorganic salts decrease the TiO_2 photocatalytic efficiency. *Int. J. Photoenergy* **2005**, *7*, 1–9.
198. Kwon, M.; Kim, S.; Yoon, Y.; Jung, Y.; Hwang, T.M.; Lee, J.; Kang, J.W. Comparative evaluation of ibuprofen removal by UV/H_2O_2 and UV/$S_2O_8^{2-}$ processes for wastewater treatment. *Chem. Eng. J.* **2015**, *269*, 379–390.
199. Leech, D.M.; Snyder, M.T.; Wetzel, R.G. Natural organic matter and sunlight accelerate the degradation of 17ß-estradiol in water. *Sci. Total Environ.* **2009**, *407*, 2087–2092.
200. Antoniou, M.G.; Zhao, C.; O'Shea, K.E.; Zhang, G.; Dionysiou, D.D.; Zhao, C.; Han, C.; Nadagouda, M.N.; Choi, H.; Fotiou, T.; et al. *Photocatalytic degradation of organic contaminants in water: Process optimization and degradation pathways*; The Royal Society of Chemistry, 2016; Vol. 2016-Janua; ISBN 9781782620419.
201. Duan, X.; Su, C.; Zhou, L.; Sun, H.; Suvorova, A.; Odedairo, T.; Zhu, Z.; Shao, Z.; Wang, S. Surface controlled generation of reactive radicals from persulfate by carbocatalysis on nanodiamonds. *Appl. Catal. B Environ.* **2016**, *194*, 7–15.
202. Ding, H.; Hu, J. Degradation of ibuprofen by UVA-LED/TiO_2/persulfate process: Kinetics, mechanism, water matrix effects, intermediates and energy consumption. *Chem. Eng. J.* **2020**, *397*.
203. Lin, D.; Ji, J.; Long, Z.; Yang, K.; Wu, F. The influence of dissolved and surface-bound humic acid on the toxicity of TiO2 nanoparticles to Chlorella sp. *Water Res.* **2012**, *46*, 4477–4487.
204. Dai, X.; Lu, G.; Hu, Y.; Xie, X.; Wang, X.; Sun, J. Reversible redox behavior of Fe_2O_3/TiO_2 composites in the gaseous photodegradation process. *Ceram. Int.* **2019**, *45*, 13187–13192.
205. Lassoued, A.; Dkhil, B.; Gadri, A.; Ammar, S. Control of the shape and size of iron oxide (α-Fe_2O_3) nanoparticles synthesized through the chemical precipitation method. *Results Phys.* **2017**, *7*, 3007–3015.
206. Hua, J.; Gengsheng, J. Hydrothermal synthesis and characterization of monodisperse α-Fe_2O_3 nanoparticles. *Mater. Lett.* **2009**, *63*, 2725–2727.
207. Peña-flores, J.I.; Palomec-garfias, A.F.; Márquez-beltrán, C.; Sánchez-mora, E. Fe effect on the optical properties of TiO_2:Fe_2O_3 nanostructured composites supported on SiO_2 microsphere assemblies. *Nanoscale Res. Lett.* **2014**, *9*, 499.
208. Ohsaka, T. Temperature Dependence of the Raman Spectrum in Anatase TiO_2. *J. Phys. Soc. Japan* **1980**, *48*.
209. Mansour, H.; Omri, K.; Bargougui, R.; Ammar, S. Novel α-Fe_2O_3/TiO_2 nanocomposites with enhanced photocatalytic activity. *Appl. Phys. A* **2020**, *126*, 151.

210. Faria, D.L.A. De; Lopes, F.N. Heated goethite and natural hematite : Can Raman spectroscopy be used to differentiate them ? *Vib. Spectrosc.* **2007**, *45*, 117–121.
211. Jubb, A.M.; Allen, H.C. Vibrational Spectroscopic Characterization of Hematite , Maghemite , and Magnetite Thin Films Produced by Vapor Deposition. *ACS Appl. Mater. Interfaces* **2010**, *2*, 2804–2812.
212. Cho, Y.; Huh, Y. Preparation of Hyperbranched Structures of α-Fe_2O_3. *Bull. Korean Chem. Soc.* **2009**, *30*, 1413–1415.
213. Huang, R.; Liang, R.; Fan, H.; Ying, S.; Wu, L.; Wang, X. Enhanced Photocatalytic Fuel Denitrification over TiO_2/α-Fe_2O_3 Nanocomposites under Visible Light irradiation. *Sci. Rep.* **2017**, *7*, 1–10.
214. Lamm, B.; Trześniewski, B.J.; Döscher, H.; Smith, W.A.; Stefik, M. Emerging Postsynthetic Improvements of $BiVO_4$ Photoanodes for Solar Water Splitting. *ACS Energy Lett.* **2018**, *3*, 112–124.
215. Singh, A.P.; Tossi, C.; Tittonen, I.; Hellman, A.; Wickman, B. Synergies of co-doping in ultra-thin hematite photoanodes for solar water oxidation: In and Ti as representative case. *RSC Adv.* **2020**, *10*, 33307–33316.
216. Akhavan, O. Thickness dependent activity of nanostructured TiO_2/α-Fe_2O_3 photocatalyst thin films. *Appl. Surf. Sci.* **2010**, *257*, 1724–1728.
217. Akhavan, O.; Azimirad, R.; Safa, S.; Larijani, M.M. Visible light photo-induced antibacterial activity of CNT-doped TiO_2 thin films with various CNT contents. *J. Mater. Chem.* **2010**, *20*, 7386–7392.
218. Sayed, M.; Ren, B.; Ali, A.M.; Al-Anazi, A.; Nadagouda, M.N.; Ismail, A.A.; Dionysiou, D.D. Solar light induced photocatalytic activation of peroxymonosulfate by ultra-thin Ti^{3+} self-doped Fe_2O_3/TiO_2 nanoflakes for the degradation of naphthalene. *Appl. Catal. B Environ.* **2022**, *315*, 121532.
219. Xie, W.; Li, R.; Xu, Q. Enhanced photocatalytic activity of Se-doped TiO_2 under visible light irradiation. *Sci. Rep.* **2018**, *8*, 1–10.
220. Cao, Y.Q.; Zi, T.Q.; Zhao, X.R.; Liu, C.; Ren, Q.; Fang, J. Bin; Li, W.M.; Li, A.D. Enhanced visible light photocatalytic activity of Fe_2O_3 modified TiO_2 prepared by atomic layer deposition. *Sci. Rep.* **2020**, *10*, 1–10.
221. D'Amato, C.A.; Giovannetti, R.; Zannotti, M.; Rommozzi, E.; Ferraro, S.; Seghetti, C.; Minicucci, M.; Gunnella, R.; Di Cicco, A. Enhancement of visible-light photoactivity by polypropylene coated plasmonic Au/TiO_2 for dye degradation in water solution. *Appl. Surf. Sci.* **2018**, *441*, 575–587.
222. Yuan, S.; Mu, J.; Mao, R.; Li, Y.; Zhang, Q.; Wang, H. All-Nanoparticle Self-assembly ZnO / TiO_2 Heterojunction Thin Films with Remarkably Enhanced Photoelectrochemical Activity. *ACS Appl. Mater. Interfaces* **2014**, *6*, 5719–5725.
223. Mei, Q.; Zhang, F.; Wang, N.; Yang, Y.; Wu, R.; Wang, W. TiO_2/$Fe2O_3$ heterostructures with enhanced photocatalytic reduction of Cr(VI) under visible light irradiation. *RSC Adv.* **2019**, *9*, 22764–22771.
224. Zubair, M.; Svenum, I.; Rønning, M.; Yang, J. Core-Shell Nanostructures of Graphene-Wrapped CdS Nanoparticles and TiO_2 (CdS@G@TiO_2): The Role of Graphene in Enhanced Photocatalytic H_2 Generation. *Catalysts* **2020**, *10*, 358.
225. Buscio, V.; Brosillon, S.; Mendret, J.; Crespi, M.; Gutiérrez-bouzán, C. Photocatalytic Membrane Reactor for the Removal of C.I. Disperse Red 73. *Materials (Basel).* **2015**, *8*, 3633–3647.
226. Shrimali, K.; Jin, J.; Hassas, B.V.; Wang, X.; Miller, J.D. The surface state of hematite and its wetting characteristics. *J. Colloid Interface Sci.* **2016**, *477*, 16–24.
227. Mendiola-Alvarez, S.Y.; Araña, J.; Doña Rodríguez, J.M.; Hernández-Ramírez, A.; Turnes Palomino, G.; Palomino Cabello, C.; Hinojosa-Reyes, L. Comparison of photocatalytic activity of α-Fe_2O_3-TiO_2/P on the removal of pollutants on liquid and gaseous phase. *J. Environ. Chem. Eng.* **2021**, *9*, 104828.
228. Subramonian, W.; Wu, T.Y.; Chai, S.-P. Photocatalytic degradation of industrial pulp and paper mill effluent using synthesized magnetic Fe_2O_3-TiO_2: Treatment efficiency and characterizations of reused photocatalyst. *J. Environ. Manage.* **2017**, *187*, 298–310.
229. Lee, S.C.; Lintang, H.O.; Yuliati, L. High photocatalytic activity of Fe_2O_3/TiO_2 nanocomposites prepared by photodeposition for degradation of 2,4-dichlorophenoxyacetic acid. *Beilstein J. Nanotechnol.* **2017**, *8*, 915–926.
230. Li, R.; Liu, J.; Jia, Y.; Zhen, Q. Photocatalytic degradation mechanism of oxytetracyclines using Fe_2O_3-TiO_2 nanopowders. *J. Nanosci. Nanotechnol.* **2017**, *17*, 3010–3015.
231. Khasawneh, O.; Palaniandy, P. Removal of organic pollutants from water by Fe_2O_3/TiO_2 based photocatalytic degradation: A review. *Environ. Technol. Innov.* **2021**, *21*, 101230.
232. Furman, O.S.; Teel, A.M.Y.L.; Watts, R.J. Mechanism of Base Activation of Persulfate. *Environ. Sci. Technol.* **2010**, *44*, 6423–6428.
233. Saien, J.; Jafari, F. Chapter 1 Methods of Persulfate Activation for the Degradation of Pollutants: Fundamentals and Influencing Parameters. In *Persulfate-based Oxidation Processes in Environmental Remediation*; The Royal Society of Chemistry, 2022; pp. 1–59 ISBN 978-1-83916-308-1.
234. Xia, Y.; Yin, L. Core-shell structured α-Fe_2O_3@TiO_2 nanocomposites with improved photocatalytic activity in the visible light region. *Phys. Chem. Chem. Phys.* **2013**, *15*, 18627–18634.

235. Liu, J.; Yang, S.; Wu, W.; Tian, Q.; Cui, S.; Dai, Z.; Ren, F.; Xiao, X.; Jiang, C. 3D Flowerlike α-Fe_2O_3@TiO_2 Core–Shell Nanostructures: General Synthesis and Enhanced Photocatalytic Performance. *ACS Sustain. Chem. Eng.* **2015**, *3*, 2975–2984.
236. Rao, P.S.; Hayon, E. Redox potentials of free radicals. IV. Superoxide and hydroperoxy radicals . O2- and . HO2. *J. Phys. Chem.* **1975**, *79*, 397–402.
237. Matta, R.; Tlili, S.; Chiron, S.; Barbati, S. Removal of carbamazepine from urban wastewater by sulfate radical oxidation. *Environ. Chem. Lett.* **2011**, *9*, 347–353.
238. Anipsitakis, G.P.; Dionysiou, D.D. Radical generation by the interaction of transition metals with common oxidants. *Environ. Sci. Technol.* **2004**, *38*, 3705–3712.
239. Zhu, J.; Liu, S.; Ge, J.; Guo, X.; Wang, X.; Wu, H. Synthesis of Fe_2O_3-TiO_2/fly-ash-cenosphere composite and its mechanism of photocatalytic oxidation under visible light. *Res. Chem. Intermed.* **2016**, *42*, 3637–3654.
240. Lamm, A.; Gozlan, I.; Rotstein, A.; Avisar, D. Detection of amoxicillin-diketopiperazine-2', 5' in wastewater samples. *J. Environ. Sci. Heal. Part A* **2009**, *44*, 1512–1517.
241. He, X.; Mezyk, S.P.; Michael, I.; Fatta-Kassinos, D.; Dionysiou, D.D. Degradation kinetics and mechanism of β-lactam antibiotics by the activation of H_2O_2 and $Na_2S_2O_8$ under UV-254nm irradiation. *J. Hazard. Mater.* **2014**, *279*, 375–383.
242. Wei, Z.; Liu, J.; Fang, W.; Xu, M.; Qin, Z.; Jiang, Z.; Shangguan, W. Photocatalytic hydrogen evolution with simultaneous antibiotic wastewater degradation via the visible-light-responsive bismuth spheres-g-C_3N_4 nanohybrid : Waste to energy insight. *Chem. Eng. J.* **2019**, *358*, 944–954.
243. Wei, Z.; Xu, M.; Liu, J.; Guo, W.; Jiang, Z.; Shangguan, W. Simultaneous visible-light-induced hydrogen production enhance- ment and antibiotic wastewater degradation using MoS_2@$Zn_xCd_{1-x}S$: Solid-solution-assisted photocatalysis. *Chinese J. Catal.* **2020**, *41*, 103–113.
244. Ma, D.; Zhai, S.; Wang, Y.; Liu, A.; Chen, C. TiO_2 Photocatalysis for Transfer Hydrogenation. *Molecules* **2019**, *24*, 330.
245. Solomons, T.W.G. *Organic Chemistry*; Wiley, 2011;
246. Rodea-Palomares, I.; González-Pleiter, M.; Martín-Betancor, K.; Rosal, R.; Fernández-Piñas, F. Additivity and interactions in ecotoxicity of pollutant mixtures: Some Patterns, Conclusions, and open questions. *Toxics* **2015**, *3*, 342–369.
247. Arsand, J.B.; Hoff, R.B.; Jank, L.; Meirelles, L.N.; Silvia Díaz-Cruz, M.; Pizzolato, T.M.; Barceló, D. Transformation products of amoxicillin and ampicillin after photolysis in aqueous matrices: Identification and kinetics. *Sci. Total Environ.* **2018**, *642*, 954–967.
248. Zhang, Y.; Xiao, Y.; Zhong, Y.; Lim, T.T. Comparison of amoxicillin photodegradation in the UV/H_2O_2 and UV/persulfate systems: Reaction kinetics, degradation pathways, and antibacterial activity. *Chem. Eng. J.* **2019**, *372*, 420–428.
249. Gozlan, I.; Rotstein, A.; Avisar, D. Investigation of an amoxicillin oxidative degradation product formed under controlled environmental conditions. *Environ. Chem.* **2010**, *7*, 435–442.
250. Gozlan, I.; Rotstein, A.; Avisar, D. Amoxicillin-degradation products formed under controlled environmental conditions: Identification and determination in the aquatic environment. *Chemosphere* **2013**, *91*, 985–992.

7. APPENDIX

Table S1. The structure and characteristics of AMX and the characteristics of AMX solution prior to the treatment (measured in this study)

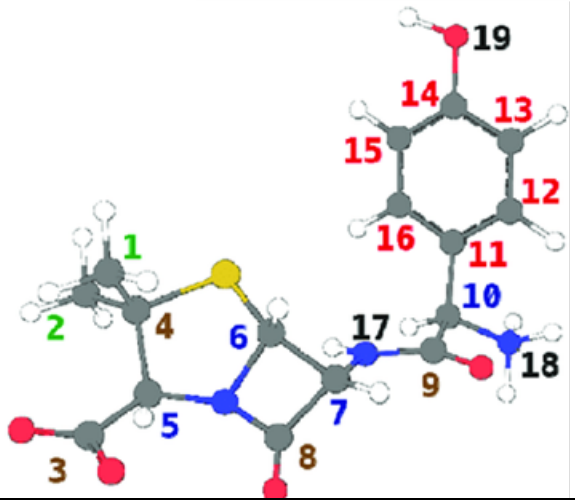	
CAS: 26787-78-0	*Aqueous solution of AMX:*
Molecular formula:	Concentration: 0.05 mM
$C_{16}H_{19}N_3O_5S$	BOD_5: 0.58 mg $O_2 \cdot L^{-1}$
Molecular weight:	COD: 34.1 mg $O_2 \cdot L^{-1}$
365.4 g mol^{-1}	Biodegradability (BOD_5/COD): 0.017
Purity of standard: 96%	TOC: 9.22 mg $C \cdot L^{-1}$
	Toxicity: (*Vibrio fisheri*): EC_{50}(15 min) = 17.79 mg$\cdot L^{-1}$, TU = 1.03 (*Daphnia magna*) EC_{50}(48 h) = 33.83 mg$\cdot L^{-1}$, TU = 0.54

Table S2.1. FFD matrix for AMX degradation rate constants (k_{obs}) by solar-TiO_2@Fe_2O_3/PS process after 50 min treatment

Exp. #	Variables		Experimental results	Response, Y
	X_1	X_2		
	coded	coded	k_{obs}(AMX), $\times 10^{-7}$ M·min^{-1}	
1	-1	-1	5.06	4.84
2	0	-1	2.10	2.64
3	1	-1	0.96	0.64
4	-1	0	7.23	7.29
5	0	0	5.45	5.13
6	1	0	2.90	3.16
7	-1	1	6.36	6.52
8	0	1	4.61	4.39
9	1	1	2.41	2.47

Table S2.2. FFD matrix for AMX removal rate constants (k_{obs}) by vis-(5% (*w/w*) Fe_2O_3/TiO_2)/PS process after 150 min treatment

Exp. #	Variables		Experimental results	Response, *Y*
	X_1	X_2		
	coded	coded	k_{obs}(AMX), × 10^{-7} M·min^{-1}	
1	-1	-1	1.29	1.31
2	0	-1	1.27	1.23
3	1	-1	0.65	0.66
4	-1	0	1.48	1.46
5	0	0	1.40	1.41
6	1	0	0.87	0.87
7	-1	1	1.35	1.34
8	0	1	1.30	1.32
9	1	1	0.82	0.81

Table S3. Analysis of variance (ANOVA) of RSM model predicting AMX degradation rate constants (k_{obs}) by solar-TiO_2@Fe_2O_3/PS process after 50 min treatment

Factor (coded)	Statistical analysis				
	SS	df	MSS	*F*	*p*
Model	35.37	5	7.07	30.50	0.0089*
X_1	25.54	1	25.54	110.16	0.0018*
X_1^2	0.02	1	0.02	0.09	0.7881
X_2	4.61	1	4.61	19.89	0.0210*
X_2^2	5.18	1	5.18	22.36	0.0179*
$X_1 \times X_2$	0.01	1	0.01	0.02	0.8861
Residual	0.70	3	0.23		
Total	36.06	8			

*p<0.05 means that model or model term is significant

Table S4. Analysis of variance (ANOVA) of RSM model predicting AMX removal rate constants (k_{obs}) by vis-(5% (*w/w*) Fe_2O_3/TiO_2)/PS process after 150 min treatment

Factor (coded)	**Statistical analysis**				
	SS	df	MSS	*F*	*p*
Model	0.7014	5	0.1403	136.37	0.0010*
X_1	0.5281	1	0.5281	513.33	0.0002*
X_1^2	0.1217	1	0.1217	118.29	0.0017*
X_2	0.0113	1	0.0113	10.95	0.0454*
X_2^2	0.0374	1	0.0374	36.31	0.0092*
$X_1 \times X_2$	0.0030	1	0.0030	2.94	0.1849
Residual	0.0031	3	0.0010		
Total	0.7045	8			

*$p<0.05$ means that model or model term is significant

Table S5. Accurate mass measurements found by LC-MS-Orbitrap of protonated AMX conversion products and their corresponding fragment ions

R_t (min)	Compound	Chemical Formula	m/z (Experimental)	RDBE	Annotated Δmass (ppm)	FISh Coverage	Suggested chemical structure	Photocatalysis	Photocatalysis + H_2O_2	Photocatalysis + Persulfate	Reference
1.180	**AMX**	$C_{16}H_{20}N_3O_5S$ $[M+H]^+$	366.11102	8.5			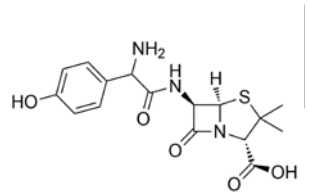	----	----	----	[189,247]
		$C_{16}H_{17}N_2O_5S$ $[M+H–(NH_3)]^+$	349.08459	9.5							
		$C_{15}H_{17}N_2O_4S$	321.09079	8.5	-1.68	64.71					
		$C_{11}H_8NO_3S$	234.02155	8.5							
		$C_{10}H_{10}NO_2S$	208.04260	6.5							
		$C_6H_{10}NO_2S$	160.04242	2.5							
		C_4H_4NOS	114.00060	3.5							
0.397	**TP 382 (E1)**	$C_{16}H_{20}N_3O_6S$ $[M+H]^+$	382.10617	8.5	-						
		$C_{16}H_{17}N_2O_6S$ $[M+H–(NH_3)]^+$	365.07965	9.5							Proposed Structure
		$C_{10}H_9N_2O_2$	189.06583	7.5				*X*	✓	✓	
		$C_9H_8NO_2$	162.05482	6.5	-1.48	43.75	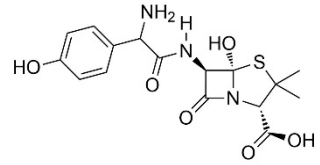				
		$C_5H_{10}NO_2S$	148.04237	1.5							
		$C_5H_7O_2S$	131.01610	2.5							
		C_5H_5OS	113.00550	3.5							
		C_7H_7O	107.04916	4.5							
0.532	**TP 382 (E2)**	$C_{16}H_{20}N_3O_6S$ $[M+H]^+$	382.10614	8.5	-						Proposed Structure
		$C_{16}H_{17}N_2O_6S$ $[M+H–(NH_3)]^+$	365.07974	9.5	-1.46	56.67					
		$C_{10}H_9N_2O_2$	189.06616	7.5							
		$C_9H_8NO_2$	162.05492	6.5				*X*	✓	✓	
		$C_5H_{10}NO_2S$	148.04259	1.5							

		$C_5H_7O_2S$	131.01564	2.5						
		C_5H_5OS	113.00517	3.5						
		C_7H_7O	107.04927	4.5						
0.929	**TP 382 (S-O)**	$C_{16}H_{20}N_3O_6S$ $[M+H]^+$	382.10602	8.5			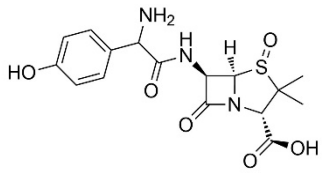	*X*	✓	✓	[248][249, 250]
		$C_{16}H_{17}N_2O_6S$ $[M+H-(NH_3)]^+$	365.07938	9.5							
		$C_{15}H_{17}N_2O_5$	337.08368	8.5	-1.44						
		$C_9H_9N_2O$	161.07129	6.5		100.00					
1.106	**TP384 (H1)**	$C_{16}H_{22}N_3O_6S$ $[M+H]^+$	384.12177	7.5	-1.71	72.73	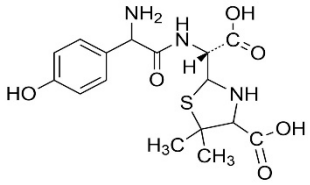	✓	✓	✓	[189]
		$C_{16}H_{19}N_2O_6S$ $[M+H-(NH_3)]^+$	367.09509	8.5							
		$C_{15}H_{19}N_2O_4S$	323.10626	7.5							
		$C_7H_{13}N_2O_4S$	189.06905	2.5							
		$C_6H_{10}NO_2S$	160.04237	2.5							
1.146	**TP384 (H2)**	$C_{16}H_{22}N_3O_6S$ $[M+H]^+$	384.12170	7.5	-1.90	80.00	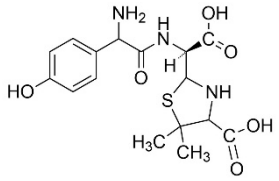	✓	✓	✓	[189]
		$C_{16}H_{19}N_2O_6S$ $[M+H-(NH_3)]^+$	367.09537	8.5							
		$C_{15}H_{19}N_2O_4S$	323.10568	7.5							
		$C_7H_{13}N_2O_4S$	189.06898	2.5							
		$C_6H_{10}NO_2S$	160.04245	2.5							
1.200	**TP367**	$C_{16}H_{19}N_2O_6S$ $[M+H]^+$	367.11459	7.5	-1.70	66.67	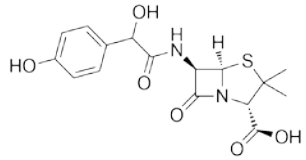	✓	✓	*X*	Proposed Structure
		$C_{16}H_{17}N_2O_5S$ $[M+H-(H_2O)]^+$	349.08456	8.5							
		$C_{11}H_8NO_3S$	234.02122	8.5							
		$C_6H_{10}NO_2S$	160.04240	2.5							
		C_4H_4NOS	114.00066	3.5							
1.669	**TP366**	$C_{16}H_{20}N_3O_5S$ $[M+H]^+$	366.11102	8.5	-1.83	66.67	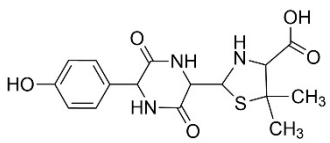	✓	✓	✓	[189]
		$C_{10}H_{11}N_2O_3$	207.07625	6.5							
		$C_6H_{10}NO_2S$	160.04257	2.5							
		C_5H_8NS	114.03694	2.5							

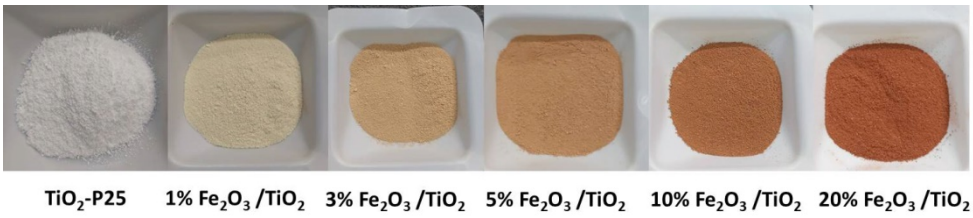

Figure S1. Photo images of TiO_2 (P25) and TiO_2/Fe_2O_3 nanocomposites

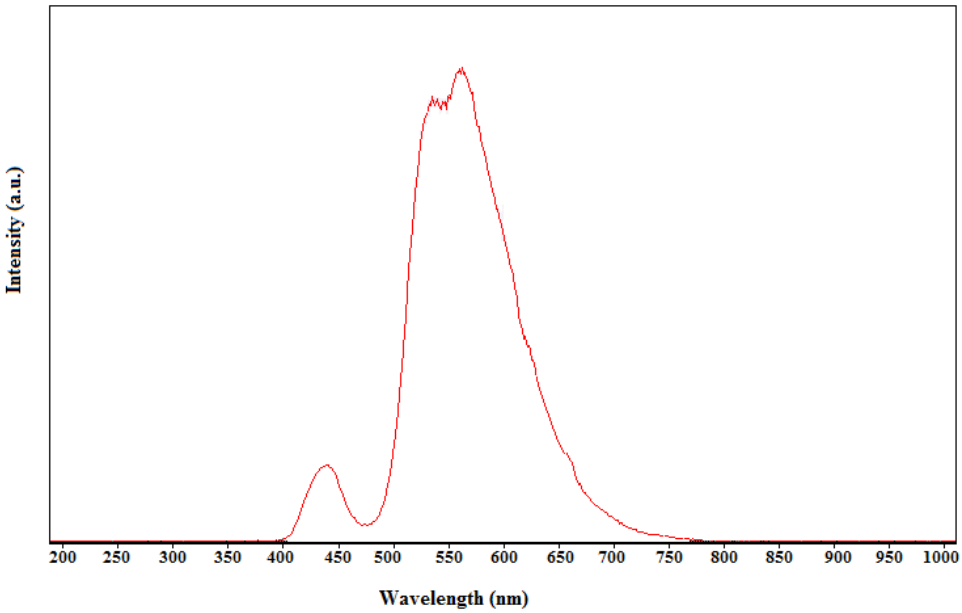

Figure S2. Full Spectrum Coverage of LED used in PEC tests

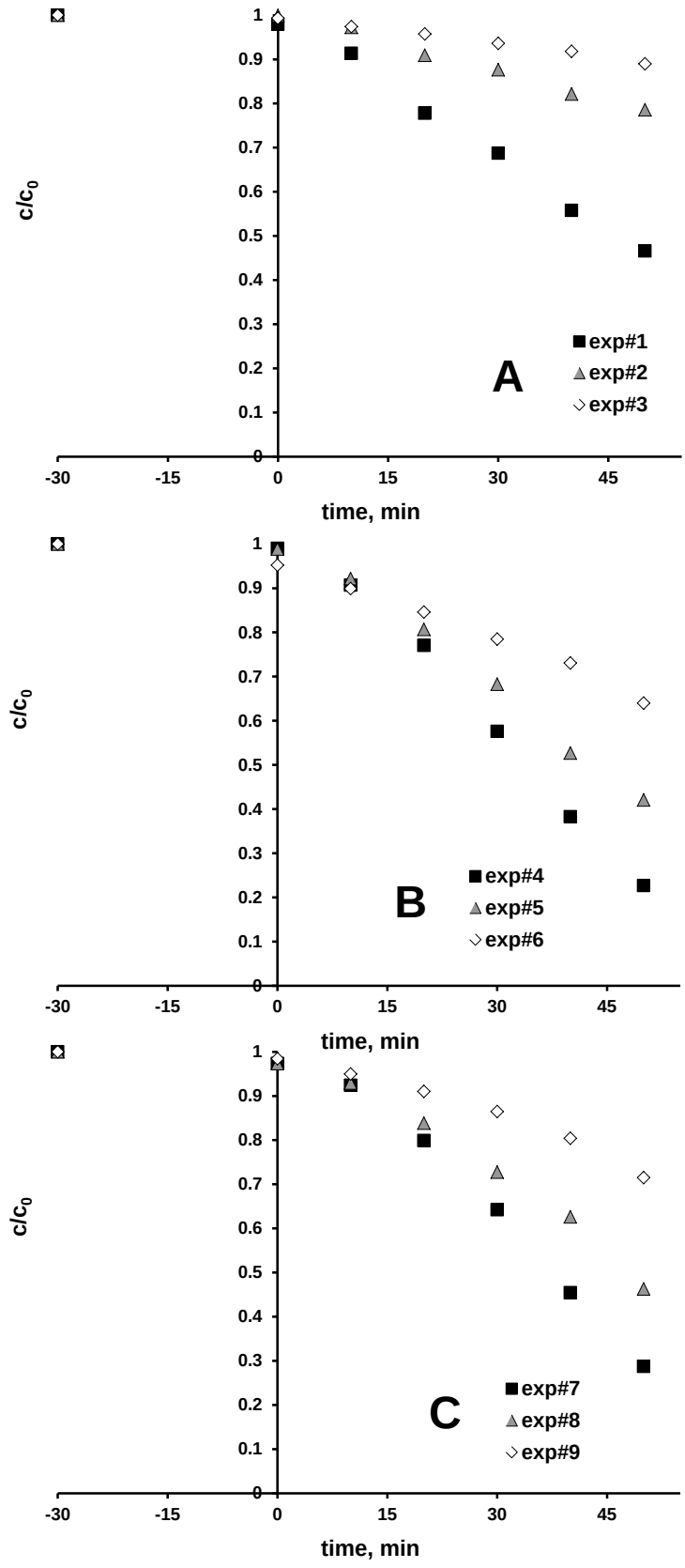

Figure S3. Kinetics of AMX degradation by solar-TiO_2@Fe_2O_3/PS, Experimental conditions set by FFD (**Table S2.1**, Appendix)

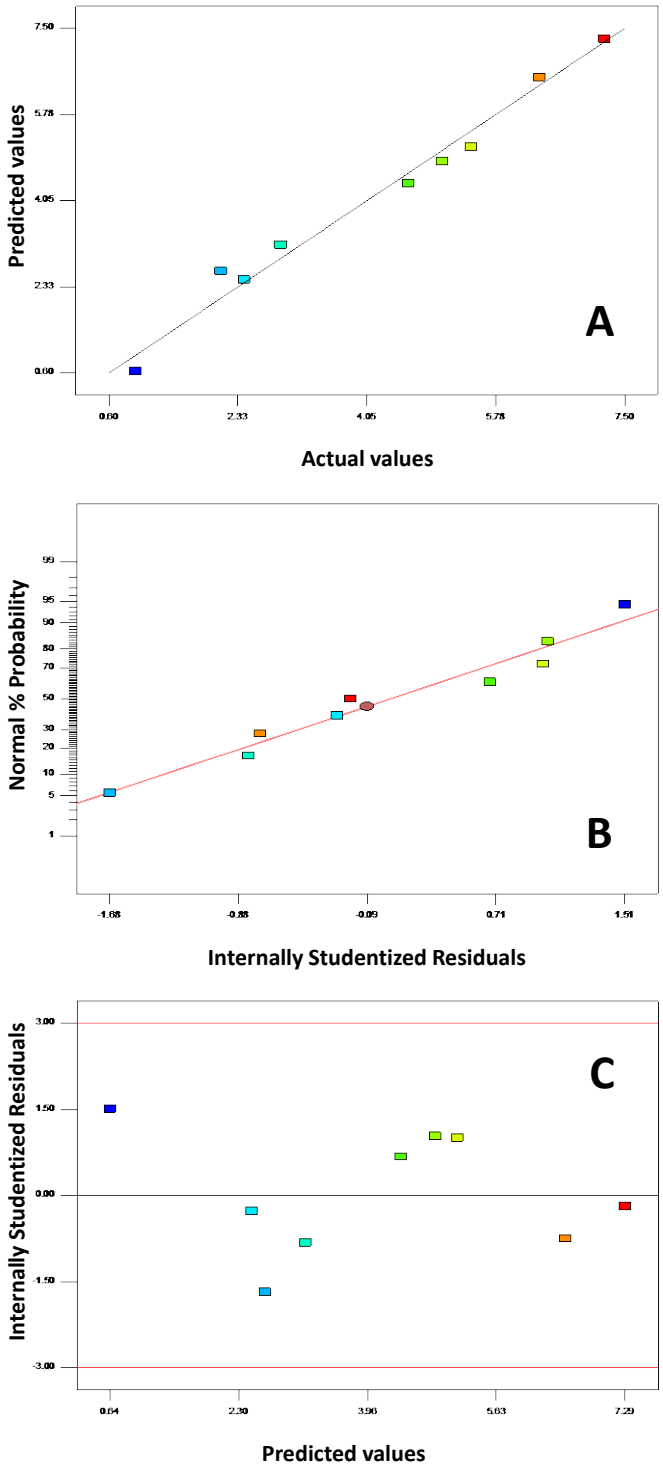

Figure S4. Residual diagnostics of RSM model predicting AMX degradation rate constants (k_{obs}) by solar-TiO_2@Fe_2O_3/PS process after 50 min treatment: (**A**) observed vs. predicted plot, (**B**) normal probability plot, and (**C**) internally studentized residuals vs. predicted values plot

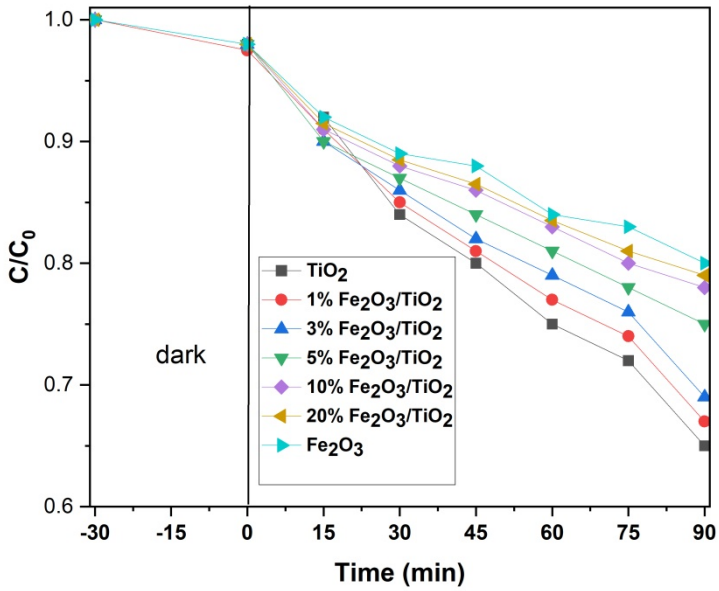

Figure S5.1. Photocatalytic removal of AMX using prepared photocatalysts under solar irradiation (*Conditions:* [catalyst dosage]= 0.5 g/L ; [AMX]= 0.050 mM ; initial pH = natural pH (5.5))

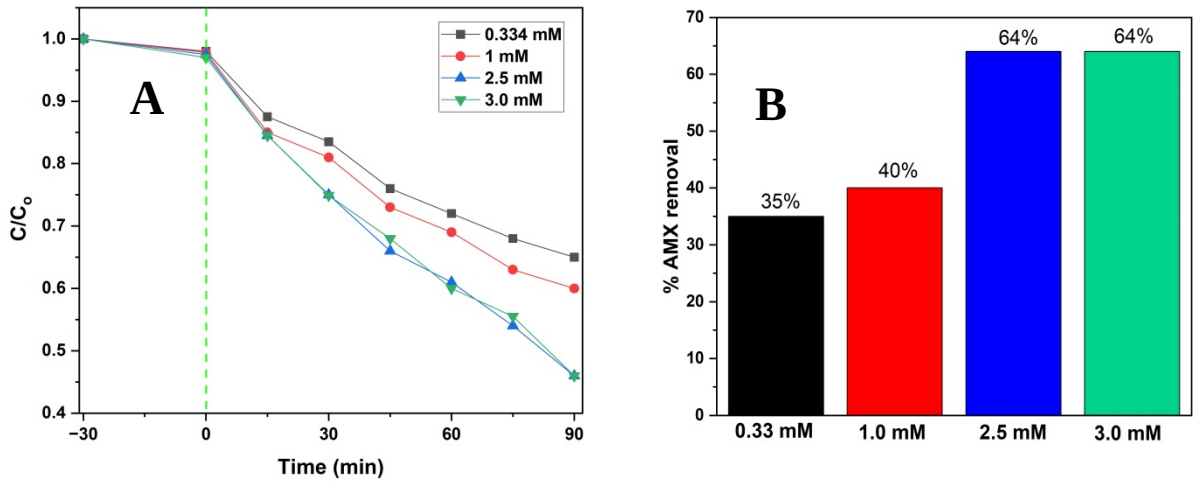

Figure S5.2. Photocatalytic removal of AMX using prepared 5% (*w/w*) Fe_2O_3/TiO_2 under visible light irradiation with different PS concentration; (**A**) removal profile and (**B**) % removal per different PS concentration (*Conditions:* [catalyst dosage]= 0.5 g/L ; [AMX]= 0.050 mM ; initial pH = natural pH (5.5))

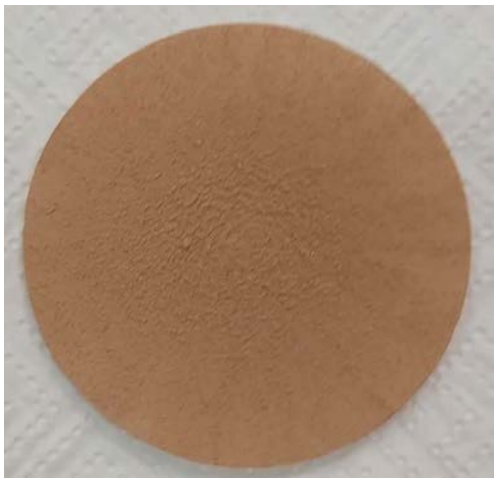

Figure S6. Photo image of immobilized 5% (*w/w*) Fe_2O_3/TiO_2 nanocomposite onto glass support

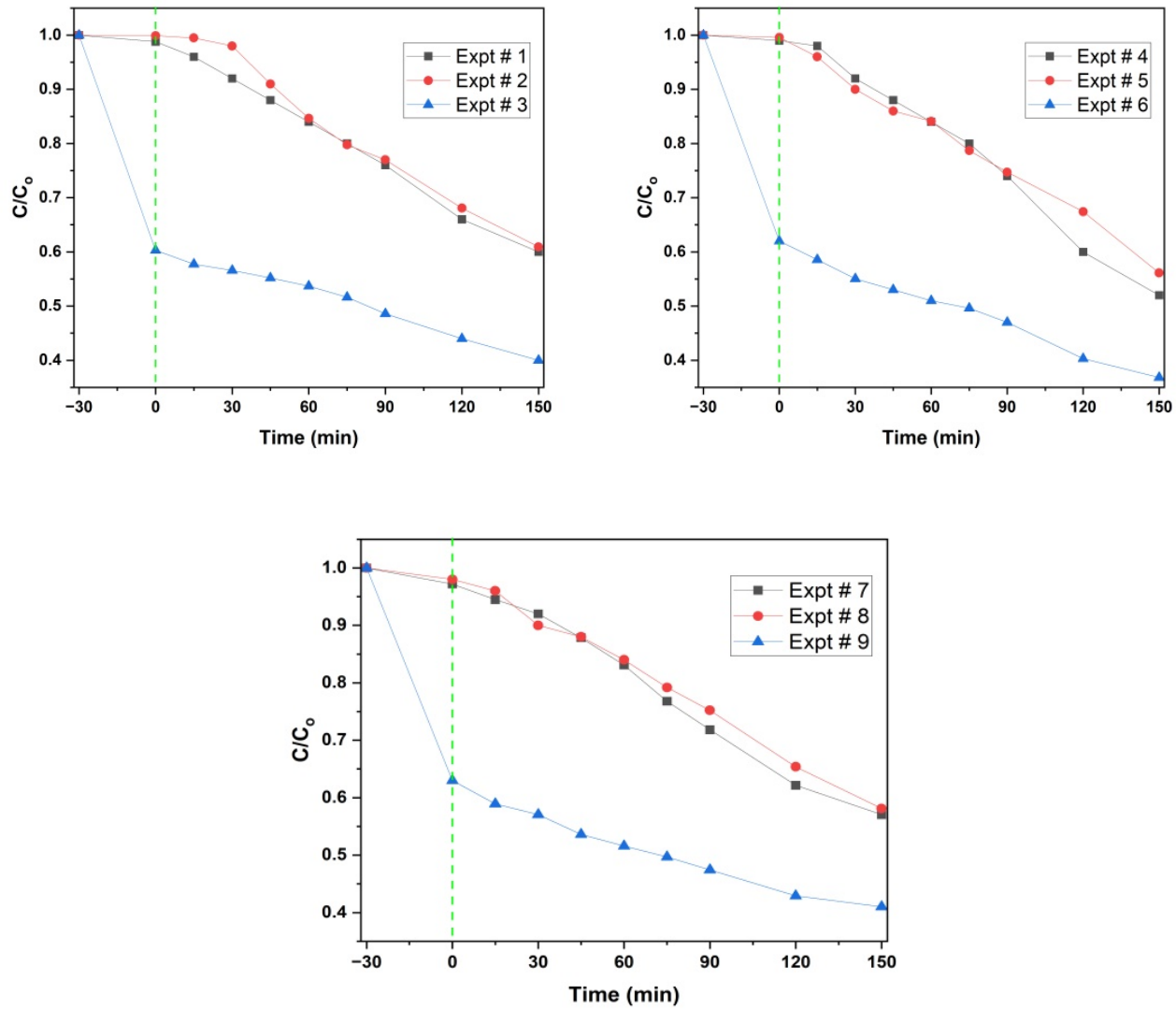

Figure S7. AMX photocatalytic treatment by vis-(5% (*w/w*) Fe_2O_3/TiO_2)/PS. Experimental conditions set by FFD (**Table S2.2**, Appendix)

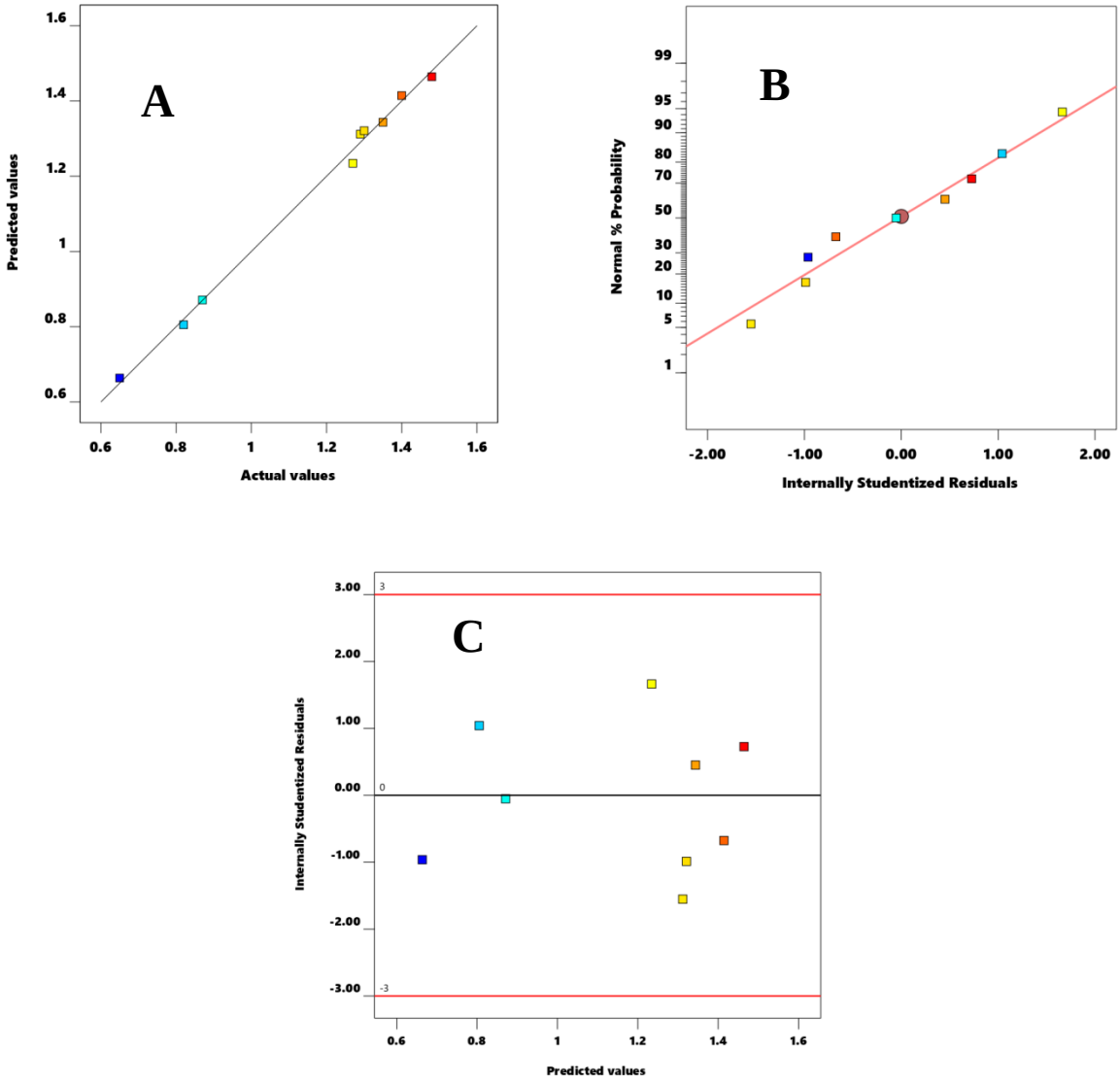

Figure S8. Residual diagnostics of RSM model predicting AMX removal rate constants (k_{obs}) by vis-(5% (*w*/*w*) Fe_2O_3/TiO_2)/PS process after 150 min treatment: (**A**) observed *vs.* predicted plot, (**B**) normal probability plot, and (**C**) internally studentized residuals *vs.* predicted values plot

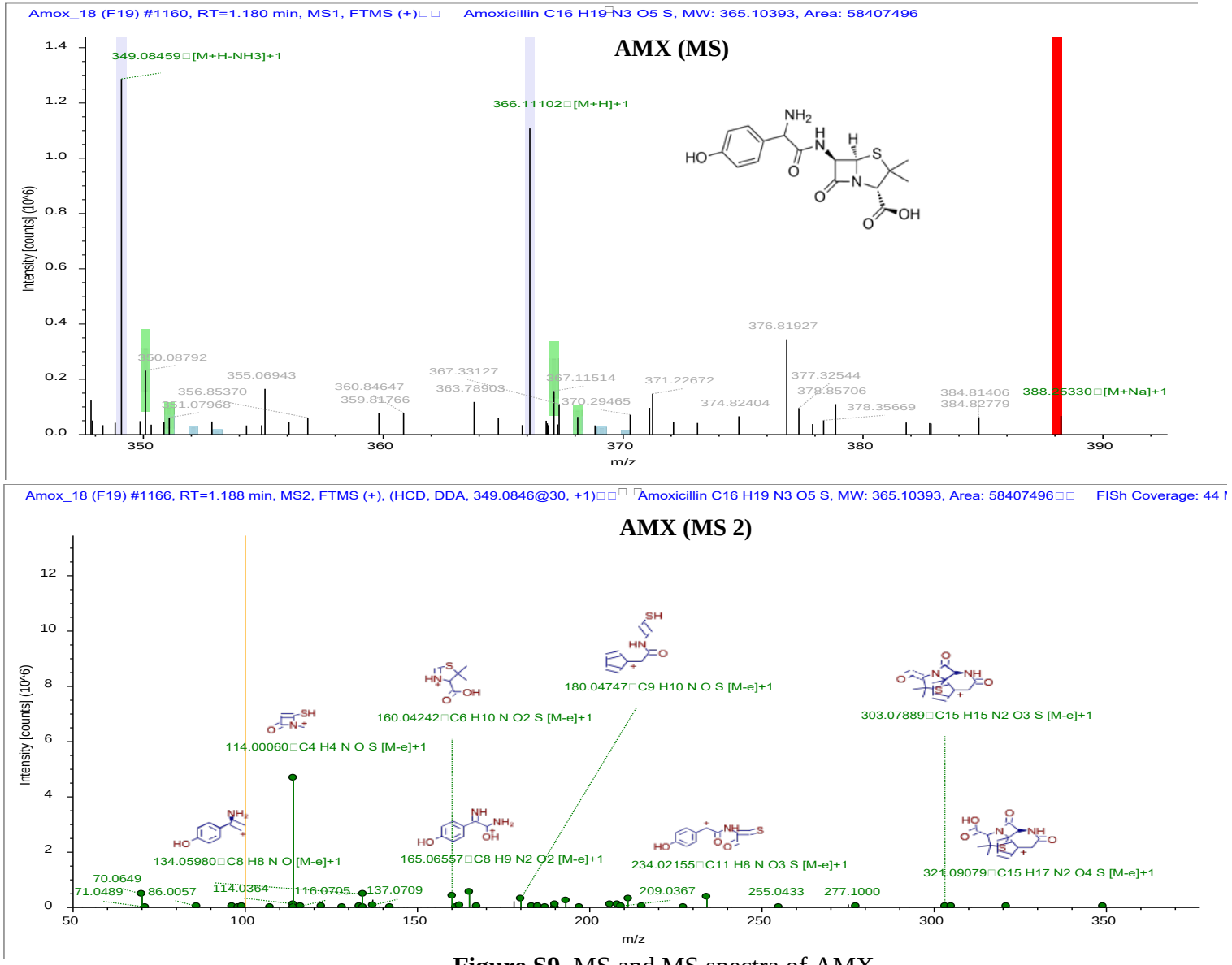

Figure S9. MS and MS spectra of AMX

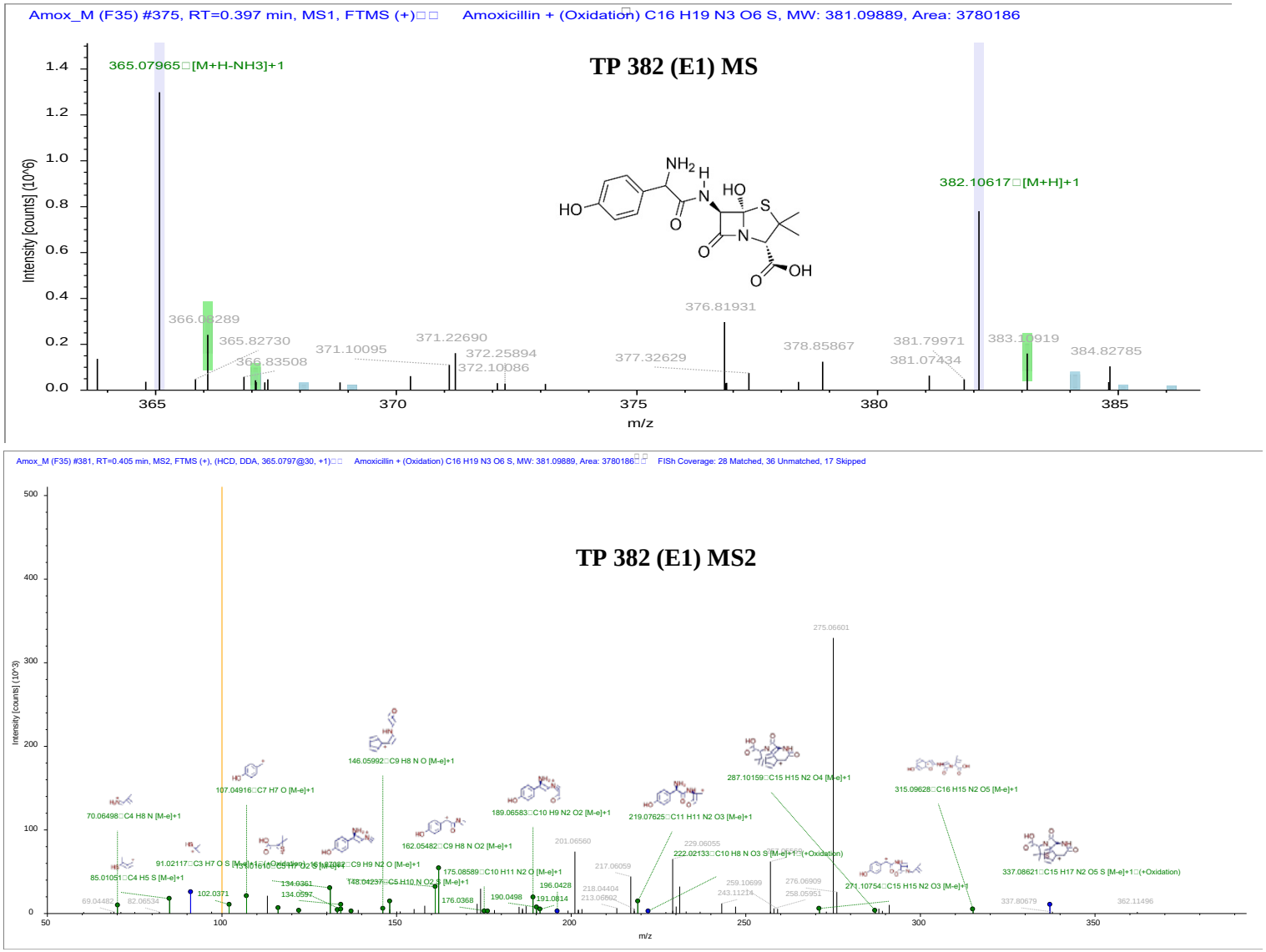

Figure S10. MS and MS spectra of TP 382 (E1)

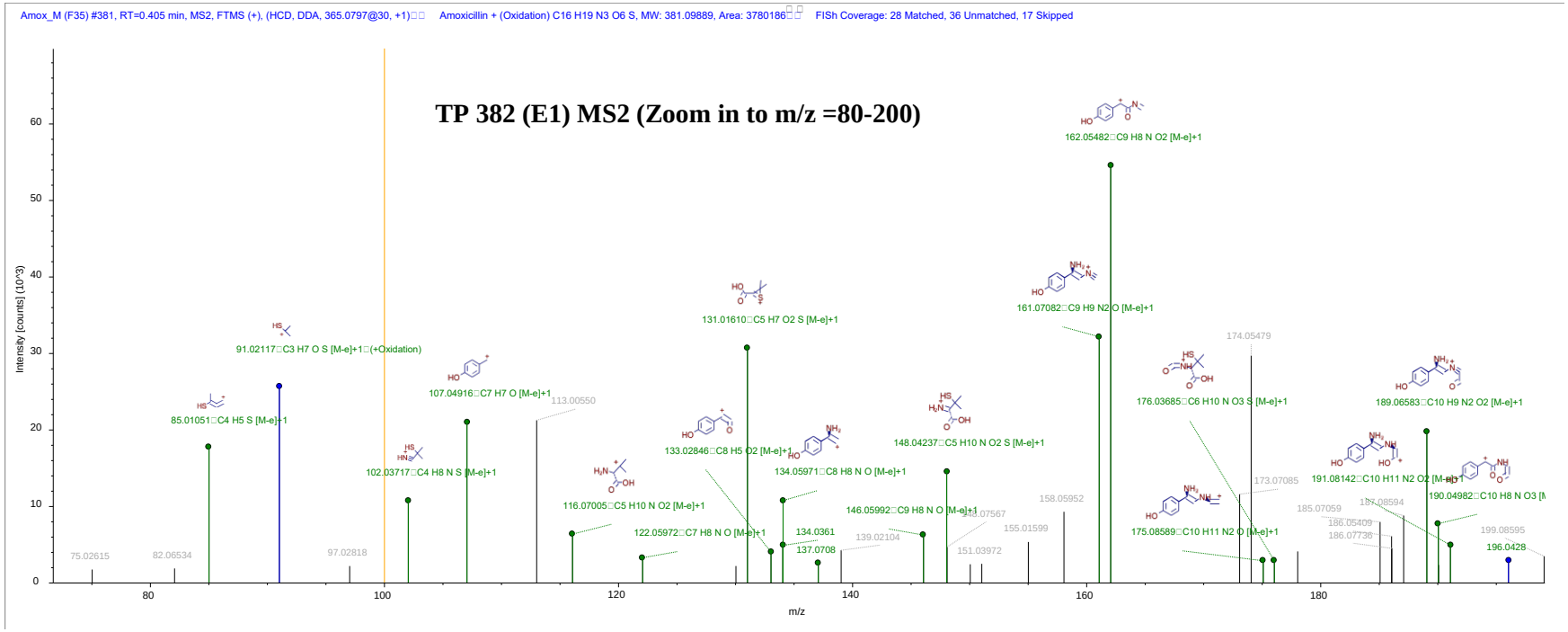

Figure S10.1. MS2 spectrum (magnified) of TP 382 (E1)

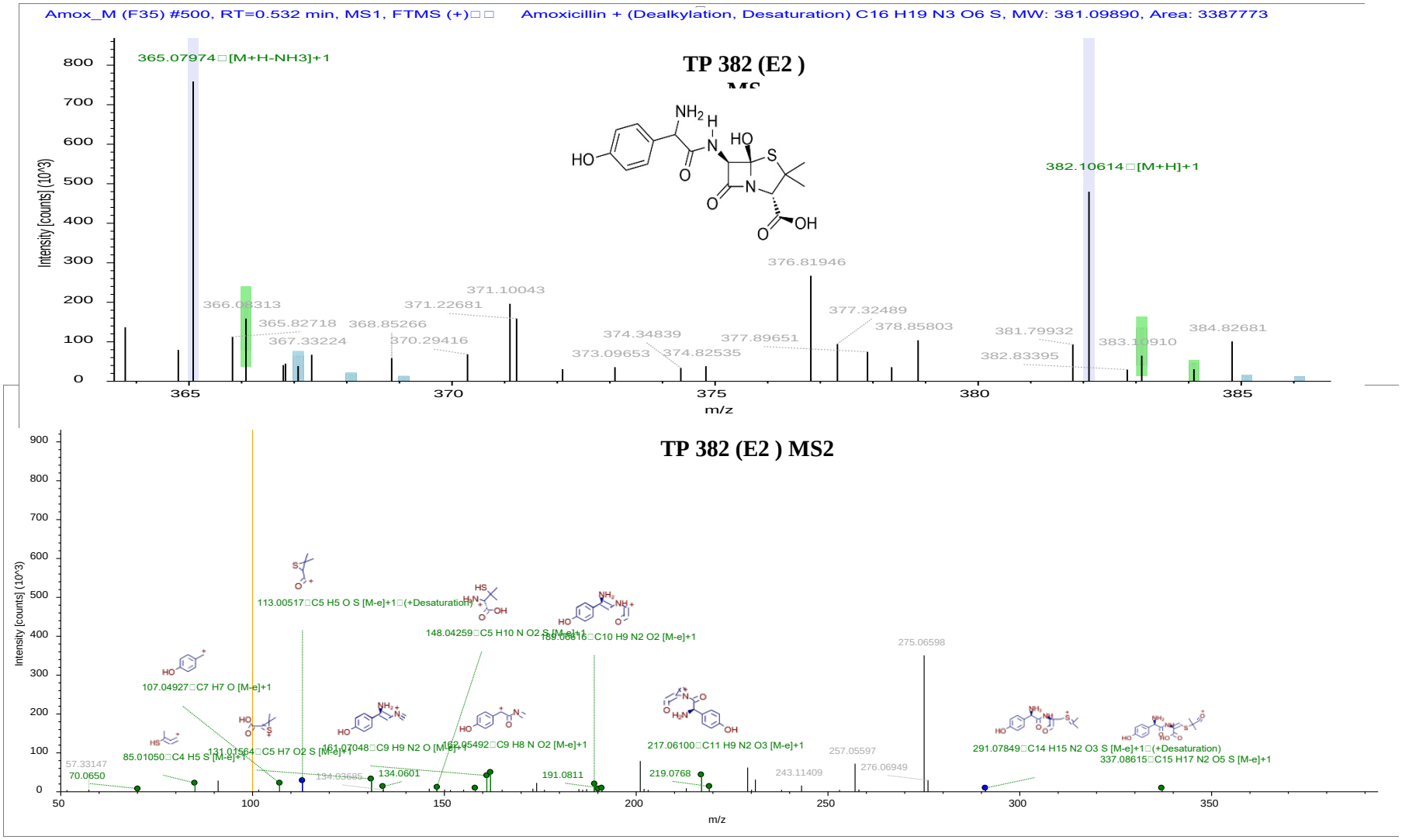

Figure S11. MS and MS2 spectra of TP 382 (E2)

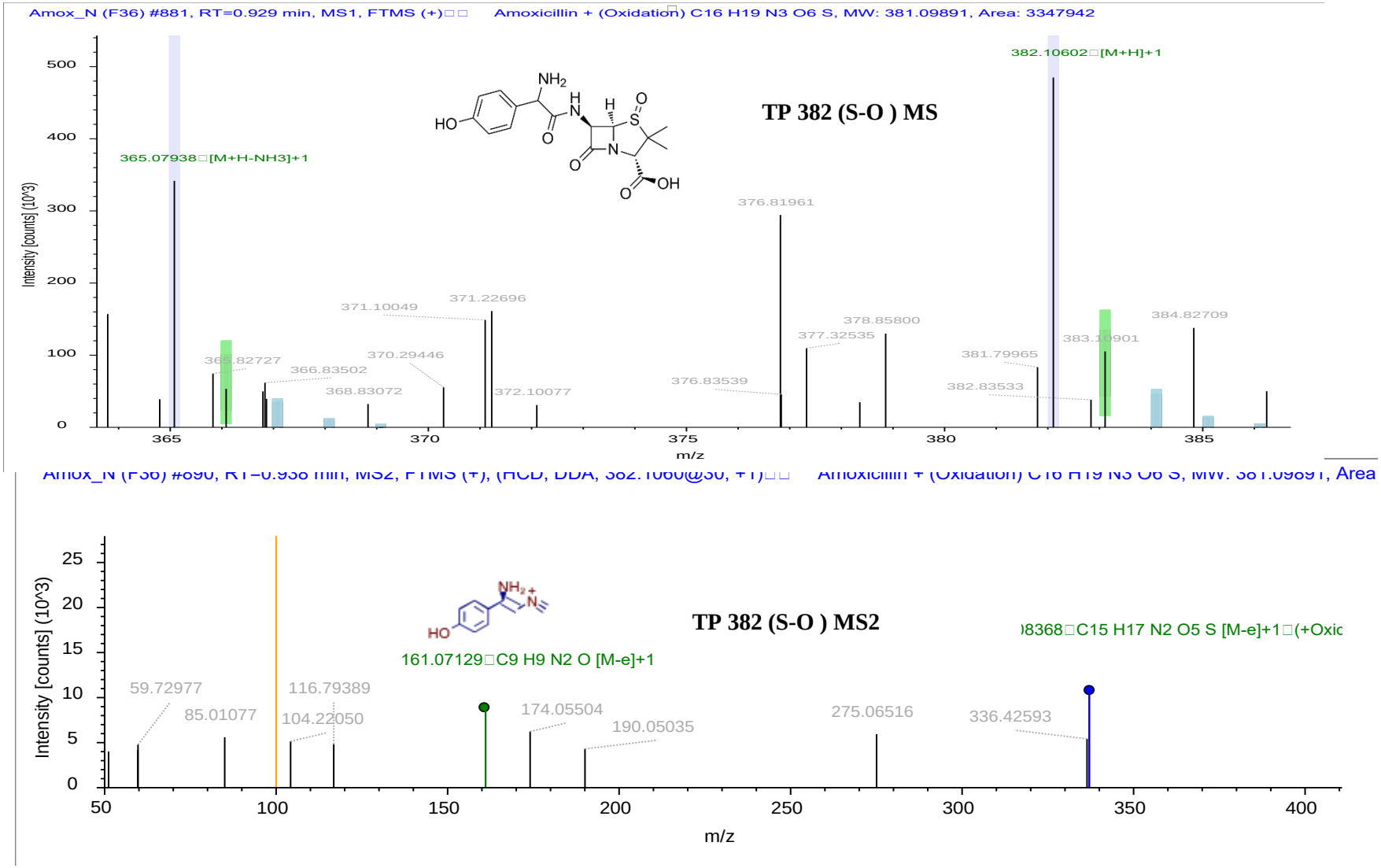

Figure S12. MS and MS2 spectra of TP 382 (S-O)

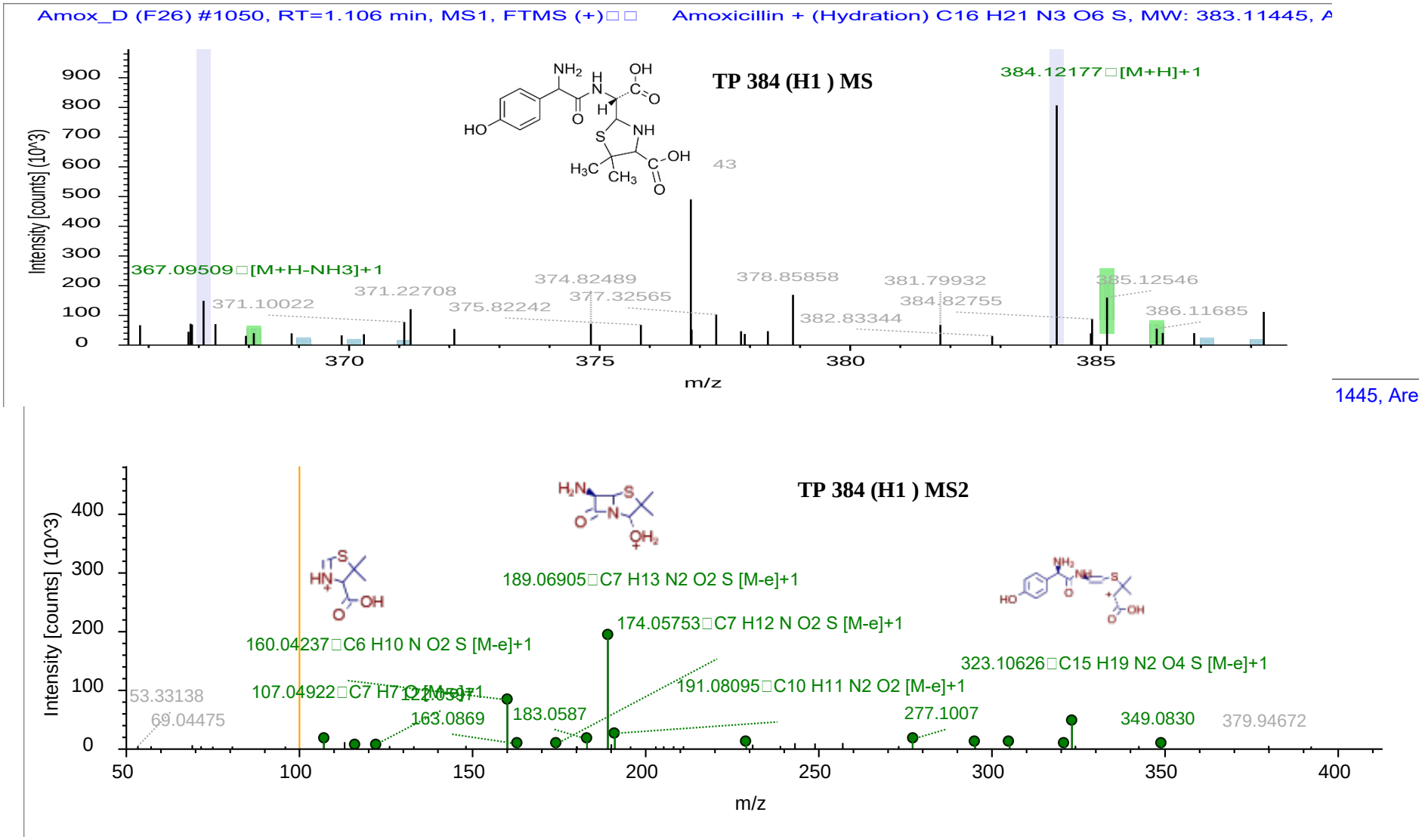

Figure S13. MS and MS2 spectra of TP 384 (H1)

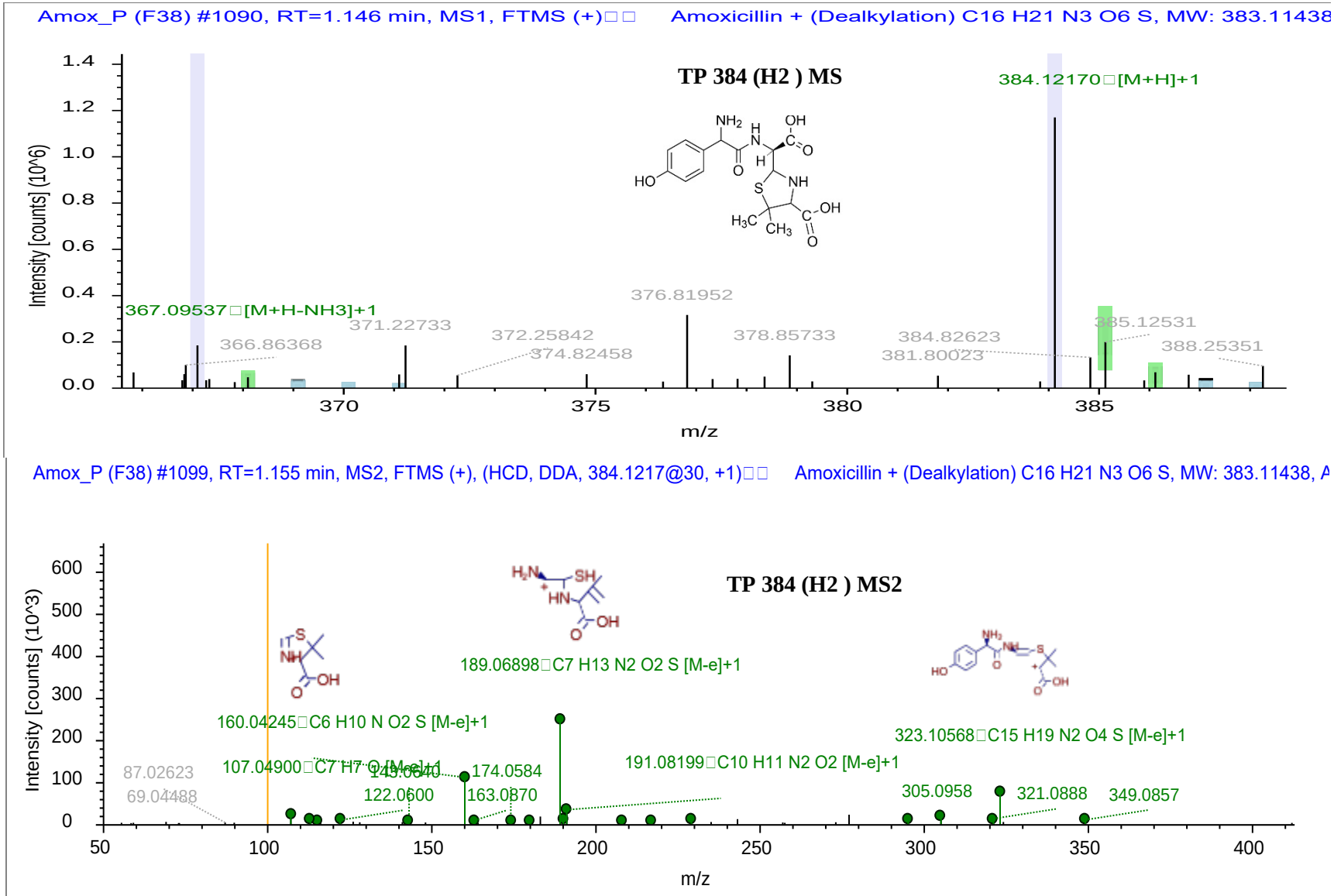

Figure S14. MS and MS2 spectra of TP 384 (H2)

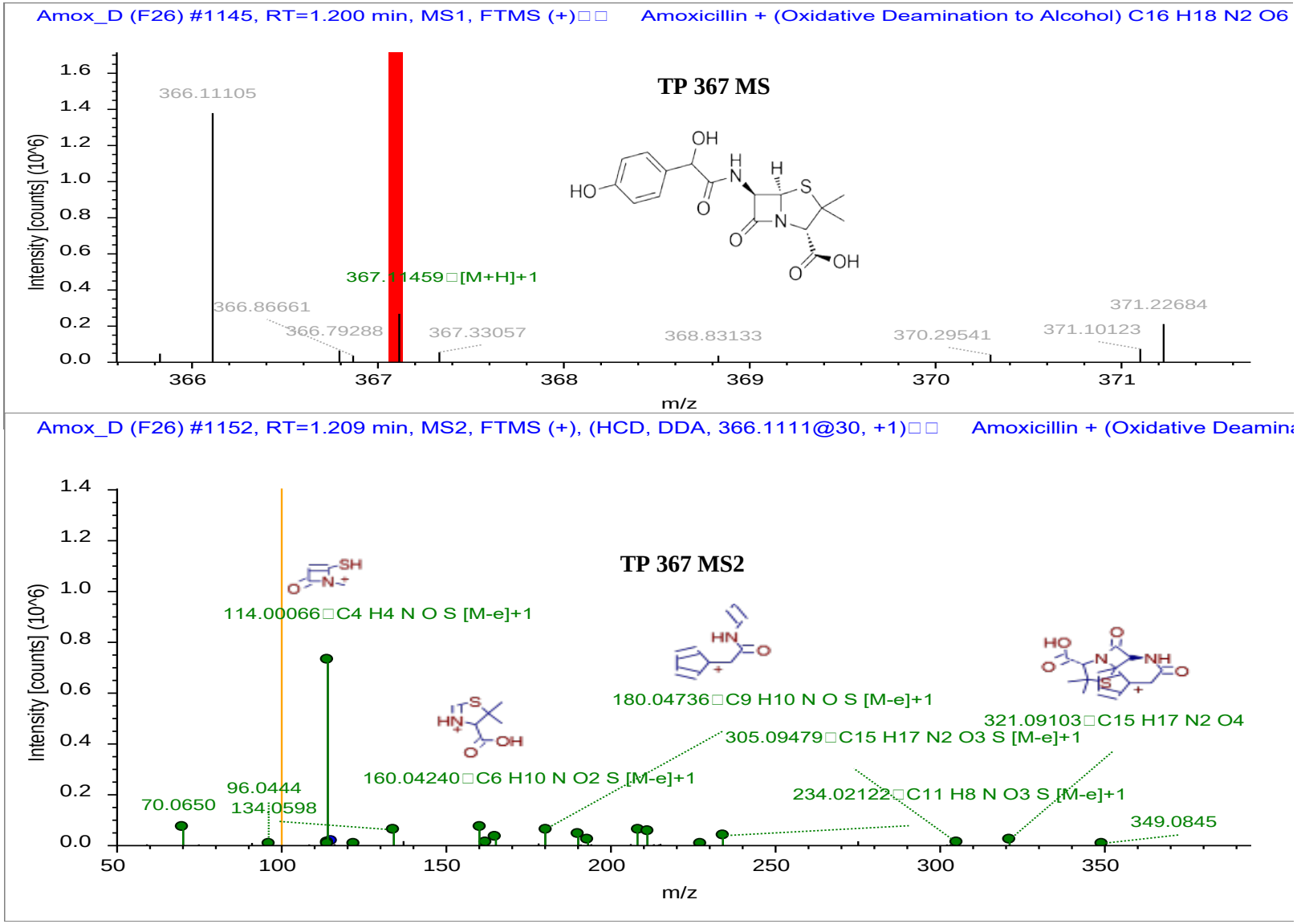

Figure S15. MS and MS2 spectra of TP 367

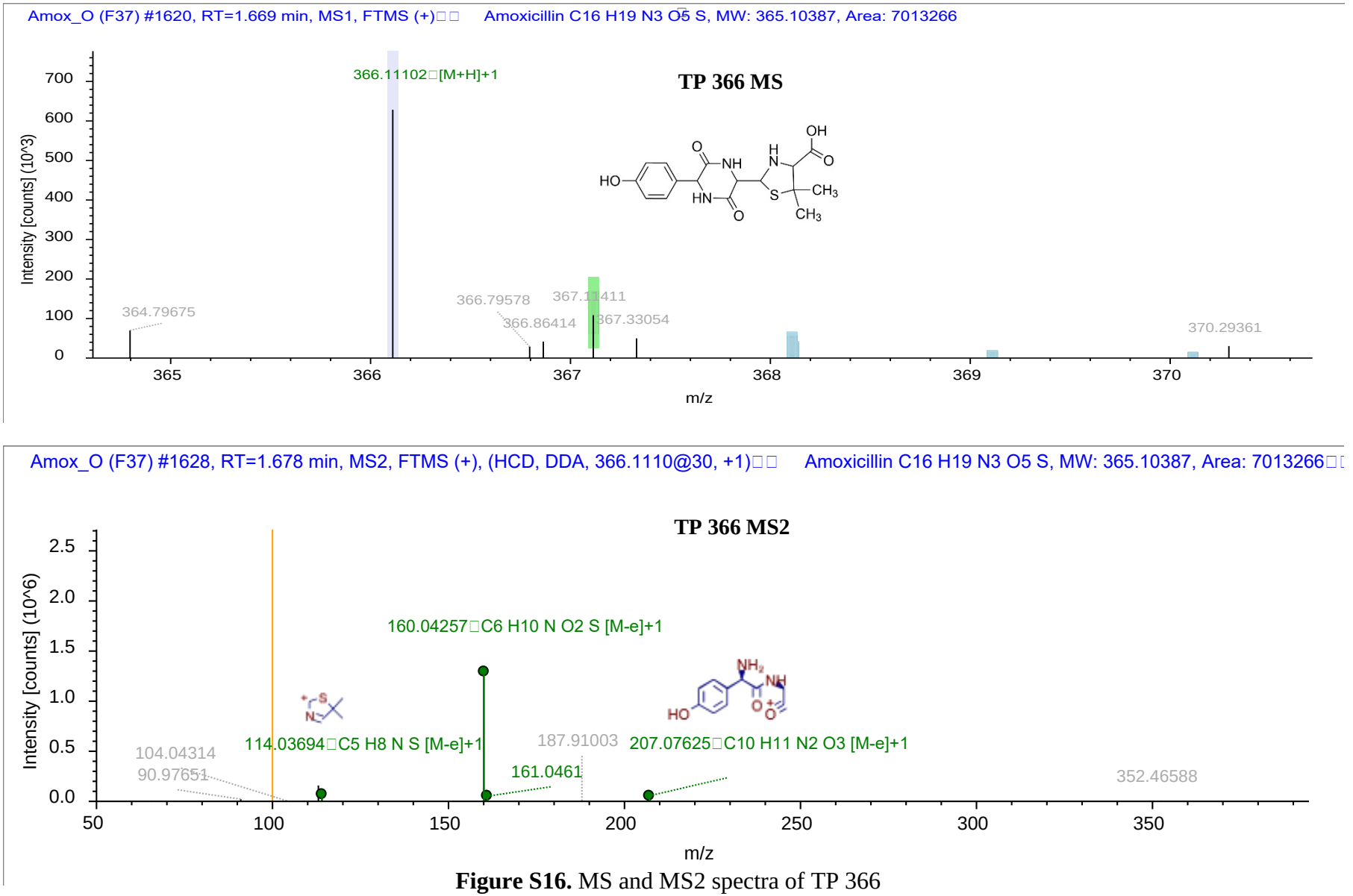

Figure S16. MS and MS2 spectra of TP 366

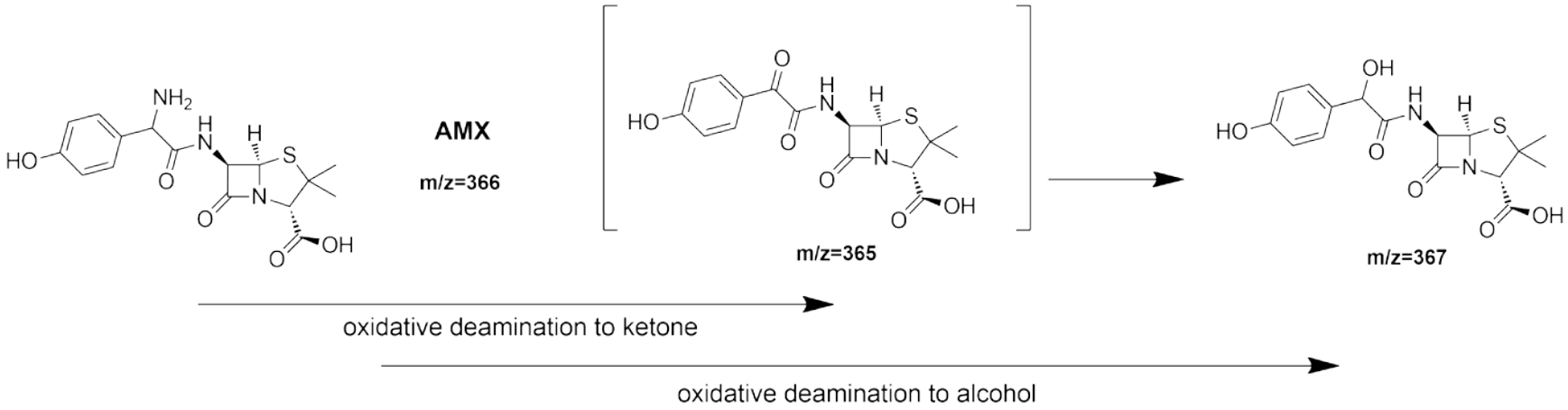

Figure S17. Formation of TP 365 (*m/z*=365) and TP 367

Author's biography

Francis Monserrata dela Rosa [redacted] Francis obtained his BS in Chemistry (Cum Laude) from the Pamantasan ng Lungsod ng Maynila (Philippines) and MS in Chemistry from the De La Salle Univesity (Philippines). He worked as a Junior Instructor in Chemistry Department at Adamson University (Philippines) while finishing his Master's degree, focusing on Visible-light activated photocatalysts and Hydroxyapatite based photocatalysts. He was a recipient of an international research internship grant in Academia Sinica (Taiwan) under TIGP-IIP program, where he developed perovskite-based catalyst for deNO_x applications. He received an award as "Outstanding Reviewer" from Elsevier's Colloids and Surfaces A: Physicochemical & Engineering Aspects and three awards as "Recognized Reviewer" from Elsevier's Ceramics International, Nano-Structures & Nano-Objects and Colloids and Surfaces A: Physicochemical & Engineering Aspects.

Francis (Franjo) was hired in 2019 as an early stage researcher by the NOWELTIES project, an Innovative Training Network part of the framework of EU Horizon 2020's Marie Skłodowska- Curie Actions. His research focuses on development of TiO_2–Fe_2O_3 nanocomposites for the removal of amoxicillin from water. During the project, he spent two and a half years in the Faculty of Chemical Engineering and Technology, University of Zagreb (Croatia) and 6 months in the Catalan Institute for Water Research (Girona, Spain).

Author's published works

(Published papers included in Dissertation)

dela Rosa, F.M.; Papac, J.; Garcia-Ballesteros, S.; Kovačić, M.; Katančić, Z.; Kušić, H.; Lončarić Božić, A. Solar Light Activation of Persulfate by TiO_2/Fe_2O_3 Layered Composite Films for Degradation of Amoxicillin: Degradation Mechanism, Matrix Effects, and Toxicity Assessments. *Adv. Sustain. Syst*. **2021**, 5.

dela Rosa, F.M.; Popović, M.; Papac Zjačić, J.; Radić, G.; Kraljić Roković, M.; Kovačić, M.; Farré, M.J.; Genorio, B.; Lavrenčič Štangar, U.; Kušić, H.; Lončarić Božić, A. Visible-Light Activation of Persulfate or H_2O_2 by Fe_2O_3/TiO_2 Immobilized on Glass Support for Photocatalytic Removal of Amoxicillin: Mechanism, Transformation Products, and Toxicity Assessment. *Nanomaterials* **2022,** 12.

Perović, K.; **dela Rosa, F.M**.; Kovačić, M.; Kušić, H.; Lavrenčič Štangar, U.; Fresno, F.; Dionysiou, D.D.; Lončarić Božić, A. Recent achievements in development of TiO_2 -based composite photocatalytic materials for solar driven water purification and water splitting. *Materials* (Basel). **2020**, 13.

(Authors other publications)

Edralin, E.J.M.; Garcia, J.L.; **dela Rosa, F.M**.; Punzalan, E.R. Sonochemical synthesis, characterization and photocatalytic properties of hydroxyapatite nano-rods derived from mussel shells. *Mater. Lett*. **2017**, 196.

Vicente Rubi, R.; Roque, E.; **dela Rosa, F.M**.; Martin Estoque, R.; Olvido, G.; Jane Perey, P.; Teresa, J.S.; Anne Tesalona, M. Photocatalytic degradation of Atrazine herbicide using nano-Hydroxyapatite from Cow Bone synthesized via Simulated Body Fluid. *IOP Conf. Ser. Mater. Sci. Eng.* **2020**, 778, 012013.

Rubi, R.V.C.; Olay, J.G.; Caleon, P.B.G.; De Jesus, R.A.F.; Indab, M.B.L.; Jacinto, R.C.H.; Sabalones, M.S.; **dela Rosa, F**.M.; Hamidah, N.L. Photocatalytic degradation of diazinon in g-C_3 N_4/Fe(III)/persulfate system under visible LED light irradiation. *Appl. Sci. Eng. Prog*. **2021**, 14, 100–107.

Go, A.D.; **dela Rosa, F.M**.; Camacho, D.H.; Punzalan, E.R. Dataset on photocatalytic degradation of Levofloxacin using hydroxyapatite photocatalyst: Optimization by response surface methodology. *Data Br*. **2022**, 42.